



BLACKLIGHT
POWER, Inc

Technical Presentation

BlackLight Power ^{TM SM}

A New Energy Source Based on a Breakthrough in Hydrogen Chemistry with Paradigm-Shifting Applications

Microdistributed Power



Heating



Specialty Chemicals

Lighting

Central Power



Motive Power

Lasers



Validation

Patents Issued in US and Abroad

Validated by Leading Scientists and Engineers

Technical

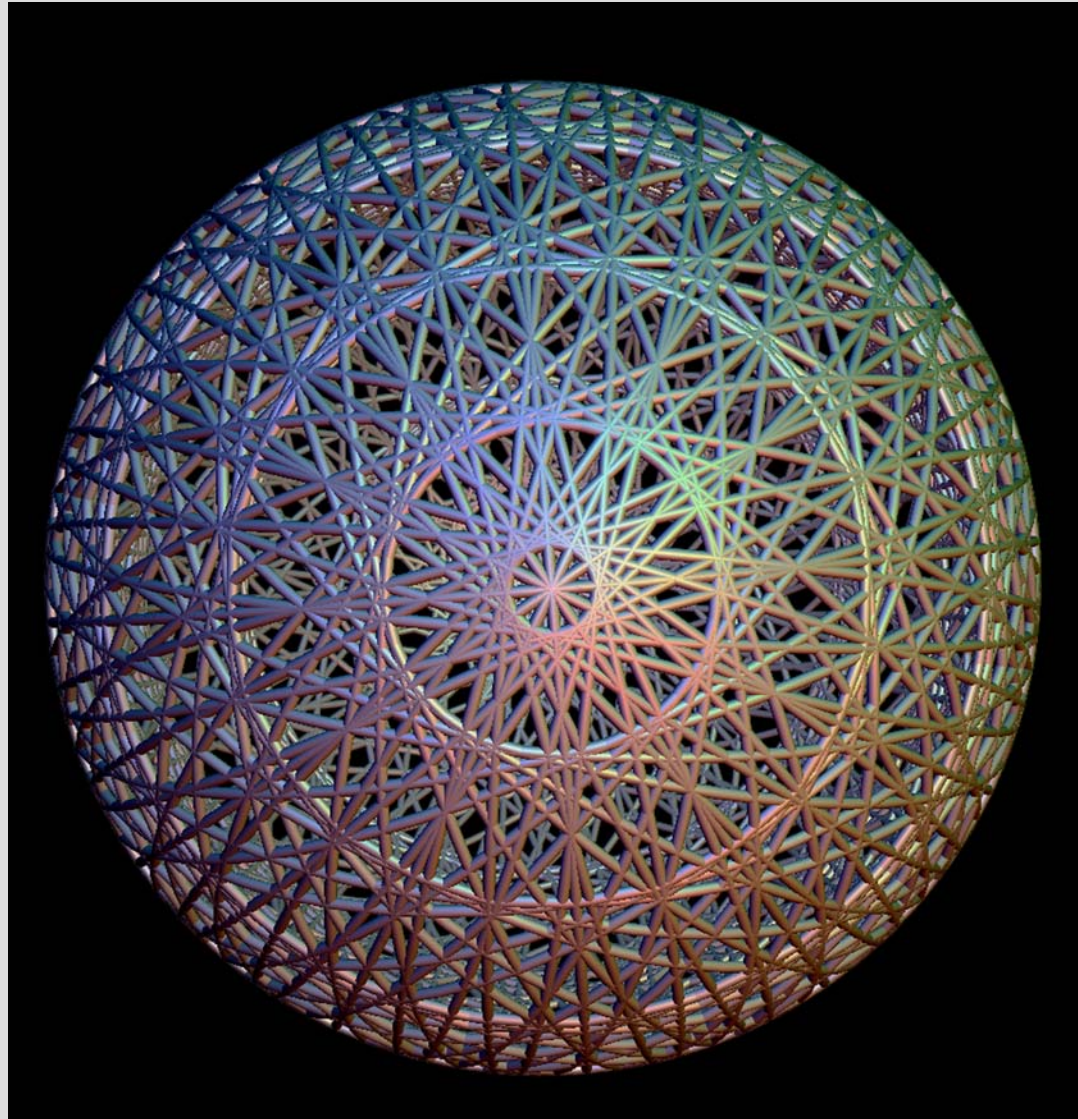
- >100 papers, (76 published) >50 conference presentations
- Spectral emission lines of lower-state atomic hydrogen, molecular hydrogen, hydrogen molecular ion and hydride ion
- Isolation of lower-energy-state molecular hydrogen
- Compounds containing new states of hydrogen
- Chemically generated or assisted plasmas, plasma afterglow, hydrogen line broadening, catalyst emission, high optical output power, inverted hydrogen population
- Calorimetry, water-bath measurements of significant net heat

Applications

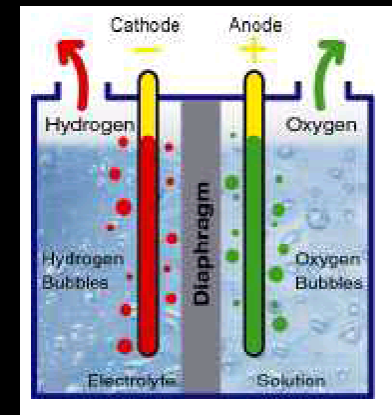
- 1/20th scale power-source prototype
 - Plasma dynamic plasma to electric converter device
 - Bright light sources
 - Laser media
 - Chemical Compounds – Synthetic diamonds, silicon hydrides and many others
- **Highly predictive theory** – application of Maxwell's equations precisely predicts hundreds of fundamental spectral observations in exact equations with no adjustable parameters as well as laboratory results of novel H reaction

Validations and Technical Due Diligence – underway with National labs, defense contractors, electronics manufacturers, large conglomerates, multi-national energy companies and others

Visualizing Classical Physics



Enabling Electric Generation and H₂ Production



The BlackLight Process



Animation of the
Blacklight Process



Solid Fuel Reactor



Blacklight
Plant Process

Products are
lower-energy H
atoms, molecular
ions, molecules,
and hydride ions

Advantages of BLP Technology

BlackLight's catalysis of atomic hydrogen represents *a new source of energy* with H₂O as the source of hydrogen fuel obtained by diverting a fraction of the output energy of the process to split water into its elemental constituents.

Moreover, rather than air pollutants or radioactive waste, *novel hydride compounds* with potential commercial applications are the products

Review of Theory

- Assume physical laws apply on all scales including the atomic scale
- Start with first principles
 - Conservation of mass-energy
 - Conservation of linear and angular momentum
 - Maxwell's Equations
 - Newton's Laws
 - Special Relativity

Review of Theory

- Bohr model of the atom

$$E_n = -\frac{e^2}{n^2 8\pi\epsilon_0 a_H} = \frac{13.598 \text{ eV}}{n^2} \quad n=1,2,3,4,\dots$$

Posulated stability in defiance of Maxwell's equations. Failed at He, excited state spectra, nature of the chemical bond, etc.

- Schrödinger equation introduced nonphysical point-particle-probability-density-waves, Ψ^2 . No stability to radiation and missed spin.
- Textbook Uncertainty Principle argument is FALSE.
E. H. Lieb, The stability of matter, Rev. Mod. Phys. **48**(4), 553 (1976).
- NO first-principles-based prediction of the Rydberg series of spectral lines— only a circular argument regarding definitions for parameters and the ground state in the infinite number of solutions of the Laguerre differential equation and those lines.

Review of Theory

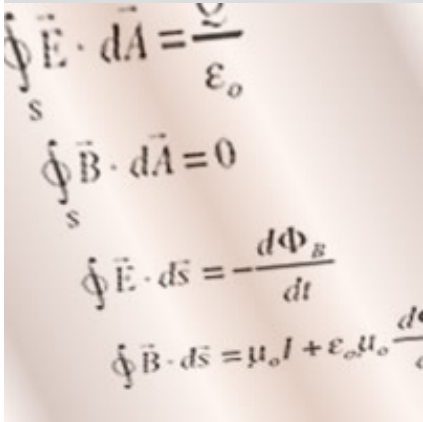
- Dirac equation introduced negative KE and rest mass, virtual particles of the vacuum, requires renormalization of infinities, and gives rise to an infinite cosmological constant, the Klein Paradox, and lack of Einstein causality. There is also **no stability to radiation**.

V. F. Weisskopf, Rev. Mod. Phys. **21**(2), 305 (1949).

- Dirac originally attempted to solve the bound electron physically with stability with respect to Maxwell's equations with the further constraints that it was relativistically invariant and gave rise to electron spin.

P. Pearle, Absence of radiationless motions of relativistically rigid classical electron, Foundations Phys. **7**(11/12), 931 (1977).

Electron as a Source Current: Maxwell's Equations Determines Its Structure

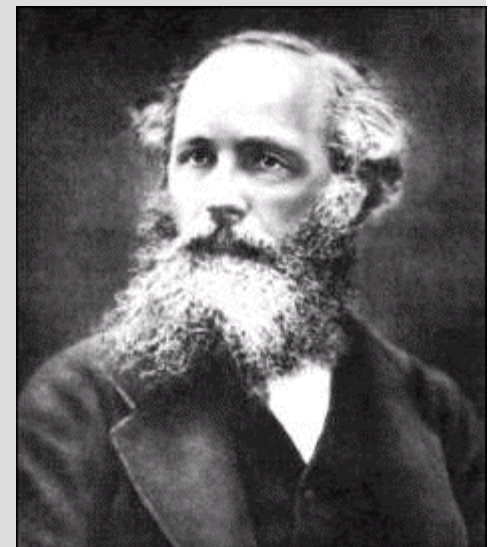


Handwritten Maxwell's equations:

$$\oint_S \vec{E} \cdot d\vec{A} = \frac{Q}{\epsilon_0}$$
$$\oint_S \vec{B} \cdot d\vec{A} = 0$$
$$\oint \vec{E} \cdot d\vec{s} = -\frac{d\Phi_B}{dt}$$
$$\oint \vec{B} \cdot d\vec{s} = \mu_0 I + \epsilon_0 \mu_0 \frac{d\Phi_E}{dt}$$

Using Maxwell's equations, the structure of the electron is derived as a boundary-value problem wherein the electron comprises the source current of time-varying electromagnetic fields during transitions with the constraint that the bound $n=1$ state electron cannot radiate energy.

Although an **accelerated point particle** radiates, an *extended distribution* modeled as a superposition of accelerating charges comprising a current does not have to radiate. The physical boundary condition of nonradiation that was imposed on the bound electron follows from a derivation by Haus.



In place of the Schrödinger boundary condition, $\Psi \rightarrow 0$ as $r \rightarrow \infty$; apply a new boundary condition derived from Maxwell's equations:

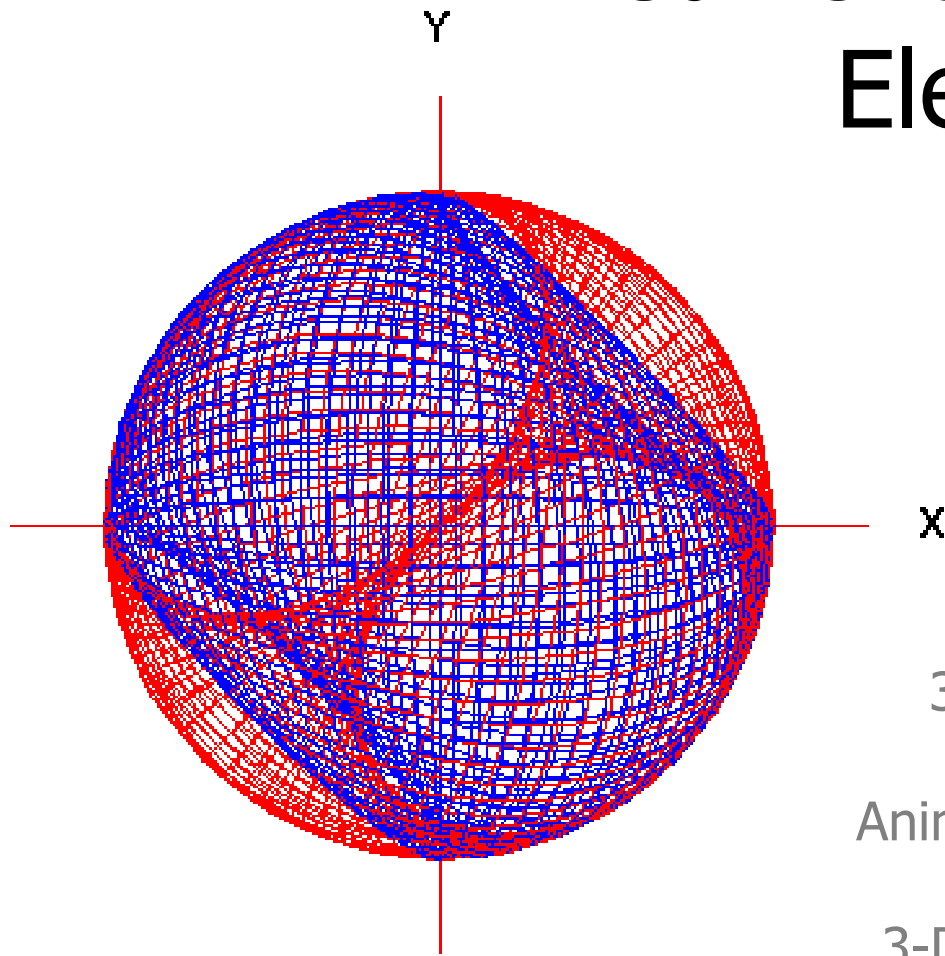
For non-radiative states, the current-density function must not possess space-time Fourier components that are synchronous with waves traveling at the speed of light

H. A. Haus, Am. J. Phys., 54, 1126 (1986)

T. A. Abbott, D. J. Griffiths, Am. J. Phys., 53, 1203 (1985)

G. Goedecke, Phys. Rev. B, 135, 281 (1964)

Current pattern of the Electron Current- Vector Field



View Along the Positive Z Axis

3-D View of Orbitsphere



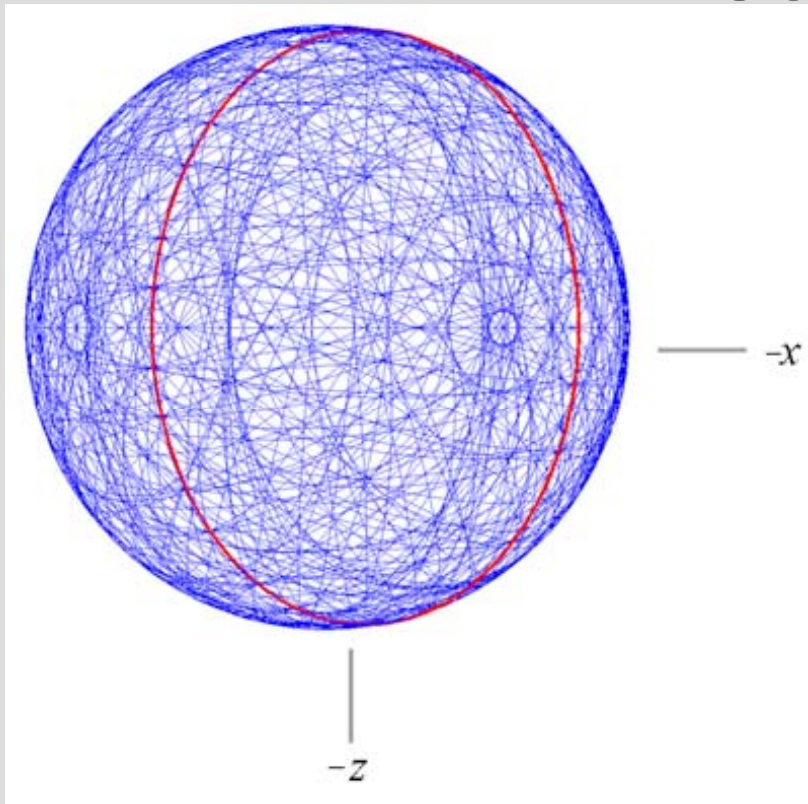
Animation of Current Points



3-D View of Current Points



Exact Generation of the Uniform Current Pattern $Y_0^0(\phi, \theta)$ from the Electron-CVF

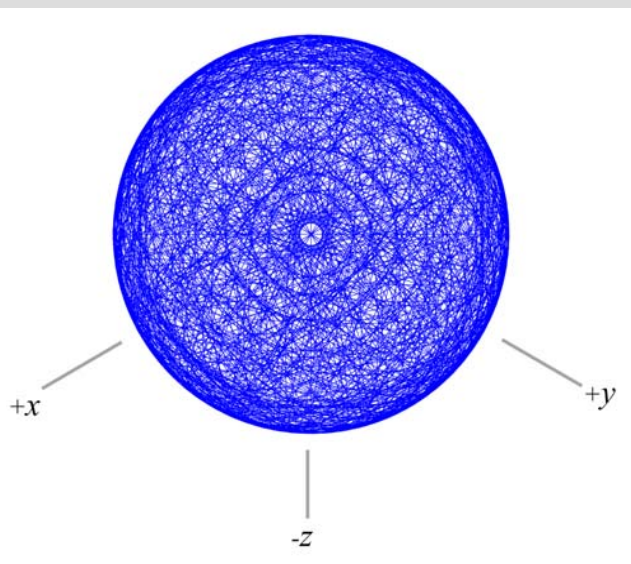


The further constraint that the current density is uniform such that the charge density is uniform, corresponding to an equipotential, minimum energy surface is exactly satisfied by using the electron-cvf as a basis element in an autocorrelation-type convolution operation involving each of the two orthogonal components of the CVF to generate $Y_0^0(\phi, \theta)$.

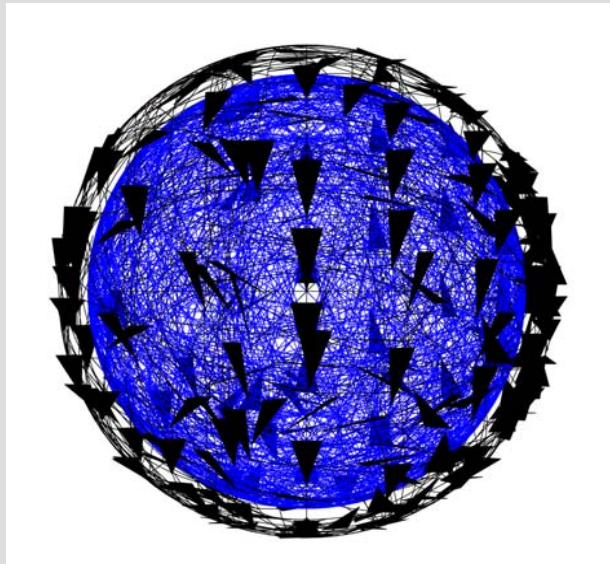
3-D View of
Uniform Function



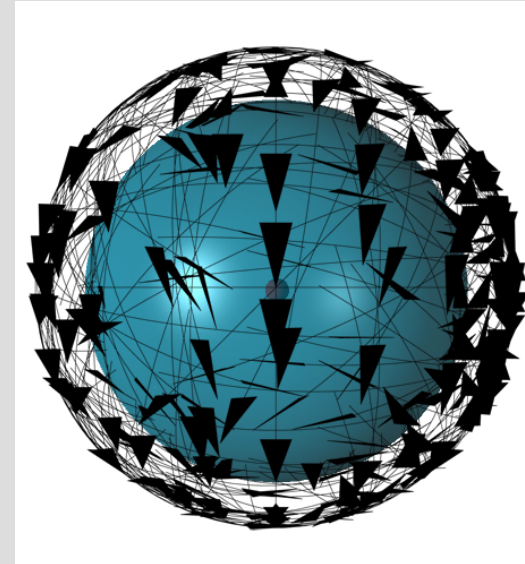
Orbitsphere Supercurrent. The bound electron exists as a spherical two-dimensional supercurrent, an extended distribution of charge completely surrounding the nucleus. Unlike a spinning sphere, there is a complex pattern of motion on its surface (indicated by arrows) that give rise to two orthogonal angular momentum vectors $\mathbf{L}_{xy} = \frac{\hbar}{4}$ and $\mathbf{L}_z = \frac{\hbar}{2}$ that give rise to the phenomenon of electron spin.



A great-circle representation of the positive Cartesian quadrant view of the total uniform current-density pattern of the $Y_0^0(\phi, \theta)$ orbitsphere comprising the superposition of the representations of STEP ONE and STEP TWO, each with 144 great circle current elements



The great-circle representation with 144 vectors per STEP overlaid giving the direction of the current of each great circle element.



A representation with 144 vectors per STEP overlaid on the continuous bound-electron current density giving the direction of the current of each great circle element (nucleus not to scale)

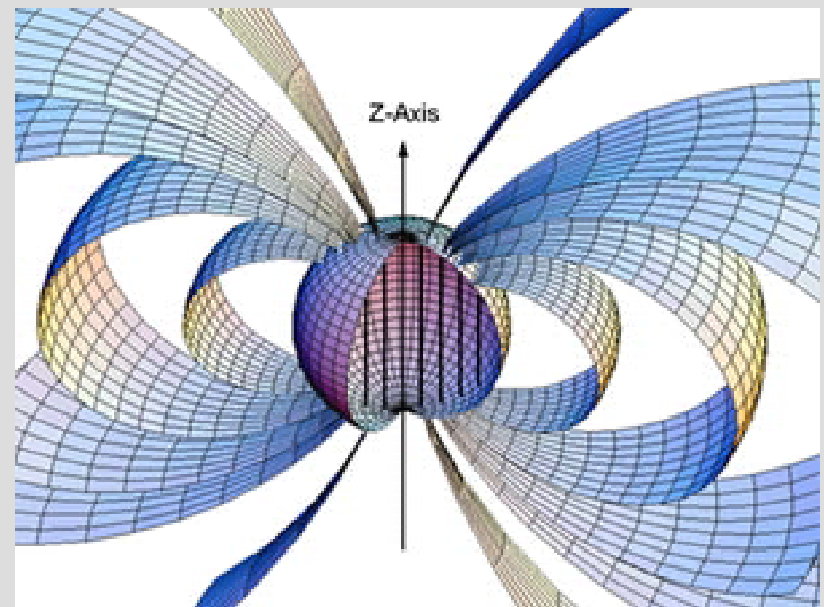
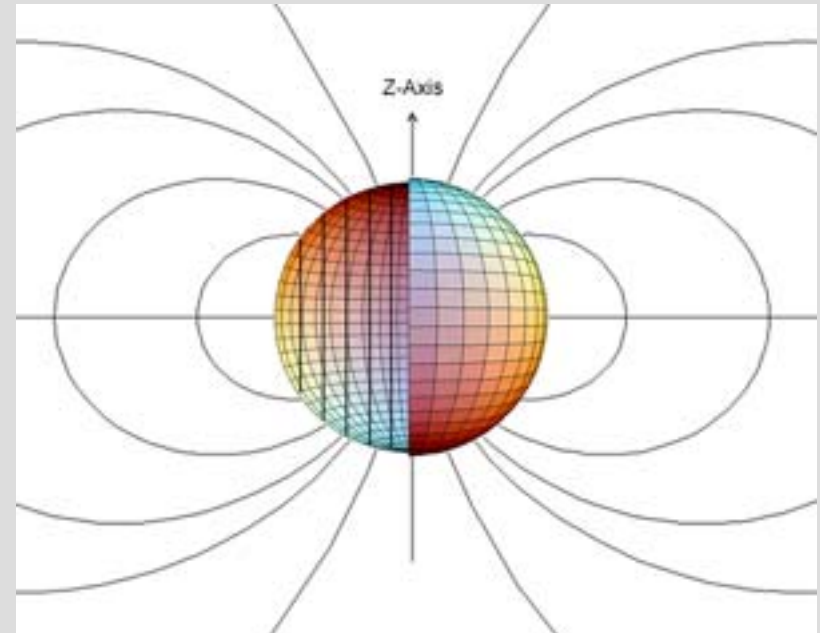
Magnetic Fields of the Electron

$$\mathbf{H} = \frac{e\hbar}{m_e r_n^3} (\mathbf{i}_r \cos \theta - \mathbf{i}_\theta \sin \theta)$$

for $r < r_n$

$$\mathbf{H} = \frac{e\hbar}{2m_e r^3} (\mathbf{i}_r 2 \cos \theta + \mathbf{i}_\theta \sin \theta)$$

for $r > r_n$



Stern-Gerlach Experiment

The Stern-Gerlach experiment implies a magnetic moment of one Bohr magneton and an associated angular momentum quantum number of $1/2$ ($s = 1/2$; $m_s = \pm 1/2$). The superposition of the vector projection of the orbitalsphere angular momentum on the z-axis is $\hbar/2$ with an orthogonal component of $\hbar/4$. Excitation of a resonant Larmor precession gives rise to \hbar on an axis \mathbf{S} that precesses about the z-axis called the spin axis at the Larmor frequency at an angle of $\theta = \pi/3$ to give a perpendicular projection of

$$\mathbf{S}_{\perp} = \pm \hbar \sin \frac{\pi}{3} = \pm \sqrt{\frac{3}{4}} \hbar \mathbf{i}_{Y_R}$$

and a projection onto the axis of the applied magnetic field of

$$\mathbf{S}_{\parallel} = \pm \hbar \cos \frac{\pi}{3} = \pm \frac{\hbar}{2} \mathbf{i}_{Z_R}$$

The superposition of the $\hbar/2$ z-axis component of the orbitalsphere angular momentum and the $\hbar/2$ z-axis component of \mathbf{S} gives \hbar corresponding to the observed electron magnetic moment of a Bohr magneton, μ_B

Electron g Factor

Conservation of angular momentum of the orbitsphere permits a discrete change of its "kinetic angular momentum" ($\mathbf{r} \times m\mathbf{v}$) by the applied magnetic field of $\frac{\hbar}{2}$, and concomitantly the "potential angular momentum" ($\mathbf{r} \times e\mathbf{A}$) must change by $-\frac{\hbar}{2}$.

$$\begin{aligned}\Delta\mathbf{L} &= \frac{\hbar}{2} - \mathbf{r} \times e\mathbf{A} \\ &= \left[\frac{\hbar}{2} - \frac{e\phi}{2\pi} \right] \hat{z}\end{aligned}$$

In order that the change of angular momentum, $\Delta\mathbf{L}$, equals zero, ϕ must be $\Phi_0 = \frac{h}{2e}$, the magnetic flux quantum.

The magnetic moment of the electron is parallel or antiparallel to the applied field only.

Electron g Factor cont'd

Power flow during the spin-flip transition is governed by the Poynting power theorem,

$$\nabla \cdot (\mathbf{E} \times \mathbf{H}) = -\frac{\partial}{\partial t} \left[\frac{1}{2} \mu_0 \mathbf{H} \cdot \mathbf{H} \right] - \frac{\partial}{\partial t} \left[\frac{1}{2} \varepsilon_0 \mathbf{E} \cdot \mathbf{E} \right] - \mathbf{J} \cdot \mathbf{E}$$

The total energy of the flip transition is the sum of the energy of reorientation of the magnetic moment, the magnetic energy, the electric energy, and the dissipated energy of a fluxon trading the orbitsphere, respectively.

$$\Delta E_{mag}^{spin} = 2 \left(1 + \frac{\alpha}{2\pi} + \frac{2}{3} \alpha^2 \left(\frac{\alpha}{2\pi} \right) - \frac{4}{3} \left(\frac{\alpha}{2\pi} \right)^2 \right) \mu_B B$$

$$\Delta E_{mag}^{spin} = g \mu_B B$$

Where the stored magnetic energy corresponding to the $\frac{\partial}{\partial t} \left[\frac{1}{2} \mu_0 \mathbf{H} \cdot \mathbf{H} \right]$ term increases, the stored electric energy corresponding to the $\frac{\partial}{\partial t} \left[\frac{1}{2} \varepsilon_0 \mathbf{E} \cdot \mathbf{E} \right]$ term increases, and the $\mathbf{J} \cdot \mathbf{E}$ term is dissipative.

The spin-flip transition can be considered as involving a magnetic moment of g times that of a Bohr magneton. The calculated value of the $\frac{g}{2}$ factor is **1.001 159 652 137**. The experimental value of $\frac{g}{2}$ is **1.001 159 652 188(4)**.

Intractable Problems Can Easily Be Solved:

Relations Between Fundamental Particles

The relations between the lepton masses and neutron to electron mass ratio which are independent of the definition of units are given in terms of the dimensionless fine structure constant α only:

$$\frac{m_{\mu}}{m_e} = \left(\frac{\alpha^{-2}}{2\pi} \right)^{\frac{2}{3}} \frac{\left(1 + 2\pi \frac{\alpha^2}{2} \right)}{\left(1 + \frac{\alpha}{2} \right)} = 206.76828 \quad (206.76827)$$

$$\frac{m_{\tau}}{m_{\mu}} = \left(\frac{\alpha^{-1}}{2} \right)^{\frac{2}{3}} \frac{\left(1 + \frac{\alpha}{2} \right)}{\left(1 - 4\pi\alpha^2 \right)} = 16.817 \quad (16.817)$$

$$\frac{m_{\tau}}{m_e} = \left(\frac{\alpha^{-3}}{4\pi} \right)^{\frac{2}{3}} \frac{\left(1 + 2\pi \frac{\alpha^2}{2} \right)}{\left(1 - 4\pi\alpha^2 \right)} = 3477.2 \quad (3477.3)$$

$$\frac{m_N}{m_e} = \frac{12\pi^2}{1-\alpha} \sqrt{\frac{\sqrt{3}}{\alpha}} \frac{\left(1 + 2\pi \frac{\alpha^2}{2} \right)}{\left(1 - 2\pi \frac{\alpha^2}{2} \right)} = 1838.67 \quad (1838.68)$$

Maxwellian Solution Allows Energy to be Extracted from a Hydrogen Atom

Using a Maxwellian nonradiative boundary constraint to solve the wave equation, an exothermic reaction is predicted whereby certain atoms or ions serve as catalysts to release energy from hydrogen to produce an increased binding energy hydrogen atom called a hydrino having a binding energy of

$$\text{Binding Energy} = \frac{13.6 \text{ eV}}{\left(\frac{1}{p}\right)^2} \quad (1)$$

where p is an integer greater than 1 and ≤ 137 , designated as $H\left[\frac{a_H}{p}\right]$ where a_H is the radius of the hydrogen atom. Hydrinos are predicted to form by reacting an ordinary hydrogen atom with a catalyst having a net enthalpy of reaction of about

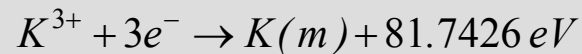
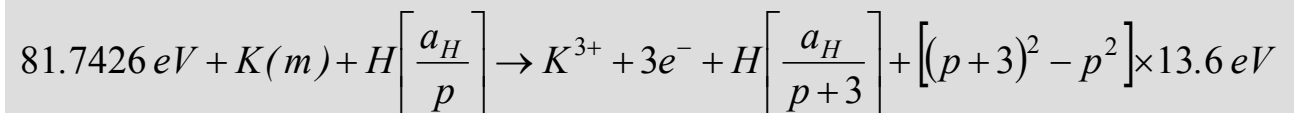
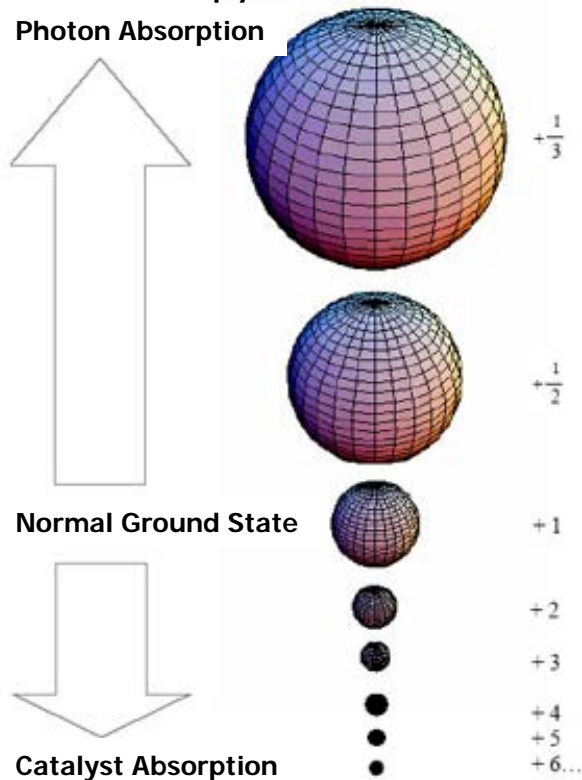
$$m \cdot 27.2 \text{ eV} \quad (2)$$

where m is an integer. This catalysis releases energy from the hydrogen atom with a commensurate decrease in size of the hydrogen atom, $r_n = na_H$. For example, the catalysis of $H(n = 1)$ to $H(n = 1/2)$ releases 40.8 eV, and the hydrogen radius decreases from a_H to $\frac{1}{2}a_H$.

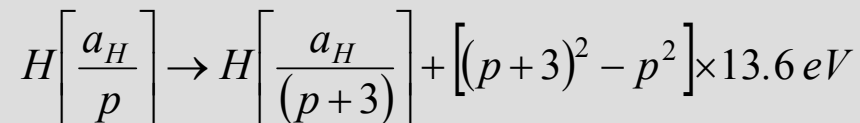
The Theory Predicts Catalysts that Allow Energy to be Extracted from a Hydrogen Atom

Hydrogen electrons are stimulated to a fractional quantum state by the presence of a catalyst with a net enthalpy of reaction of $m \cdot 27.2 \text{ eV}$.

A catalytic system is provided by the ionization of t electrons from an atom each to a continuum energy level such that the sum of the ionization energies of the t electrons is approximately $m \cdot 27.2 \text{ eV}$, where m is an integer. One such catalytic system involves potassium. The first, second, and third ionization energies of potassium are 4.34066 eV , 31.63 eV , 45.806 eV respectively. The triple ionization ($t=3$) reaction of K to K^{3+} , then, has a net enthalpy of reaction of 81.7426 eV , which is equivalent to $m=3$.

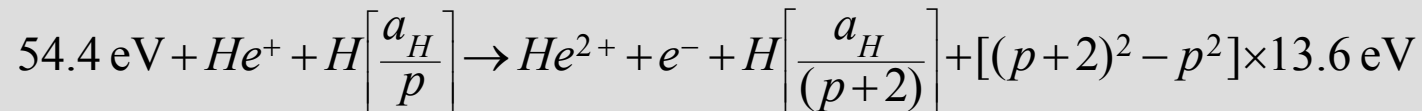


And, the overall reaction is:

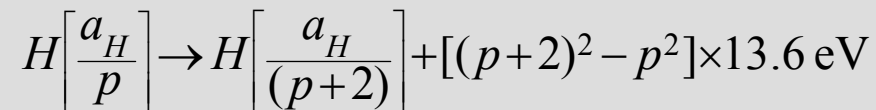


Helium (II) Ion Catalyst

Helium (II) ions satisfy the catalyst criterion of a reaction that can provide a net enthalpy of a multiple of that of the potential energy of the hydrogen atom. The second ionization energy is 54.4 eV which is $2 \cdot 27.2$ eV.

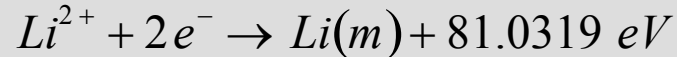
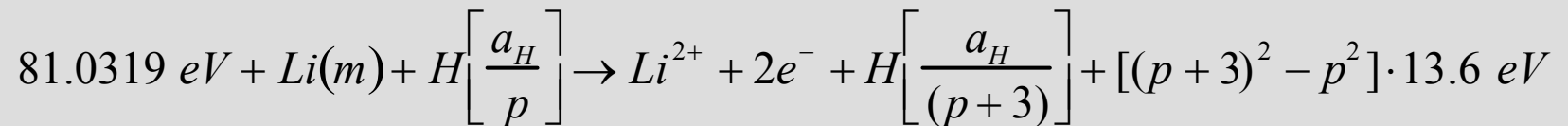


And, the overall reaction is

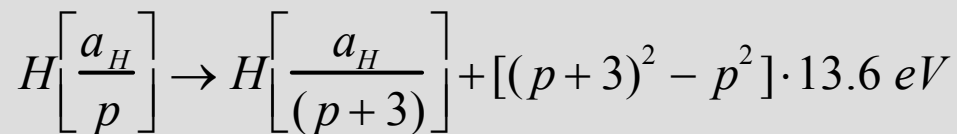


Atomic Li Catalyst

The first and second ionization energies of lithium are 5.39172 eV and 75.64018 eV , respectively. The double ionization reaction of Li to Li^{2+} then, has a net enthalpy of reaction of 81.0319 eV , which is equivalent to $3 \cdot 27.2 \text{ eV}$.



And, the overall reaction is:

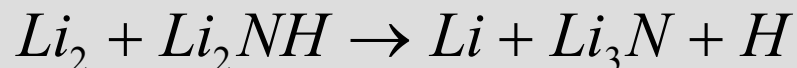


Atomic Li Source Reaction

Lithium is a metal in the solid and liquid states, and the gas comprises covalent Li_2 molecules, each having a bond energy of 110.4 kJ/mole. In order to generate atomic lithium, $LiNH_2$ was added to the reaction mixture. $LiNH_2$ generates atomic hydrogen as well, according to the reversible reactions:

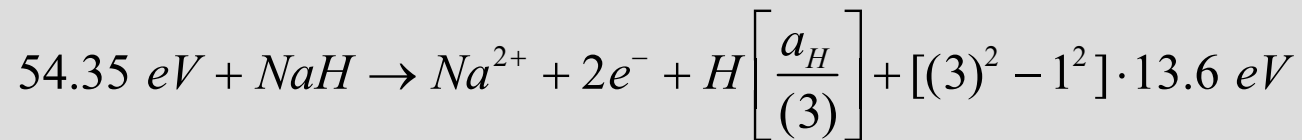


and

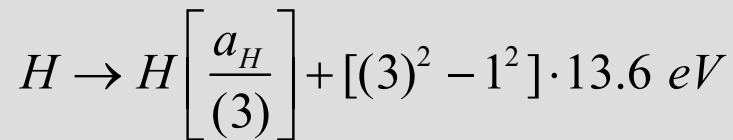


NaH Molecular Catalyst

NaH molecule can serve as a catalyst and *H* source, since the *NaH* bond energy of 1.9245 eV plus the double ionization of *Na* to *Na*²⁺ is 54.35 eV (2 · 27.2 eV). The catalyst reactions are given by



And, the overall reaction is



followed by fast transition of *H*(1/3) (*p* = 3) to *H*(1/4) with *H* as the catalyst:



NaH Molecular Source Reaction

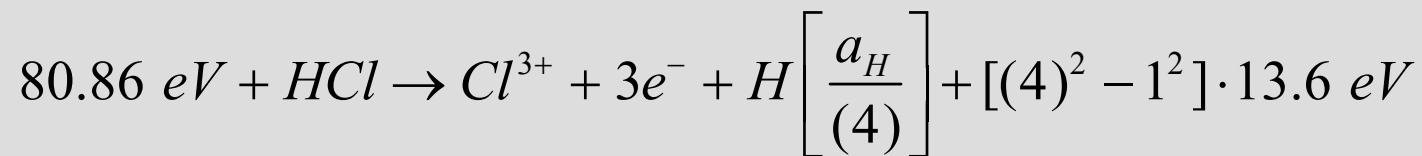
To achieve high power, a chemical system was designed to greatly increase the amount and rate of formation of $NaH(g)$. The reaction of $NaOH$ and Na to Na_2O and $NaH(s)$ calculated from the heats of formation releases $\Delta H = -44.7 \text{ kJ / mole } NaOH$:



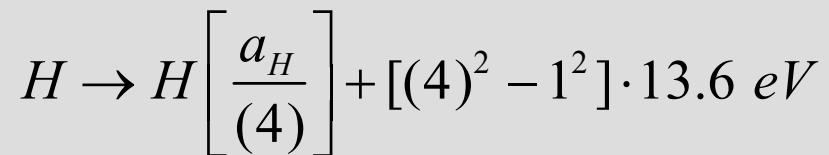
This exothermic reaction can drive the formation of $NaH(g)$ and was exploited to drive the very exothermic catalyst reaction. R-Ni having a high surface area of about $100 \text{ m}^2/g$ was surface coated with $NaOH$ and reacted with Na metal to form $NaH(g)$.

HCl Molecular Catalyst

Another catalytic system of the type MH involves chlorine. The bond energy of HCl is 4.4703 eV . The first, second, and third ionization energies of Cl are 12.96764 eV , 23.814 eV , and 39.61 eV . Based on these energies, HCl can serve as a catalyst and H source, since the bond energy of HCl plus the triple ionization of Cl to Cl^{3+} is 80.86 eV ($3 \cdot 27.2 \text{ eV}$). The catalyst reactions are given by



And, the overall reaction is

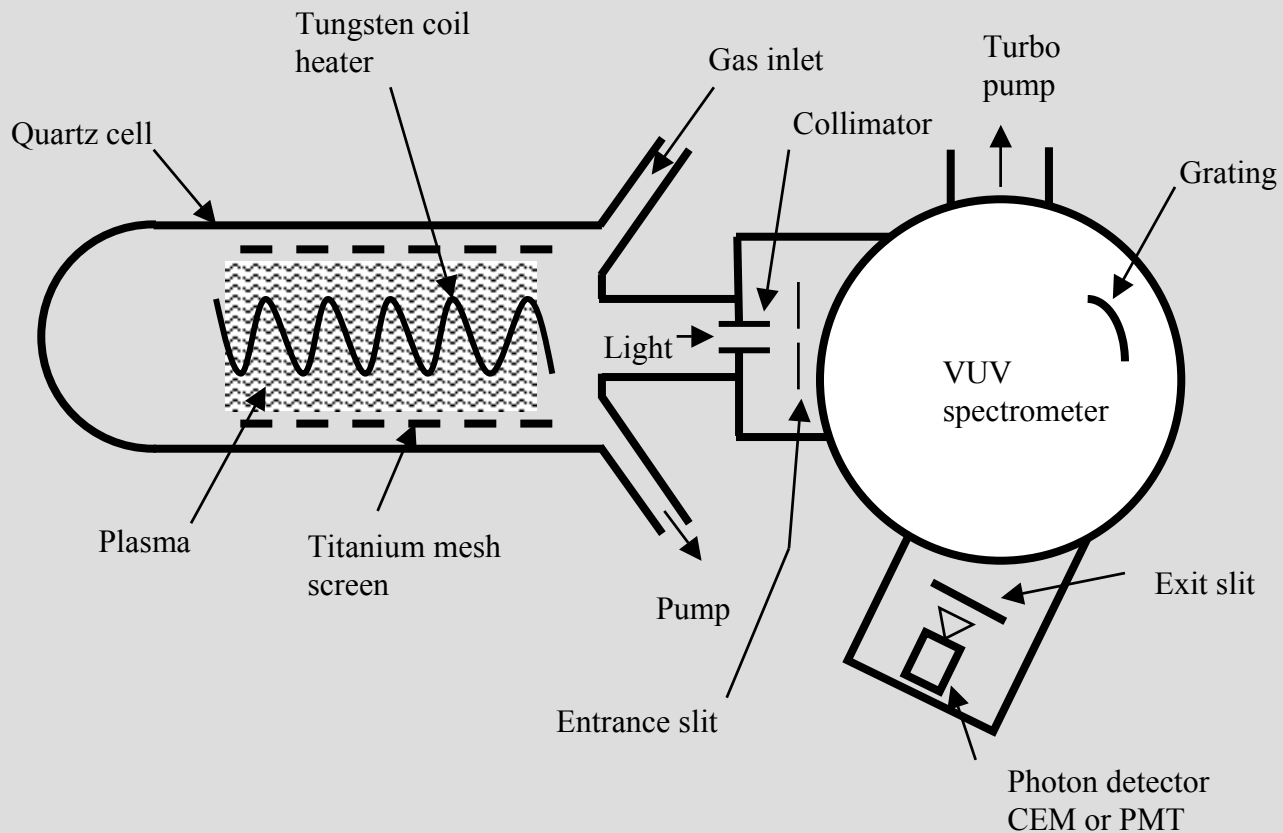


The predicted product then is $H_2(1/4)$.

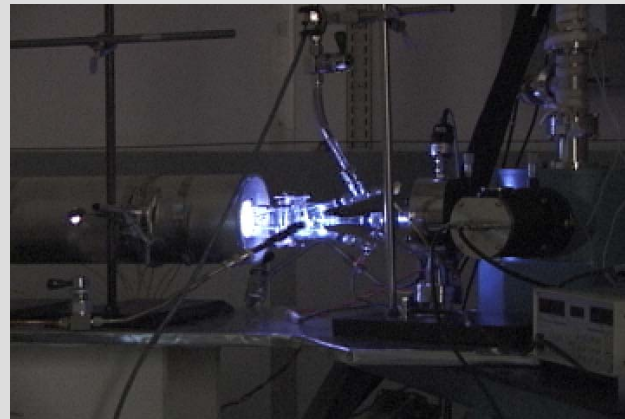
Catalyst Resonant Energy Transfer

- $\text{NaH} + 54.35 \text{ eV} (2 \times 27.2 \text{ eV}) \rightarrow \text{Na}^{2+} + 2\text{e}^-$
- $\text{HCl} + 80.86 \text{ eV} (3 \times 27.2 \text{ eV}) \rightarrow \text{Cl}^{3+} + 3\text{e}^-$
- $\text{Li} + 81.0319 \text{ eV} (3 \times 27.2 \text{ eV}) \rightarrow \text{Li}^{2+} + 2\text{e}^-$
- $\text{K(m)} + 81.742 \text{ eV} (3 \times 27.2 \text{ eV}) \rightarrow \text{K}^{3+} + 3\text{e}^-$
- $\text{Sr}^+ + 54.4 \text{ eV} (2 \times 27.2 \text{ eV}) \rightarrow \text{Sr}^{3+} + 2\text{e}^-$
- $\text{He}^+ + 54.4 \text{ eV} (2 \times 27.2 \text{ eV}) \rightarrow \text{He}^{2+} + \text{e}^-$
- $\text{Ar}^+ + 27.2 \text{ eV} \rightarrow \text{Ar}^{2+} + \text{e}^-$

Experimental Set-up for Chemically-Generated RT Plasma



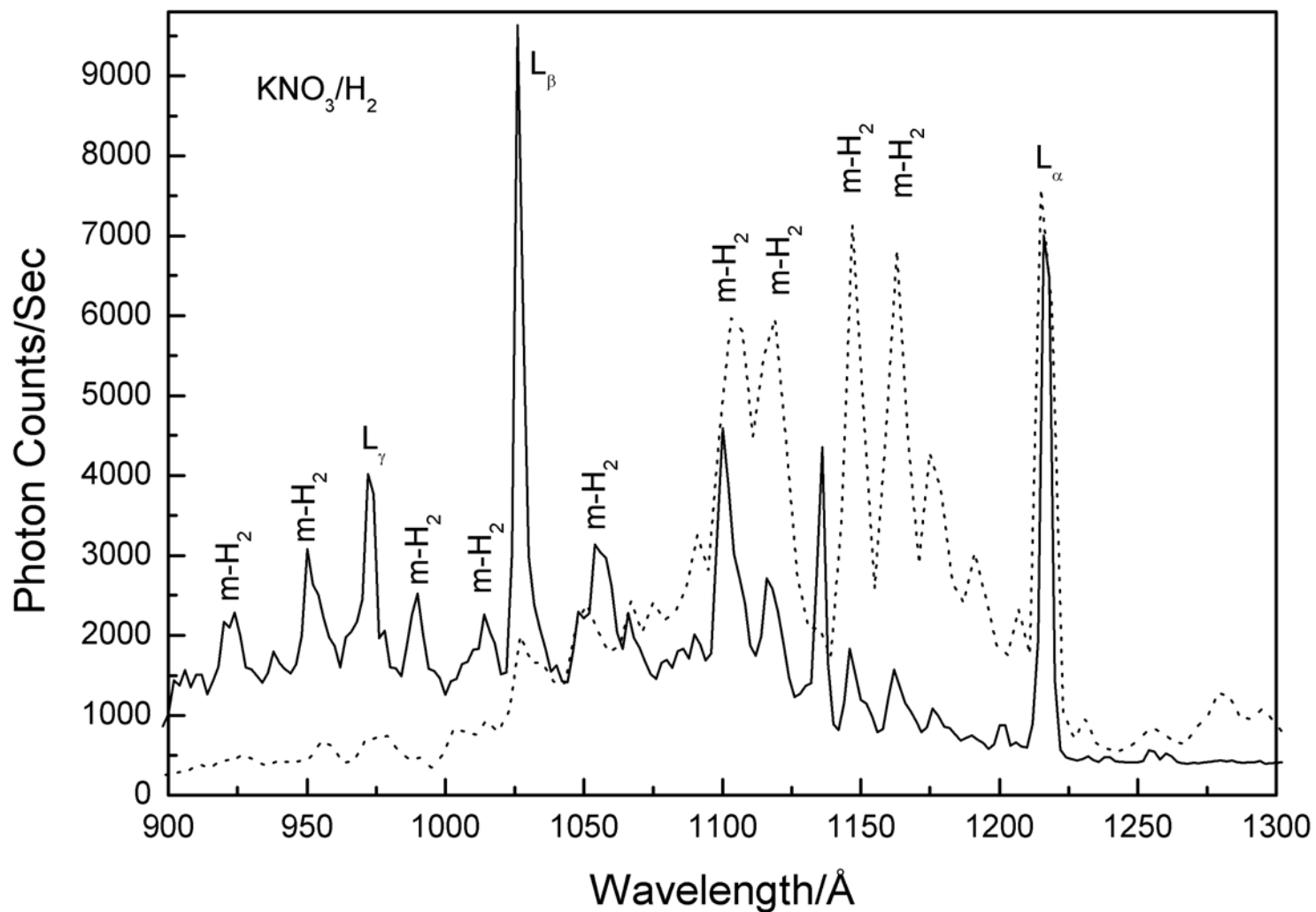
Chemically-Generated RT Plasma



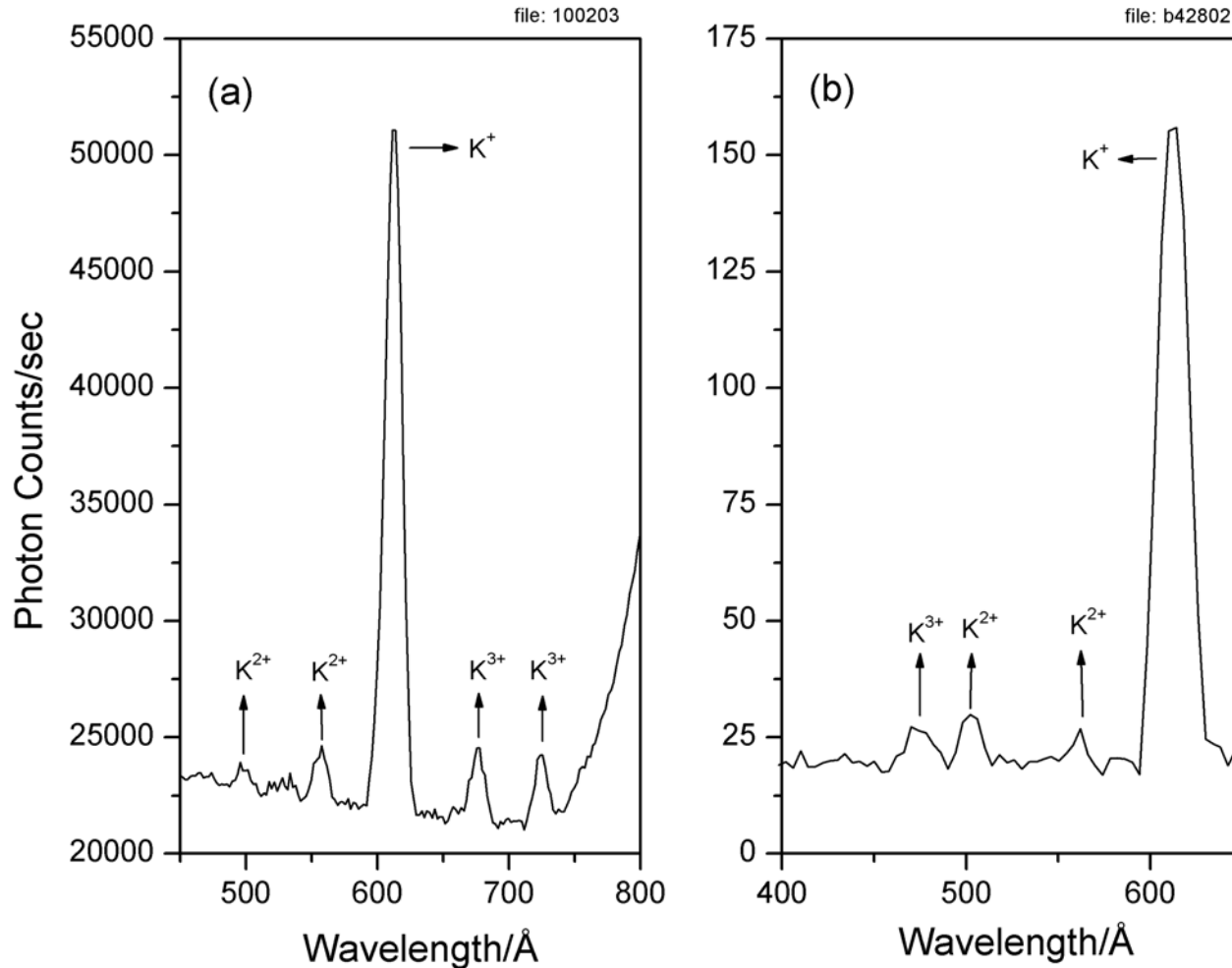
- Process generates: Plasma, light, heat, novel chemicals
- Process consumes: Hydrogen

H. Conrads, R. Mills, Th. Wrubel, "Emission in the Deep Vacuum Ultraviolet from a Plasma Formed by Incandescently Heating Hydrogen Gas with Trace Amounts of Potassium Carbonate," *Plasma Sources Science and Technology*, Vol. 12, (2003), pp. 389-395.

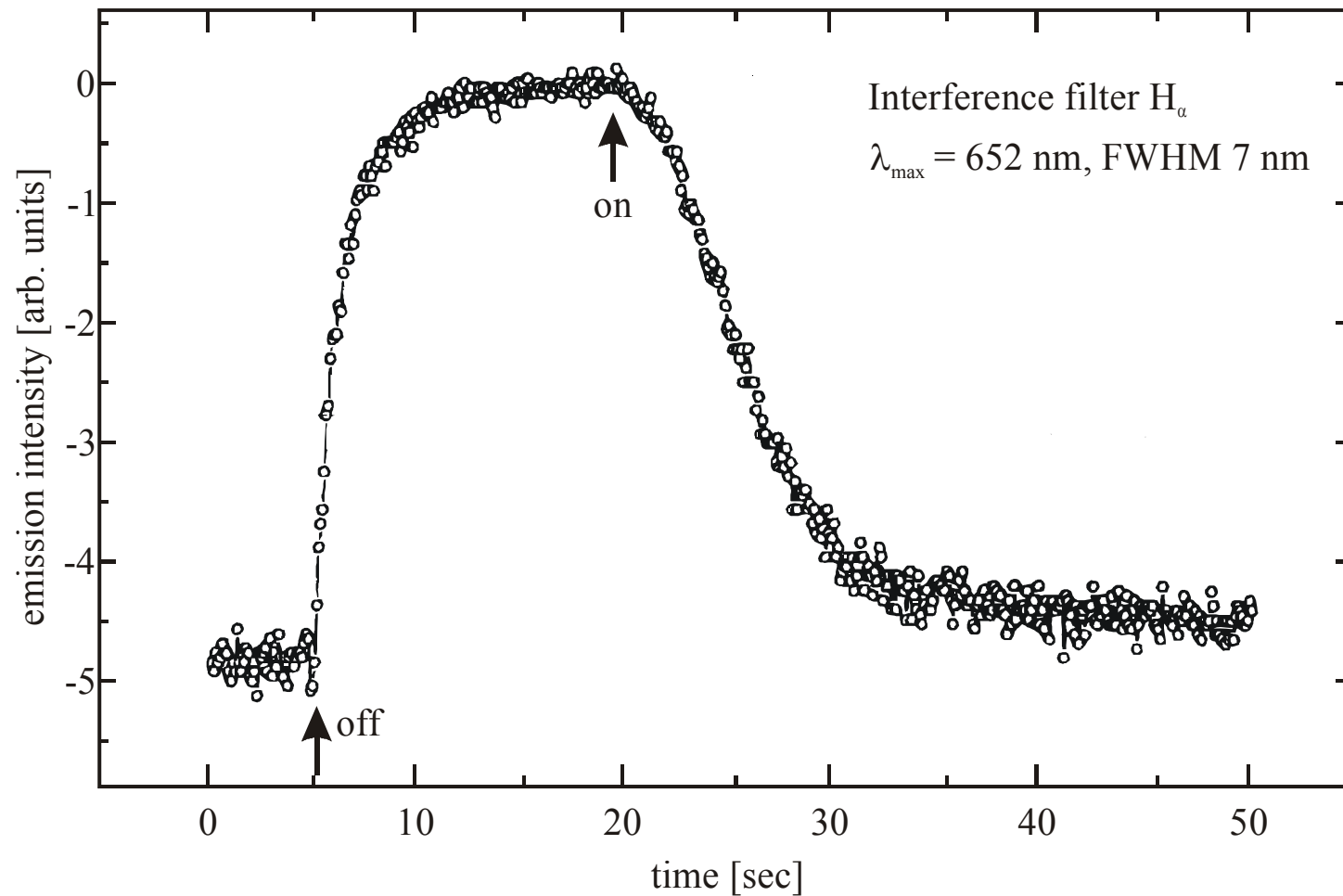
R. Mills, M. Nansteel, and P. Ray, "Excessively Bright Hydrogen-Strontium Plasma Light Source Due to Energy Resonance of Strontium with Hydrogen," *J. of Plasma Physics*, Vol. 69, (2003), pp. 131-158. R. Mills and M. Nansteel, P. Ray, "Argon-Hydrogen-Strontium Discharge Light Source," *IEEE Transactions on Plasma Science*, Vol. 30, No. 2, (2002), pp. 639-653.



The VUV spectra (900–1300 Å) of the cell emission from hydrogen microwave plasma (dotted line) and the KNO₃-H₂ rt-plasma (solid line) with an inverted Lyman population. The increase in intensity at 1100Å compared to hydrogen emission alone was assigned to a contribution from H⁻(1/4).



The VUV spectrum (450–800Å) of the cell emission recorded at about the point of the maximum Lyman α emission from a gas cell at a cell temperature of 700 °C comprising a tungsten filament, a titanium dissociator, 300 mtorr hydrogen, and vaporized K and K^+ from KNO_3 that was recorded with a CEM. (a) Line emission corresponding to K^{2+} was observed at 497Å and 550Å, and K^+ was observed at 613Å. K^{3+} was observed at 673 Å and 726 Å. (b) Line emission corresponding to K^{2+} was observed at 497 Å and 550 Å, and K^+ was observed at 613Å. K^{3+} was observed at 473 Å.

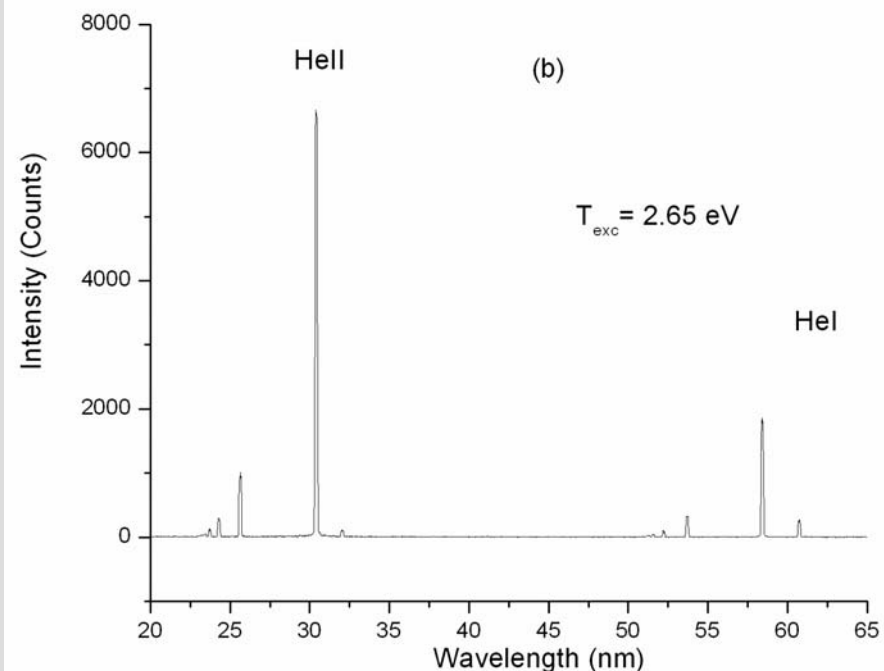
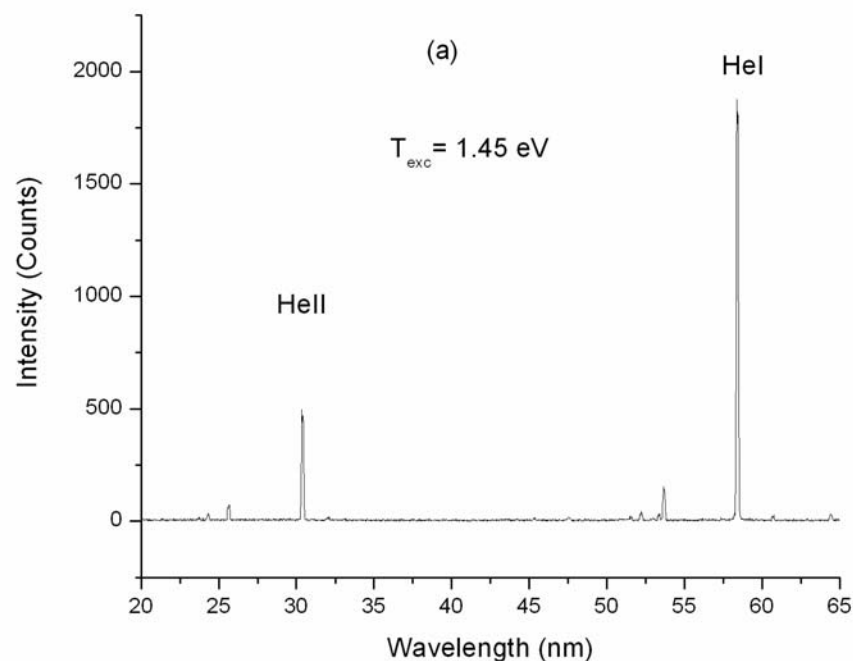


Emission of the cell as a function of time while the filament current was turned off and on. The plasma decay with no electric field present followed the decay of atomic hydrogen from the filament dissociator. Upon restoration of the filament temperature, dissociation and the plasmas resumed.

J. Conrads, R. Mills, Th. Wrübel, Plasma Sources Sci. Technol. **12**, 389 (2003).

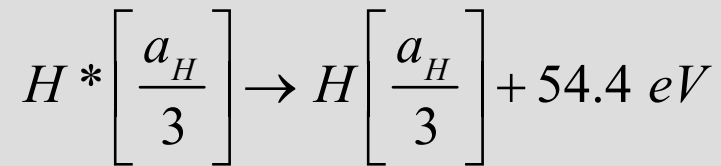
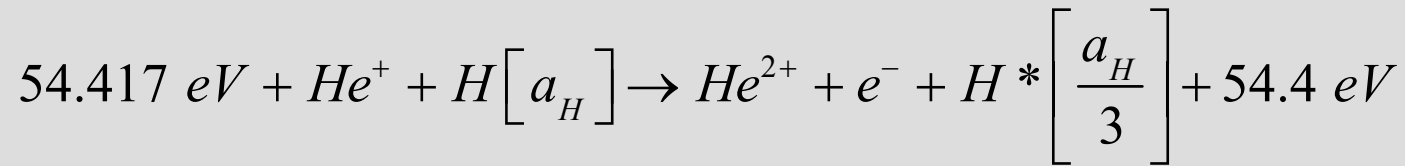
Hydrino Reaction Mechanism Proved

- Pumping of the Helium Ion Lines due to the Catalyst Reaction
- 22.8 nm Continuum Band
- Extraordinary Fast H

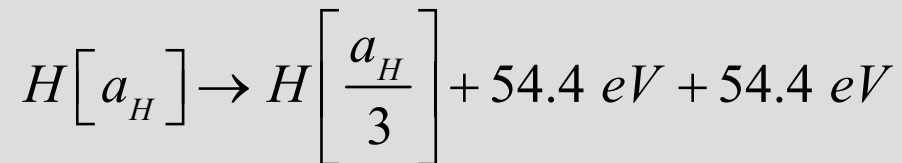


Relative intensity of ionic helium line (30.4nm) increases with respect to atomic helium line (58.4 nm) as the hydrogen concentration is increased in the plasma due to the catalyst reaction of He^+ to He^{2+} driven by production of hydrido $\text{H}(1/3)$. (a) 850mTorr He + 50 mTorr H_2 . (b) 750mTorr He + 150 mTorr H_2 .

Helium is one of the catalysts that can cause a transition reaction because the second ionization energy is 54.4 eV. Since the reactions involve two steps of energy release, it may be written as follows:



And, the overall reaction is



wherein $\text{H}^* \left[a_H/3 \right]$ has the radius of the hydrogen atom and a central field equivalent to 3 times that of a proton and $\text{H} \left[a_H/3 \right]$ is the corresponding stable state with the radius of 1/3 that of H.

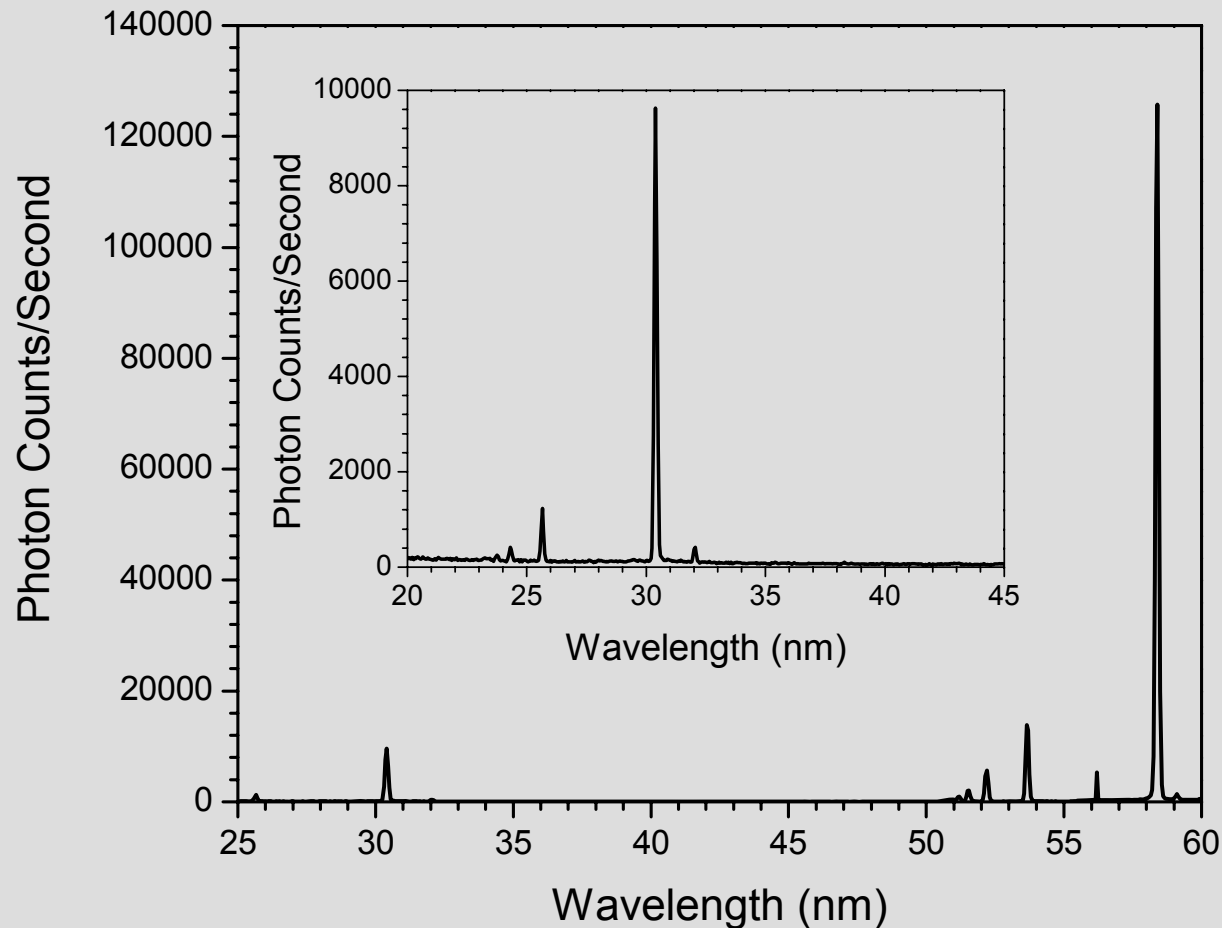
As the electron undergoes radial acceleration from the radius of the hydrogen atom to a radius of $1/3$ this distance, energy is released as characteristic light emission or as third-body kinetic energy.

The emission may be in the form of an extreme-ultraviolet continuum radiation having an edge at 54.4 eV and extending to longer wavelengths.

Alternatively, a resonant kinetic energy transfer to form fast H may occur.

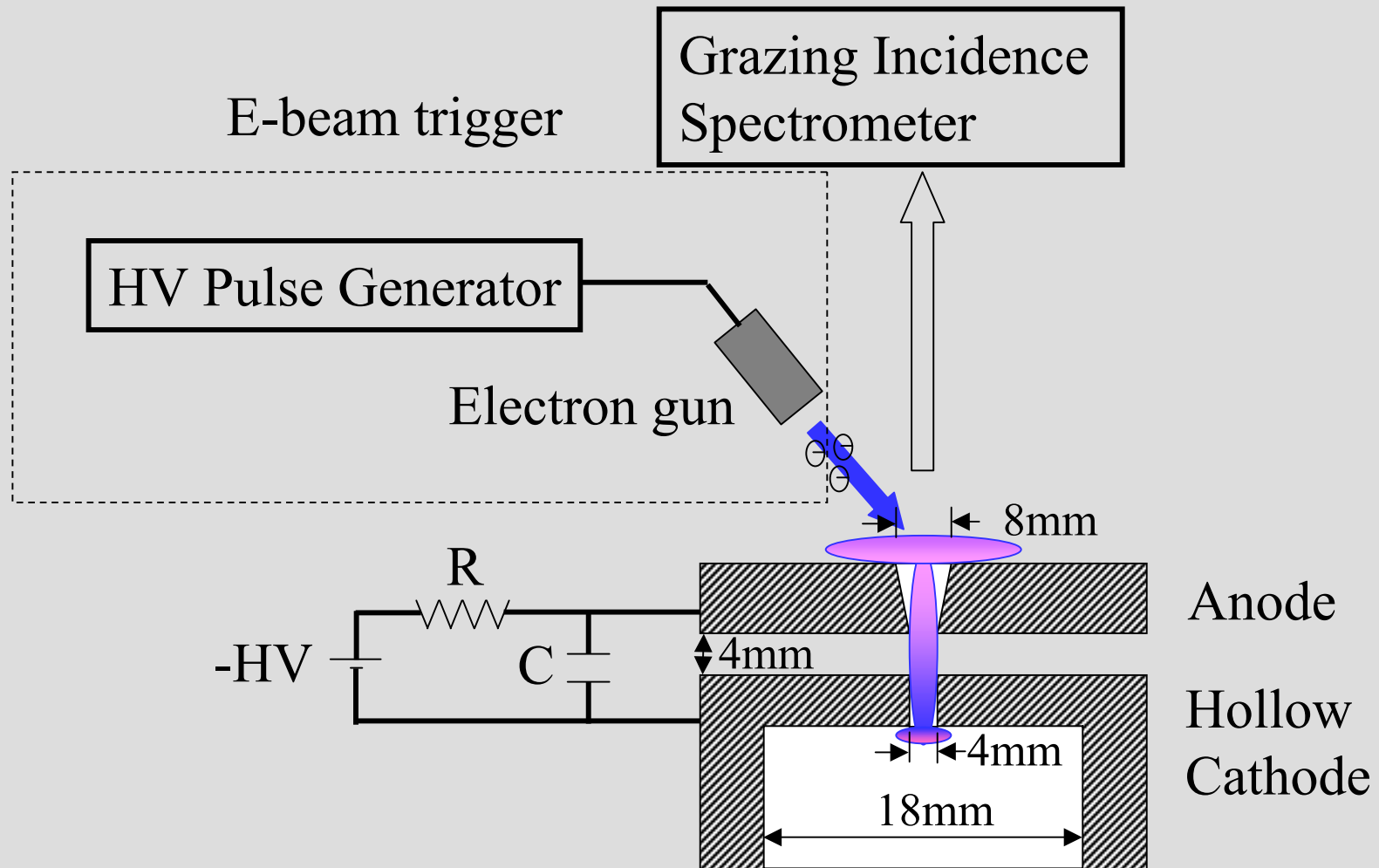
The predicted 22.8 nm continuum band and extraordinary fast H recorded as extraordinary ($>100 \text{ eV}$) Balmer α line broadening were observed consistent with predictions.

Microwave Discharge in Helium at 500 mTorr

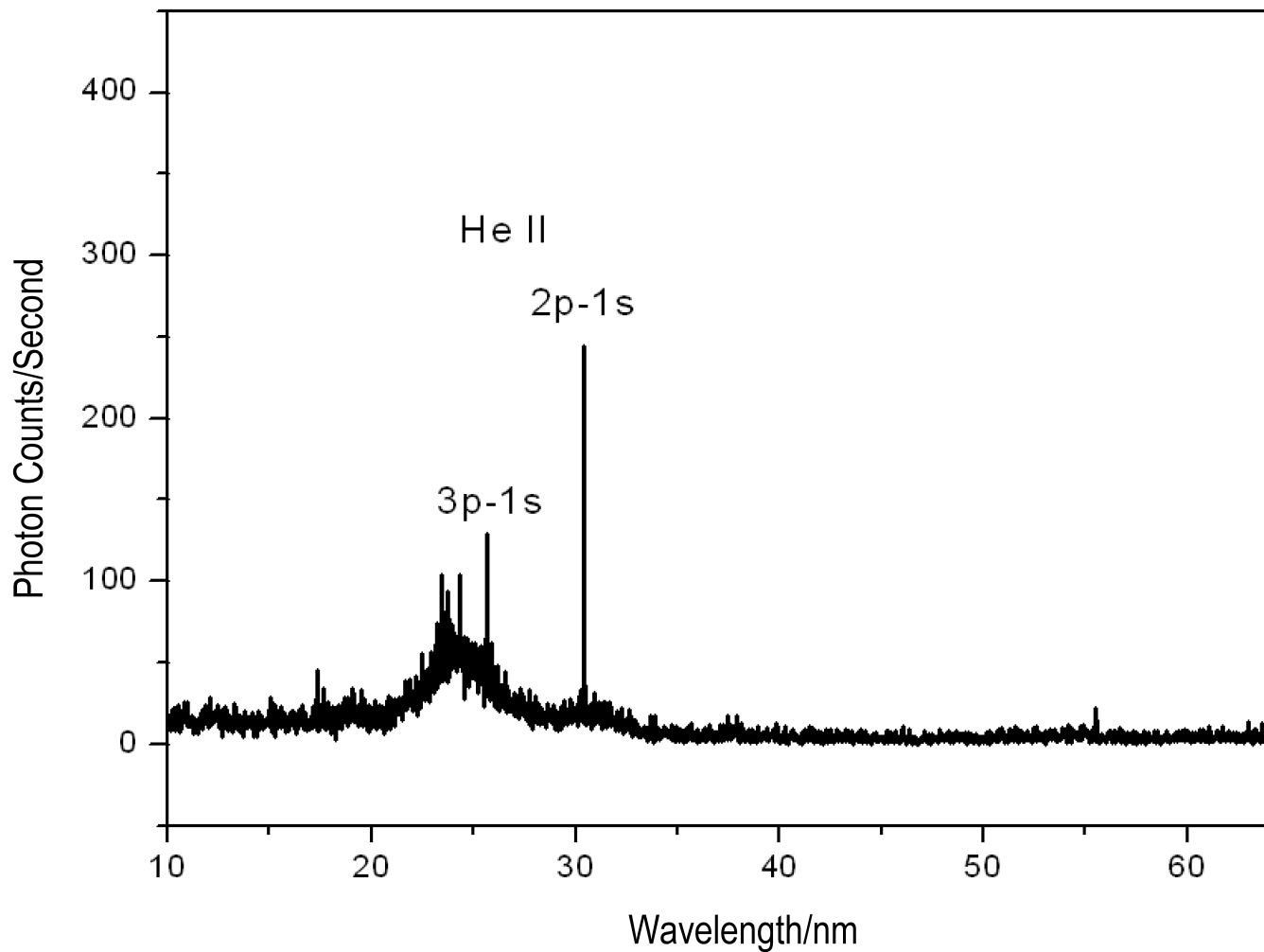


Microwave power: 100 W

Control emission spectrum (25-60 nm) of helium alone recorded by the EUV grazing incidence spectrometer. Essentially only helium atomic lines were observed with the $1s^2 \rightarrow 1s^1 2p^1$ transition being dominant. The insert (20-45 nm region) shows only the helium ion lines in the normal intensity ratios as a Rydberg series.

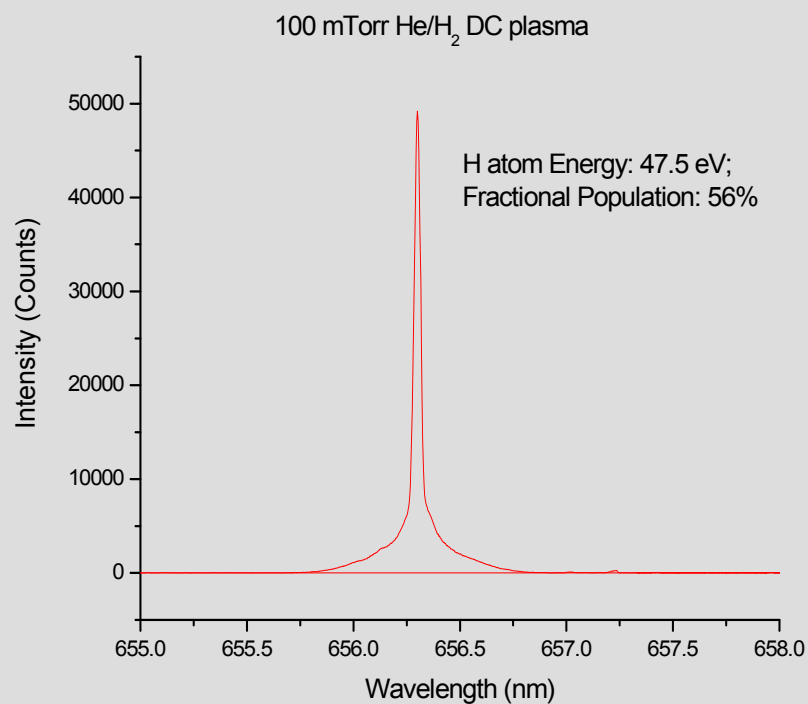


Experimental Setup for the high voltage discharge cell.

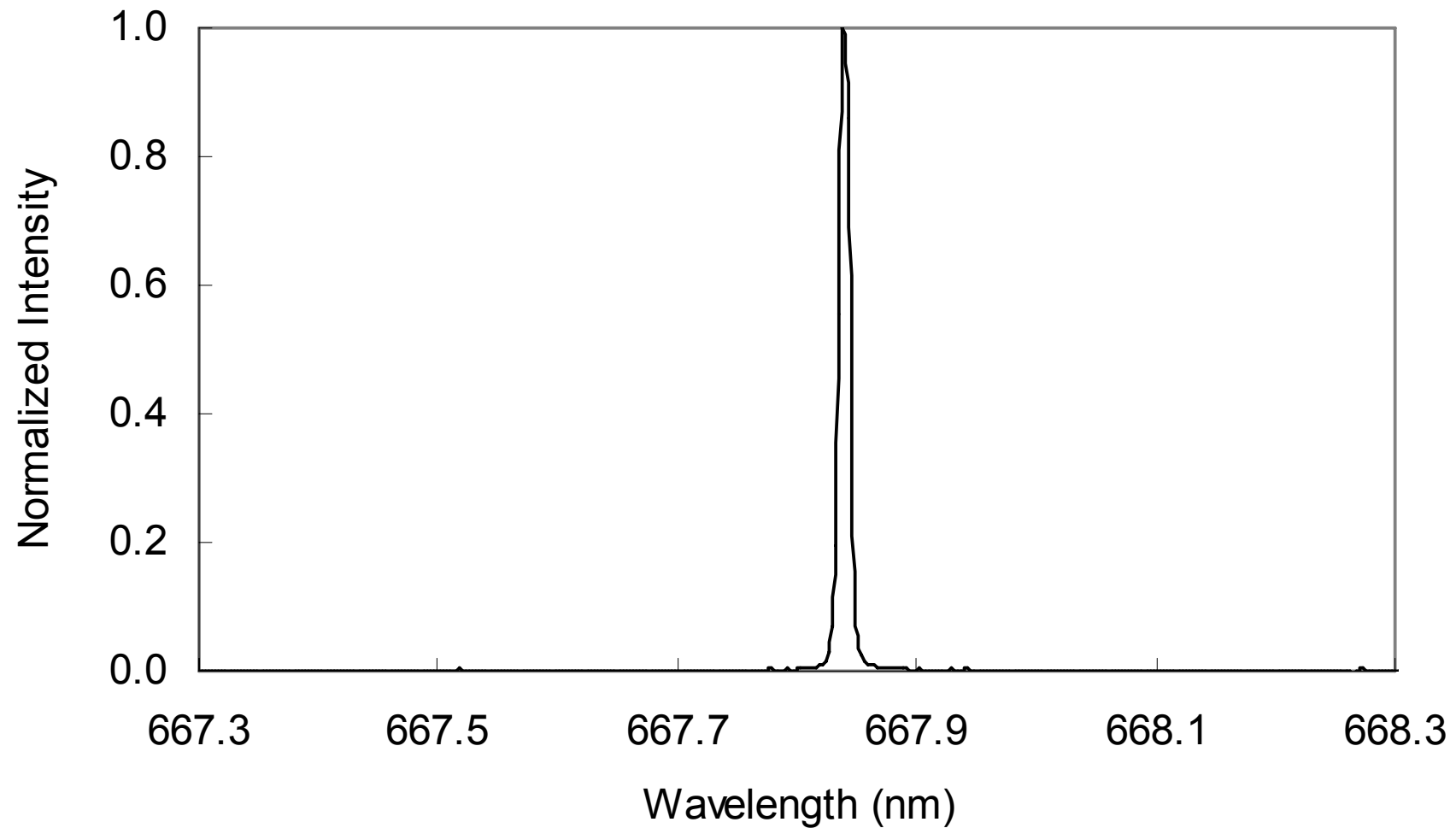


Emission spectrum (10-65 nm) of an electron-beam-initiated, high-voltage pulsed discharge in a helium-hydrogen mixture (98/2%), recorded by the EUV grazing incidence spectrometer.

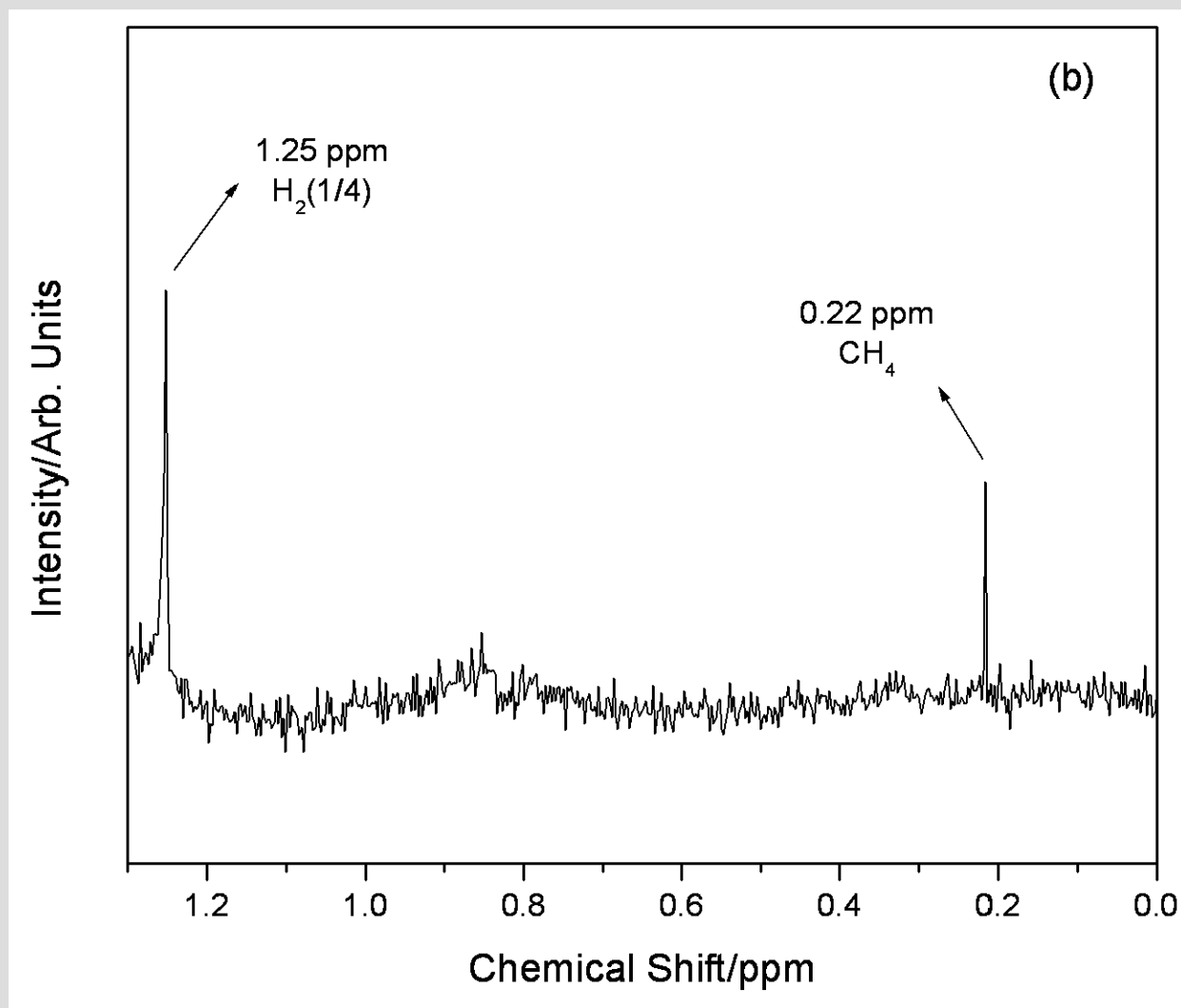
The predicted continua for the transition $H * \left[\frac{a_H}{3} \right] \rightarrow H \left[\frac{a_H}{3} \right] + 54.4 \text{ eV}$ and $H_{fast} (KE=27.2 \text{ eV}) * \left[\frac{a_H}{4} \right] + \rightarrow H \left[\frac{a_H}{4} \right] + 40.8 \text{ eV}$ were observed.



Excessive hydrogen line broadening in He/H₂ discharge corresponding to fast H atom with energies of 50 eV.

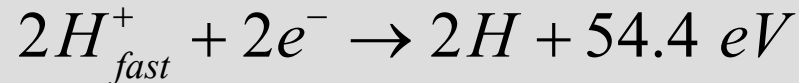
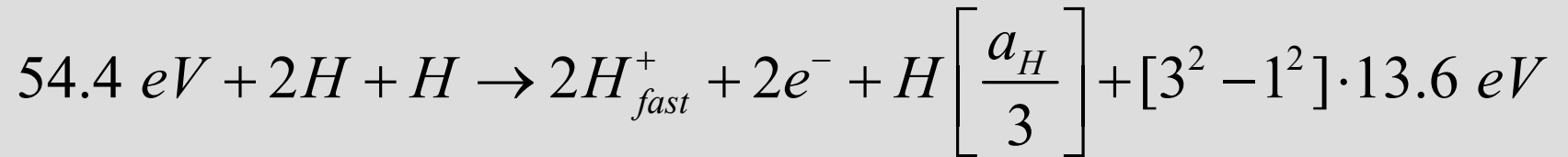


The 667.816 nm *HeI* line width for 1 Torr He/H₂ (95/5%) at 400 V and 20 mA. No broadening was observed.

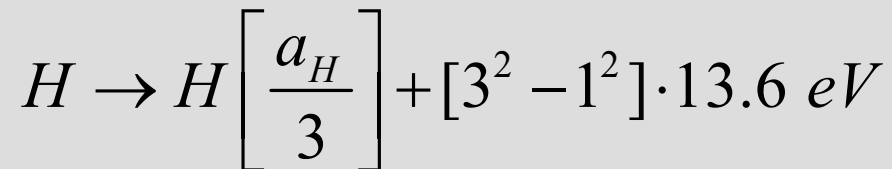


1H NMR (0 ppm to 1.3 ppm region) relative to tetramethylsilane (TMS) of He/H_2 plasma gases collected at 4K and dissolved in $CDCl_2$ showing isolated $H_2(1/4)$ at 1.25 ppm.

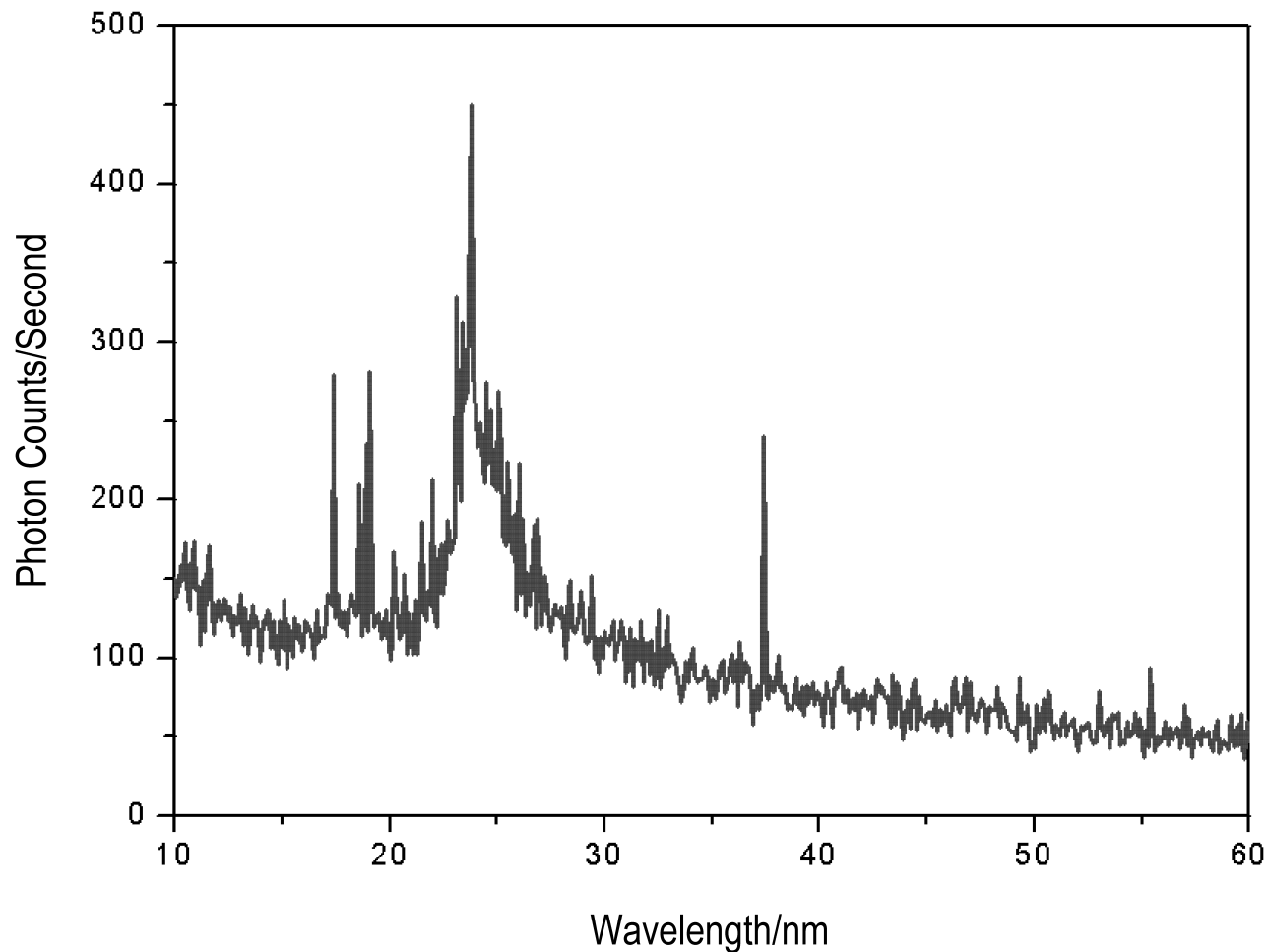
The reaction between three hydrogen atoms whereby two atoms resonantly and nonradiatively accept 54.4 eV from the third hydrogen atom such that 2H serve as the catalyst is given by



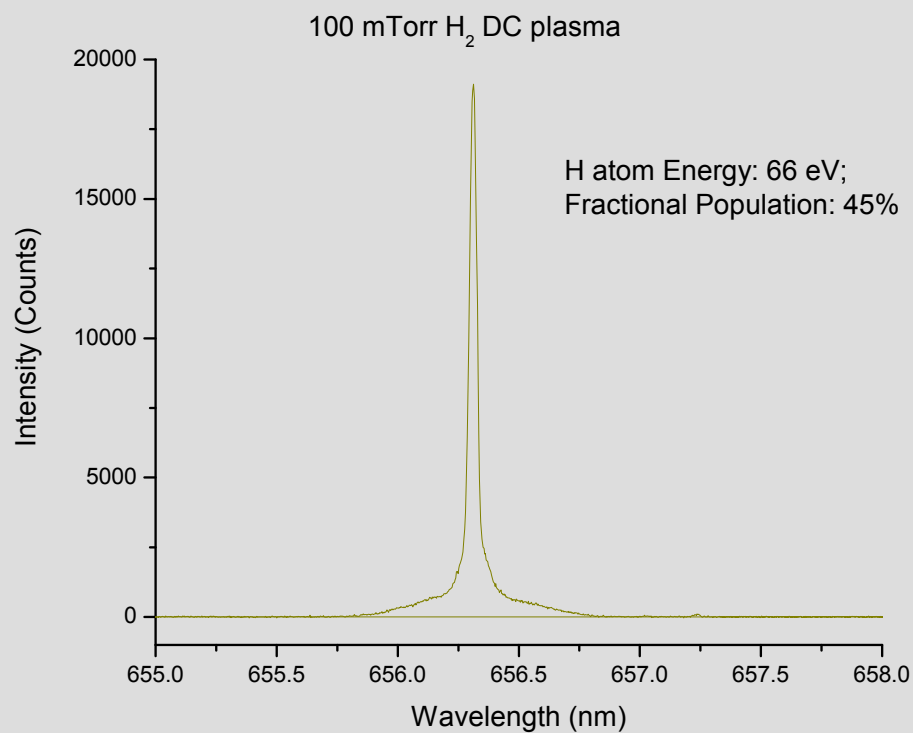
And, the overall reaction is



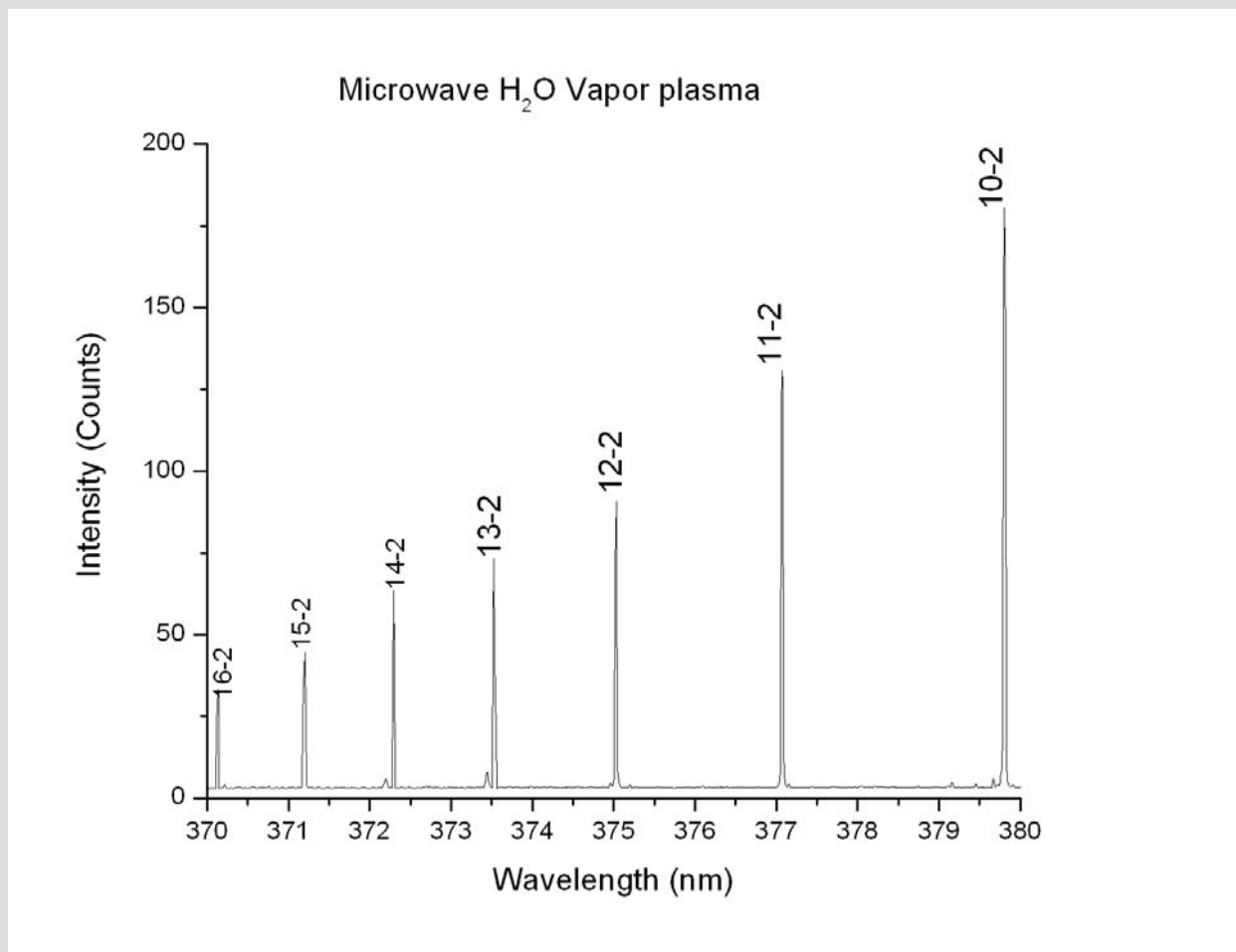
The predicted 22.8 nm continuum band and extraordinary fast H were also observed with hydrogen plasmas.



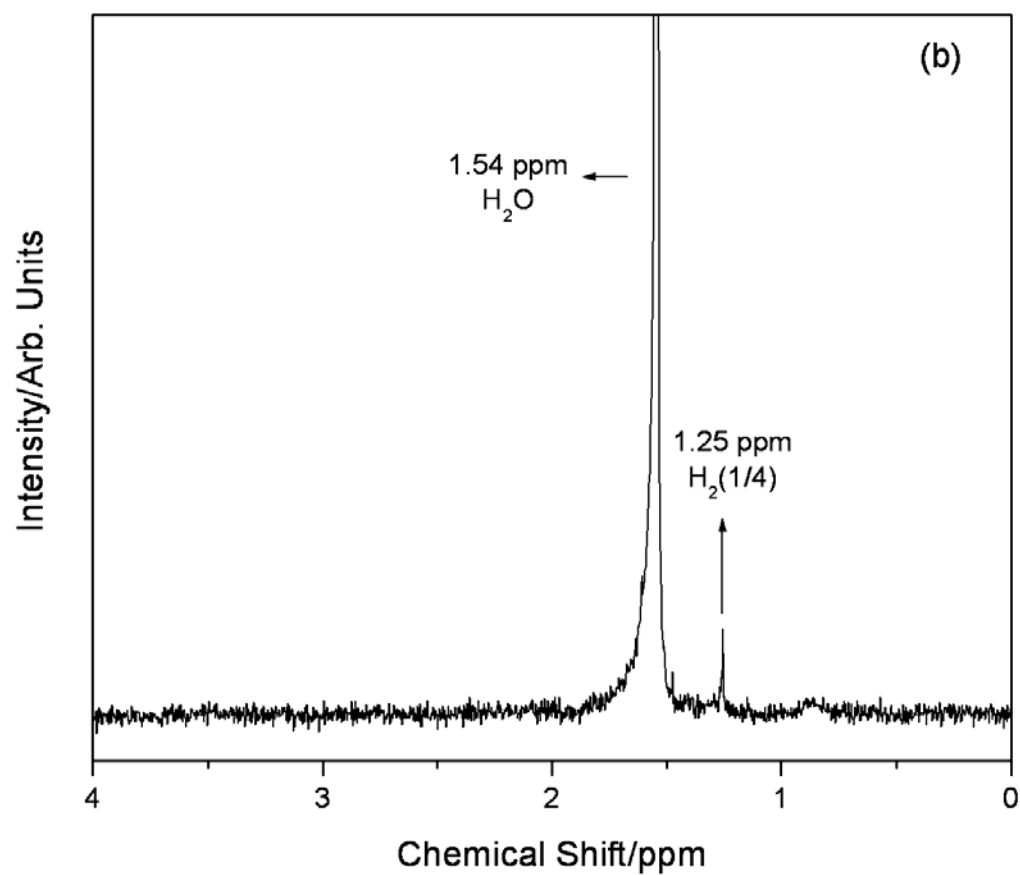
Emission spectrum (10-60 nm) of an electron-beam-initiated, high-voltage pulsed discharge in hydrogen, recorded by the EUV grazing incidence spectrometer. The predicted continuum for the transition $H^* \left[\frac{a_H}{3} \right] \rightarrow H \left[\frac{a_H}{3} \right] + 54.4 \text{ eV}$ was observed. The sharp peaks are oxygen.



Excessive hydrogen line broadening in H₂ discharge corresponding to fast H atom with energies of 60-70 eV.



Emission spectrum (370-660 nm) of a water-vapor microwave discharge plasma wherein the $2H$ catalyst served to maintain a high hydrino transition reaction rate as demonstrated by the pumping of the H lines to extraordinarily high levels. Specifically, the hydrogen Balmer lines corresponding to the transitions from the n th principal quantum level beyond the 16th state to the $n=2$ level were observed.



1H NMR (0 ppm to 4 ppm) relative to tetramethylsilane (TMS) of water-vapor plasma gases collected at 4K and dissolved in $CDCl_2$ showing isolated $H_2(1/4)$ at 1.25 ppm.

Exact Closed-Form Solutions of H_2^+ and H_2

The Laplacian in ellipsoidal coordinates is solved with the constraint of nonradiation

$$(\eta - \zeta)R_\xi \frac{\partial}{\partial \xi} \left(R_\xi \frac{\partial \phi}{\partial \xi} \right) + (\zeta - \xi)R_\eta \frac{\partial}{\partial \eta} \left(R_\eta \frac{\partial \phi}{\partial \eta} \right) + (\xi - \eta)R_\zeta \frac{\partial}{\partial \zeta} \left(R_\zeta \frac{\partial \phi}{\partial \zeta} \right) = 0$$

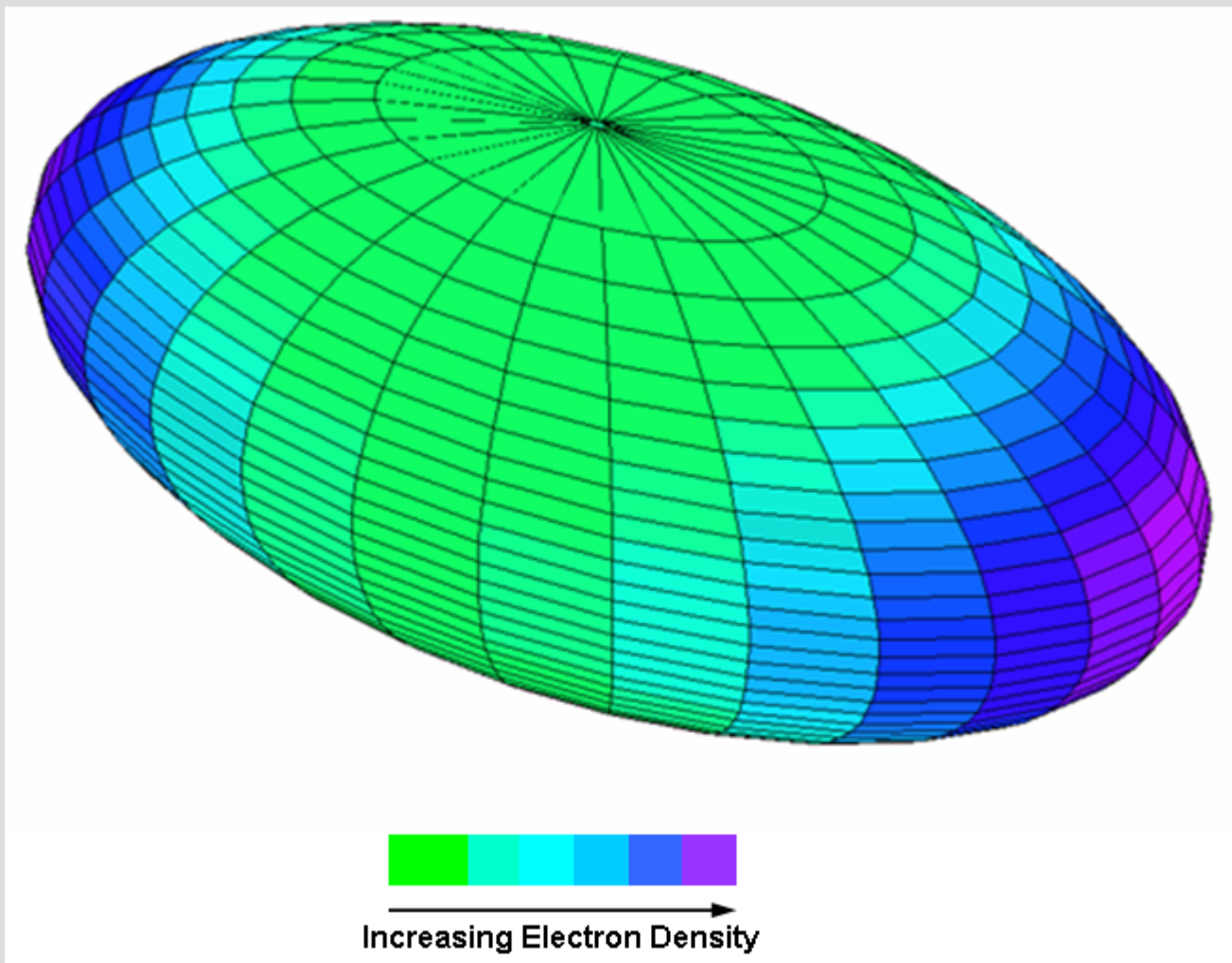
The total energy of the hydrogen molecular ion having a central field of $+pe$ at each focus of the prolate spheroid molecular orbital

$$E_T = -p^2 \left\{ \frac{e^2}{8\pi\epsilon_0 a_H} (4 \ln 3 - 1 - 2 \ln 3) \left[1 + \sqrt{\frac{2e^2}{4\pi\epsilon_0 (2a_H)^3} \frac{2\hbar}{m_e}} \right] - \frac{1}{2} \hbar \sqrt{\frac{k}{\mu}} \right\} = -p^2 16.13392 \text{ eV} - p^3 0.118755 \text{ eV}$$

The total energy of the hydrogen molecule having a central field of $+pe$ at each focus of the prolate spheroid molecular orbital

$$E_T = -p^2 \left\{ \frac{e^2}{8\pi\epsilon_0 a_0} \left[\left(2\sqrt{2} - \sqrt{2} + \frac{\sqrt{2}}{2} \right) \ln \frac{\sqrt{2}+1}{\sqrt{2}-1} - \sqrt{2} \right] \left[1 + p \sqrt{\frac{e^2}{4\pi\epsilon_0 a_0^3} \frac{2\hbar}{m_e}} \right] - \frac{1}{2} \hbar \sqrt{\frac{k}{\mu}} \right\} = -p^2 31.351 \text{ eV} - p^3 0.326469 \text{ eV}$$

Charge-Density Function



The calculated and experimental parameters of H_2 , D_2 , H_2^+ and D_2^+ .

The calculated and experimental parameters of H_2 , D_2 , H_2^+ and D_2^+ .

| Parameter | Calculated | Experimental | Eqs. ^a |
|---|---|---|--------------------|
| H_2 Bond Energy | 4.478 eV | 4.478 eV | 12.251 |
| D_2 Bond Energy | 4.556 eV | 4.556 eV | 12.253 |
| H_2^+ Bond Energy | 2.654 eV | 2.651 eV | 12.220 |
| D_2^+ Bond Energy | 2.696 eV | 2.691 eV | 12.222 |
| H_2 Total Energy | 31.677 eV | 31.675 eV | 12.247 |
| D_2 Total Energy | 31.760 eV | 31.760 eV | 12.248 |
| H_2 Ionization Energy | 15.425 eV | 15.426 eV | 12.249 |
| D_2 Ionization Energy | 15.463 eV | 15.466 eV | 12.250 |
| H_2^+ Ionization Energy | 16.253 eV | 16.250 eV | 12.218 |
| D_2^+ Ionization Energy | 16.299 eV | 16.294 eV | 12.219 |
| H_2^+ Magnetic Moment | $9.274 \times 10^{-24} \text{ JT}^{-1}$ | $9.274 \times 10^{-24} \text{ JT}^{-1}$ | 14.1-14.7 |
| Absolute H_2 Gas-Phase NMR Shift | μ_B -28.0 ppm | μ_B -28.0 ppm | 12.362 |
| H_2 Internuclear Distance ^b | 0.748 Å $\sqrt{2}a_0$ | 0.741 Å | 12.238 |
| D_2 Internuclear Distance ^b | 0.748 Å $\sqrt{2}a_0$ | 0.741 Å | 12.238 |
| H_2^+ Internuclear Distance ^c | 1.058 Å $2a_0$ | 1.06 Å | 12.207 |
| D_2^+ Internuclear Distance ^b | 1.058 Å $2a_0$ | 1.0559 Å | 12.207 |
| H_2 Vibrational Energy | 0.517 eV | 0.516 eV | 12.259 |
| D_2 Vibrational Energy | 0.371 eV | 0.371 eV | 12.264 |
| H_2 $\omega_e x_e$ | 120.4 cm^{-1} | 121.33 cm^{-1} | 12.261 |
| D_2 $\omega_e x_e$ | 60.93 cm^{-1} | 61.82 cm^{-1} | 12.265 |
| H_2^+ Vibrational Energy | 0.270 eV | 0.271 eV | 12.228 |
| D_2^+ Vibrational Energy | 0.193 eV | 0.196 eV | 12.232 |
| H_2 J=1 to J=0 Rotational Energy ^b | 0.0148 eV | 0.01509 eV | 14.45 |
| D_2 J=1 to J=0 Rotational Energy ^b | 0.00741 eV | 0.00755 eV | 14.37-14.45 |
| H_2^+ J=1 to J=0 Rotational Energy ^b | 0.00740 eV | 0.00739 eV | 14.49 |
| D_2^+ J=1 to J=0 Rotational Energy ^c | 0.00370 eV | 0.003723 eV | 14.37-14.43, 14.49 |

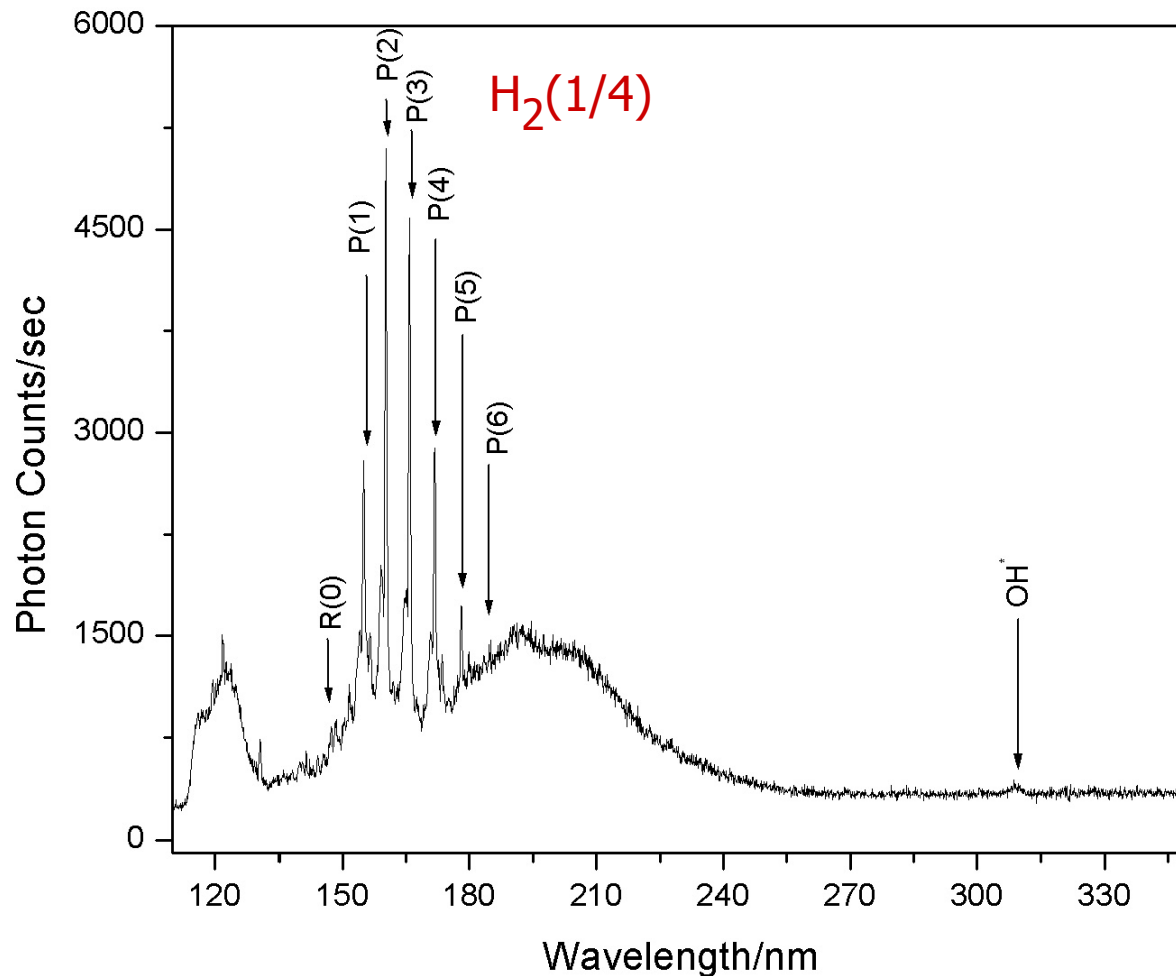
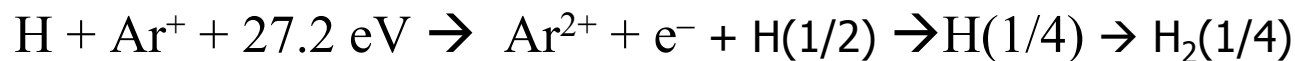
^a R. Mills, *The Grand Unified Theory of Classical Quantum Mechanics*, September 2001 Edition, BlackLight Power, Inc., Cranbury, New Jersey, Distributed by Amazon.com; January (2003) Edition posted at www.blacklightpower.com.

^b The internuclear distances are not corrected for the reduction due to \bar{E}_{osc} .

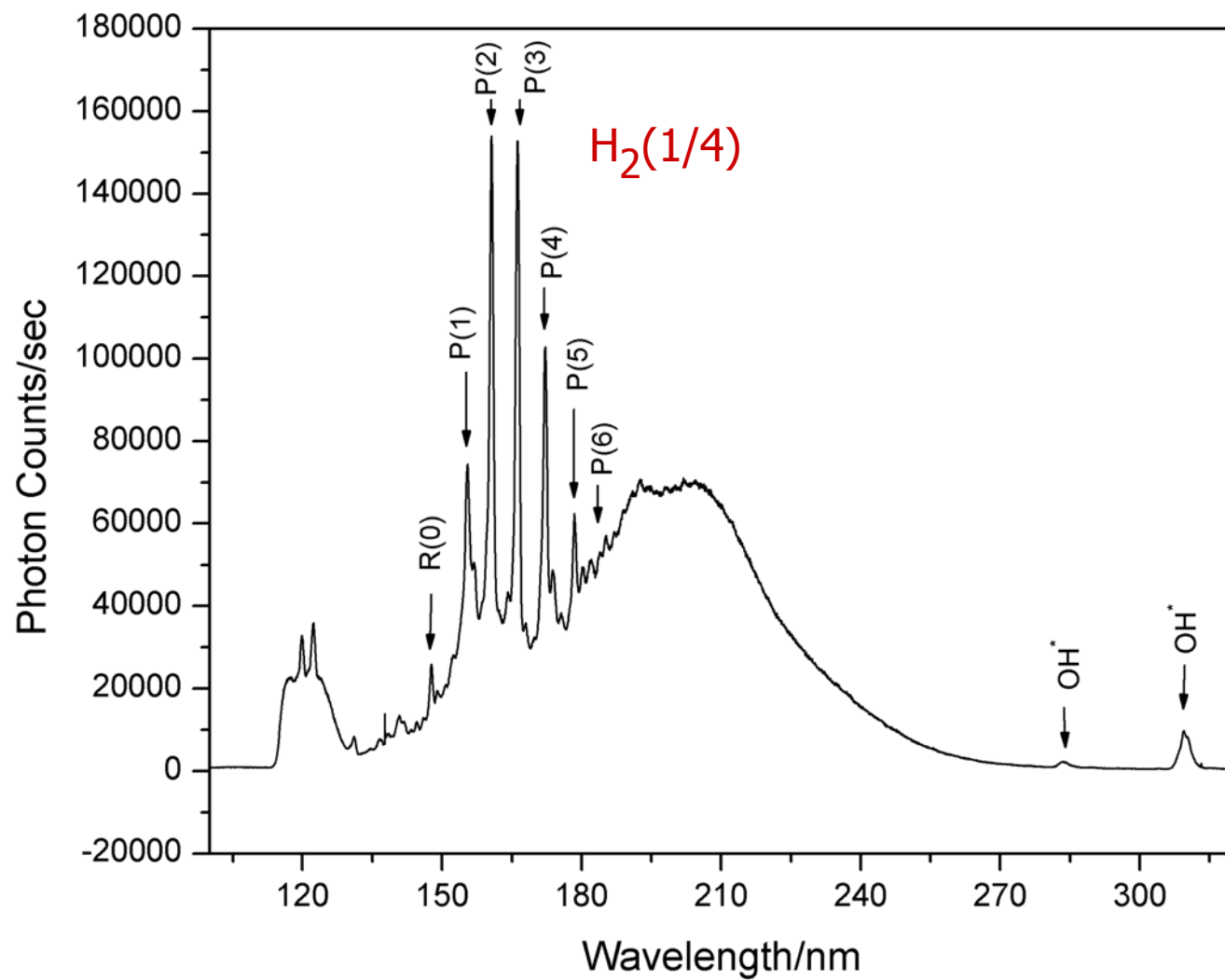
^c The internuclear distances are not corrected for the increase due to \bar{E}_{osc} .

Identification of Fractional-Principal-Quantum-Energy-Level Molecular Hydrogen

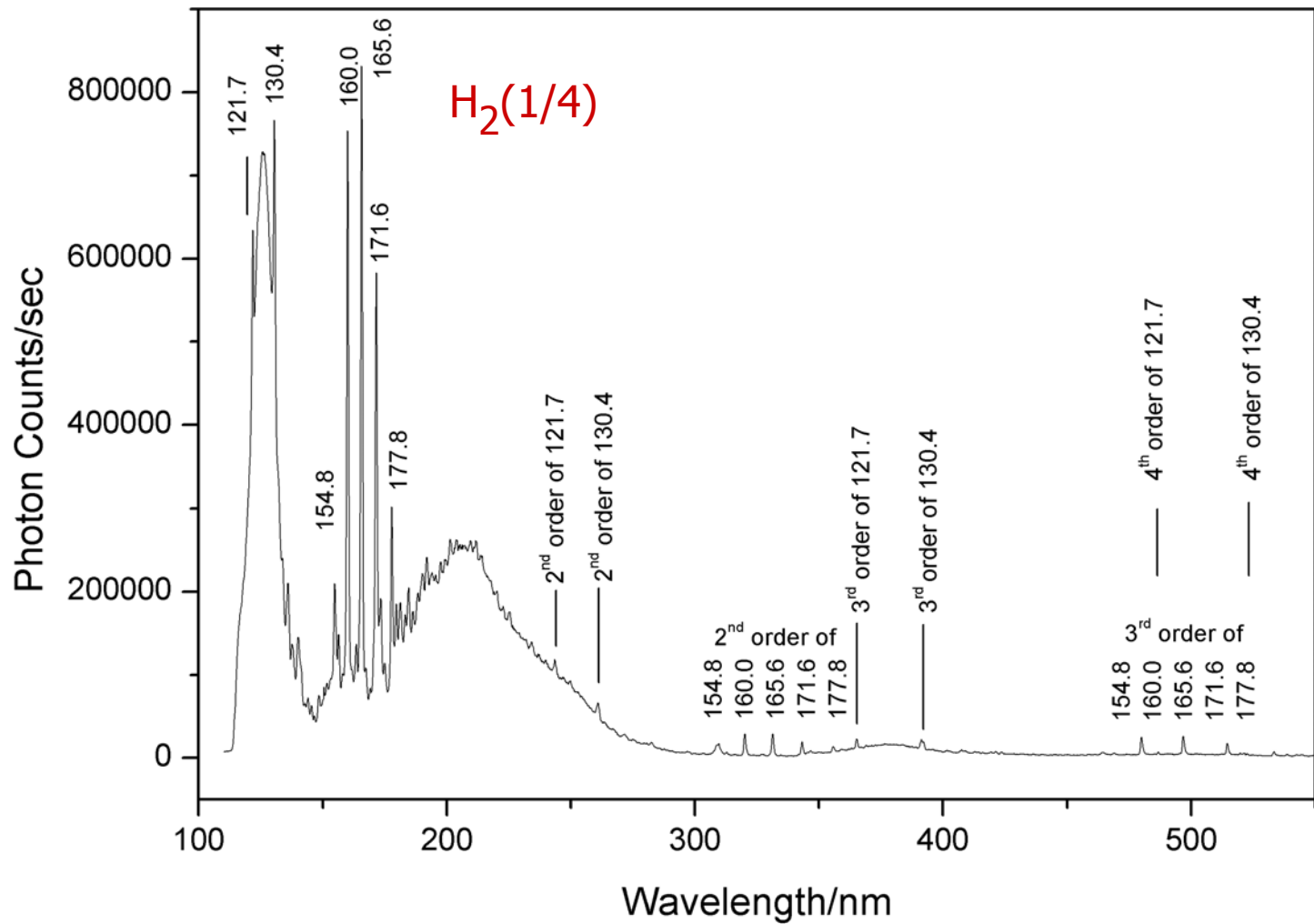
by the Gold Standard:
Rotational Energies
that Match the Predicted p^2 energies
of H_2



A series of sharp, evenly-spaced lines observed in the region 145-185 matched the P branch of H₂(1/4) for the vibrational transition $\nu = 1 \rightarrow \nu = 0$. P(1), P(2), P(3), P(4), P(5), and P(6) were observed at 154.94 nm, 159.74 nm, 165.54 nm, 171.24 nm, 178.14 nm, and 183.14 nm, respectively. The sharp peak at 146.84 nm may be the first member of the R branch, R(0). The R-branch lines appeared to correspond to forbidden transitions.



The P branch of H₂(1/4) for the vibrational transition $v = 1 \rightarrow v = 0$. P(1), P(2), P(3), P(4), P(5), and P(6).



The 100-560 nm spectrum of 750 Torr, 12.5 keV-electron-beam-maintained plasma of argon containing about 1% hydrogen showing the ro-vibrational peaks of $H_2(1/4)$ to 4th order as single peaks.

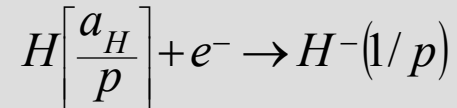


BLACKLIGHT
POWER, Inc

Novel Hydride Compounds

Hydride Ion with a Higher Binding Energy

A novel hydride ion referred to as a hydrino hydride ion and designated as $H^-(1/p)$ is predicted to form by the reaction of an electron with a hydrino:



Hydride ions comprise a hydrogen nucleus and two indistinguishable electrons at a binding energy of

$$\text{Ionization Energy} = \frac{\hbar^2 \sqrt{s(s+1)}}{8\mu_e a_0^2 [1 + \sqrt{s(s+1)}]^2} - \frac{\pi\mu_0 e^2 \hbar^2}{m_e^2} \left(\frac{1}{a_H^3} + \frac{2^2}{a_0^3 [1 + \sqrt{s(s+1)}]^3} \right)$$

where p is an integer greater than one. The ionic radii are

$$r_1 = \frac{a_0}{p} (1 + \sqrt{s(s+1)}); s = \frac{1}{2}$$

The calculated ionization energy of the hydride ion is **0.75418 eV**.

The experimental value given by Lykke is $6082.99 \pm 0.15 \text{ cm}^{-1}$ (**0.75418 eV**).

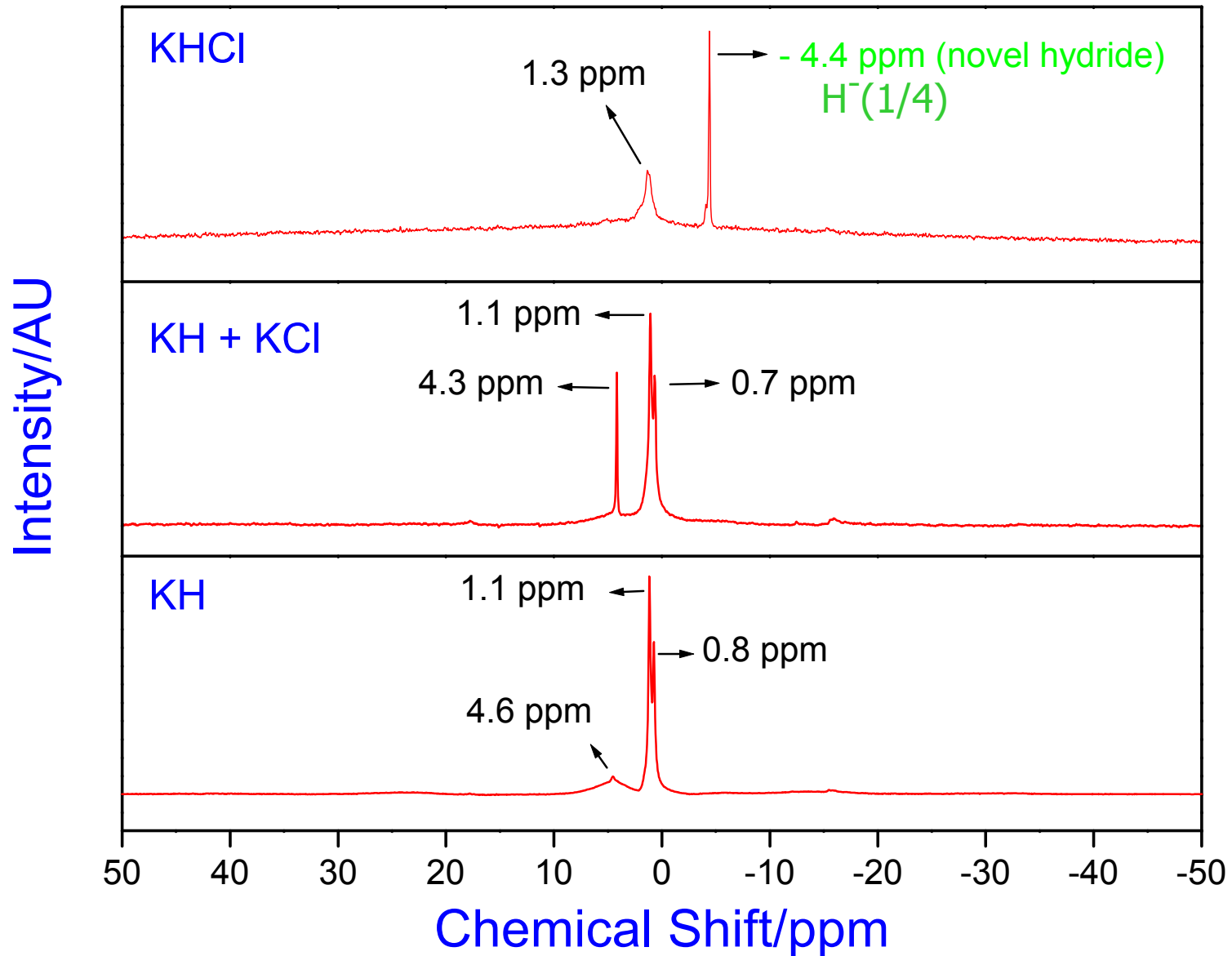
The radii and ionization energies of the
hydrino hydride ions $H^-(n = 1/p)$ as a
function of p

| Hydride Ion | r_1 (a_o) | Calculated Ionization Energy (eV) | Calculated Wavelength (nm) |
|----------------|--------------------|---|----------------------------------|
| $H^-(n = 1)$ | 1.8660 | 0.7542 | 1644 |
| $H^-(n = 1/2)$ | 0.9330 | 3.047 | 406.9 |
| $H^-(n = 1/3)$ | 0.6220 | 6.610 | 187.6 |
| $H^-(n = 1/4)$ | 0.4665 | 11.23 | 110.4 |

Solid-State MAS ^1H -NMR

- Chemical environment of hydrogen
- Unusual upfield shifts – relative to normal hydride

(the electron is closer to the nucleus in a smaller hydride ion called a hydrido hydride ion)



Upfield-shifted NMR peak demonstrates novel hydride.

NMR of KH and Hydrino Hydride KH*C1

The predicted shift $\frac{\Delta B_T}{B}$ for H⁻(1/*p*) is given by the sum of that of H⁻(1/1) and a relativistic term that depends on *p* > 1:

$$\frac{\Delta B_T}{B} = -\mu_0 \frac{e^2}{12m_e a_0 (1 + \sqrt{s(s+1)})} (1 + 2\pi\alpha p) = -(29.9 + 1.37 p) \text{ ppm}$$

The experimental absolute resonance shift of TMS is **-31.5 ppm** relative to the proton's gyromagnetic frequency.

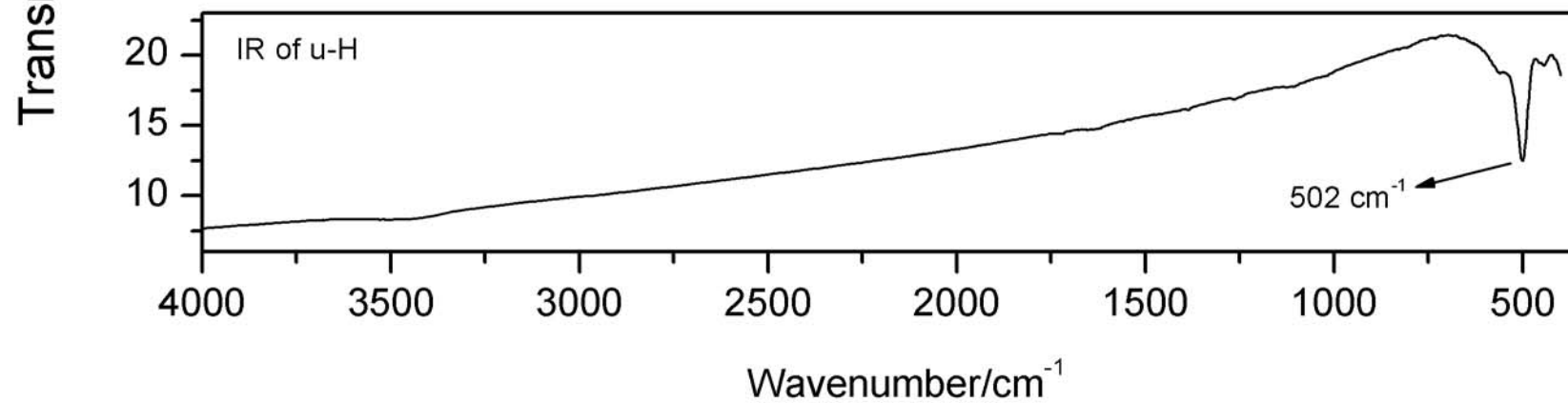
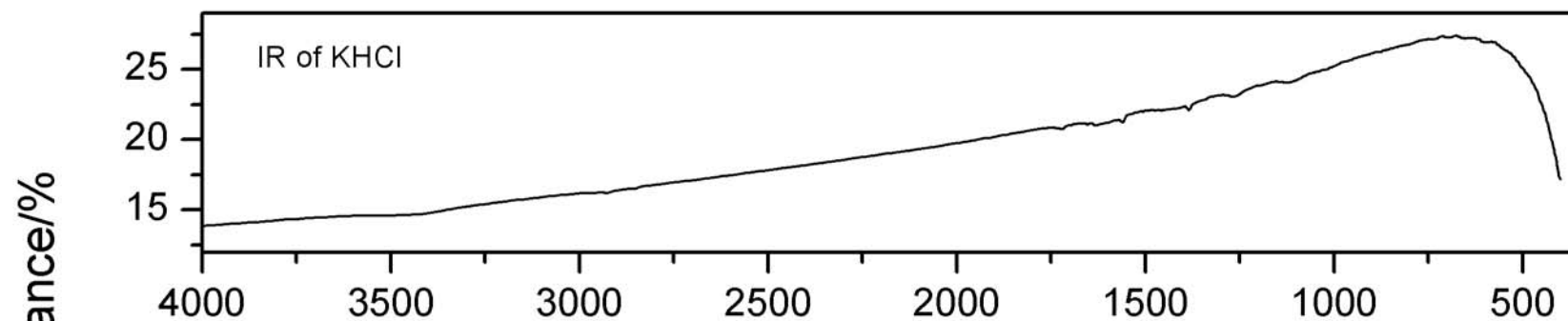
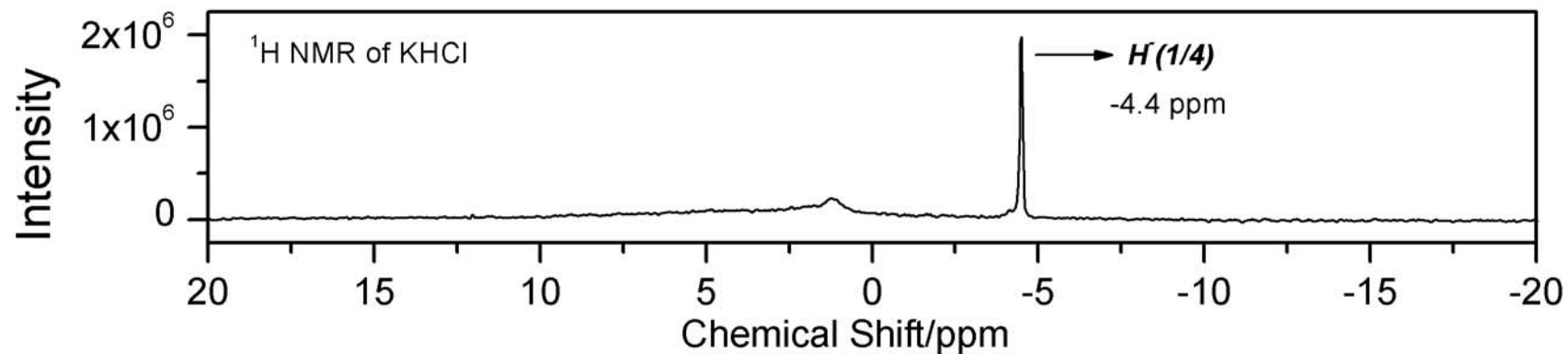
The experimental frequency of H⁻(1/1) of **1.3 ppm** matched the calculated frequency corresponding to an absolute resonance shift of **-30.2 ppm**.

The novel peak of KH*C1 at **-4.4 ppm** relative to TMS corresponding to an absolute resonance shift of **-35.9 ppm** indicates that *p* = **4** corresponding to H⁻(1/4).

H⁻(1/4) is the predicted product of K catalyst.

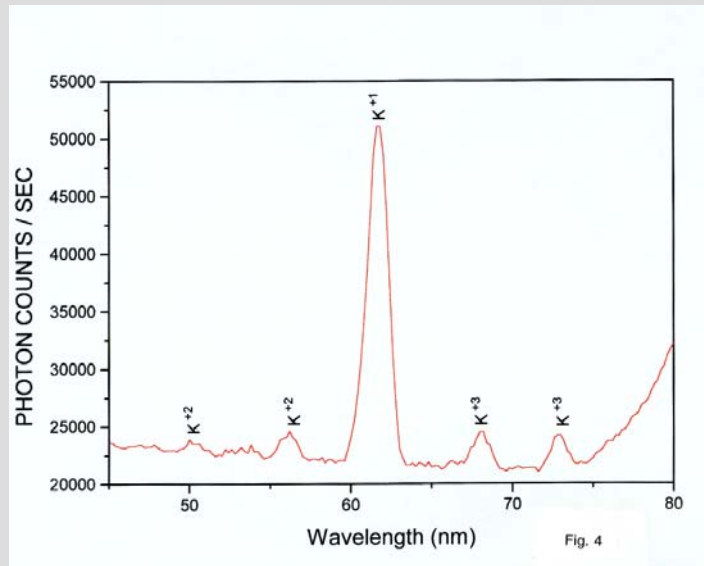
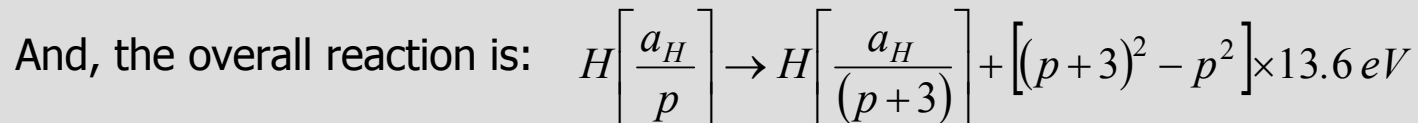
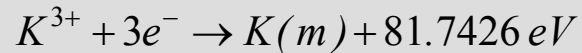
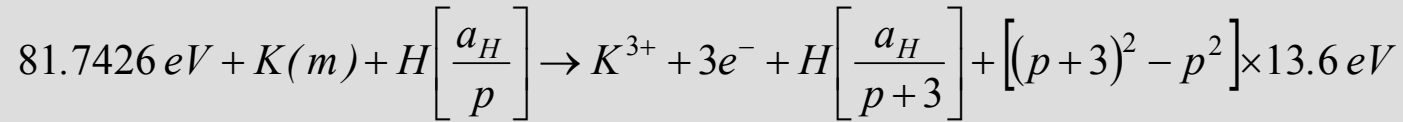
H⁻(1/4) was observed in the VUV at 110 nm.

Upfield Shifted Peak Due to H⁻(1/4) Cannot Be Assigned to U-H

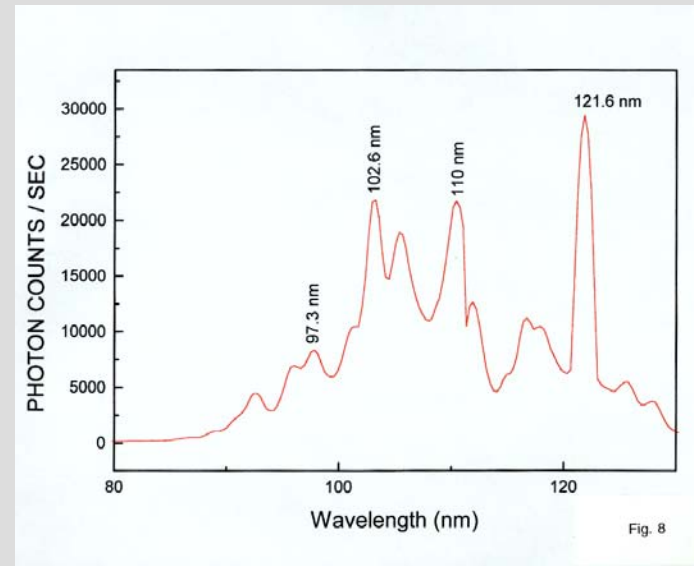


Potassium

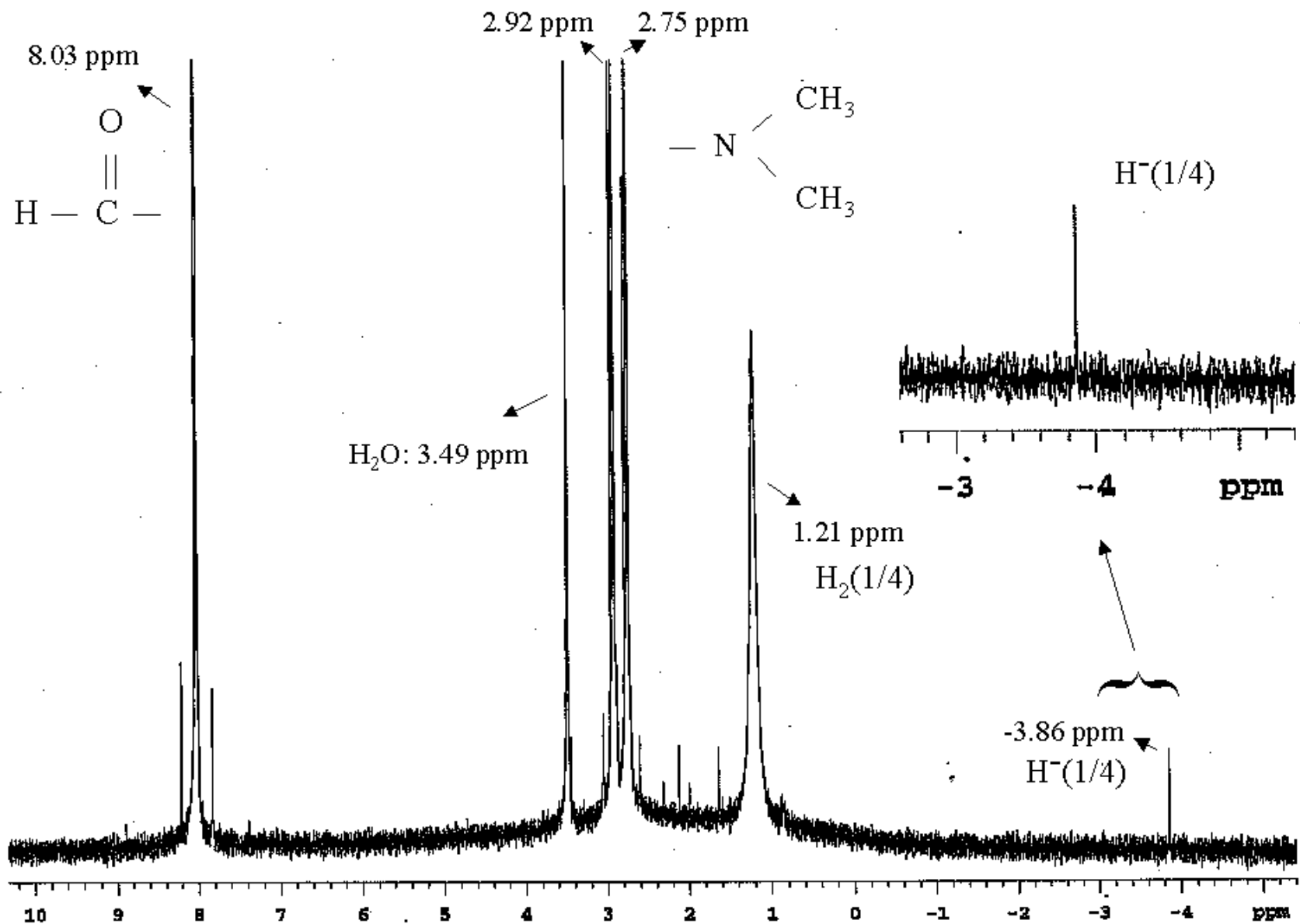
A catalytic system is provided by the ionization of t electrons from an atom each to a continuum energy level such that the sum of the ionization energies of the t electrons is approximately $m \cdot 27.2 \text{ eV}$, where m is an integer. One such catalytic system involves potassium. The first, second, and third ionization energies of potassium are 4.34066 eV , 31.63 eV , 45.806 eV respectively. The triple ionization ($t=3$) reaction of K to K^{3+} , then, has a net enthalpy of reaction of 81.7426 eV , which is equivalent to $m=3$.



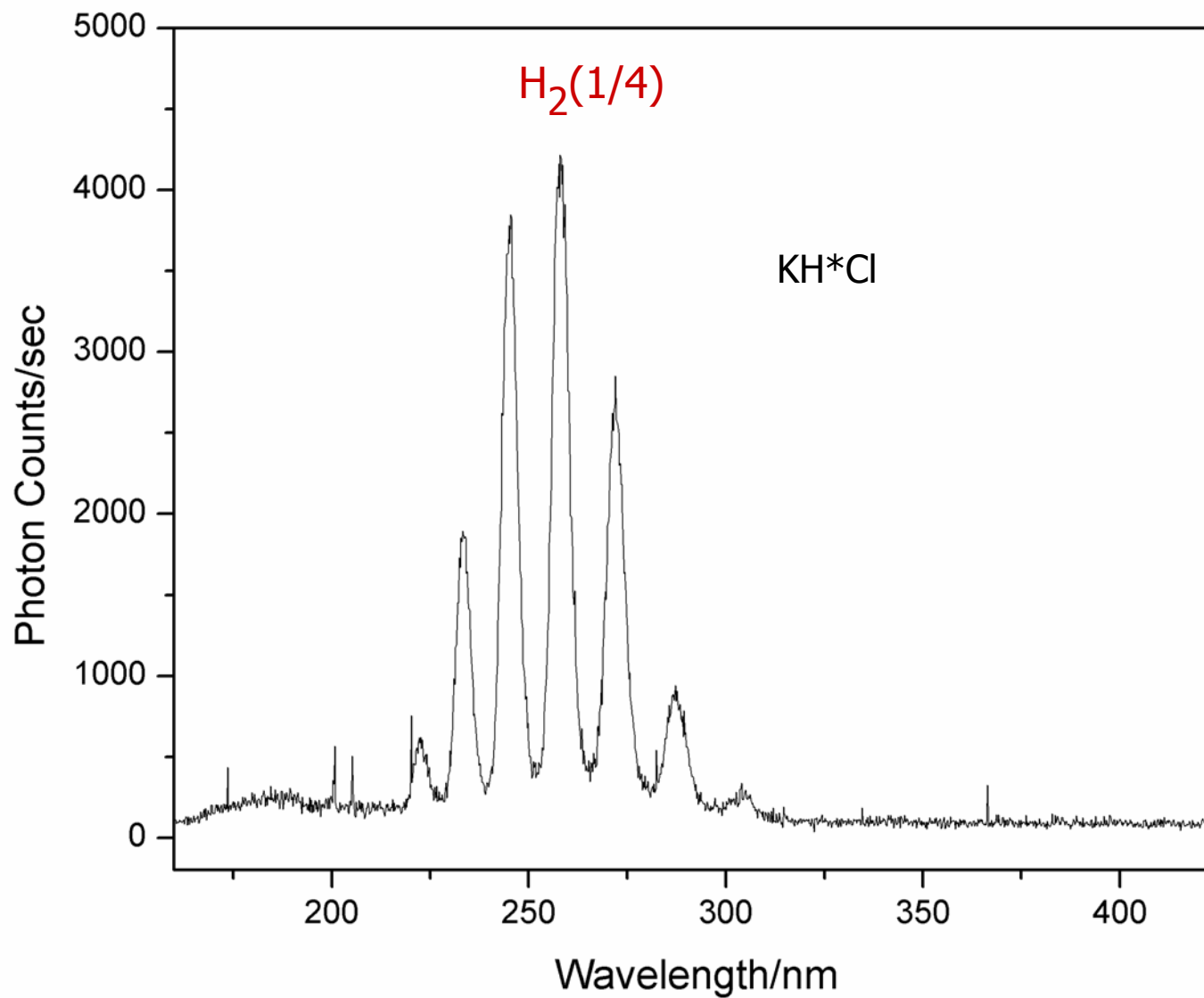
Characteristic emission was observed from K^{3+} which confirmed the resonant nonradiative energy transfer of $3 \cdot 27.2 \text{ eV}$ from atomic hydrogen to atomic potassium.



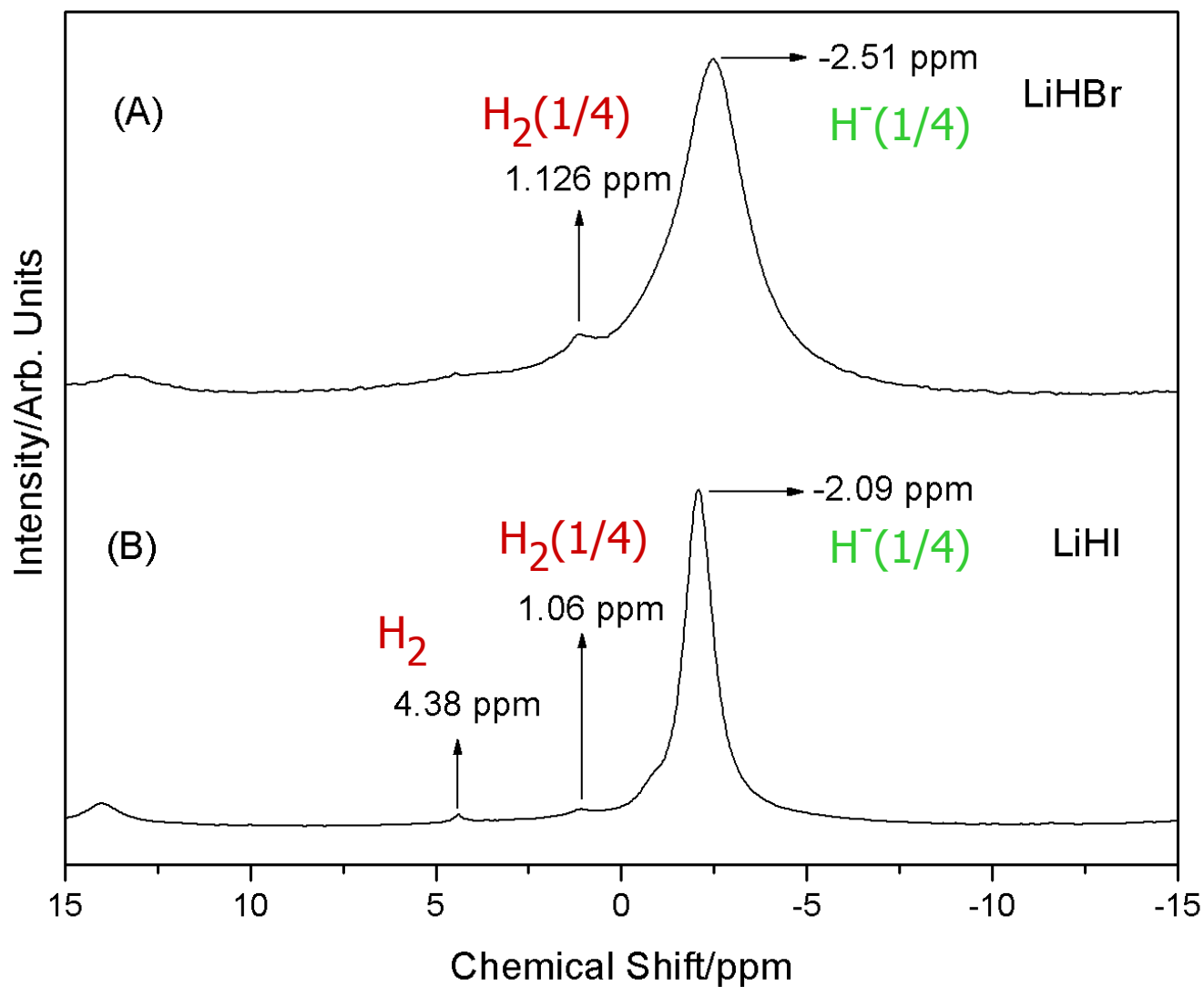
Novel hydride ion emission of atomic K catalyst predicted and observed at 110 nm .



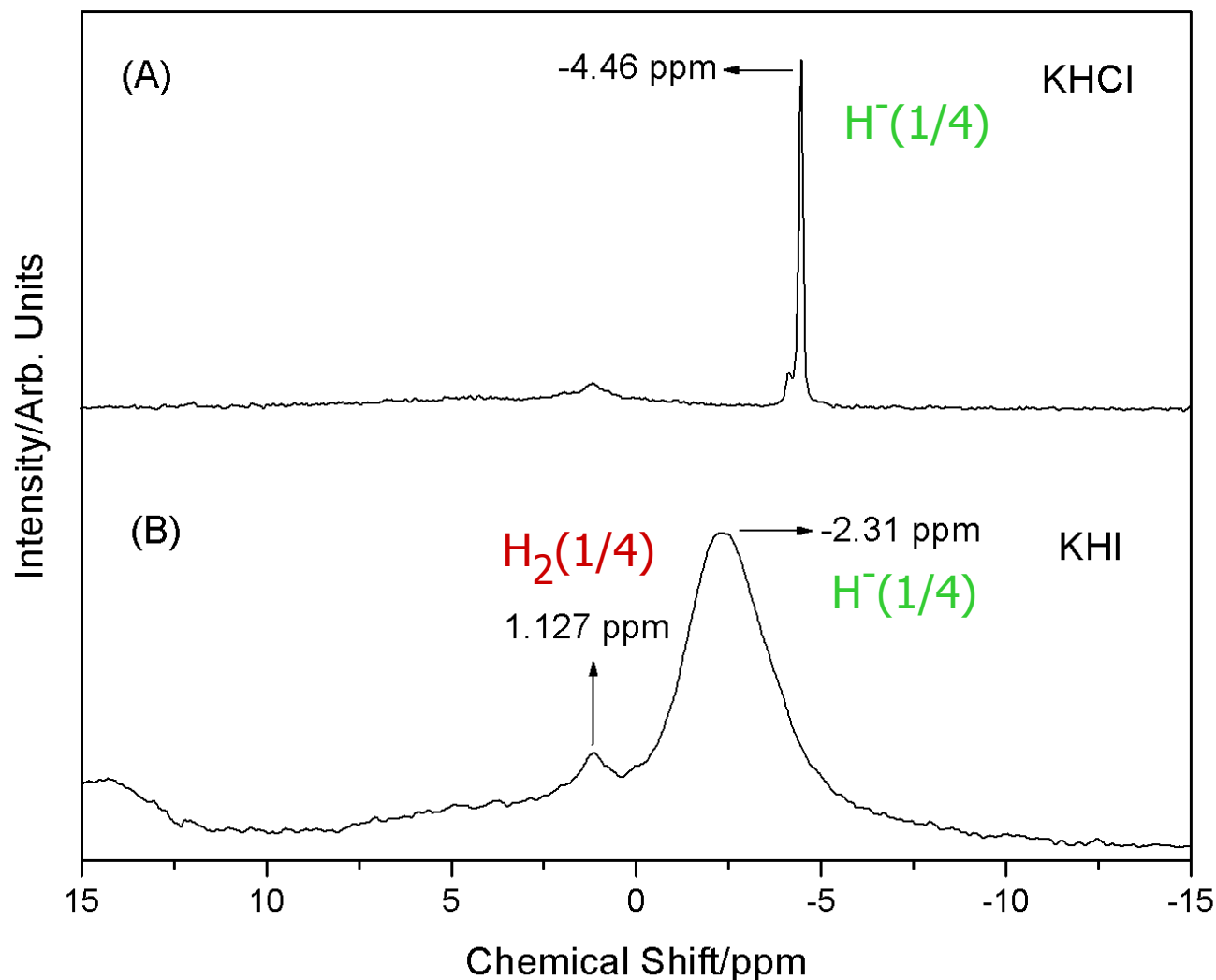
^1H NMR of KH^*Cl dissolved in DMF-d_7 showing isolated $\text{H}_2(1/4)$ and $\text{H}^-(1/4)$ at 1.2 ppm and -3.86 ppm, respectively, wherein the absence of any solid matrix effect or the possibly of alternative assignments such as U-centered H or F centers in solid matrix confirm the solid NMR assignment of the 1.13 ppm and -4.4 ppm peaks of KH^*Cl to $\text{H}_2(1/4)$ and $\text{H}^-(1/4)$, respectively.



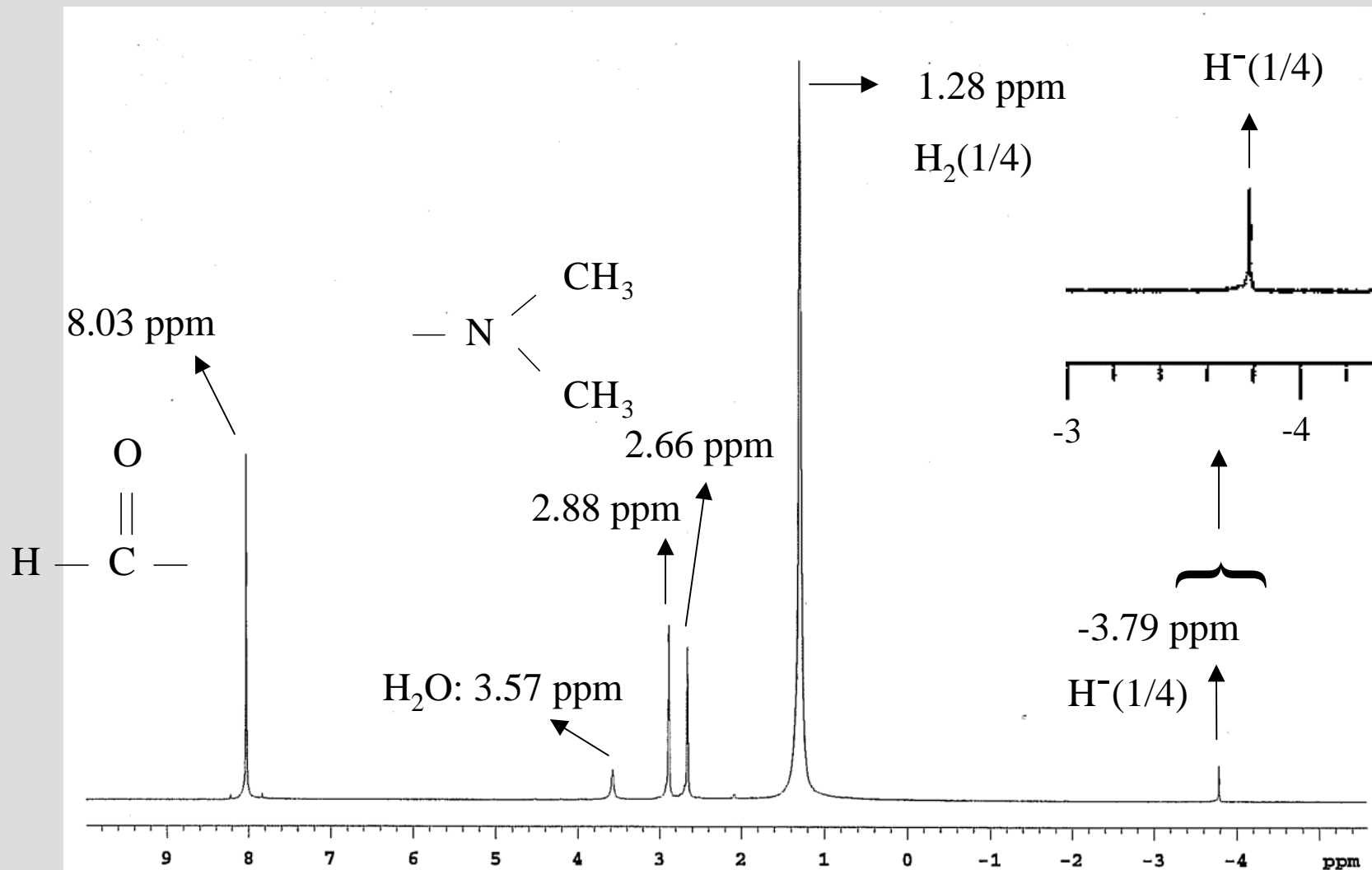
The 150-450 nm spectrum of electron-beam-excited KH^*Cl having a -4.4 ppm NMR peak assigned to $H^-(1/4)$. The intensity pattern and the energy spacing of 0.25 eV matched the P-branch of $H_2(1/4)$.



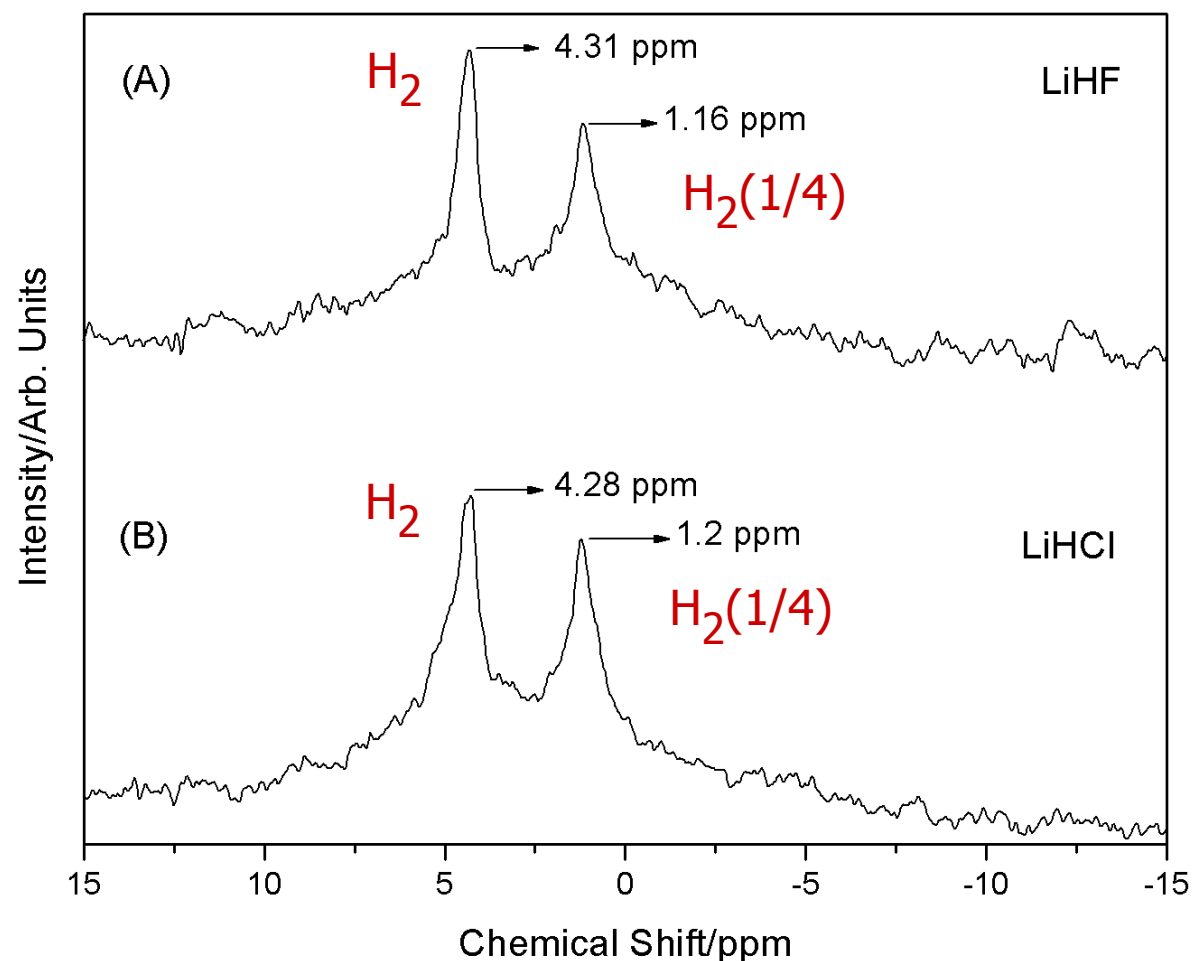
^1H MAS NMR spectra relative to external TMS. (A) LiH^*Br showing a broad -2.5 ppm upfield-shifted peak and a peak at 1.13 ppm assigned to $\text{H}^-(1/4)$ and $\text{H}_2(1/4)$, respectively. (B) LiH^*I showing a broad -2.09 ppm upfield-shifted peak assigned to $\text{H}^-(1/4)$ and peaks at 1.06 ppm and 4.38 ppm assigned to $\text{H}_2(1/4)$ and H_2 , respectively.



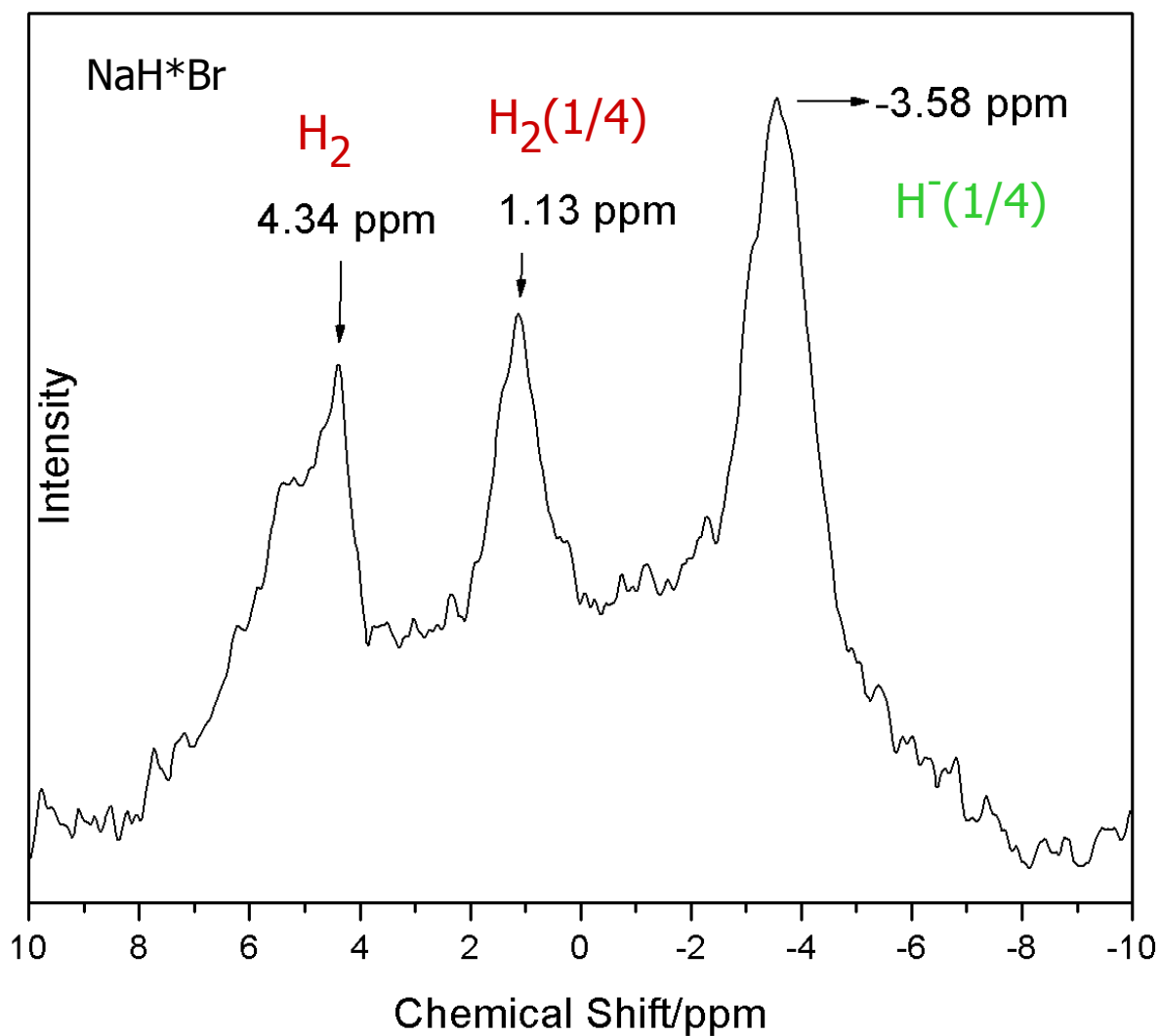
^1H MAS NMR spectra relative to external TMS. (A) KH^*Cl showing a very sharp -4.46 ppm upfield-shifted peak corresponding to an environment that is essentially that of a free ion. (B) KH^*I showing a broad -2.31 ppm upfield-shifted peak similar to the case of LiH^*Br and LiH^*I . Both spectra also had a 1.13 ppm peak assigned to $\text{H}_2(1/4)$.



¹H solution NMR of *KH*I* dissolved to saturation in DMF-d₇ that showed increasing intensities and slight downfield shifts of the H₂(1/4) and H(1/4) peaks to 1.28 ppm and -3.79 ppm, respectively, as the concentration of *KH*I* increased. The concentration-dependent solution matrix effect confirmed the solid matrix effect corresponding to the NMR assignment of H₂(1/4) and H(1/4) to the peaks at 1.13 ppm and -2.31 ppm.

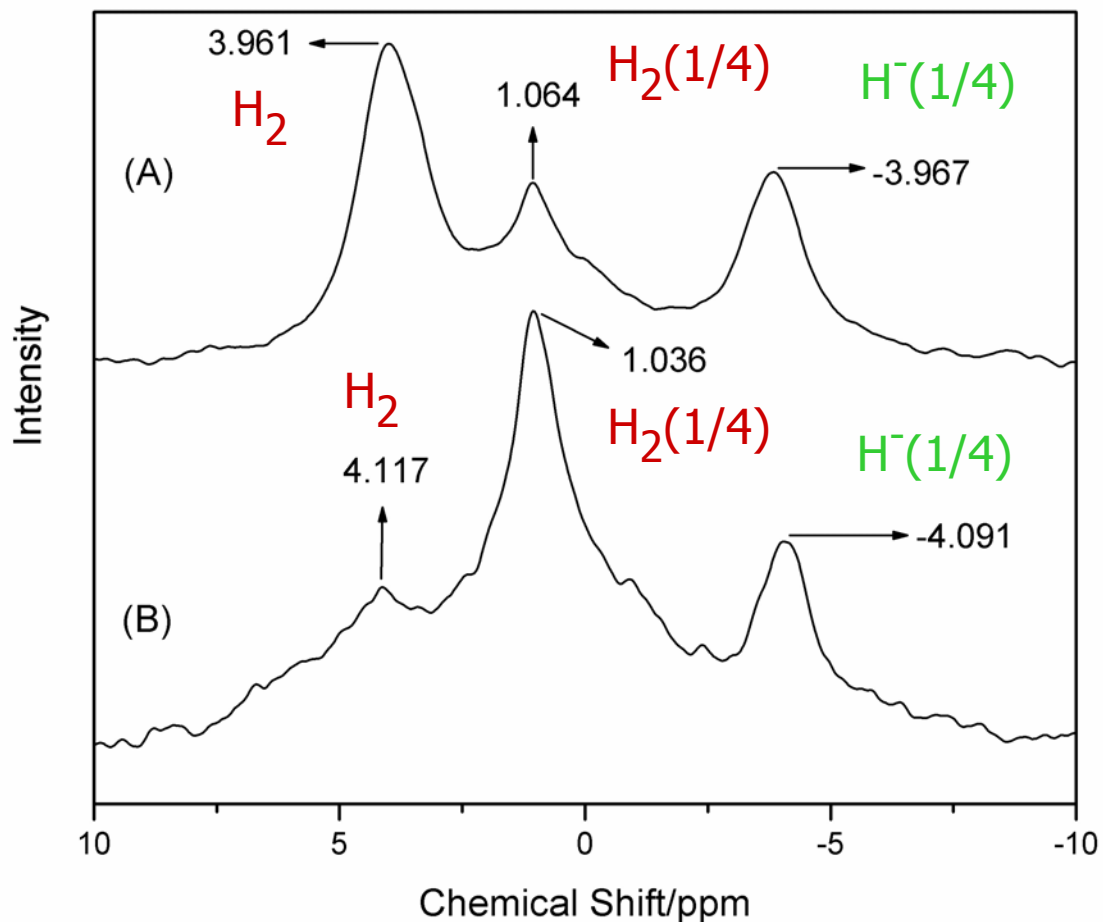


^1H MAS NMR spectra relative to external TMS showing an H-content selectivity of LiH^*X for molecular species alone based on the nonpolarizability of the halide and the corresponding nonreactivity towards $\text{H}^-(1/4)$. (A) LiH^*F comprising a nonpolarizable fluorine showing peaks at 4.31 ppm assigned to H_2 and 1.16 ppm assigned to $\text{H}_2(1/4)$ and the absence of the $\text{H}^-(1/4)$ ion peak. (B) LiH^*Cl comprising a nonpolarizable chlorine showing peaks at 4.28 ppm assigned to H_2 and 1.2 ppm assigned to $\text{H}_2(1/4)$ and the absence of the $\text{H}^-(1/4)$ ion peak.

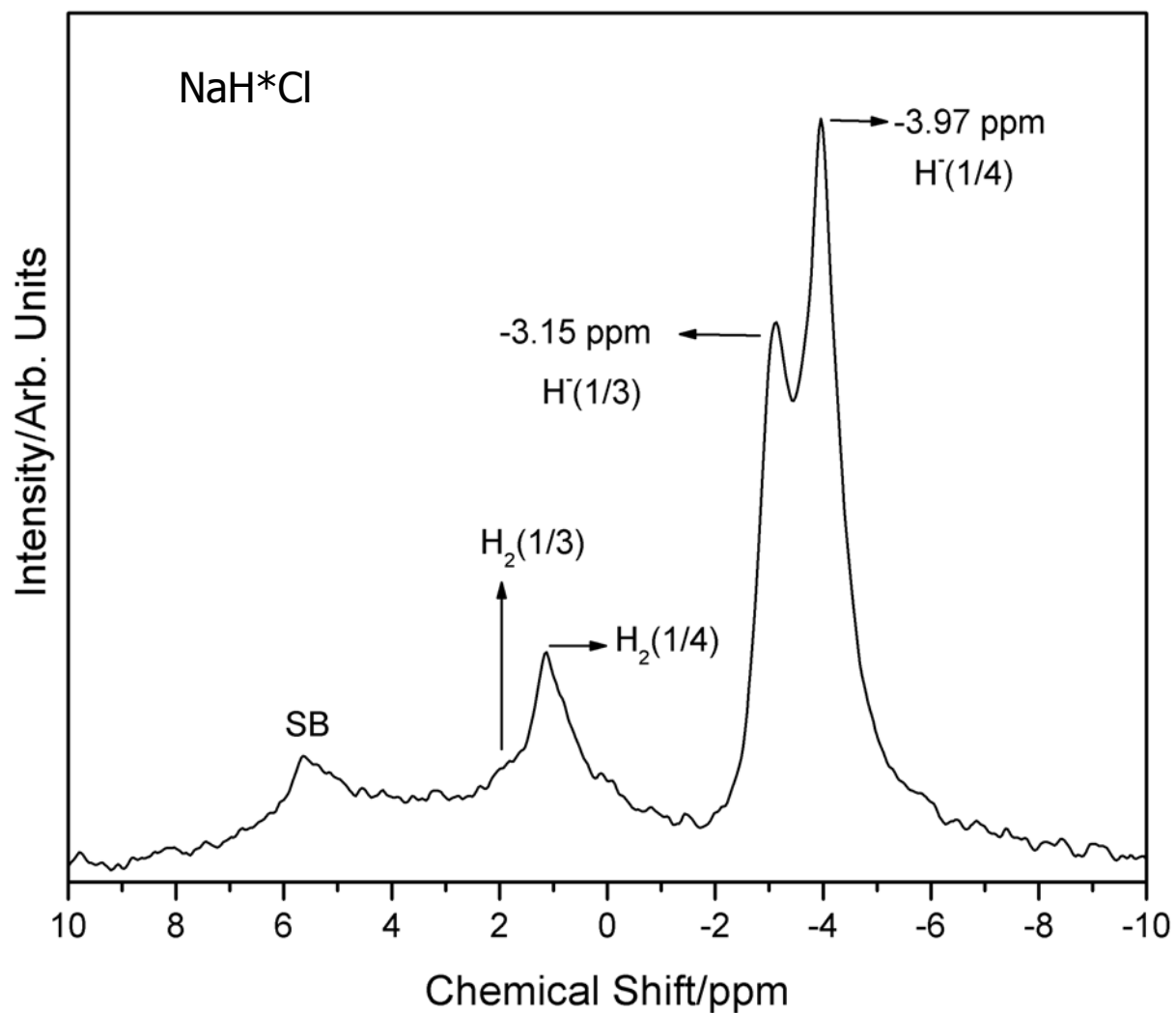


The ^1H MAS NMR spectra of NaH^*Br relative to external TMS showing a -3.58 ppm upfield-shifted peak, a peak at 1.13 ppm, and a peak at 4.3 ppm assigned to $\text{H}^-(1/4)$, $\text{H}_2(1/4)$, and H_2 , respectively.

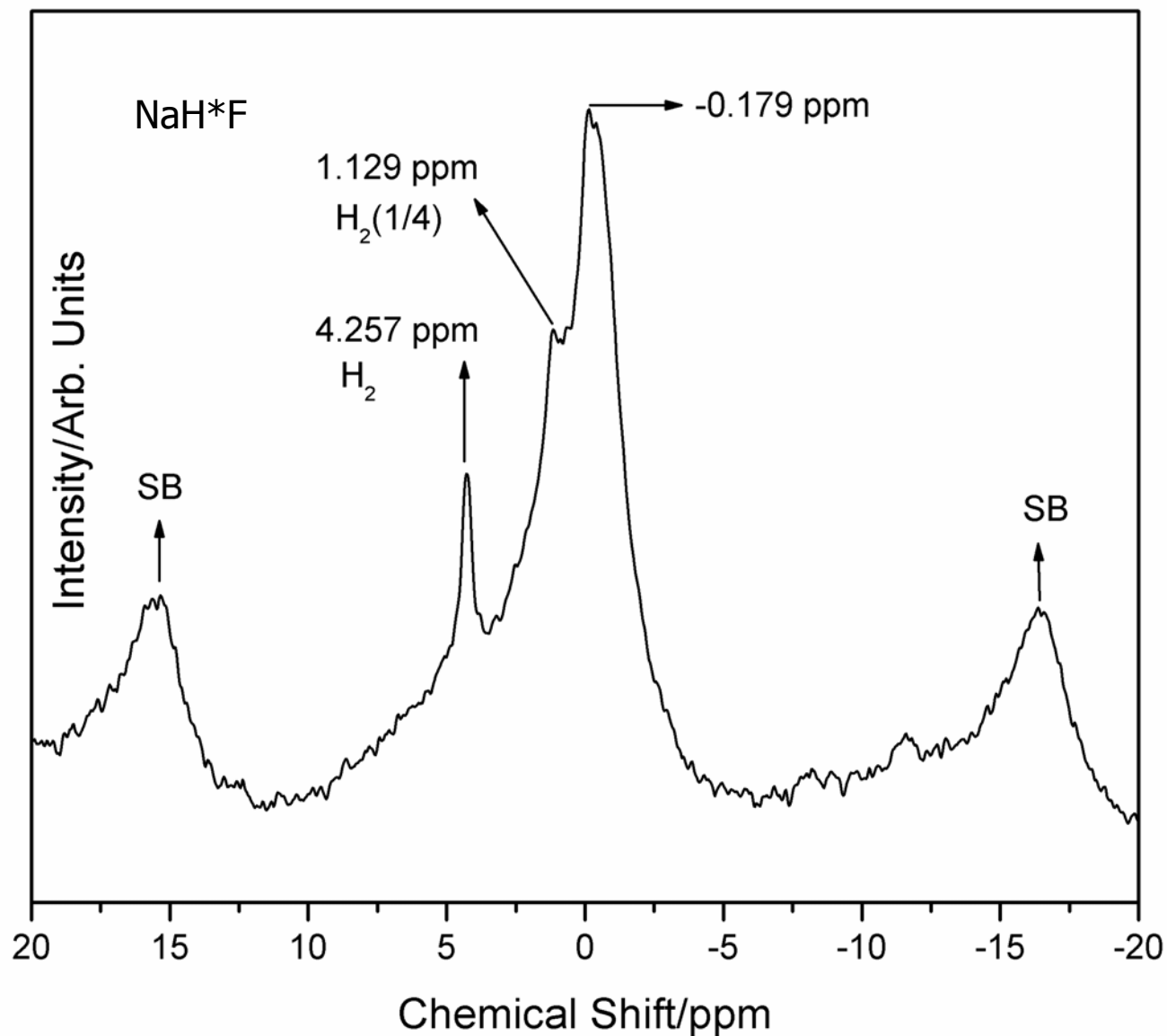
NaH*Cl



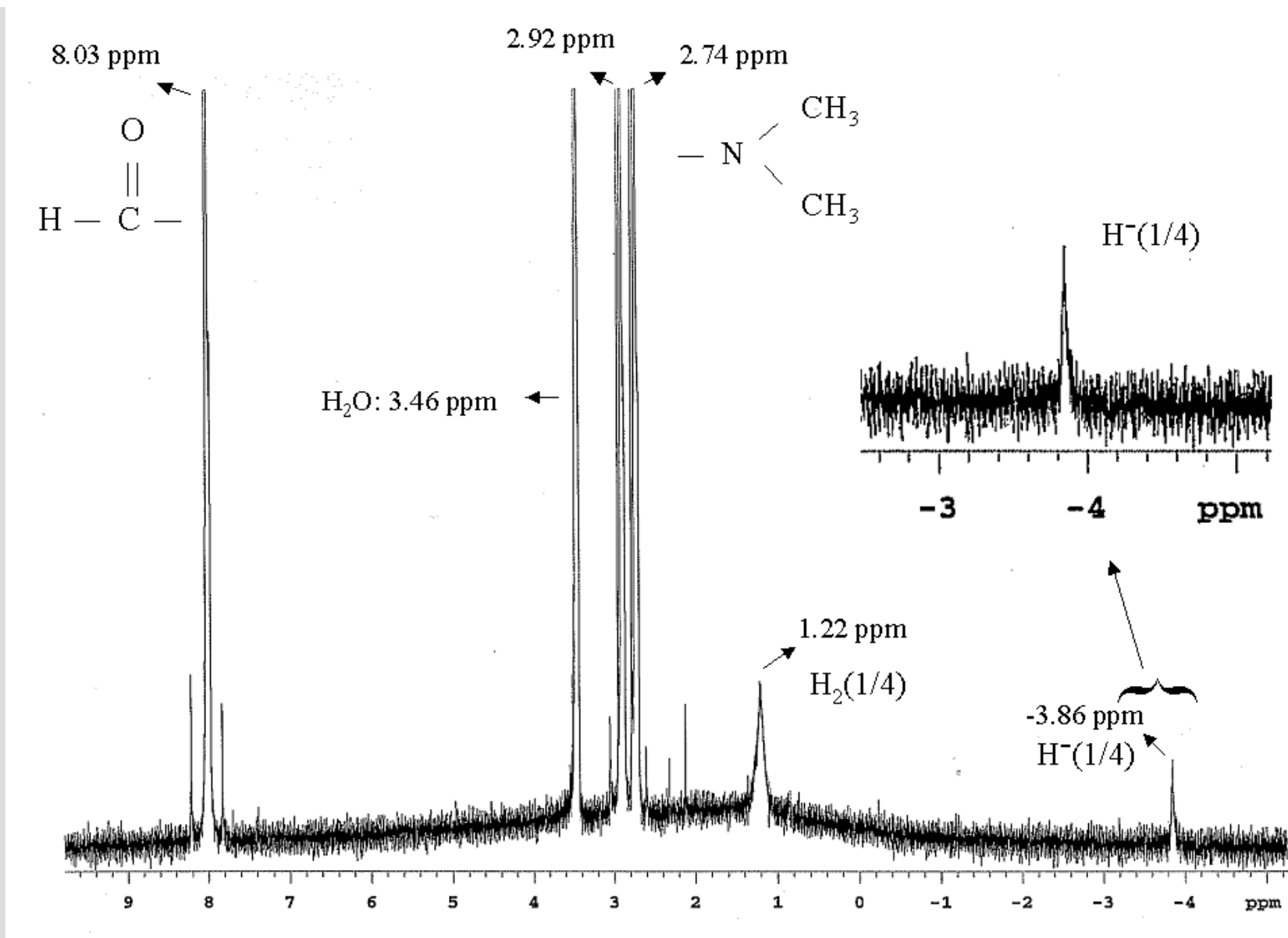
*NaH*Cl* ^1H MAS NMR spectra relative to external TMS showing the effect of hydrogen addition on the relative intensities of H_2 , $\text{H}_2(1/4)$, and $\text{H}^-(1/4)$. The addition of hydrogen increased the $\text{H}^-(1/4)$ peak and decreased the $\text{H}_2(1/4)$ while the H_2 increased. (A) *NaH*Cl* synthesized with hydrogen addition showing a -4 ppm upfield-shifted peak assigned to $\text{H}^-(1/4)$, a 1.1 ppm peak assigned to $\text{H}_2(1/4)$, and a dominant 4 ppm peak assigned to H_2 . (B) *NaH*Cl* synthesized without hydrogen addition showing a -4 ppm upfield-shifted peak assigned to $\text{H}^-(1/4)$, a dominant 1.0 ppm peak assigned to $\text{H}_2(1/4)$, and a small 4.1 ppm assigned to H_2 .



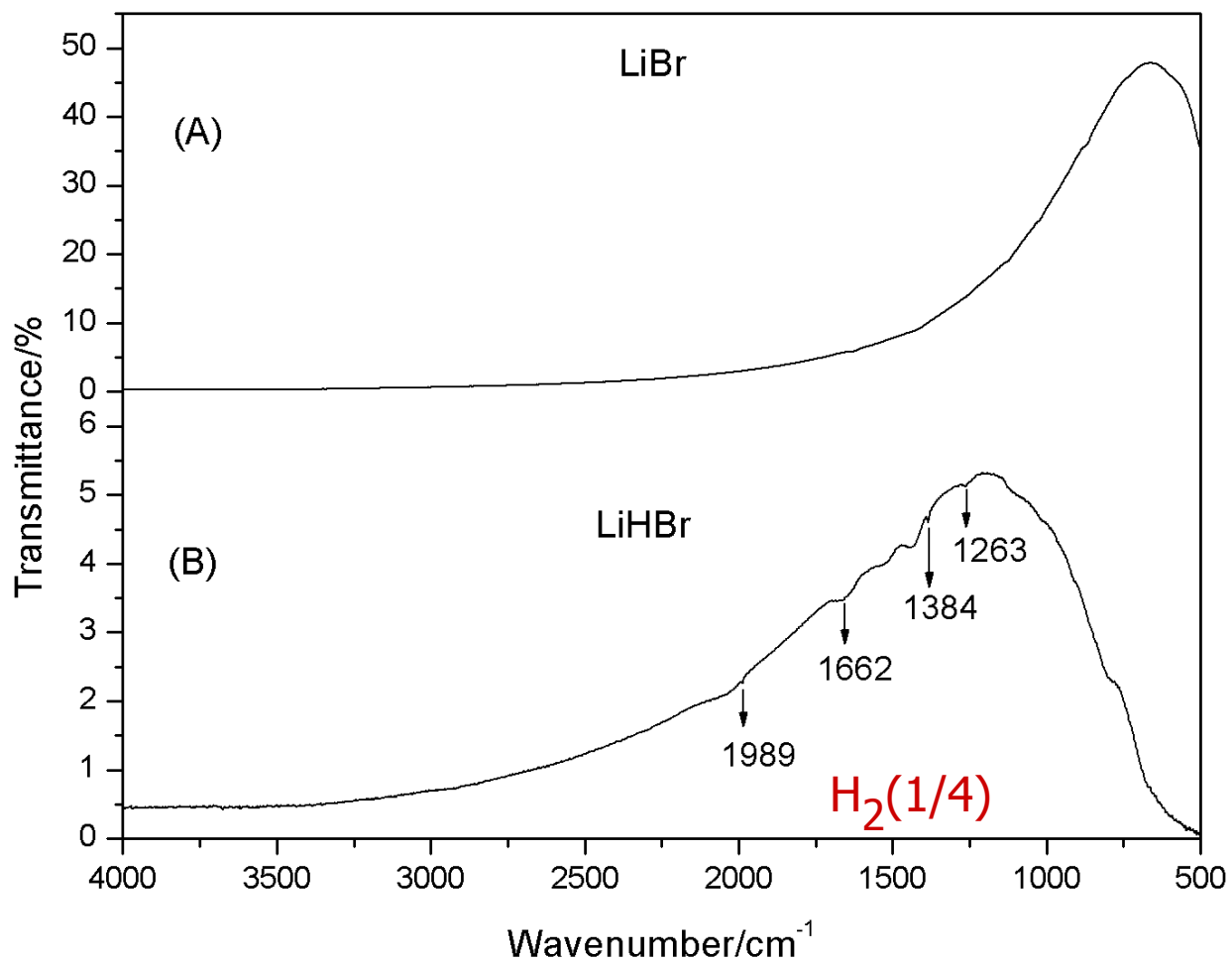
The ^1H MAS NMR spectrum relative to external TMS of NaH^*Cl from reaction of NaCl and the solid acid KHSO_4 as the only source of hydrogen showing both the $\text{H}^-(1/4)$ peak at -3.97 ppm and an upfield-shifted peak at -3.15 ppm assigned to $\text{H}^-(1/3)$. The corresponding $\text{H}_2(1/4)$ and $\text{H}_2(1/3)$ peaks are shown at 1.15 ppm and 1.7 ppm, respectively. Both fractional hydrogen states were present and the hydrogen peak was absent at 4.3 ppm due to the synthesis of NaH^*Cl using a solid acid as the H source rather than addition of hydrogen gas and a dissociator. (SB=side band).



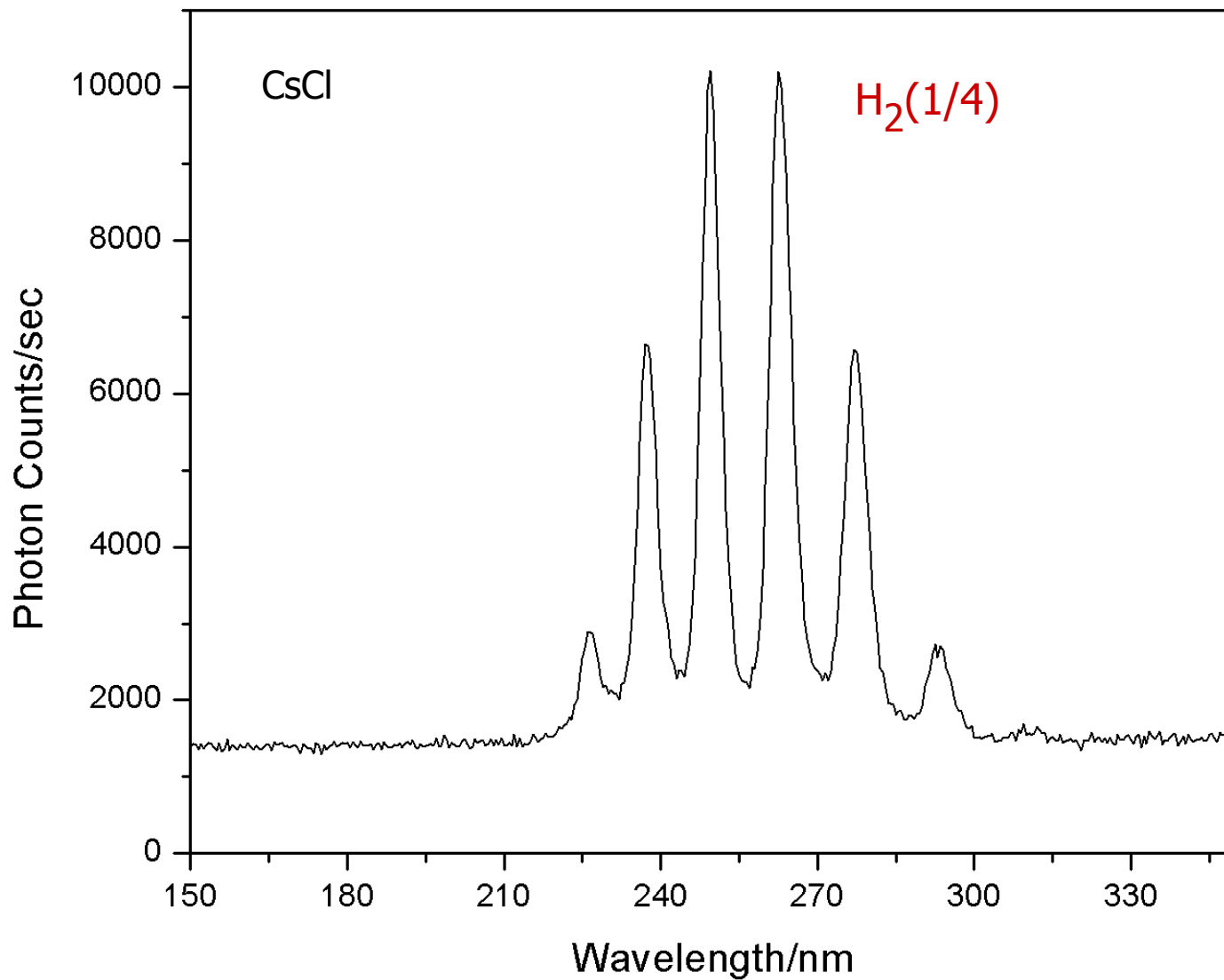
The ^1H MAS NMR spectrum of NaH^*F relative to external TMS showing a matrix-shifted $\text{H}(1/4)$ peak at -0.18 ppm, and unshifted $\text{H}_2(1/4)$ and H_2 peaks at 1.13 ppm and 4.3 ppm, respectively. The smallest lattice spacing of NaF relative to any other sodium halide gives rise to a large matrix effect in NaH^*F . (SB=side band).



^1H NMR of NaHF dissolved in DMF-d_7 showing isolated $\text{H}_2(1/4)$ and $\text{H}^-(1/4)$ at 1.2 ppm and -3.86 ppm , respectively, wherein the absence of any solid matrix effect or the possibly of alternative assignments such as U-centered H or F centers in solid matrix confirm the solid NMR assignments.

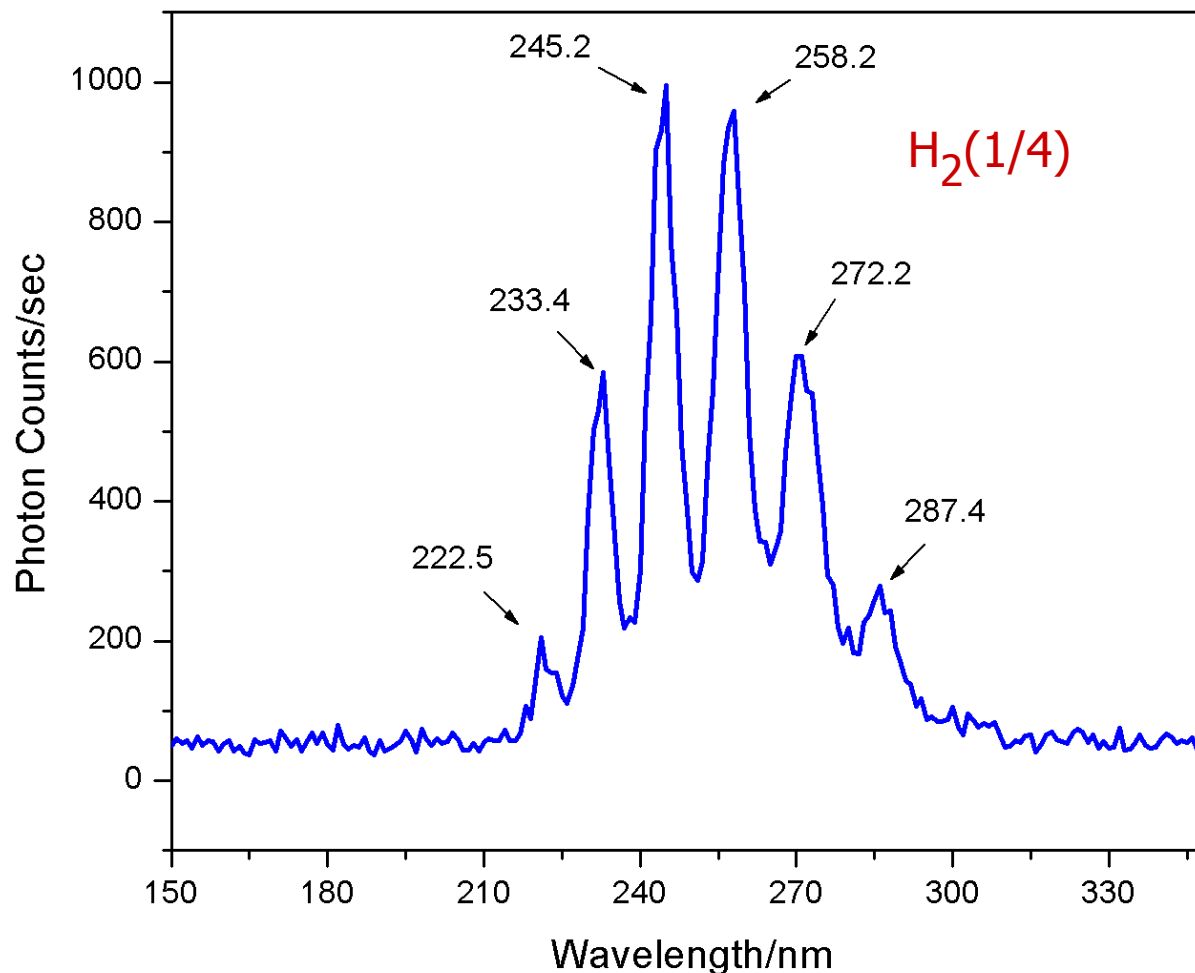


High resolution (0.5 cm^{-1}) FTIR spectra ($490\text{--}4000\text{ cm}^{-1}$). (A) *LiBr*. (B) *LiH*Br* sample having a NMR peak assigned to $H^-(1/4)$ that was heated to $>600^\circ\text{C}$ under dynamic vacuum that retained the -2.5 ppm NMR peak. The amide peaks at 3314 , 3259 , 2079 (broad), 1567 , and 1541 cm^{-1} and the imide peaks at 3172 (broad), 1953 , and 1578 cm^{-1} were eliminated; thus, they were not the source of the -2.5 ppm NMR peak that remained. The -2.5 ppm peak in ^1H NMR spectrum was assigned to the $H^-(1/4)$ ion. In addition, the 1989 cm^{-1} FTIR peak could not be assigned to any known compound, but matched the predicted frequency of para $H_2(1/4)$.



The 150-350 nm spectrum of electron-beam excited *CsCl* crystals having trapped $H_2(1/4)$. A series of evenly spaced lines was observed in the 220-300 nm region that matched the spacing and intensity profile of the P branch of $H_2(1/4)$.

NaHCl coated on Si wafer, e beam 30uA/9KeV, slits 300x300um

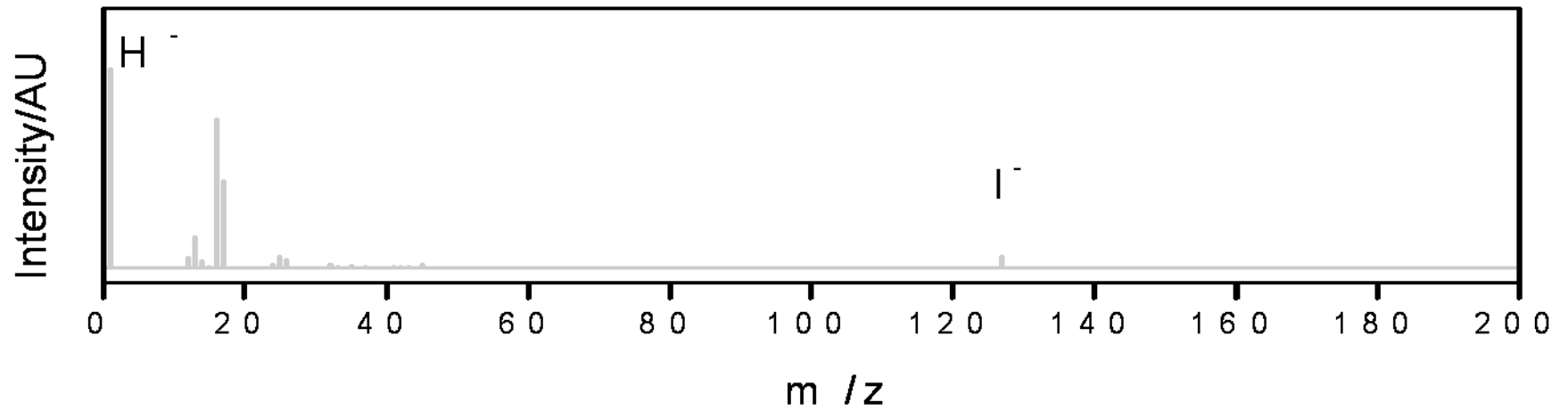


The 100-550 nm spectrum of an electron-beam excited silicon wafer coated with NaH^*Cl having trapped $H_2(1/4)$. A series of evenly spaced lines was observed in the 220-300 nm region that matched the spacing and intensity profile of the P branch of $H_2(1/4)$.

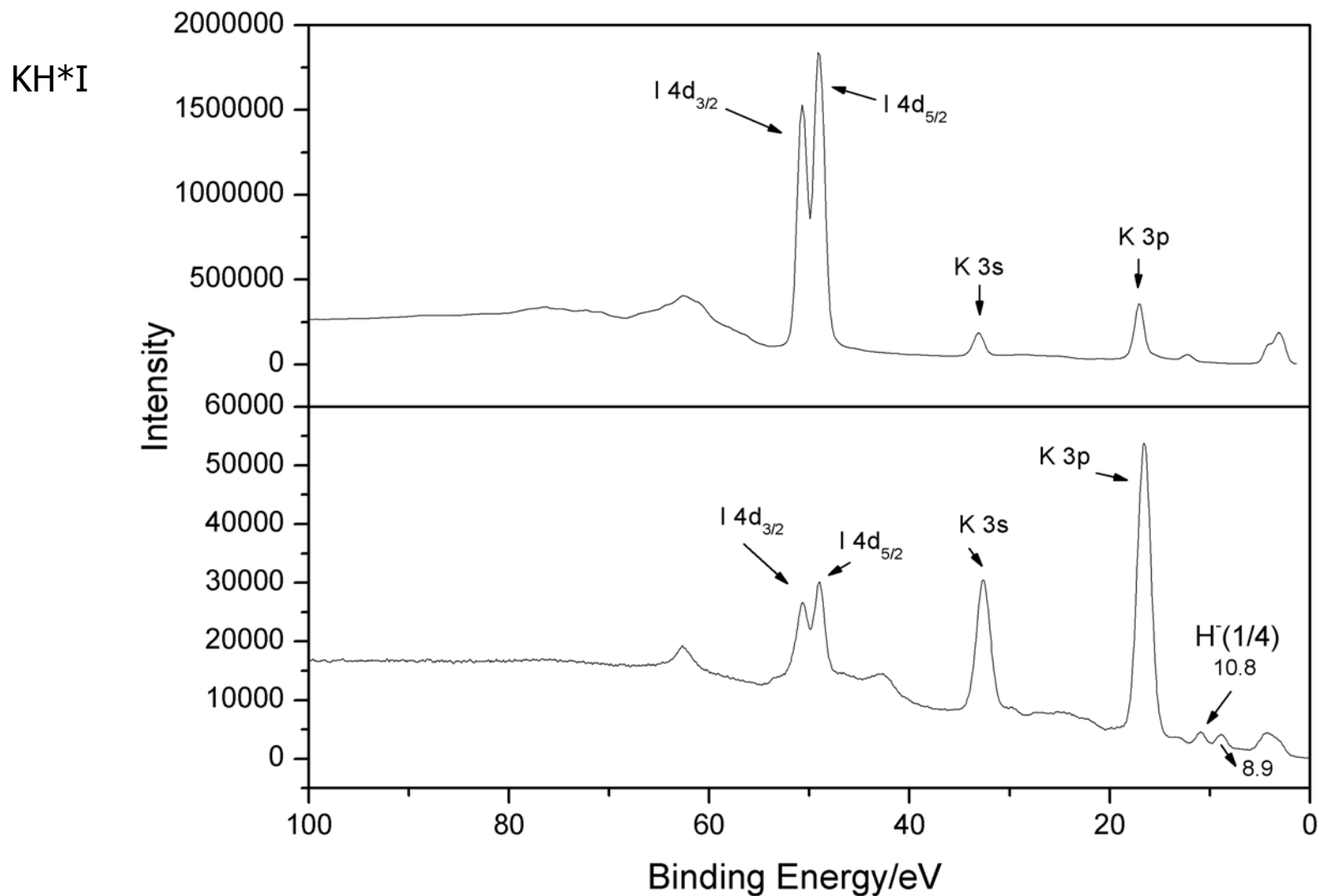
Further Identification of Novel Hydrides

- ToF-SIMS
- XPS

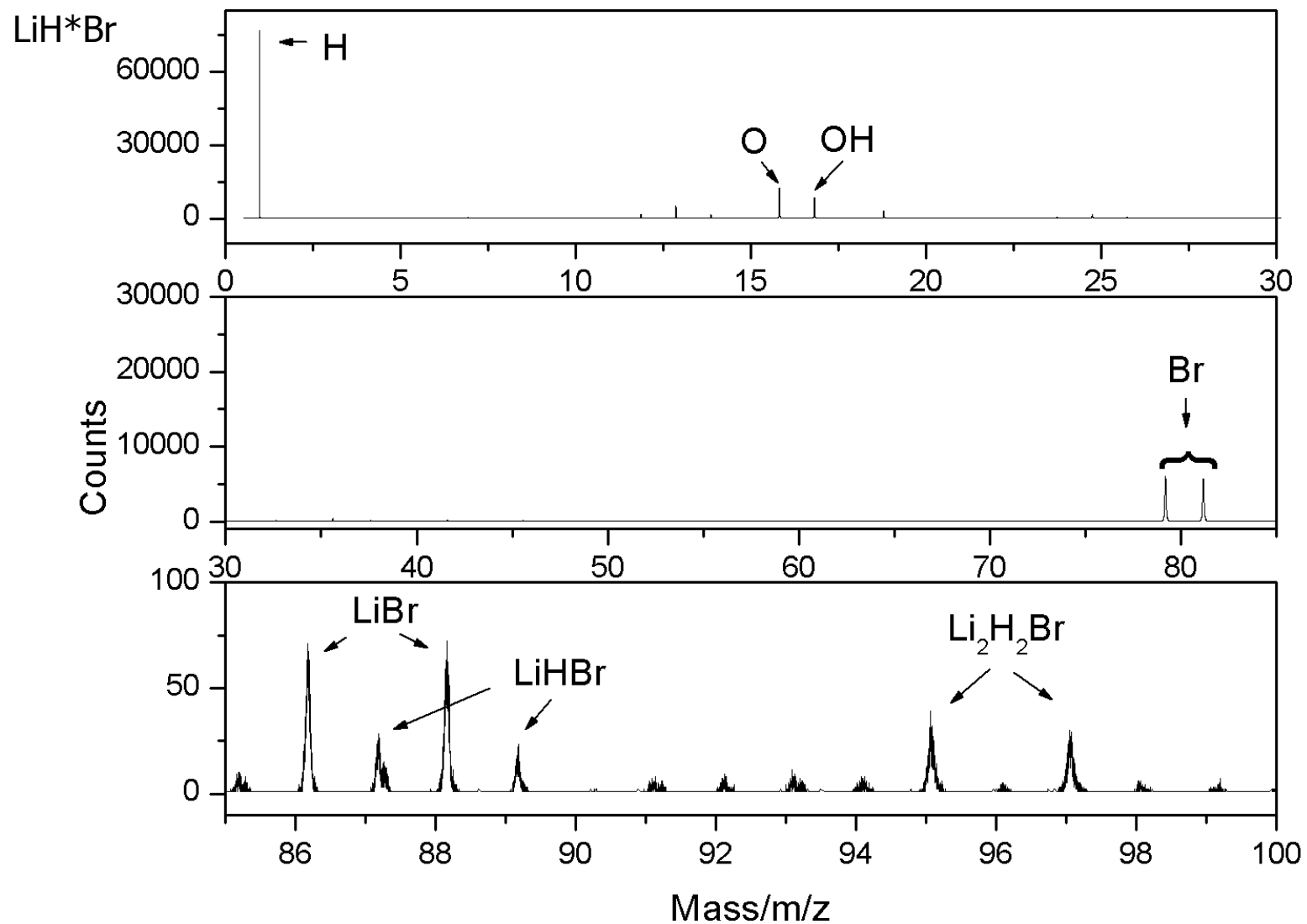
KH*I



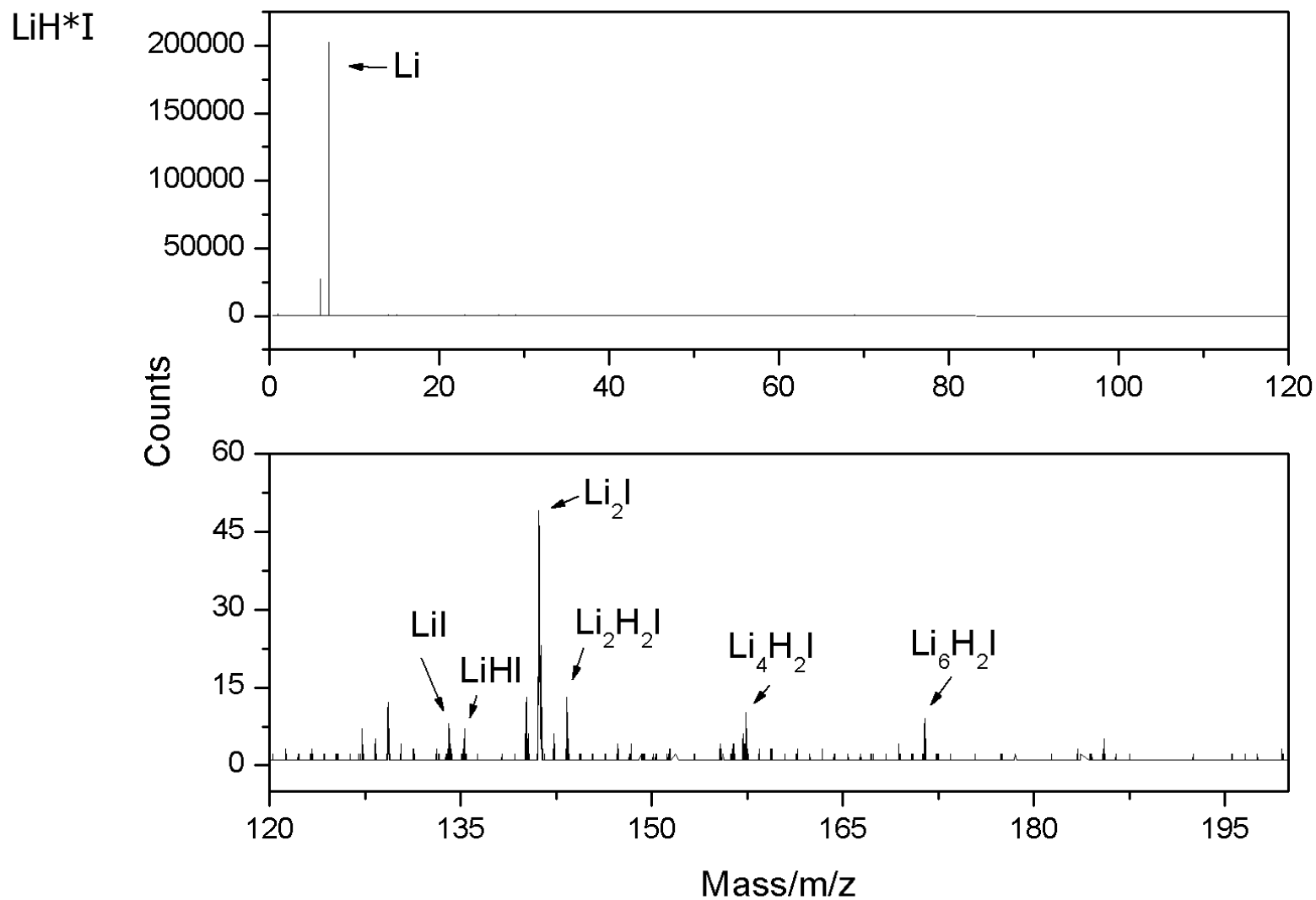
The negative ToF-SIMS spectrum ($m/e = 0-200$) of KH*I showing a dominant hydride peak.



The 0–100 eV binding energy region of a high resolution XPS spectrum of the control KI (top) and KH*I (bottom) showing the H⁻(1/4) peak.

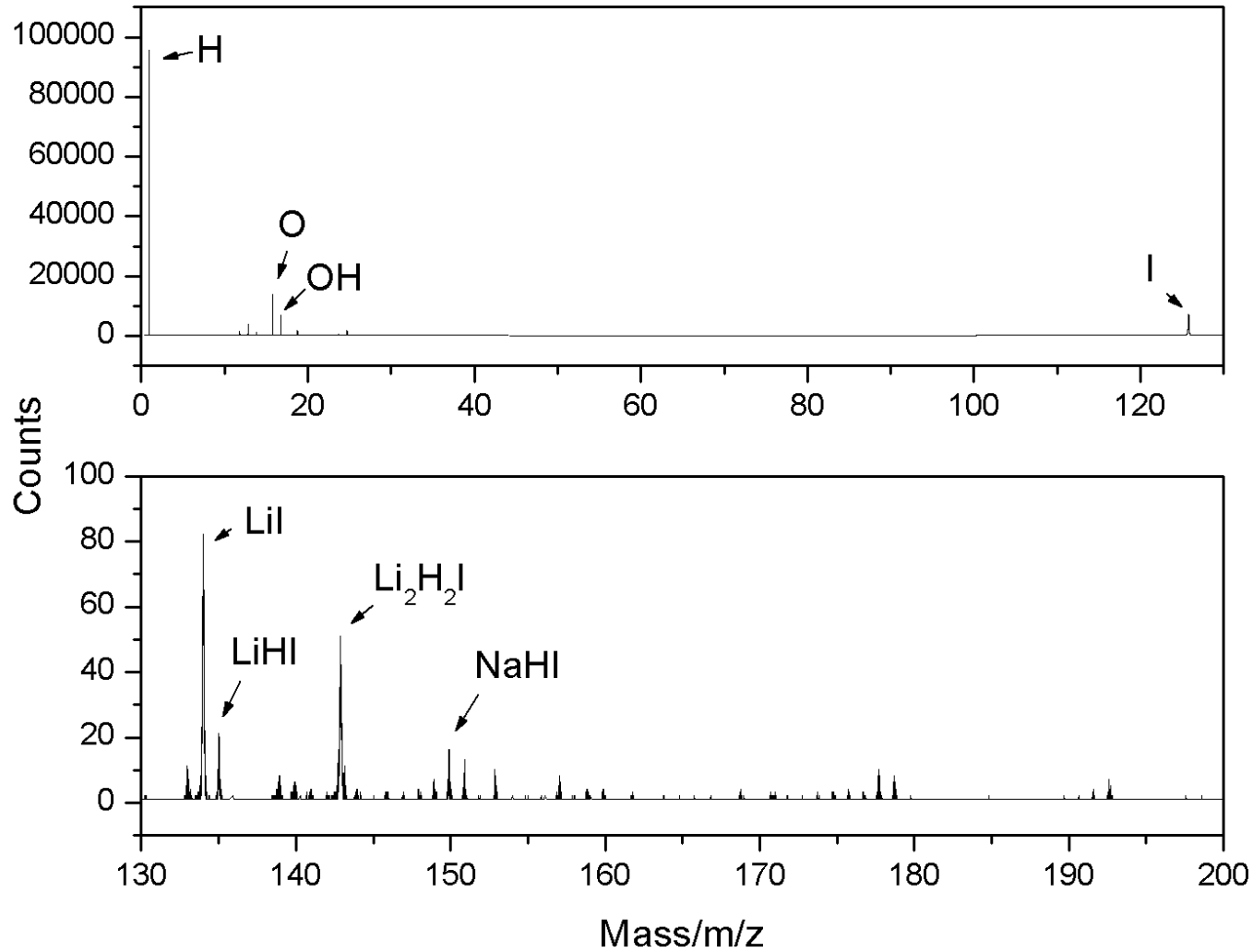


The negative ToF-SIMS spectrum ($m/e = 0-100$) of the LiH^*Br crystals. A dominant hydride, LiHBr^- , and $\text{Li}_2\text{H}_2\text{Br}^-$ peaks were uniquely observed.



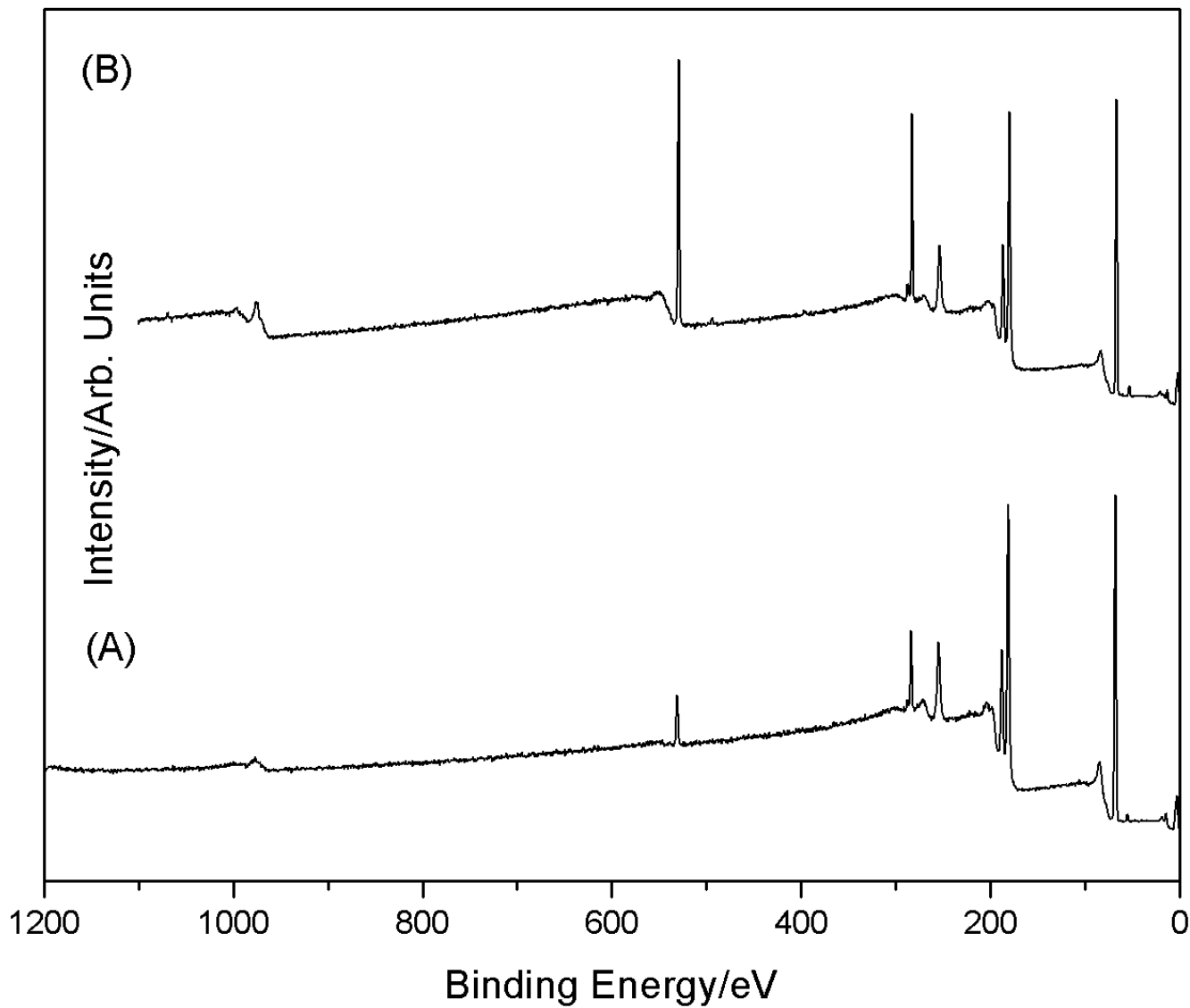
The positive ToF-SIMS spectrum ($m/e = 0-200$) of the LiH^*I crystals. LiH^+ , $\text{Li}_2\text{H}_2\text{I}^+$, $\text{Li}_4\text{H}_2\text{I}^+$, and $\text{Li}_6\text{H}_2\text{I}^+$ were only observed in the positive ion spectrum of the LiH^*I crystals.

LiH*I

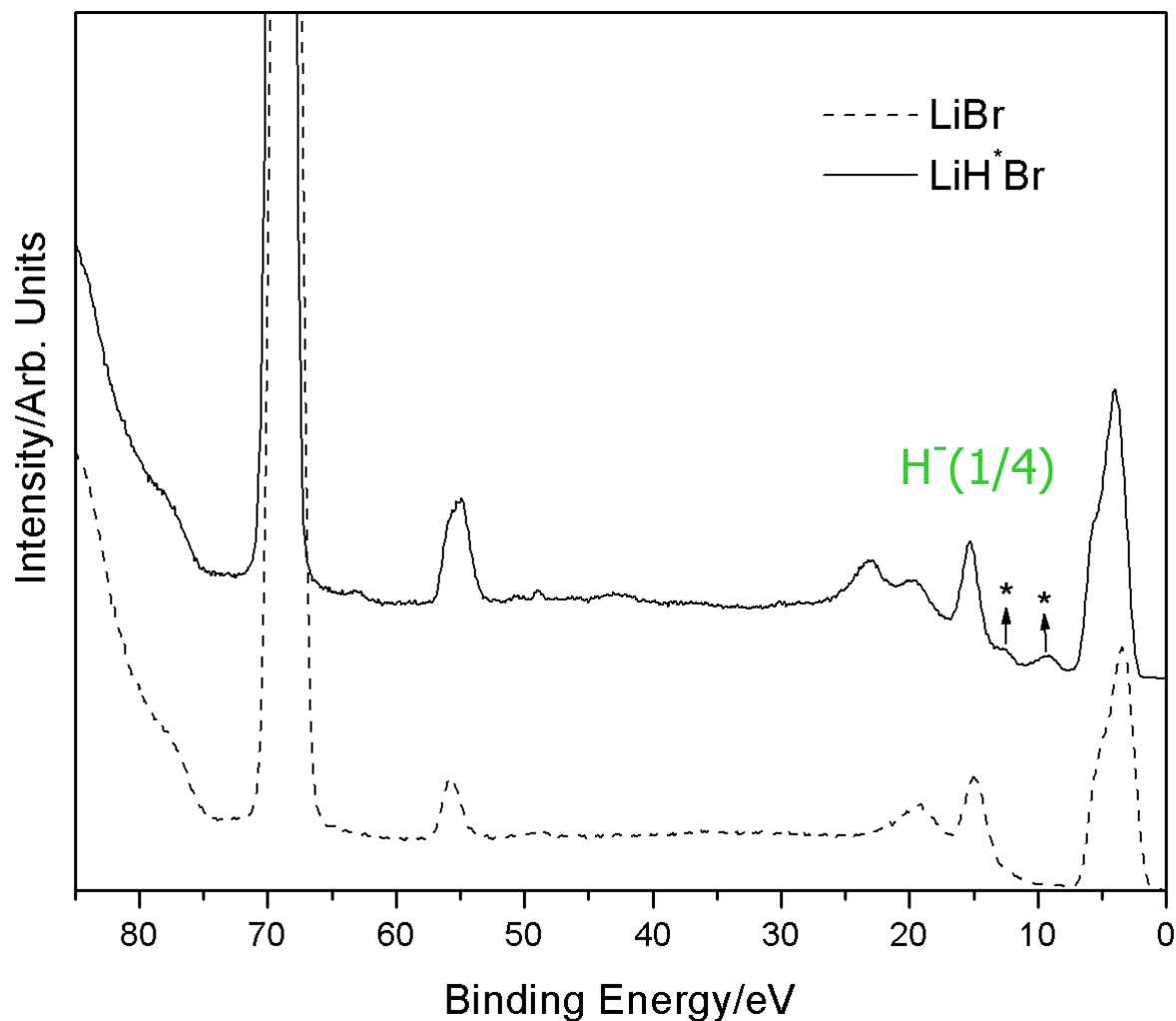


The negative ToF-SIMS spectrum ($m/e = 0-180$) of the LiH^*I crystals. A dominant hydride, $LiHI^-$, $Li_2H_2I^-$, and $NaHI^-$, peaks were uniquely observed.

LiH*Br

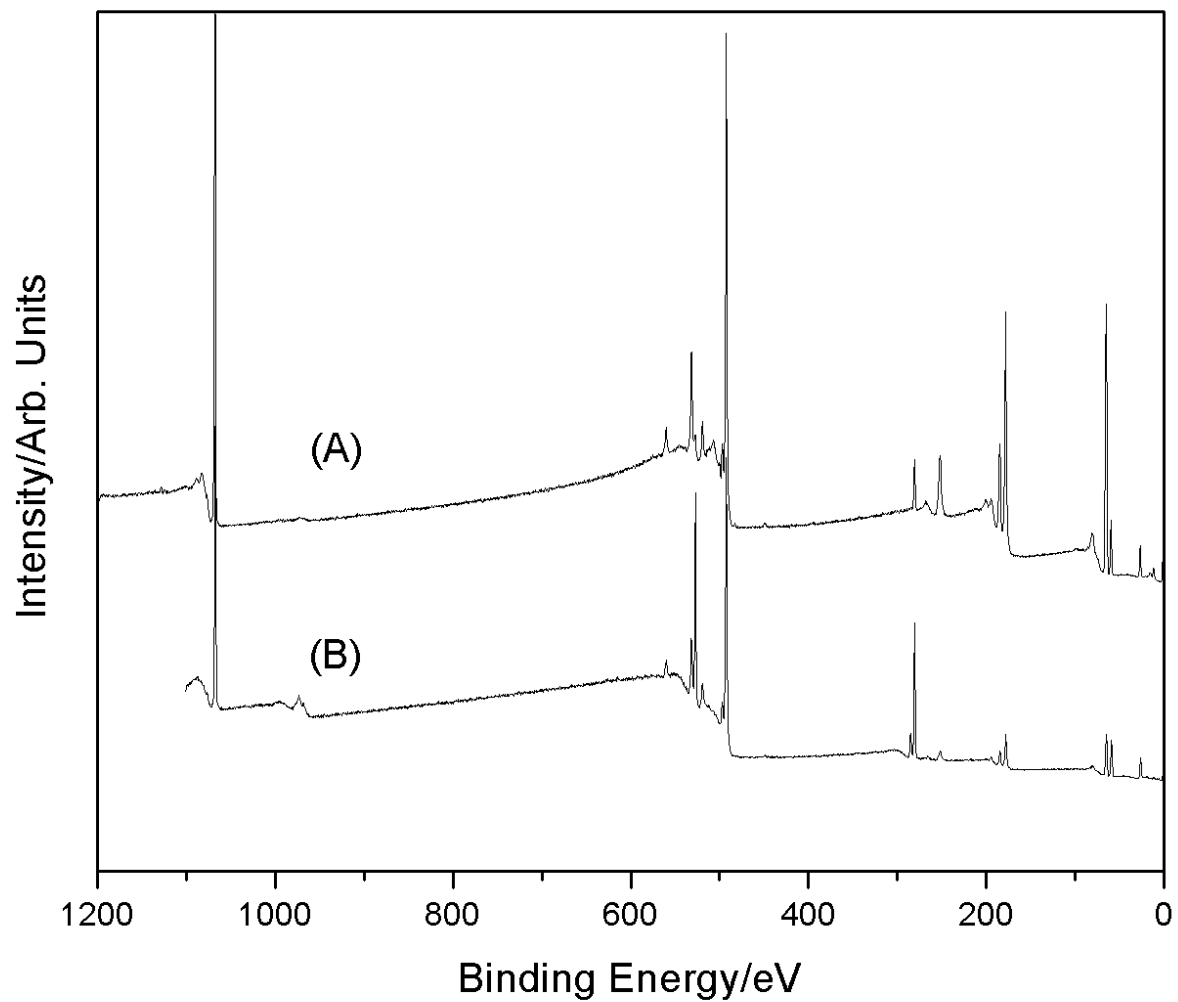


XPS survey spectra ($E_b = 0$ eV to 1200 eV). (A) *LiBr*. (B) *LiH*Br*.



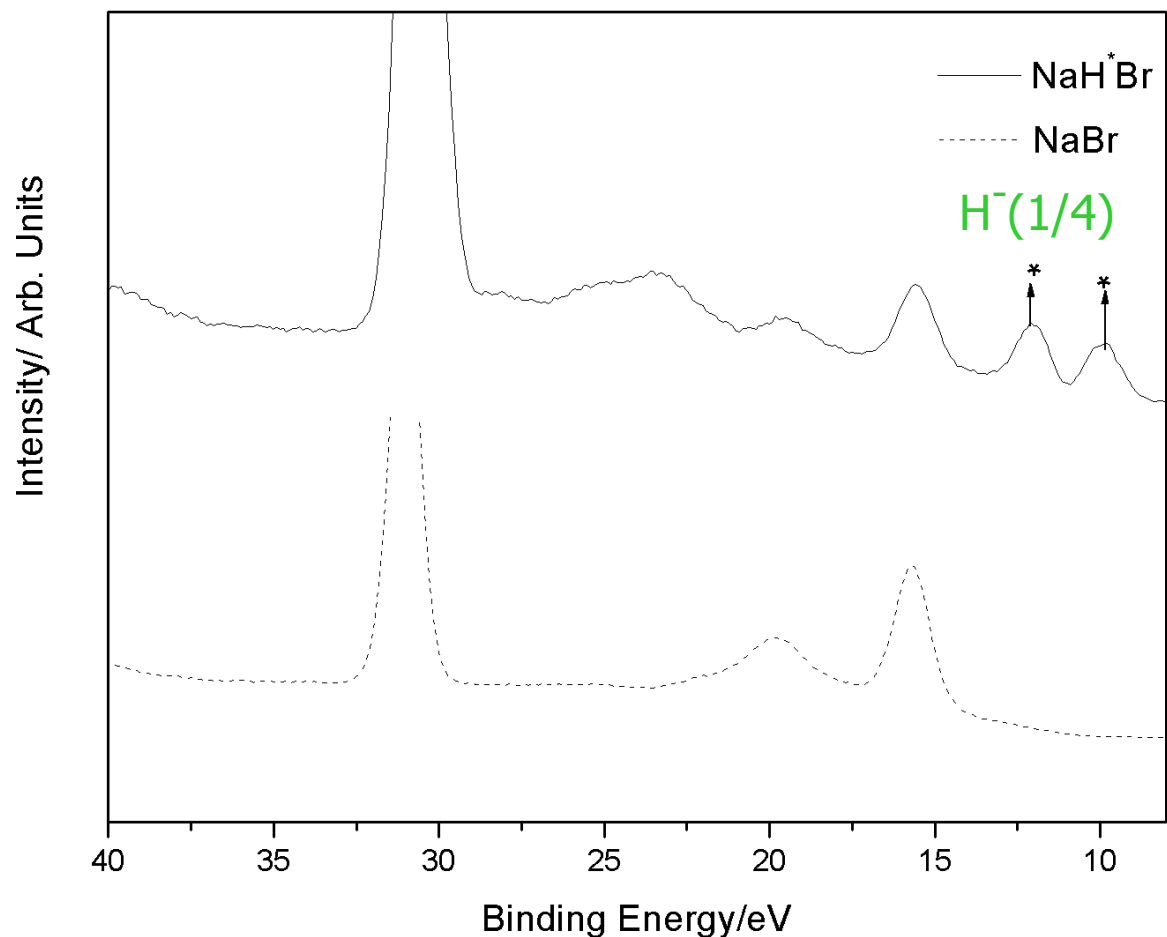
The 0-85 eV binding energy region of a high resolution XPS spectrum of *LiH*Br* and the control *LiBr* (dashed). The XPS spectrum of *LiH*Br* differs from that of *LiBr* by having additional peaks at 9.5 eV and 12.3 eV that could not be assigned to known elements and does not correspond to any other primary element peak. The peaks match $H^-(1/4)$ in two different chemical environments.

NaH*Br

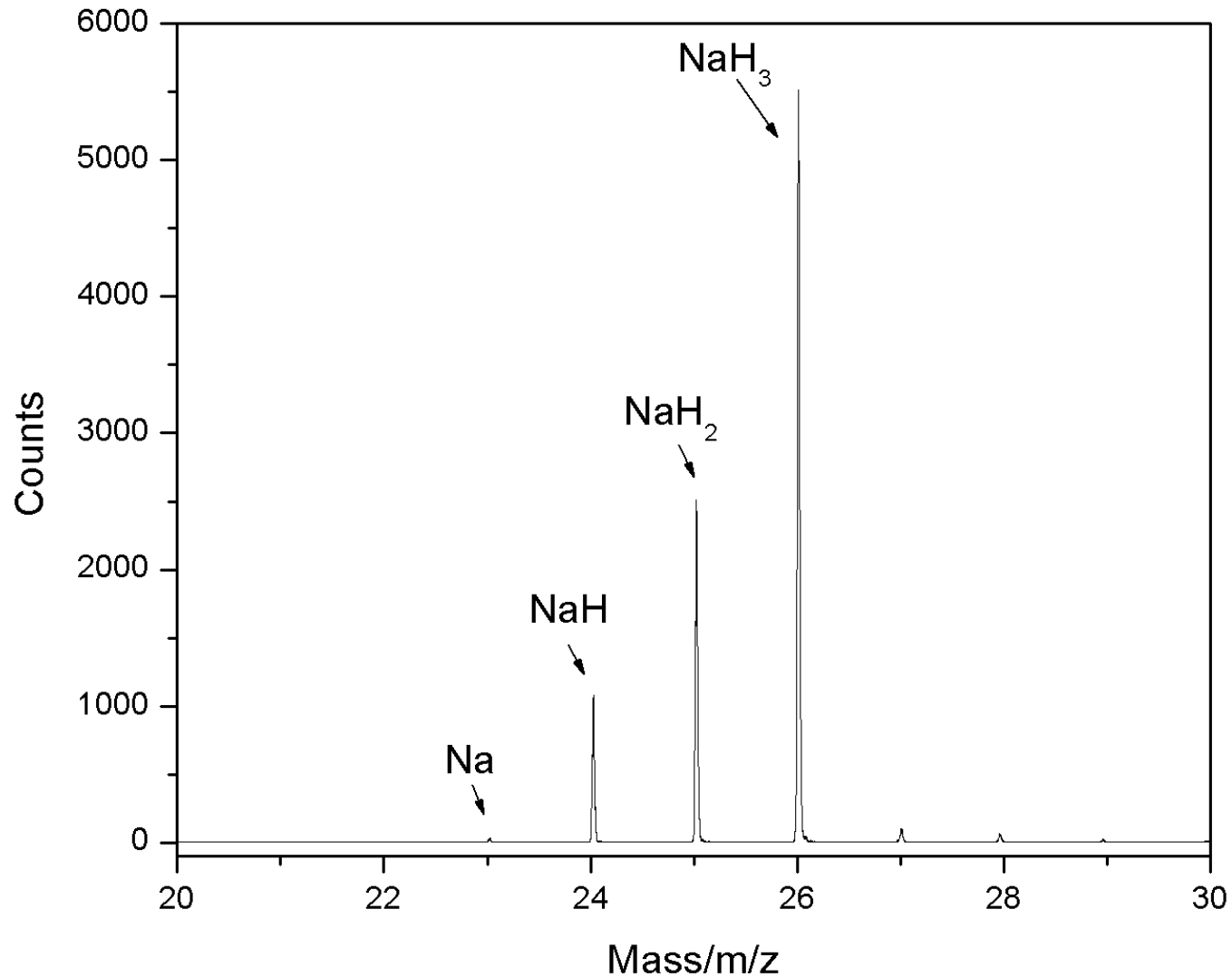


XPS survey spectra ($E_b = 0$ eV to 1200 eV). (A) *NaBr*. (B) *NaH*Br*.

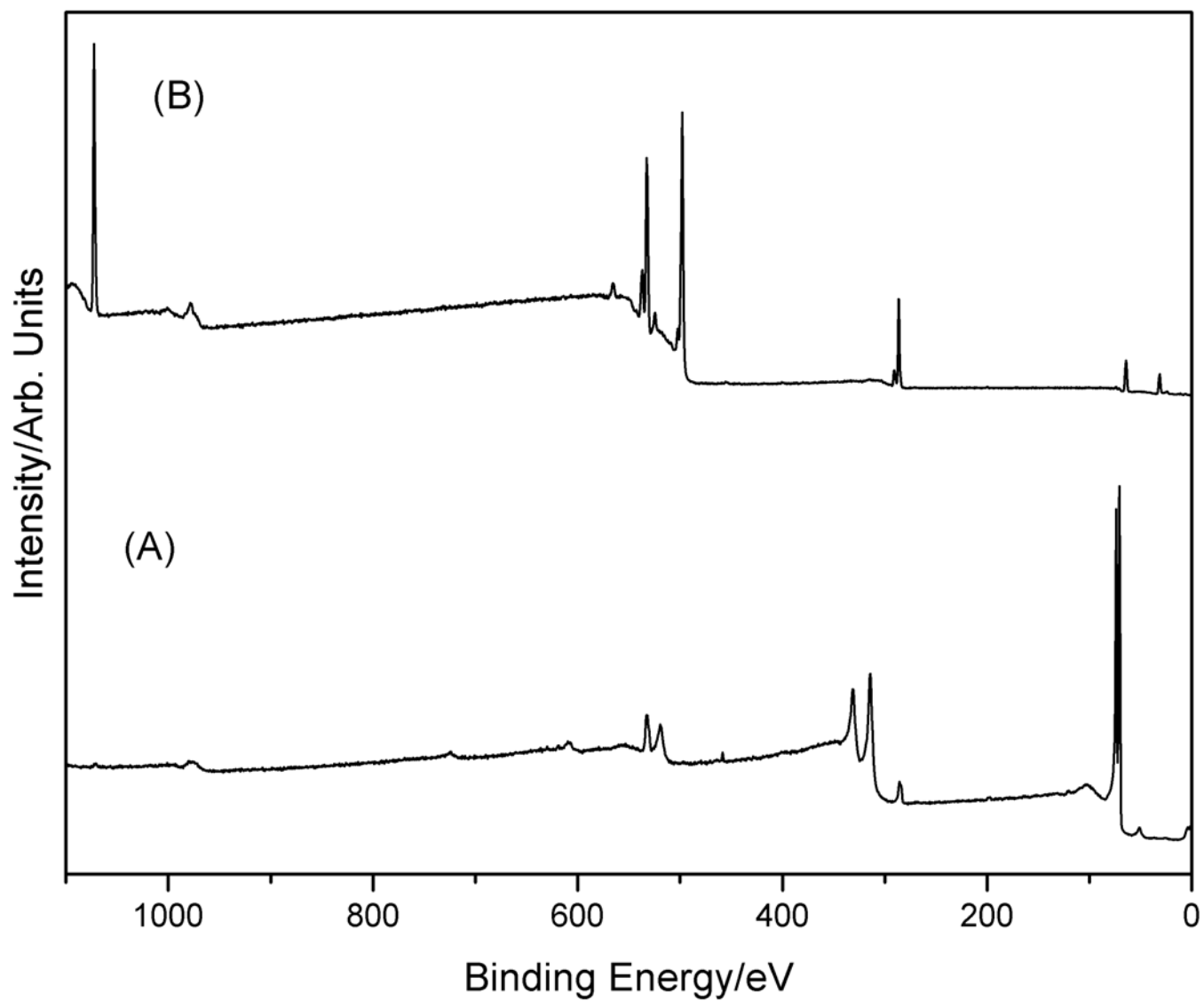
NaH*Br



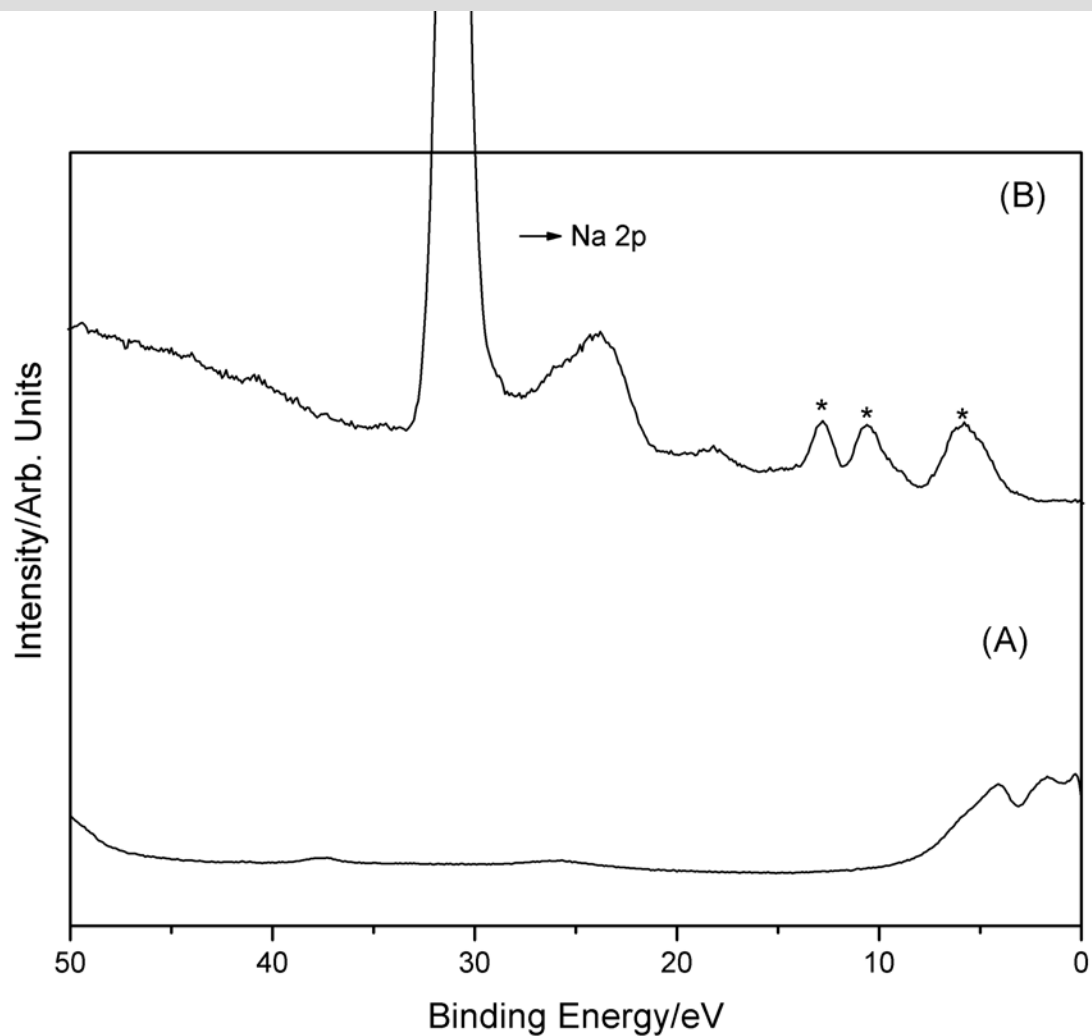
The 0-40 eV binding energy region of a high resolution XPS spectrum of *NaH*Br* and the control *NaBr* (dashed). The XPS spectrum of *NaH*Br* differs from that of *NaBr* by having additional peaks at 9.5 eV and 12.3 eV that could not be assigned to known elements and does not correspond to any other primary element peak. The peaks match $H^-(1/4)$ in two different chemical environments.



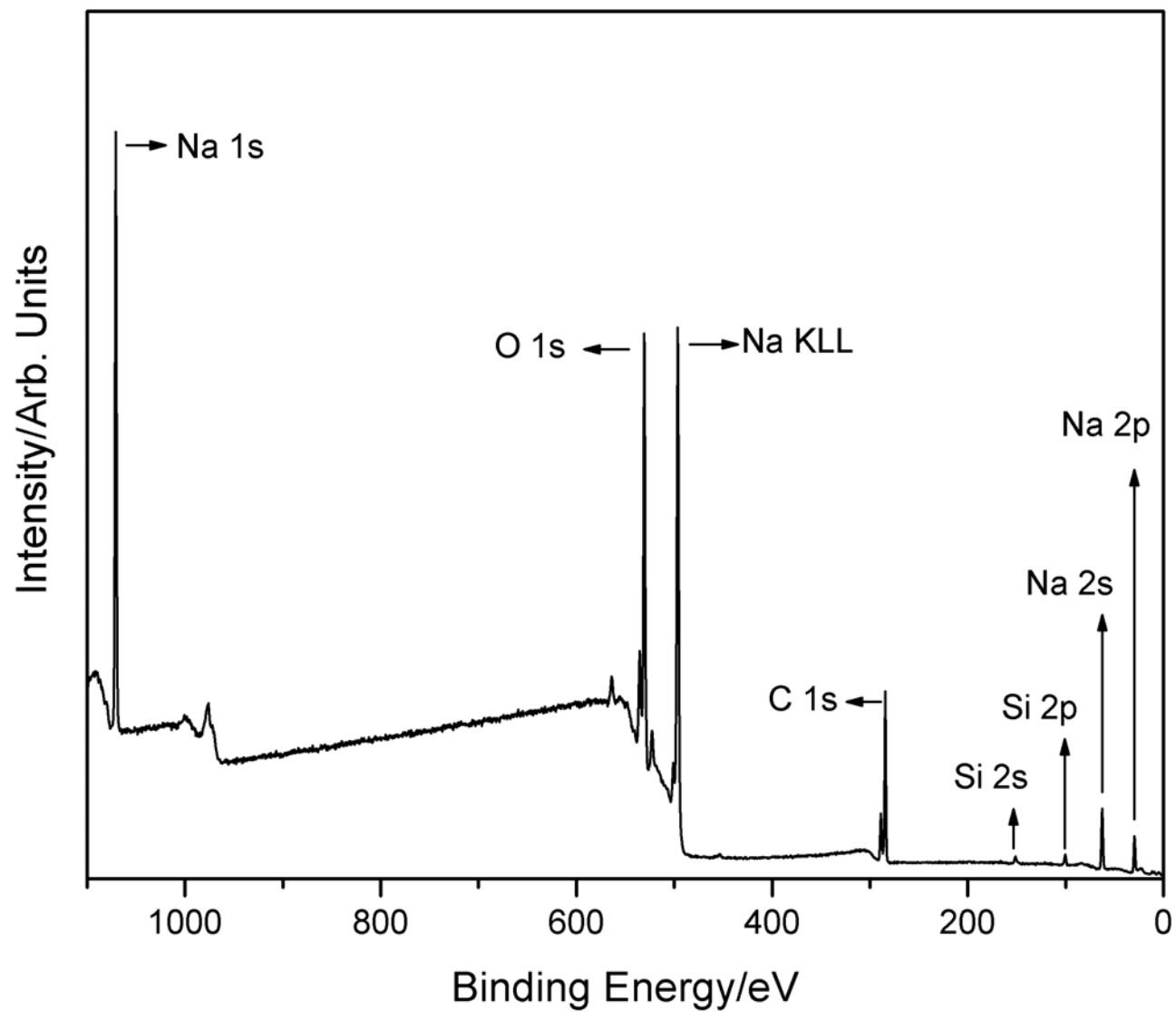
The negative ToF-SIMS spectrum ($m/e = 20-30$) of sodium hydride-coated *Pt/Ti* following the production of 15 kJ of excess heat. Hydride compounds NaH_x^- were observed.



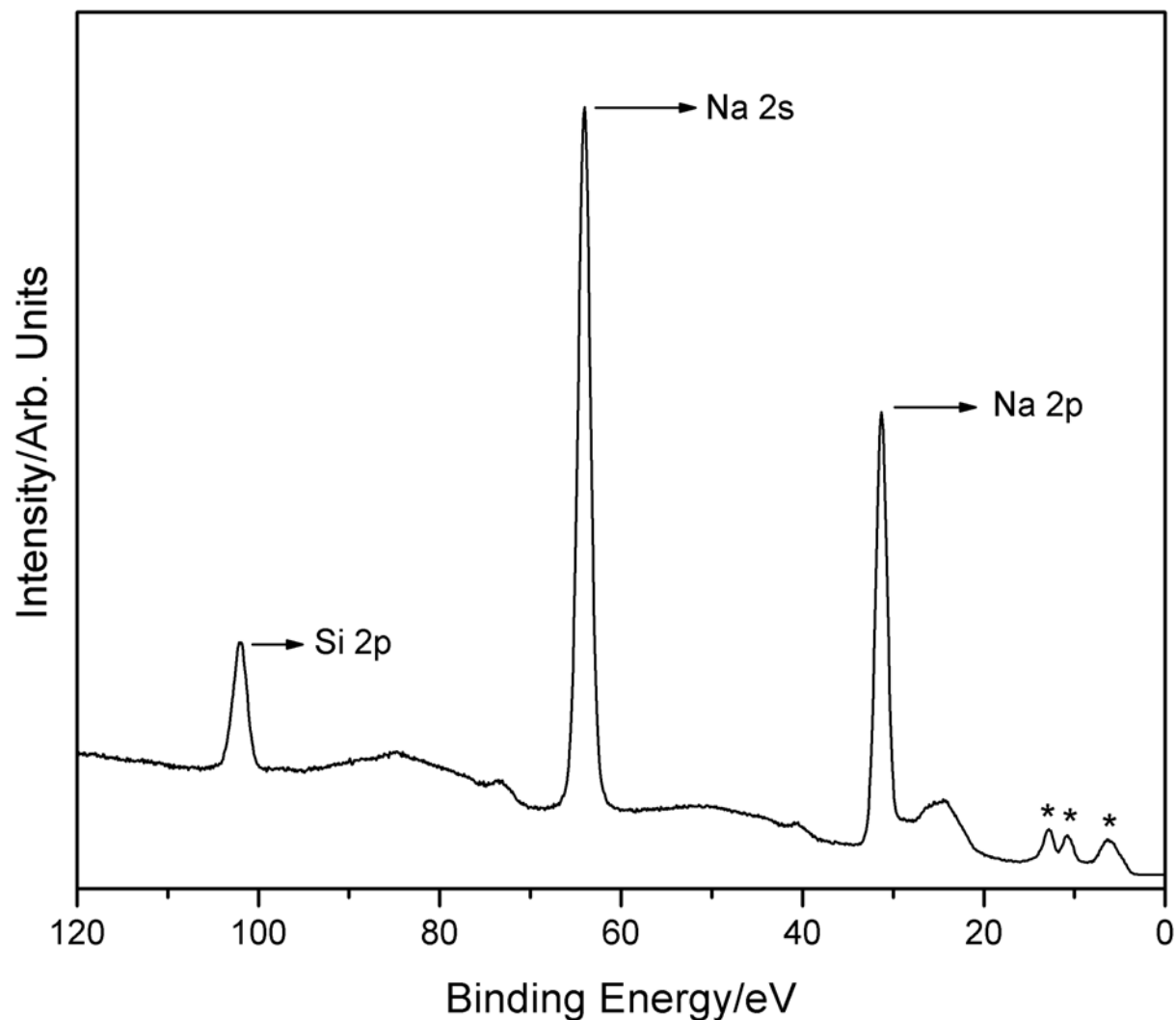
XPS survey spectra ($E_b = 0$ eV to 1200 eV). (A) *Pt/Ti*. (B) *NaH**-coated *Pt/Ti* following the production of 15 kJ of excess heat.



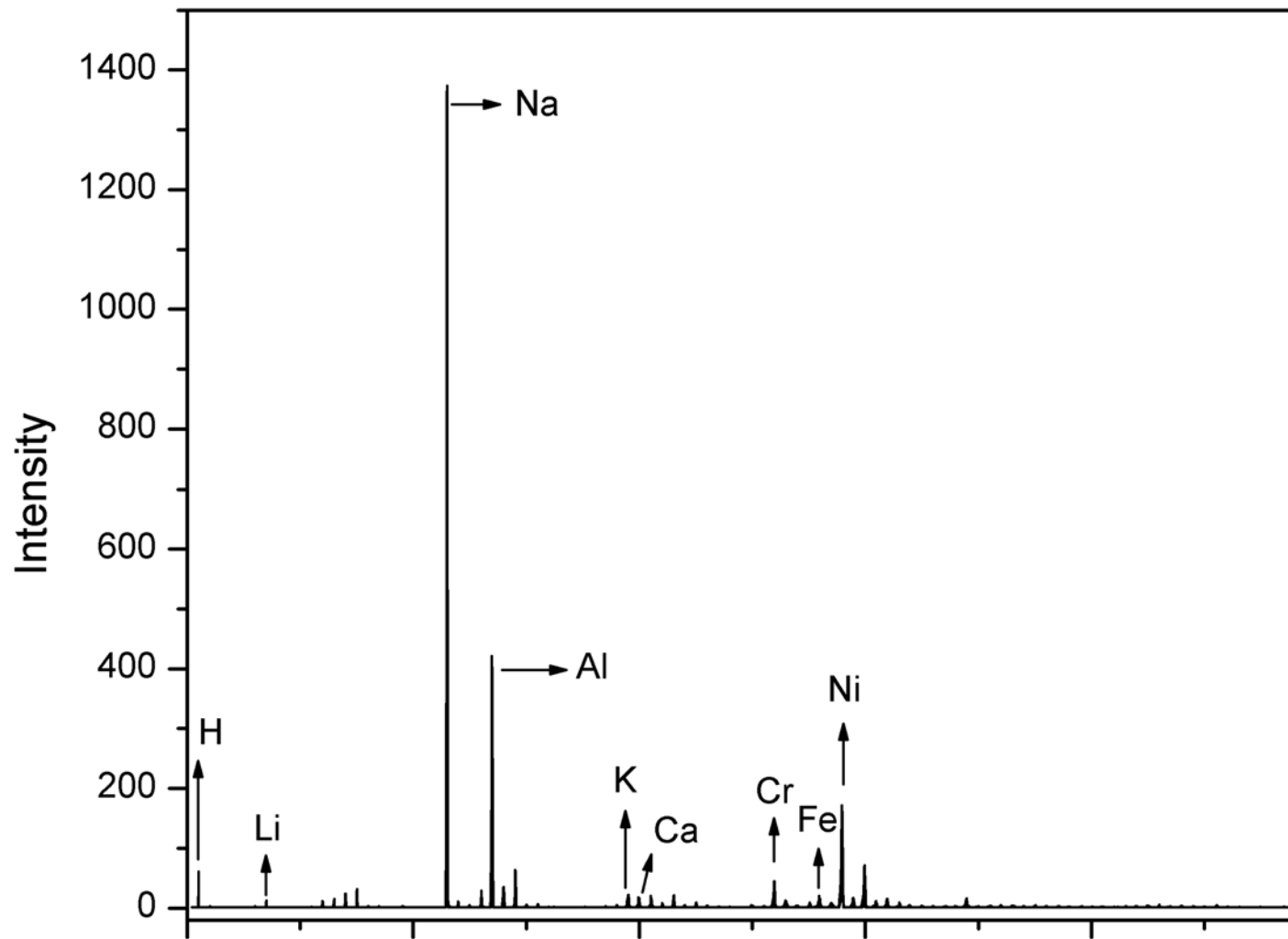
High resolution XPS spectra ($E_b = 0$ eV to 50 eV). (A) *Pt/Ti* (B) *NaH**-coated *Pt/Ti* following the production of 15 kJ of excess heat. The XPS spectrum of *NaH**-coated *Pt/Ti* differs from that of *Pt/Ti* by having additional peaks at 6 eV, 10.8 eV, and 12.8 eV that could not be assigned to known elements and do not correspond to any other primary element peak. The 10.8 eV, and 12.8 eV peaks match *H*(1/4) in two different chemical environments, and the 6 eV peak matched and was assigned to *H*(1/3). Thus, both fractional hydrogen states, 1/3 and 1/4, were present as predicted for the *NaH* catalyst reaction.



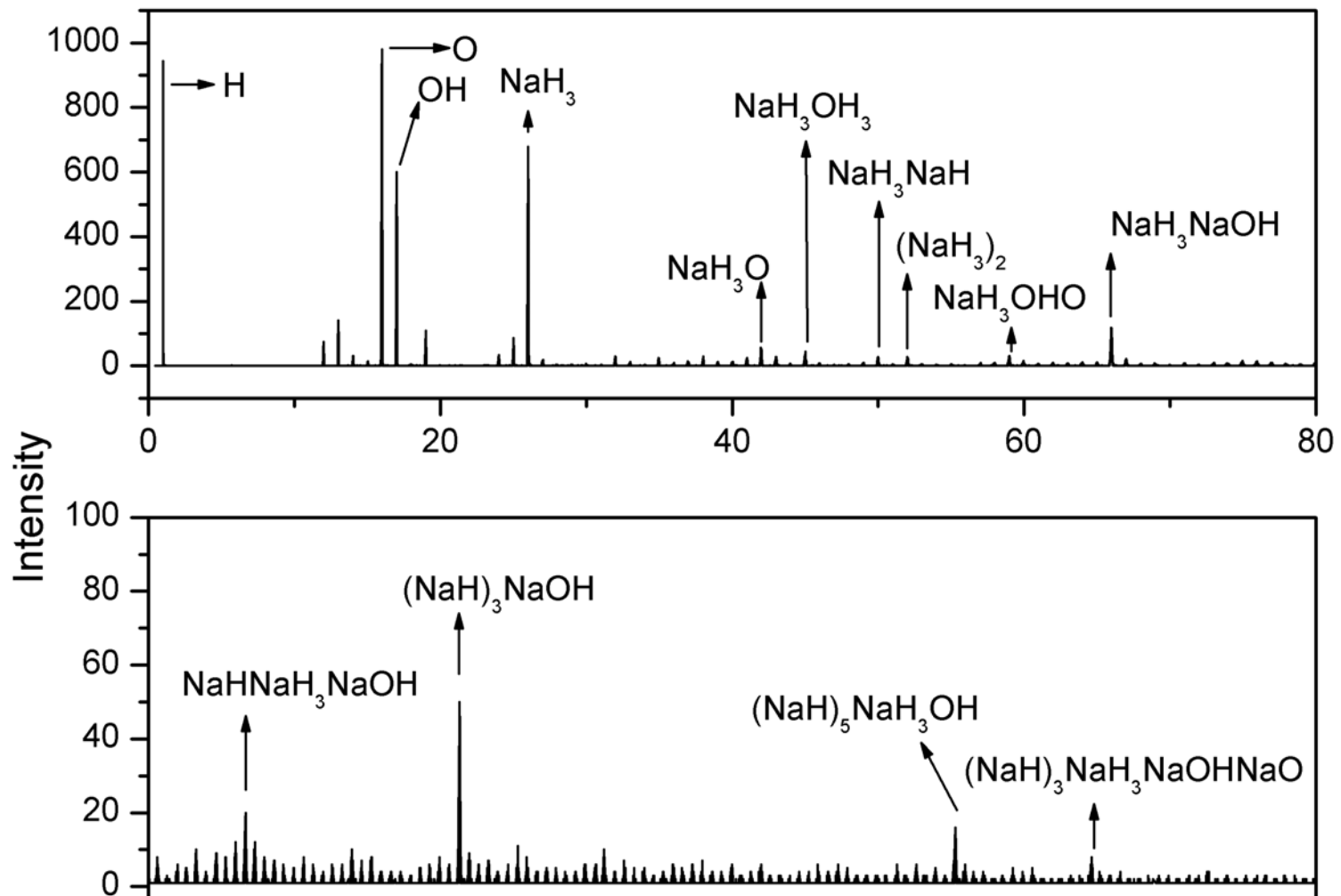
XPS survey spectrum ($E_b = 0$ eV to 120 eV) of NaH^* -coated Si with the primary-element peaks identified.



High resolution XPS spectrum ($E_b = 0$ eV to 120 eV) of NaH^* -coated Si having peaks at 6 eV, 10.8 eV, and 12.8 eV that could not be assigned to known elements and do not correspond to any other primary element peak. The 10.8 eV, and 12.8 eV peaks match $H(1/4)$ in two different chemical environments, and the 6 eV peak matched and was assigned to $H(1/3)$. Thus, both fractional hydrogen states, $1/3$ and $1/4$, were present as predicted for the NaH catalyst reaction matching the results of NaH -coated Pt/Ti .



The positive ToF-SIMS spectrum ($m/e = 0 - 100$) of R-Ni reacted over a 48 hour period at 50°C. The dominant ion on the surface was Na^+ consistent with $NaOH$ doping of the surface. The ions of the other major elements of R-Ni 2400 such as Al^+ , Ni^+ , Cr^+ , and Fe^+ were also observed.



The negative ToF-SIMS spectrum ($m/e = 0 - 180$) of R-Ni reacted over a 48 hour period at 50°C . A dominant hydride, and NaH_3NaOH assigned to sodium hydrino hydride and this ion in combination with NaOH , as well as other unique ions assignable to sodium hydrino hydrides in combinations with NaOH , NaO , OH^- and O^- were observed.

Potential Applications

- H₂(1/p) Enables laser at wavelengths from visible to soft X-ray
 - VUV photolithography (Enables next generation chip)
 - Blue Lasers
 - Line-of-sight telecom and medical devices
 - Defense applications – water is transparent to blue wavelength
 - Submarine tracking and communications, undersea mine detection, and undersea weapons targeting and communications
- High voltage metal hydride batteries
- Synthetic thin-film and single crystal diamonds

R. L. Mills, J. Sankar, A. Voigt, J. He, B. Dhandapani, "Spectroscopic Characterization of the Atomic Hydrogen Energies and Densities and Carbon Species During Helium-Hydrogen-Methane Plasma CVD Synthesis of Diamond Films," Chemistry of Materials, Vol. 15, (2003), pp. 1313-1321.
- H(1/p)-terminated silicon for chip fabrication and photovoltaics

R. L. Mills, B. Dhandapani, J. He, "Highly Stable Amorphous Silicon Hydride," Solar Energy Materials & Solar Cells, Vol. 80, No. 1, pp. 1-20.
- Metal hydrides as anticorrosive coatings

Exothermic Reaction Characterization

Optical Power Balance

>1000 times more light for plasma input power at 1% the driving voltage

R. Mills and M. Nansteel, P. Ray, "Argon-Hydrogen-Strontium Discharge Light Source," IEEE Transactions on Plasma Science, Vol. 30, No. 2, (2002), pp. 639-653.

Selective Balmer Line Broadening

100 times the H kinetic energy of noncatalyst plasmas

R. L. Mills, P. Ray, B. Dhandapani, R. M. Mayo, J. He, "Comparison of Excessive Balmer Line Broadening of Glow Discharge and Microwave Hydrogen Plasmas with Certain Catalysts," J. of Applied Physics, Vol. 92, No. 12, (2002), pp. 7008-7022.

Calorimetry

Energy balance of >100 times that of combustion of H₂
Power density of 10 W/cm³

R. L. Mills, X. Chen, P. Ray, J. He, B. Dhandapani, "Plasma Power Source Based on a Catalytic Reaction of Atomic Hydrogen Measured by Water Bath Calorimetry," Thermochemica Acta, Vol. 406/1-2, pp. 35-53.



BLACKLIGHT
POWER, Inc

Catalyst Comparison
For Optical Power Balance

8,600 Times Less Power Required to
Achieve the Same Light Emission with
Strontium-Argon Catalyst Present
Compared to Control

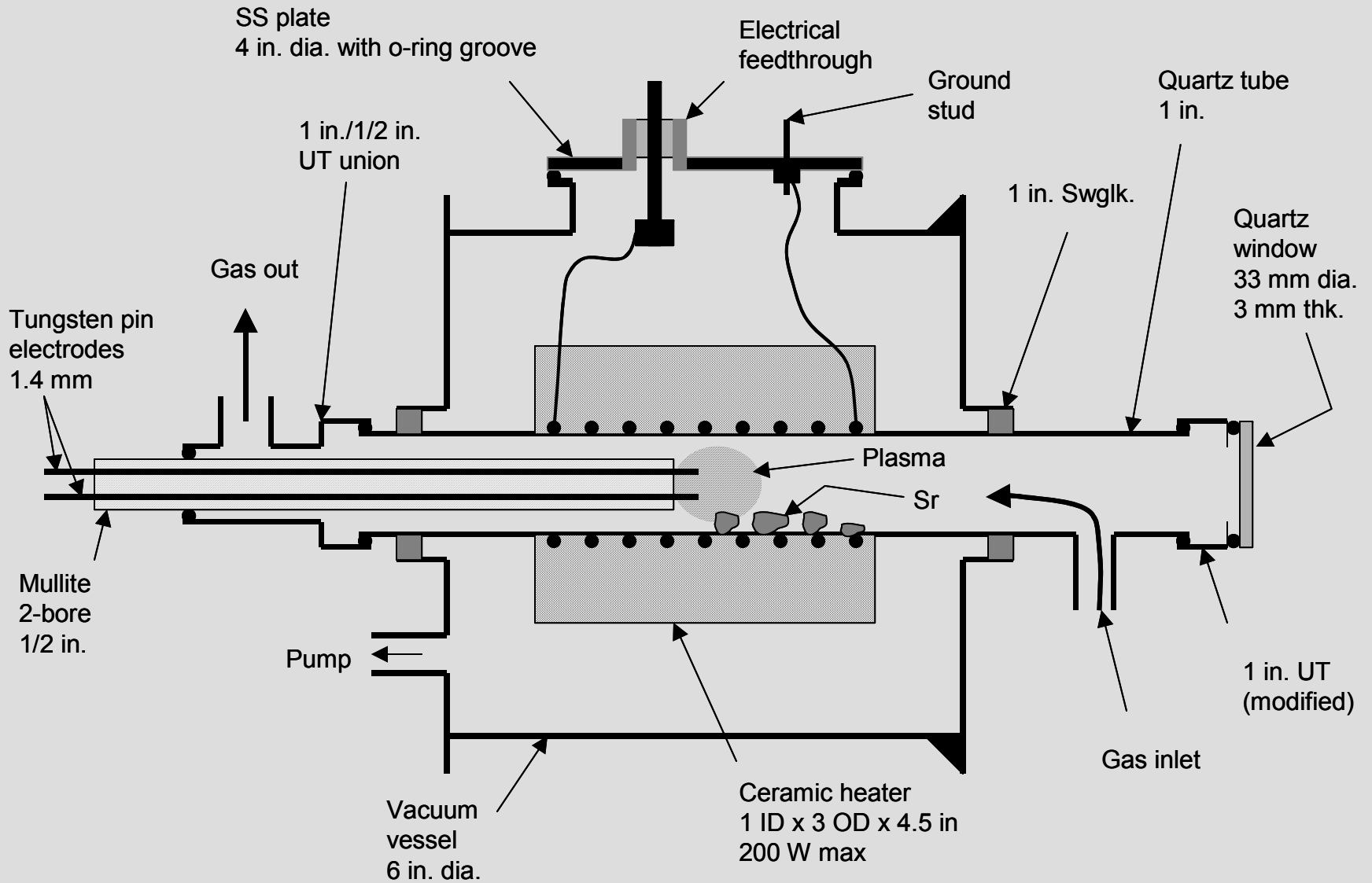
Discharge conditions and comparison of the driving power to achieve a total visible radiant flux of about $1\mu\text{W}/\text{cm}^2$

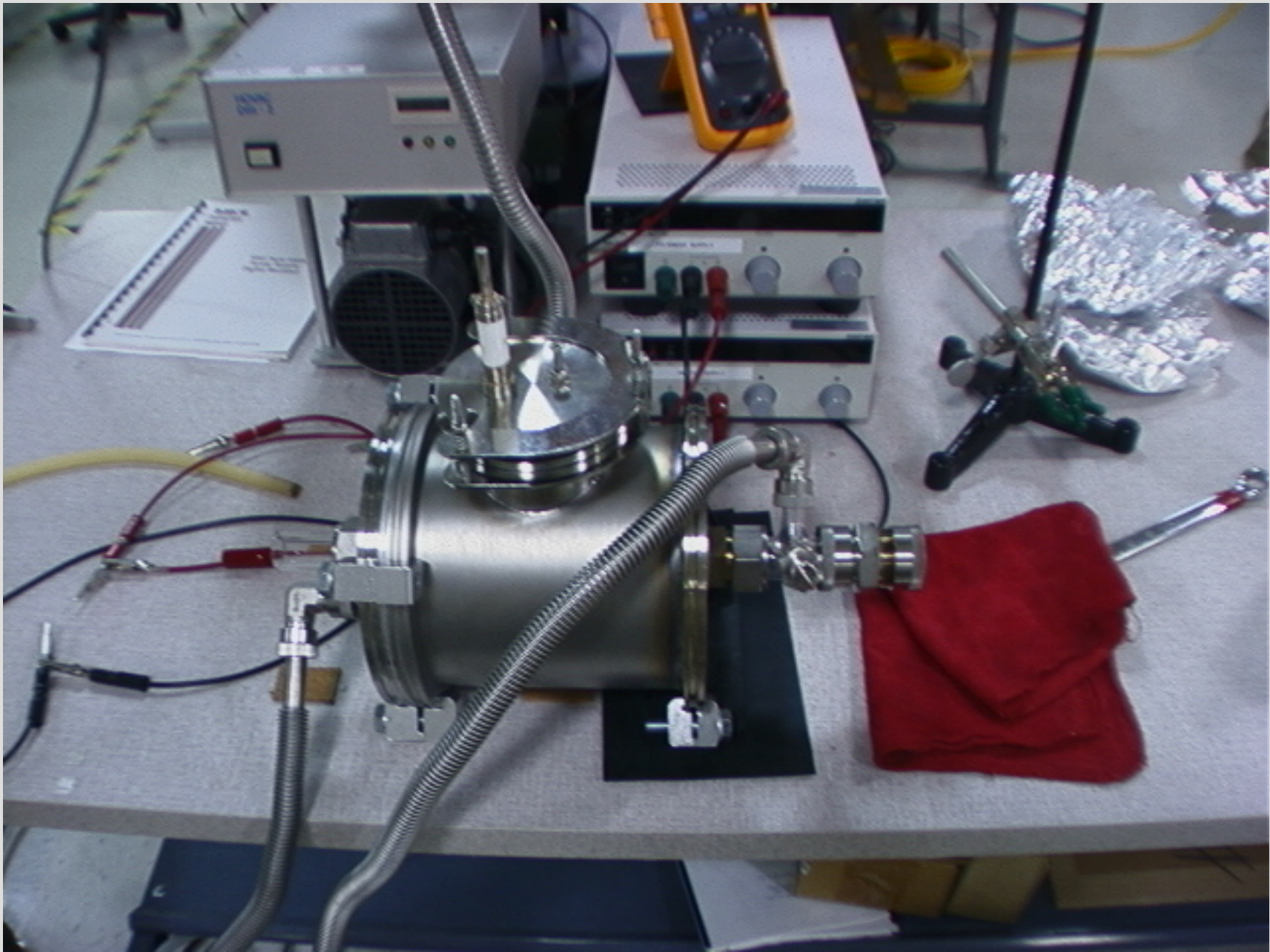
| | T (°C) | P _{hyd.} (torr) | P _{Ar} (torr) | P _v (torr) ^a | Voltage (V) | Current (mA) | Integ. time (ms) | Detector irradiation ($\mu\text{W}/\text{cm}^2$) | Power (W) |
|-----------------------|--------|-----------------------------|---------------------------|---------------------------------------|----------------|-----------------|------------------------|--|-------------------|
| Ar+H ₂ +Sr | 514 | 0.3 | 1.0 | 0.006 | 6.56 | 0.6 | 204 | 1.3 | 0.0039 |
| Ar+H ₂ | 519 | 0.295 | 0.5 | ---- | 224 | 184 | 409 | 1.9 | 33.5 ^b |
| Ar | 520 | ---- | 1.0 | ---- | 190 | 170 | 307 | 1.1 | 24.7 ^b |
| H ₂ +Sr | 664 | ---- | | 0.270 | 2.20 | 3.86 | 768 | 1.17 | 0.0085 |
| H ₂ | 664 | 1.0 | | ---- | 224 | 110 | 1130 | 2.08 | 24.6 |
| H ₂ +Na | 335 | 1.0 | | 0.051 | 272 | 124 | 122 | 1.85 | 33.7 |
| H ₂ +Na | 516 | 1.5 | | 5.3 | 220 | 68 | 768 | 0.40 | 15.0 |
| H ₂ +Na | 664 | 1.5 | | 63 | 240 | 41 | 768 | 0.41 | 9.84 |
| H ₂ +Mg | 449 | 4.0 | | 0.016 | 153 | 380 | 500 | 1.7 | 58 |
| H ₂ +Mg | 582 | 4.2 | | 0.6 | 233 | 290 | 500 | 0.16 | 68 |
| H ₂ +Mg | 654 | 3.0 | | 2.8 | 250 | 400 | 1000 | 0.18 | 100.0 |
| H ₂ +Ba | 666 | 2.0 | | 0.025 | 138 | 730 | 716 | 0.03 | 55 ^b |
| Bkgnd. | 664 | ---- | | 0.270 | 0 | 0 | 768 | 0.20 | 0 |

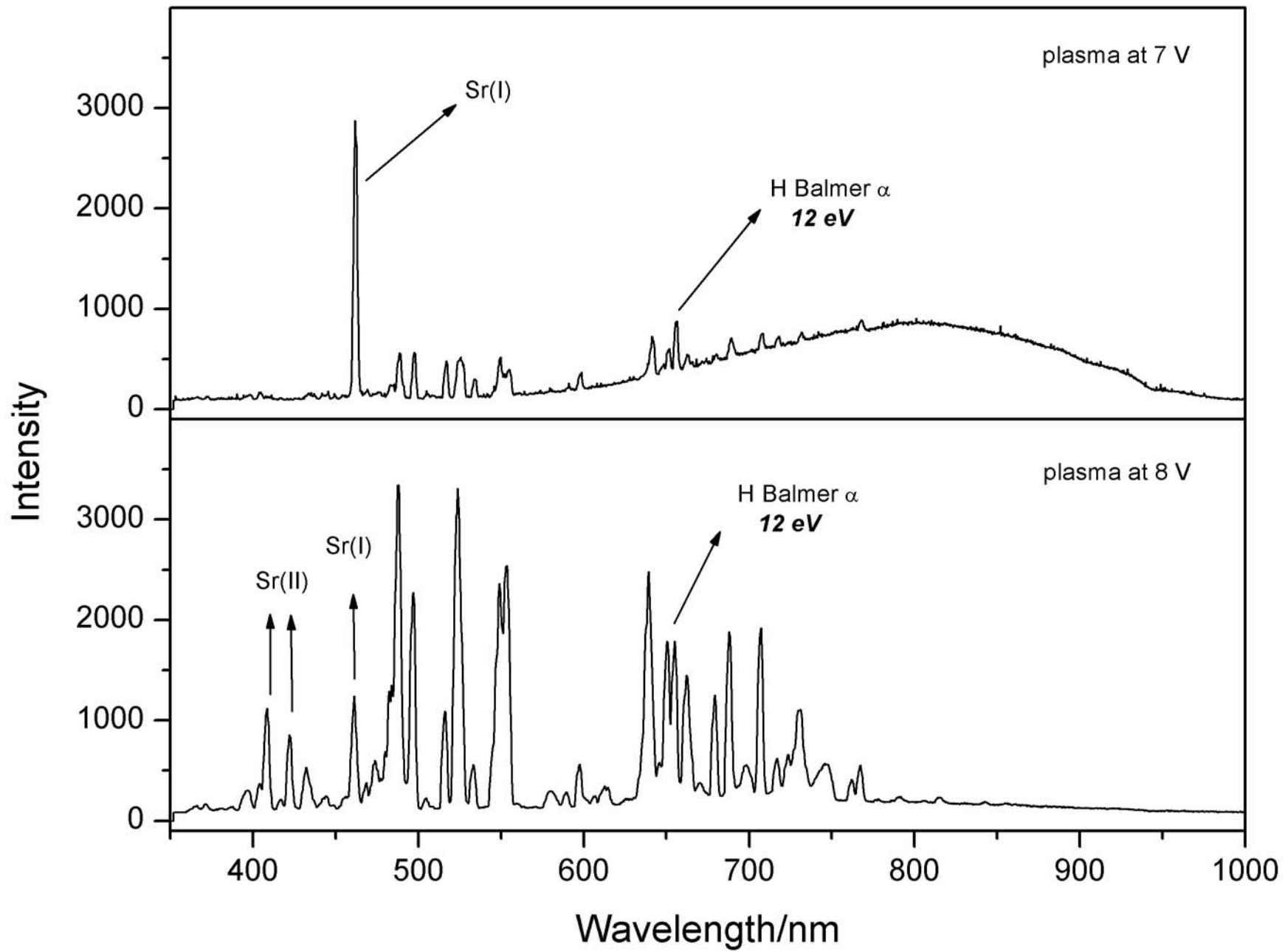
^a Calculated.

^b Power input differs from volt-amperes due to non-unity power factor.

RT Plasma Chamber

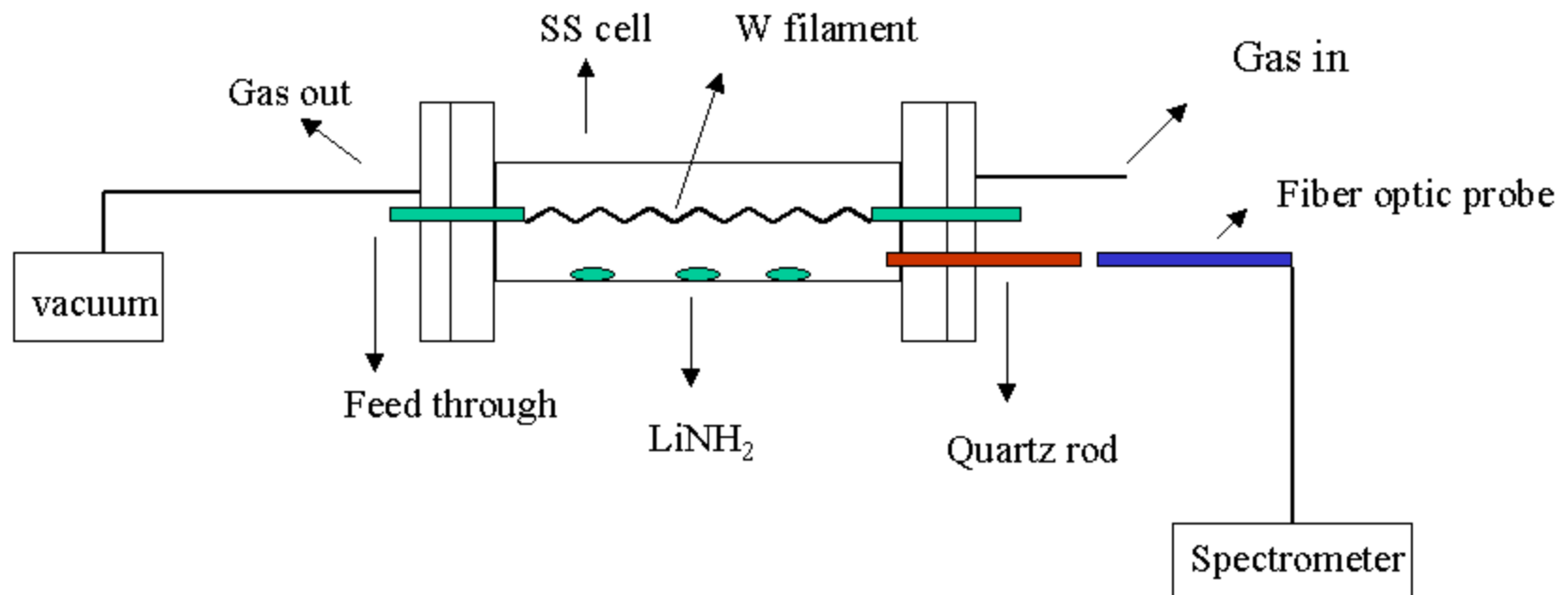




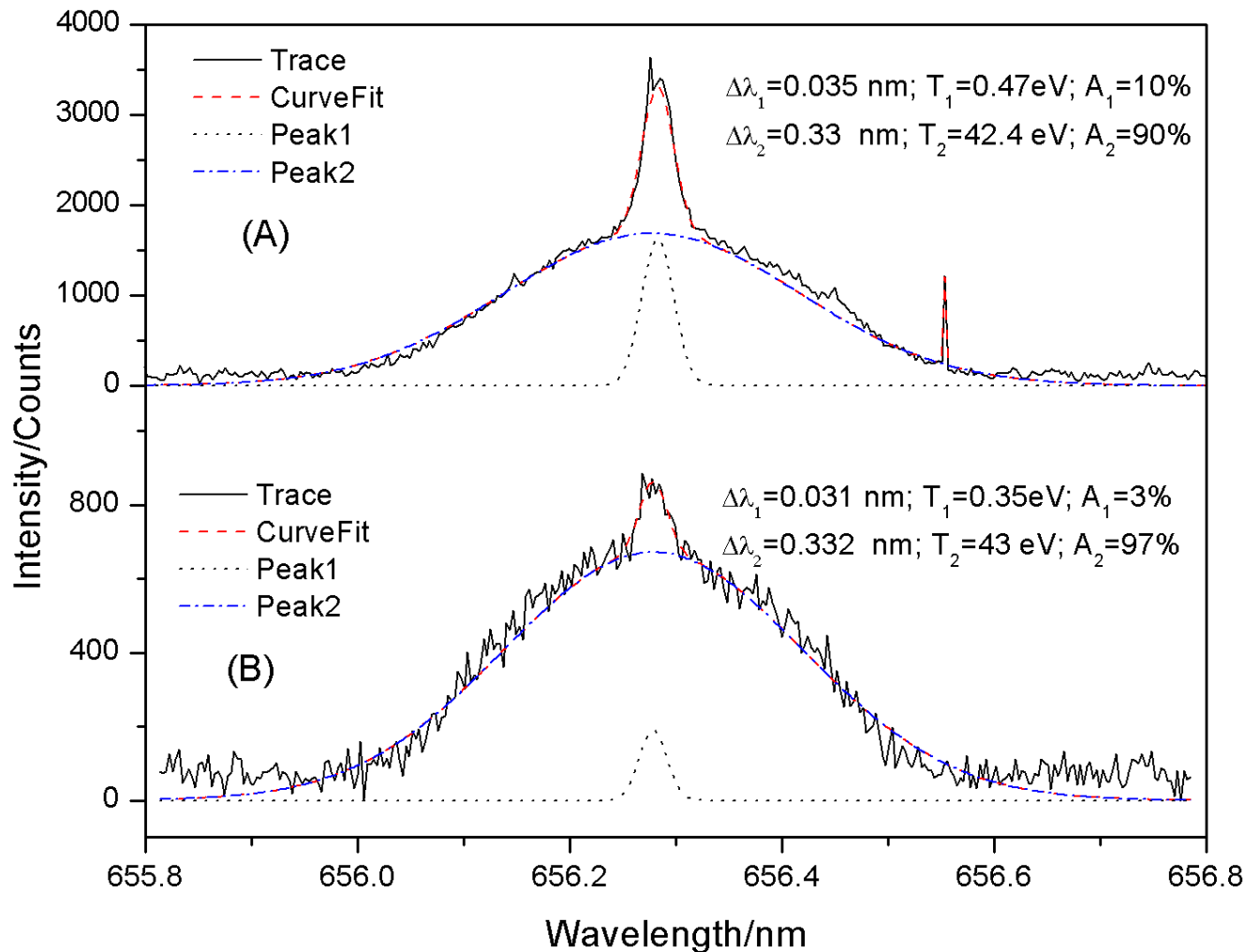


Extraordinary Selective Broadening of the Atomic Hydrogen Lines

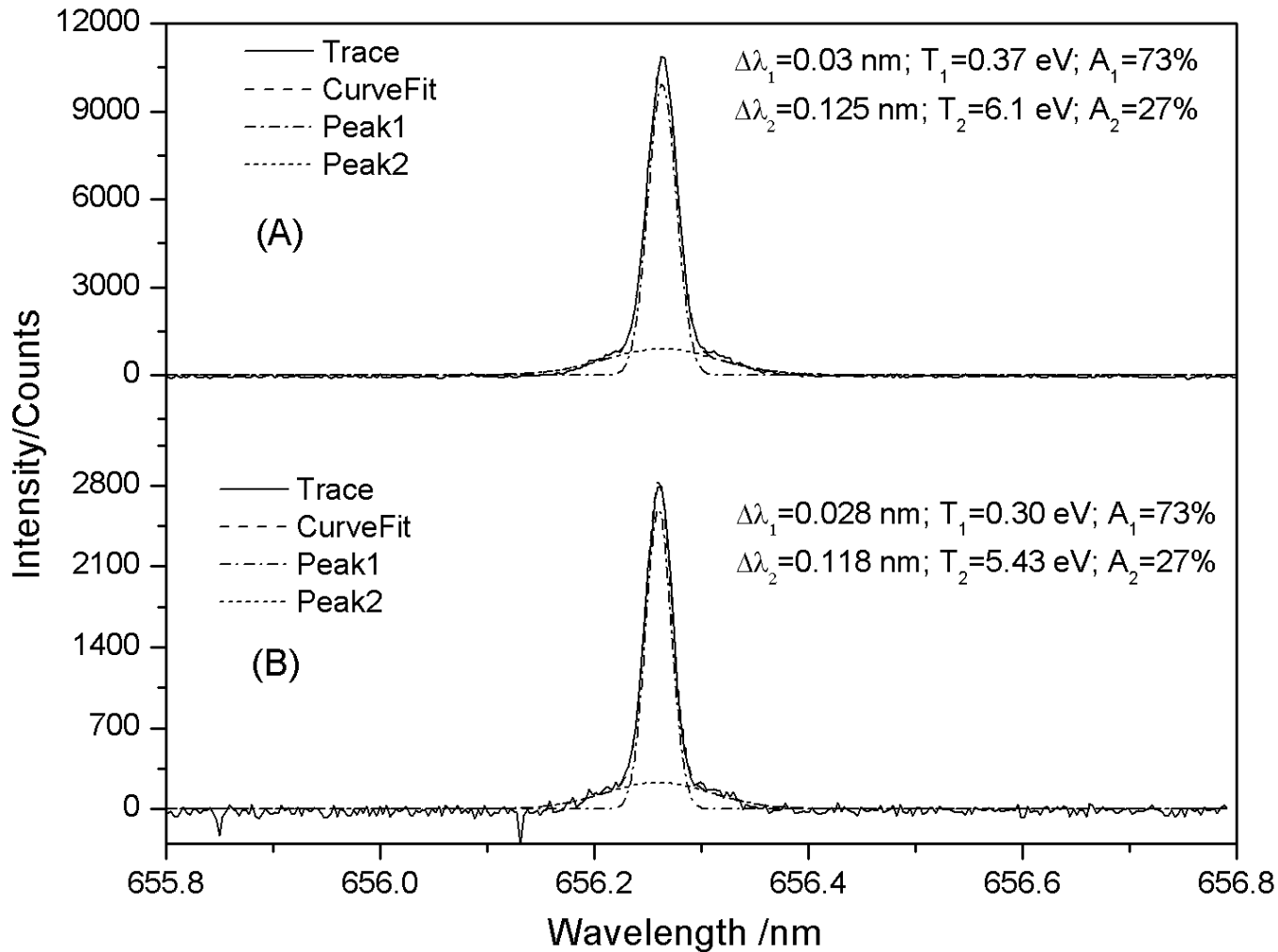
- Only Catalysts Show Broadening
- Time Dependent
- Independent of Position (Electric Field)
- Seen After Long Duration in the Rt-Plasma Cell



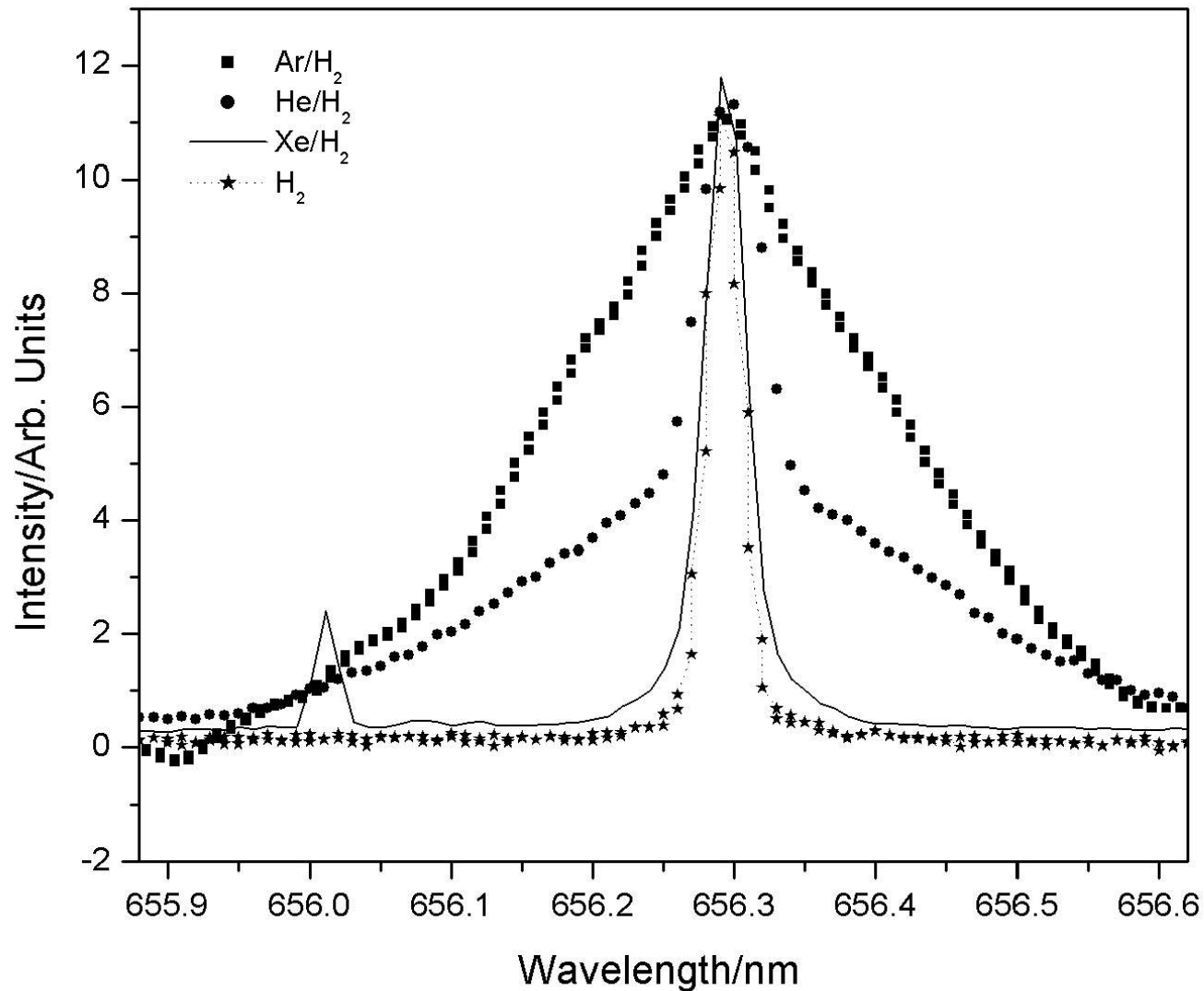
The experimental set up comprising a filament gas cell to form lithium-argon-hydrogen and lithium-hydrogen rt-plasmas



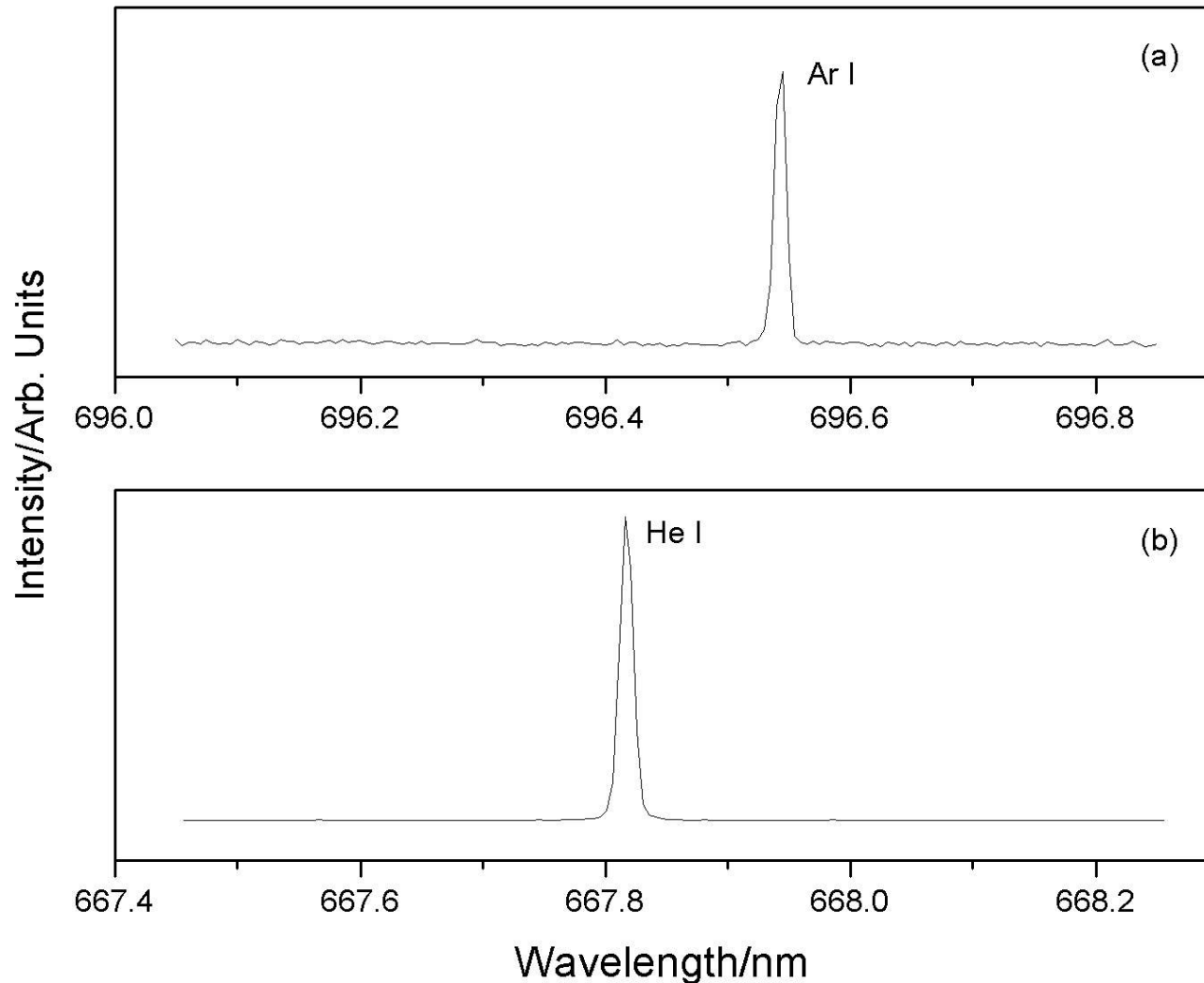
The 656.3 nm Balmer α line width recorded with a high-resolution visible spectrometer on (A) the initial emission of a lithium-argon-hydrogen rt-plasma and (B) the emission at 70 hours of operation. Lithium lines and significant broadening of only the H lines was observed over time corresponding to an average hydrogen atom temperature of >40 eV and fractional population over 90%.



The 656.3 nm Balmer α line width recorded with a high-resolution ($\pm 0.006 \text{ nm}$) visible spectrometer on (A) the initial emission of a lithium-hydrogen rt-plasma and (B) the emission at 70 hours of operation. Lithium lines and broadening of only the H lines was observed over time, but diminished relative to the case having the argon-hydrogen gas (95/5%). The Balmer width corresponded to an average hydrogen atom temperature of 6 eV and a 27% fractional population.

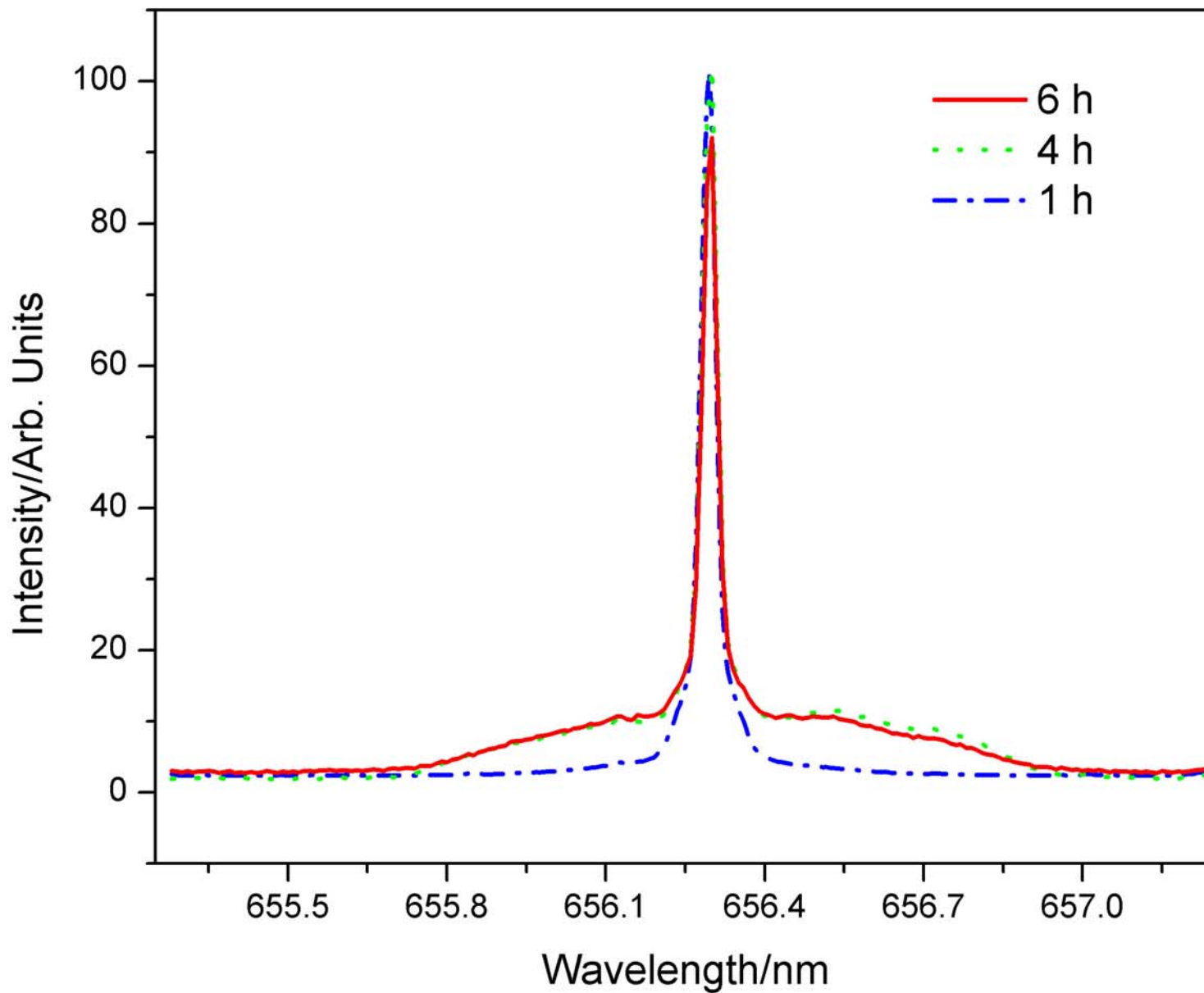


The 656.3 nm Balmer α line widths recorded normal to the applied electric field direction with a high resolution (± 0.006 nm) visible spectrometer on capacitively-coupled RF discharge plasmas of hydrogen compared with each of He/H₂ (95/5%), Ar/H₂ (95/5%), and Xe/H₂ (95/5%).

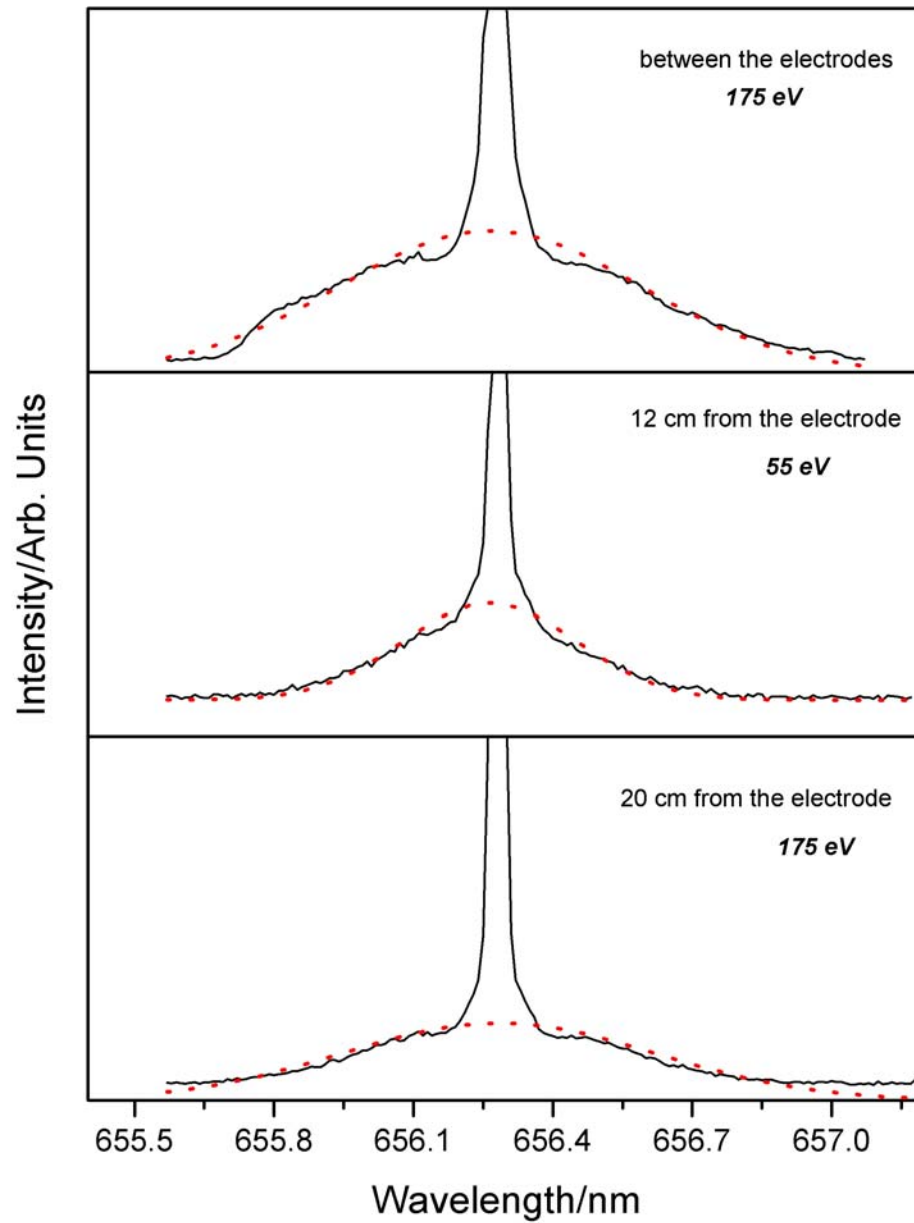


(a) The 696.54 nm Ar I line width recorded with a high resolution (± 0.006 nm) visible spectrometer on an Ar/H₂ (95/5%), capacitively-coupled RF plasma. (b) The 667.816 nm He I line width recorded with a high resolution (± 0.006 nm) visible spectrometer on a He/H₂ (95/5%), capacitively-coupled RF plasma. No broadening was observed in either case.

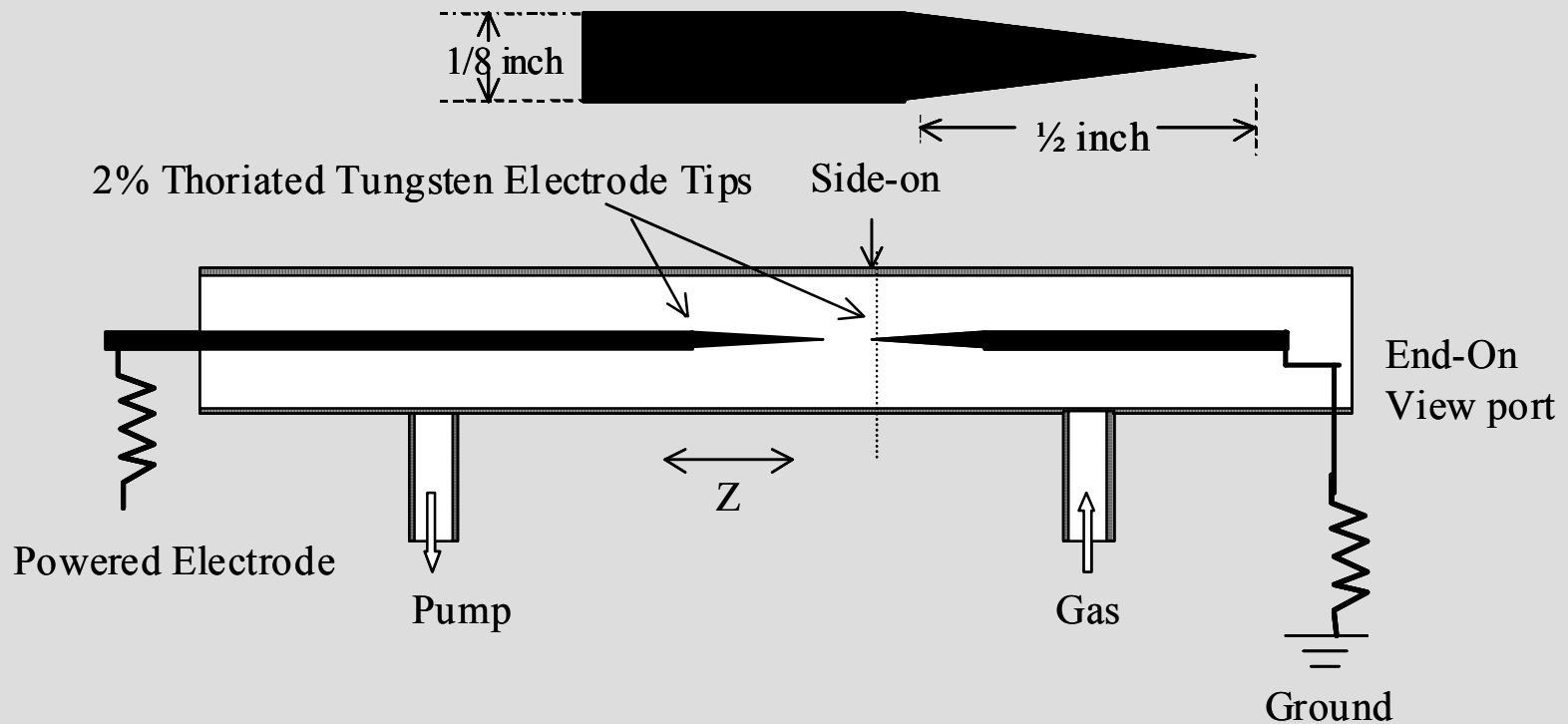
RF capacitively coupled cell, H₂O vapor plasma



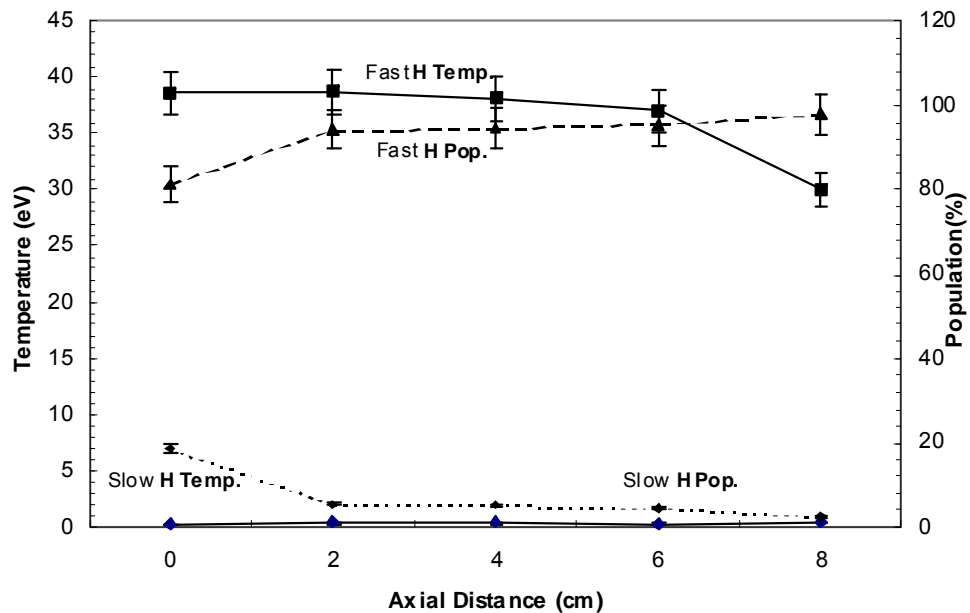
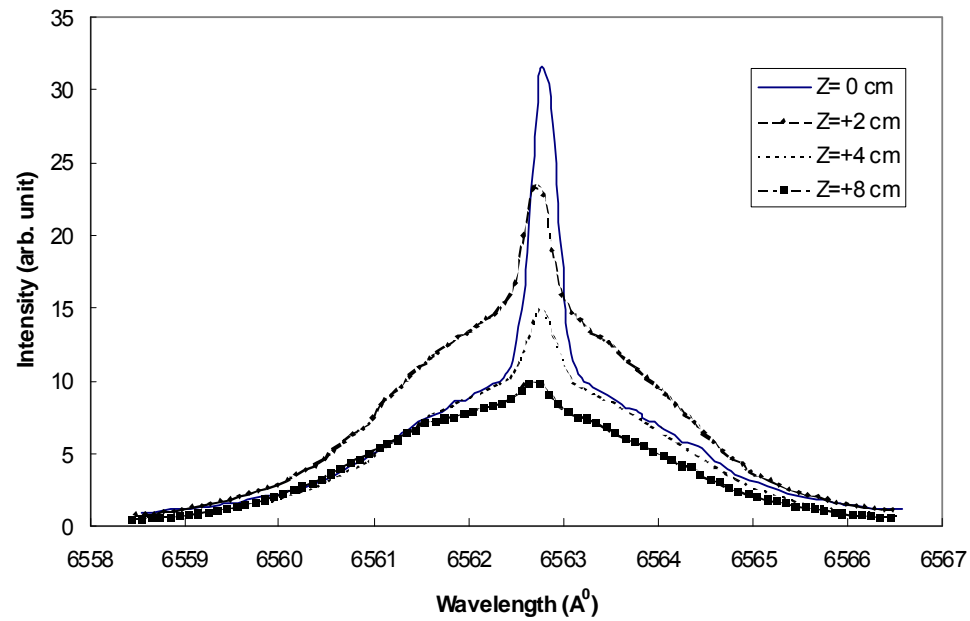
Extraordinary (>100 eV) H Broadening in Water Vapor RF Plasma is Time Dependent



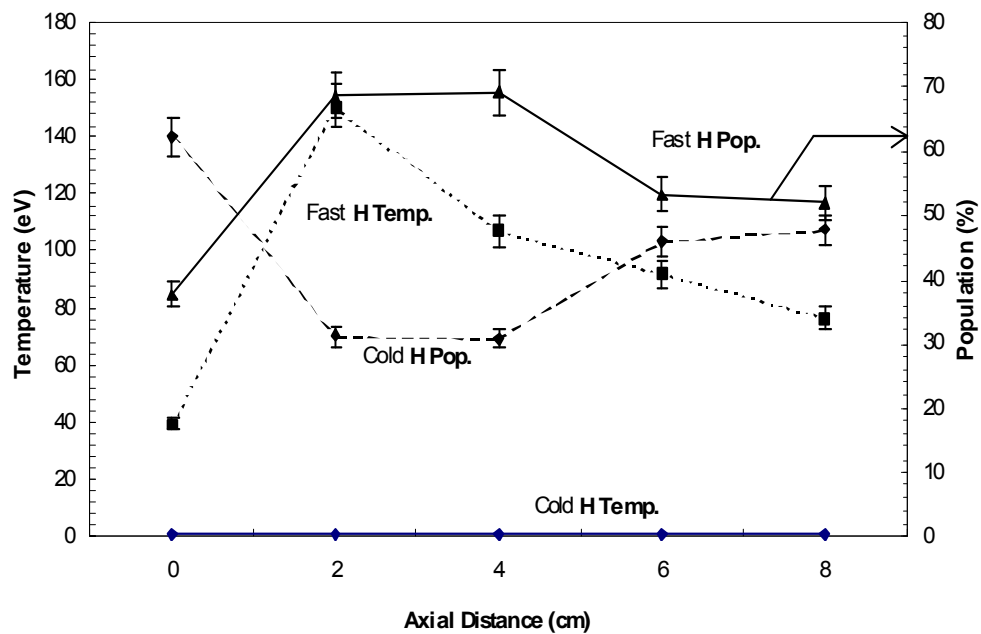
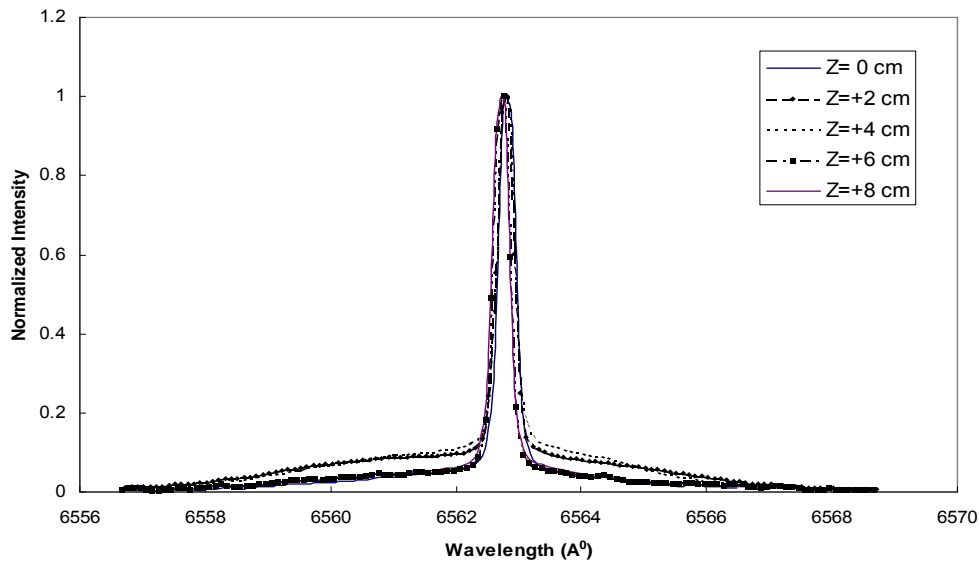
Extraordinary
Broadening in Water
Vapor is Independent of
Position in the Cell



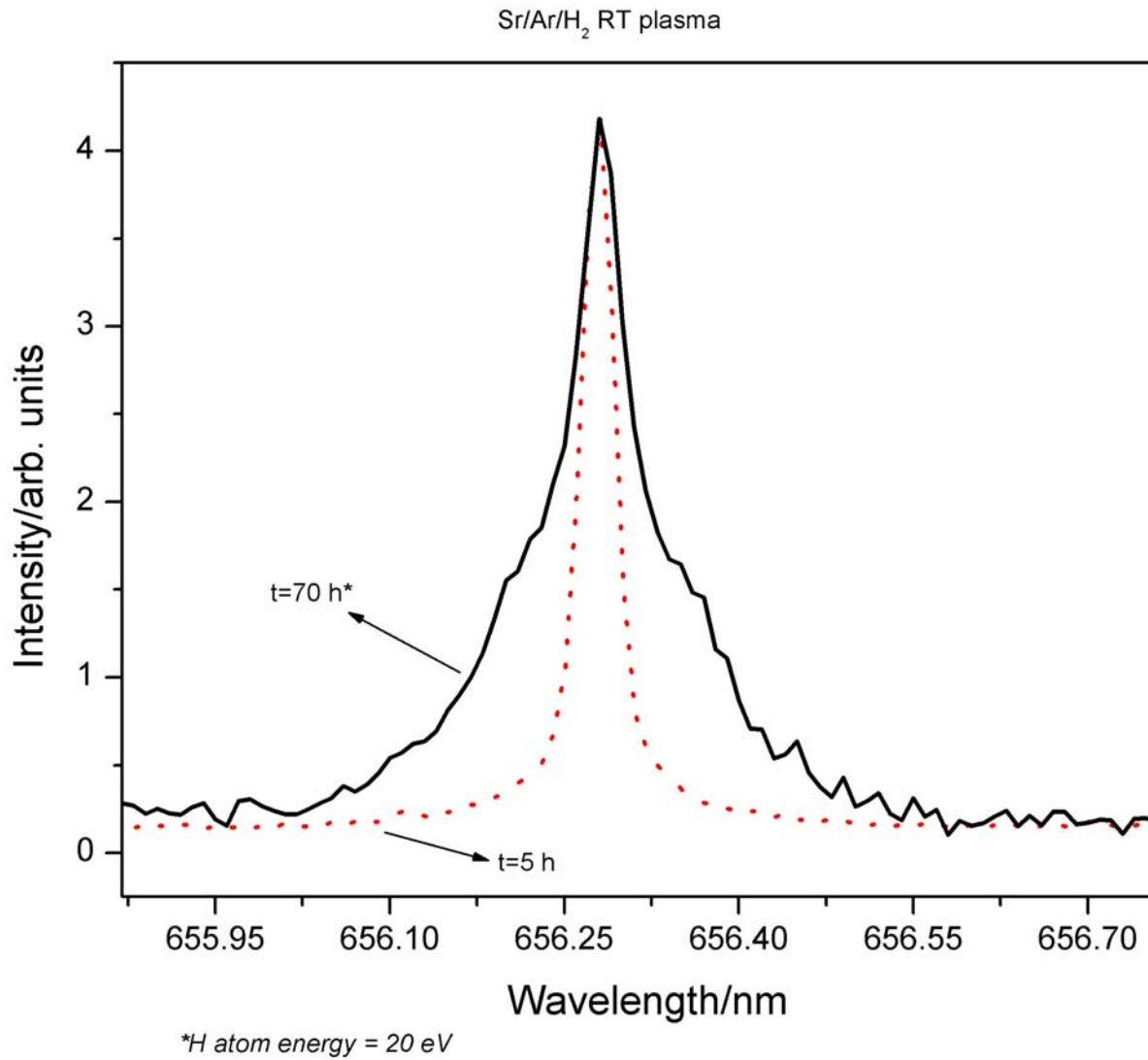
Schematic of the DC discharge created between the fine tips of 2% thoriated tungsten electrodes. For axial scan of side-on observations cathode tip is taken as $Z=0$ cm



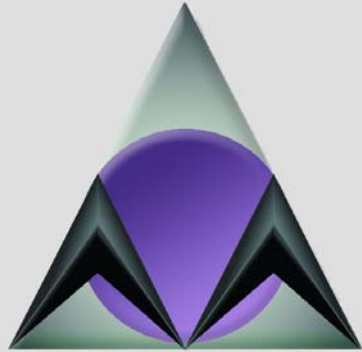
Side-on scan along the axis of the emission spectrum for 1T Ar/5% H₂ at 400V and 20 mA. Hot hydrogen population is present even at a distance of 8 cm away from the cathode tip where most of the potential falls.



Side-on scan along the axis of the emission spectrum for 1T He/5% H₂ at 800V and 20 mA. Hot hydrogen population is present even at a distance of 8 cm away from the cathode tip where most of the potential falls.

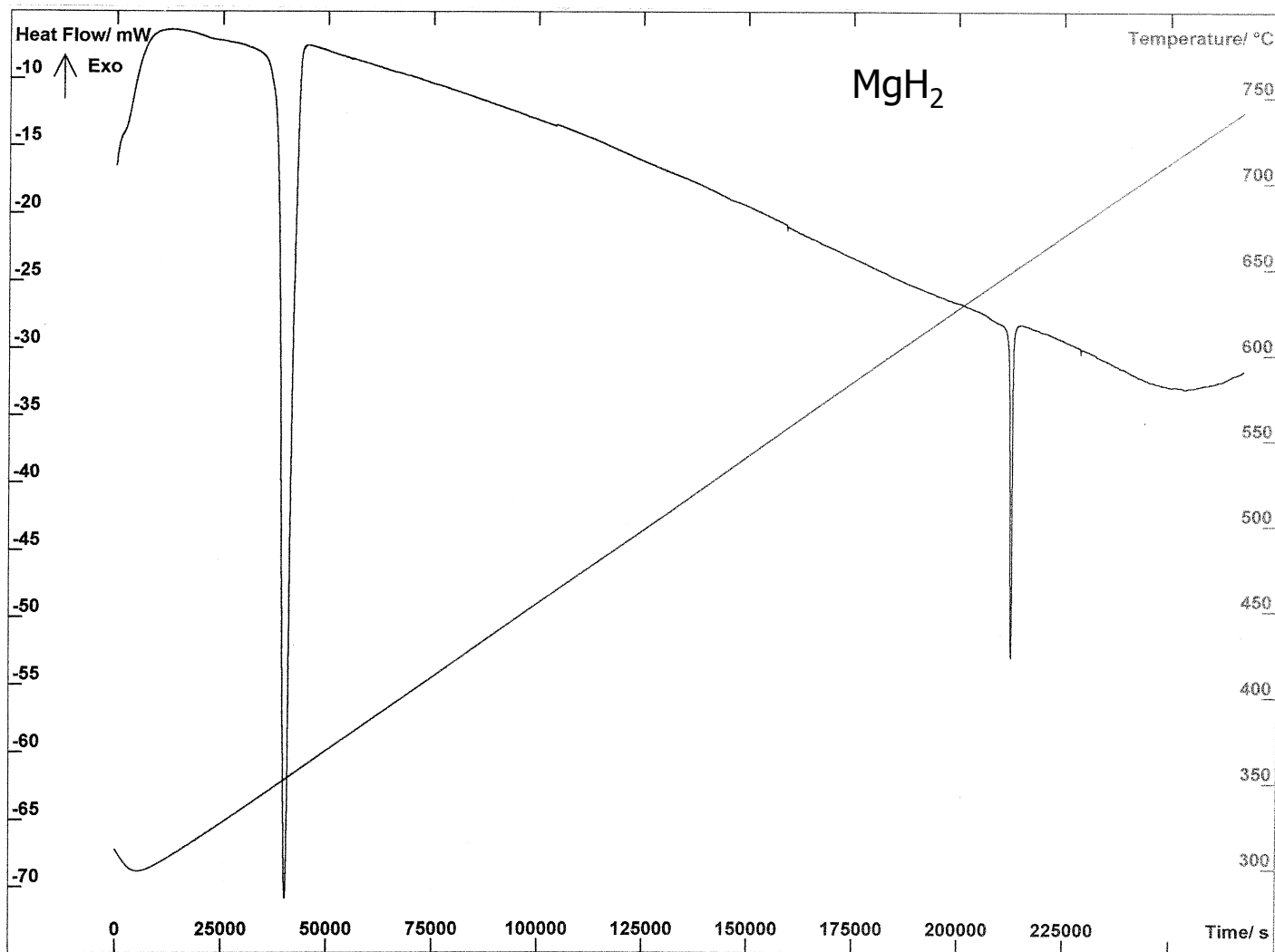


Extraordinary (>20 eV) H Broadening in Rt- Plasma is Time Dependent

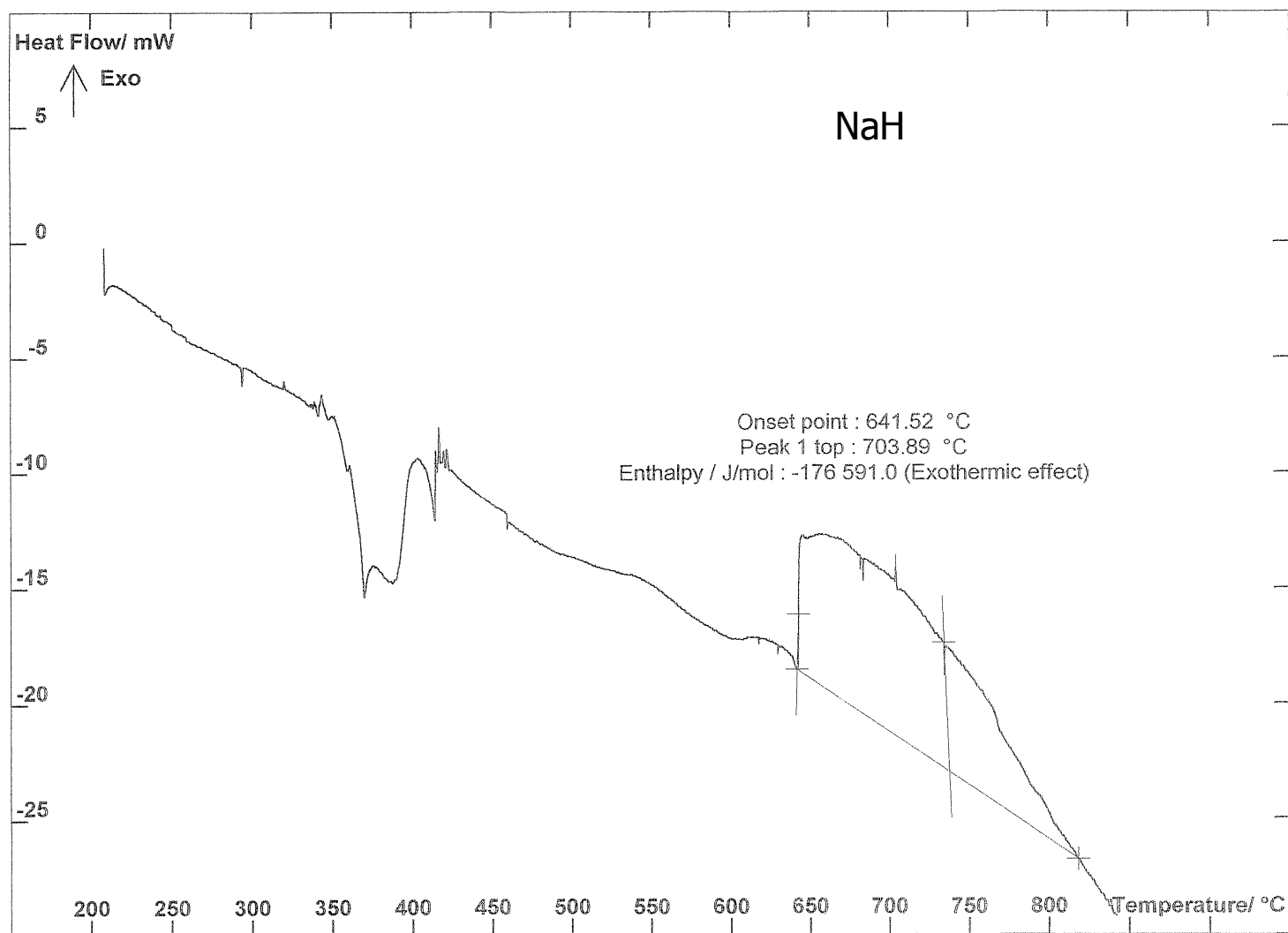


**BLACKLIGHT
POWER, Inc**

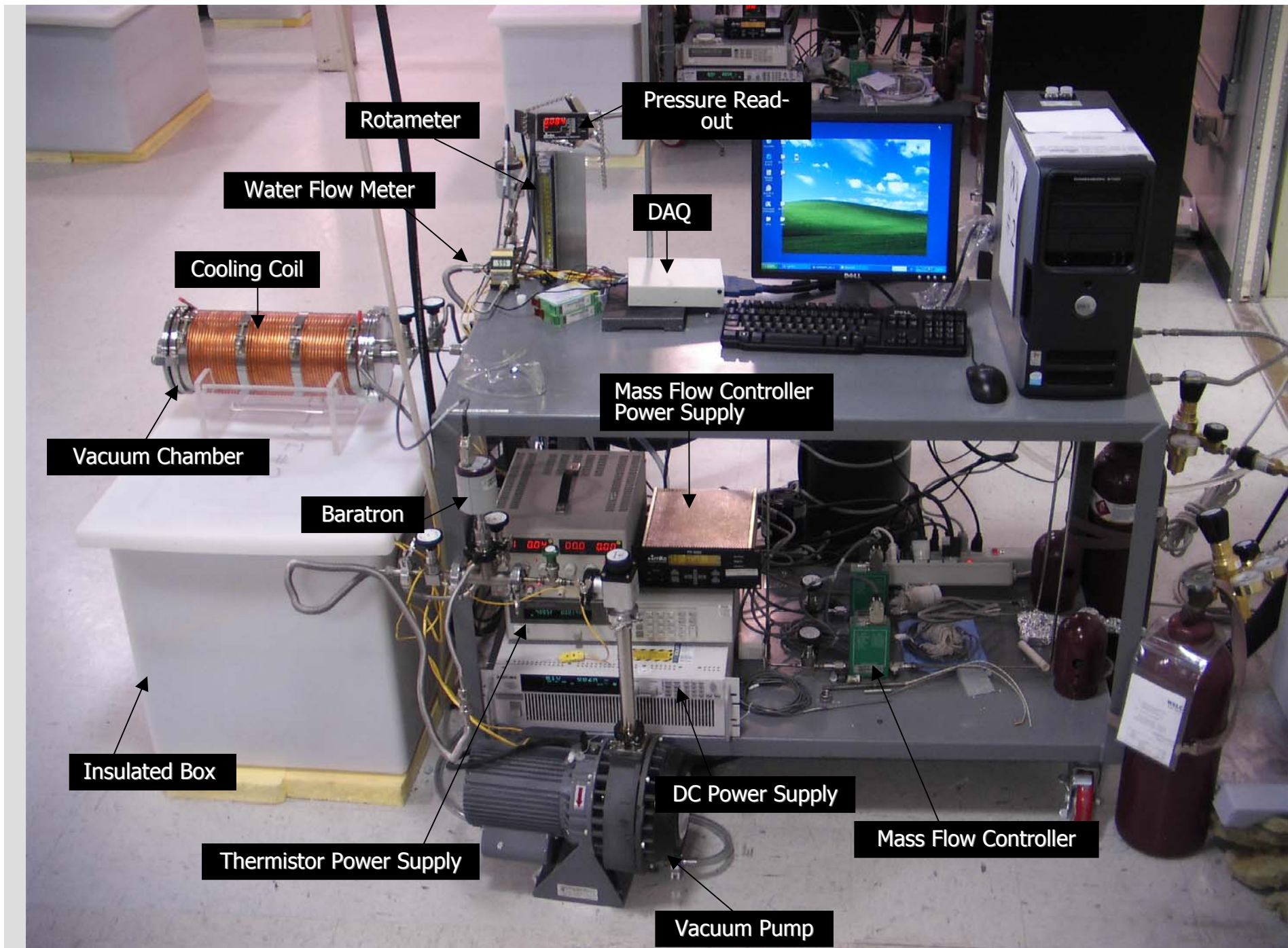
Calorimetry:
Proof of Concept Prototypes



The results of the DSC (100–750 °C) of MgH_2 at a scan rate of 0.1 degree/minute. Two sharp endothermic peaks were observed. A first peak centered at 351.75 °C corresponding to 68.61 $kJ/mole MgH_2$ matches the 74.4 $kJ/mole MgH_2$ decomposition energy. The second peak at 647.66 °C corresponding to 6.65 $kJ/mole MgH_2$ matches the known melting point of $Mg(m)$ is 650 °C and enthalpy of fusion of 8.48 $kJ/mole Mg(m)$. Thus, the expected behavior was observed for the decomposition of a control, noncatalyst hydride.



The results of the DSC (100–750 °C) of *NaH* at a scan rate of 0.1 degree/minute. A broad endothermic peak was observed at 350 °C to 420 °C which corresponded to 47 *kJ/mole* and matches sodium hydride decomposition in this temperature range with a corresponding enthalpy of 57 *kJ/mole*. A large exotherm was observed under conditions that form *NaH* catalyst in the region 640 °C to 825 °C which corresponds to at least -354 *kJ/mole H₂*, greater than that of the most exothermic reaction possible for *H*, the -241.8 *kJ/mole H₂* enthalpy of combustion of hydrogen.



Rotameter

Pressure Read-out

Water Flow Meter

DAQ

Cooling Coil

Mass Flow Controller Power Supply

Vacuum Chamber

Baratron

Insulated Box

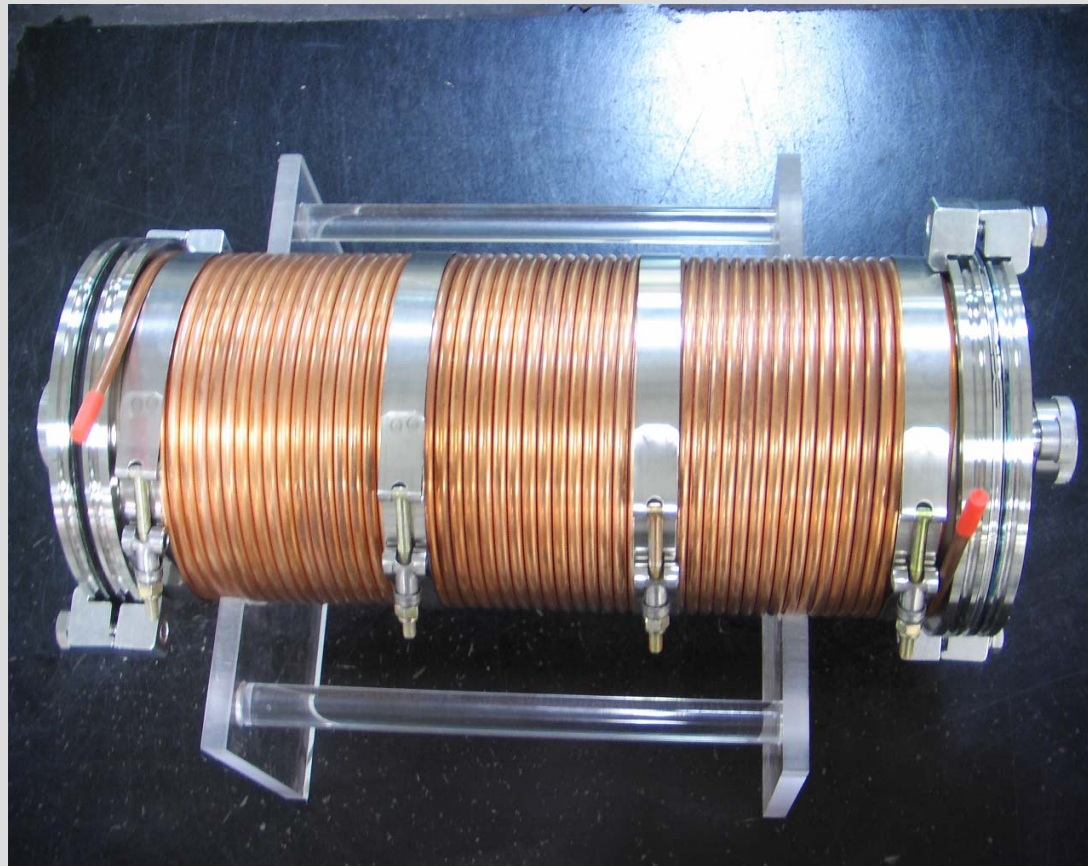
Thermistor Power Supply

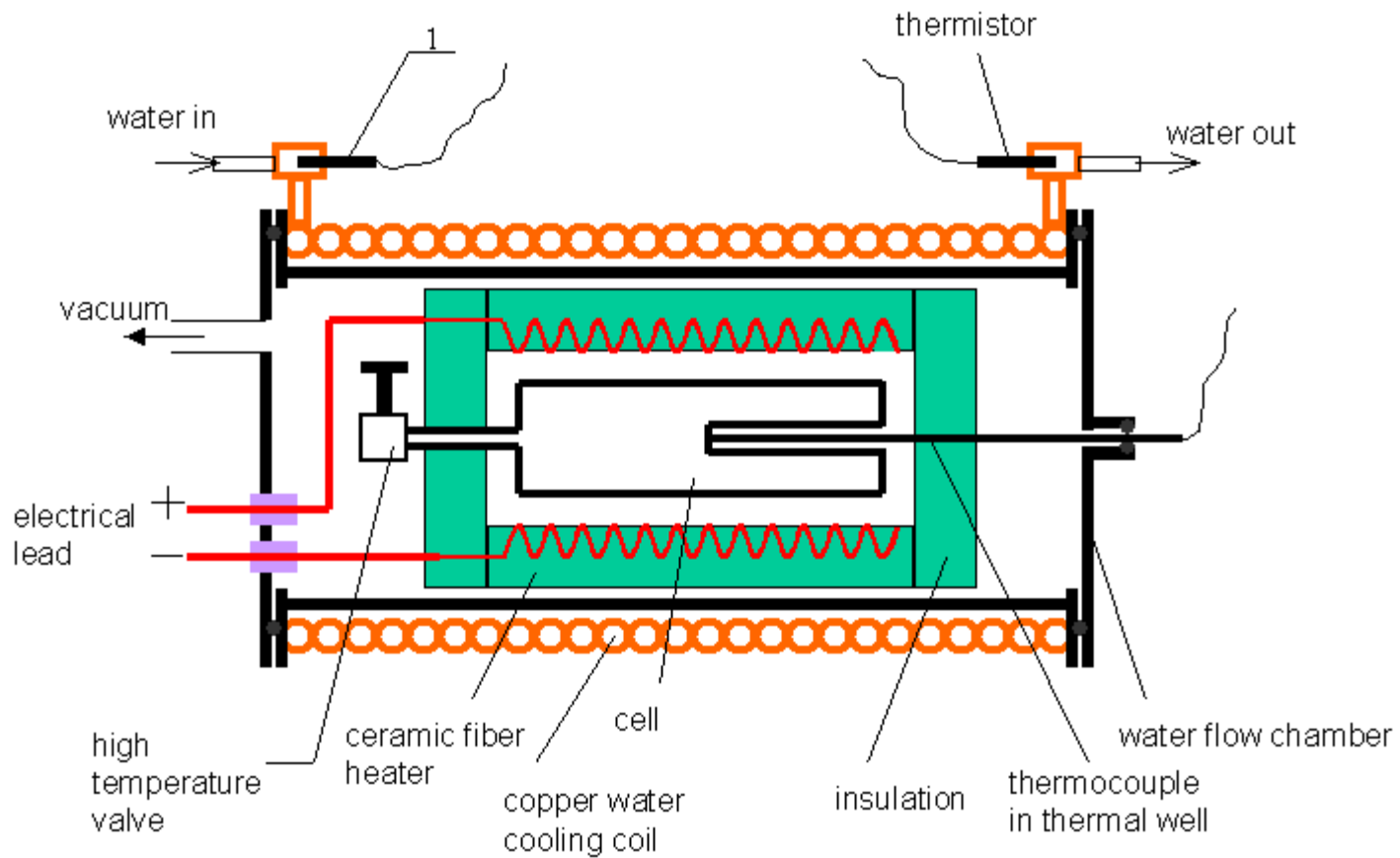
DC Power Supply

Mass Flow Controller

Vacuum Pump

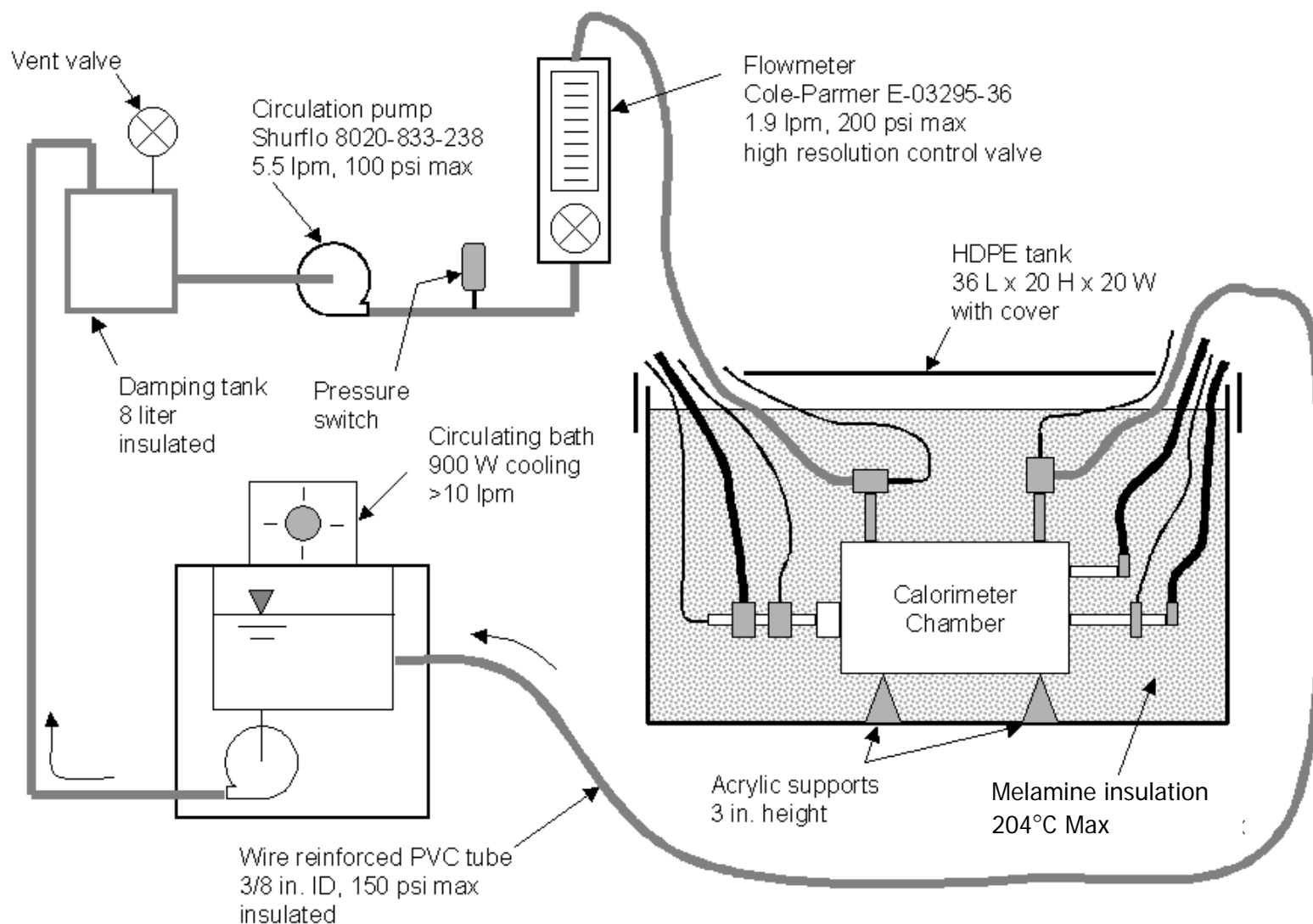
Advanced Heat Exchanger



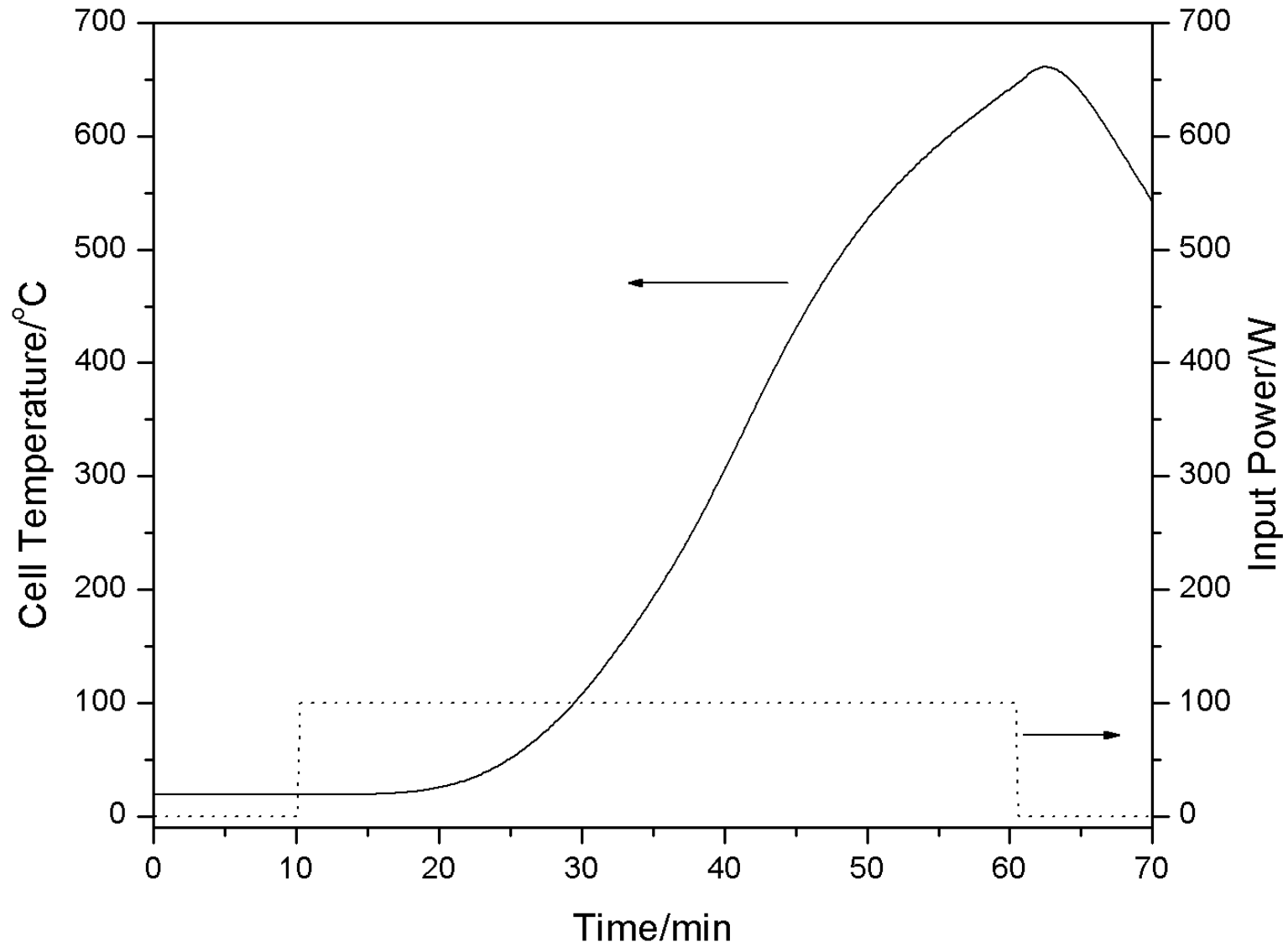


Schematic of the reaction cell and the cross sectional view of the water flow calorimeter used to measure the energy balance of the NaH catalyst reaction to form hydrinos

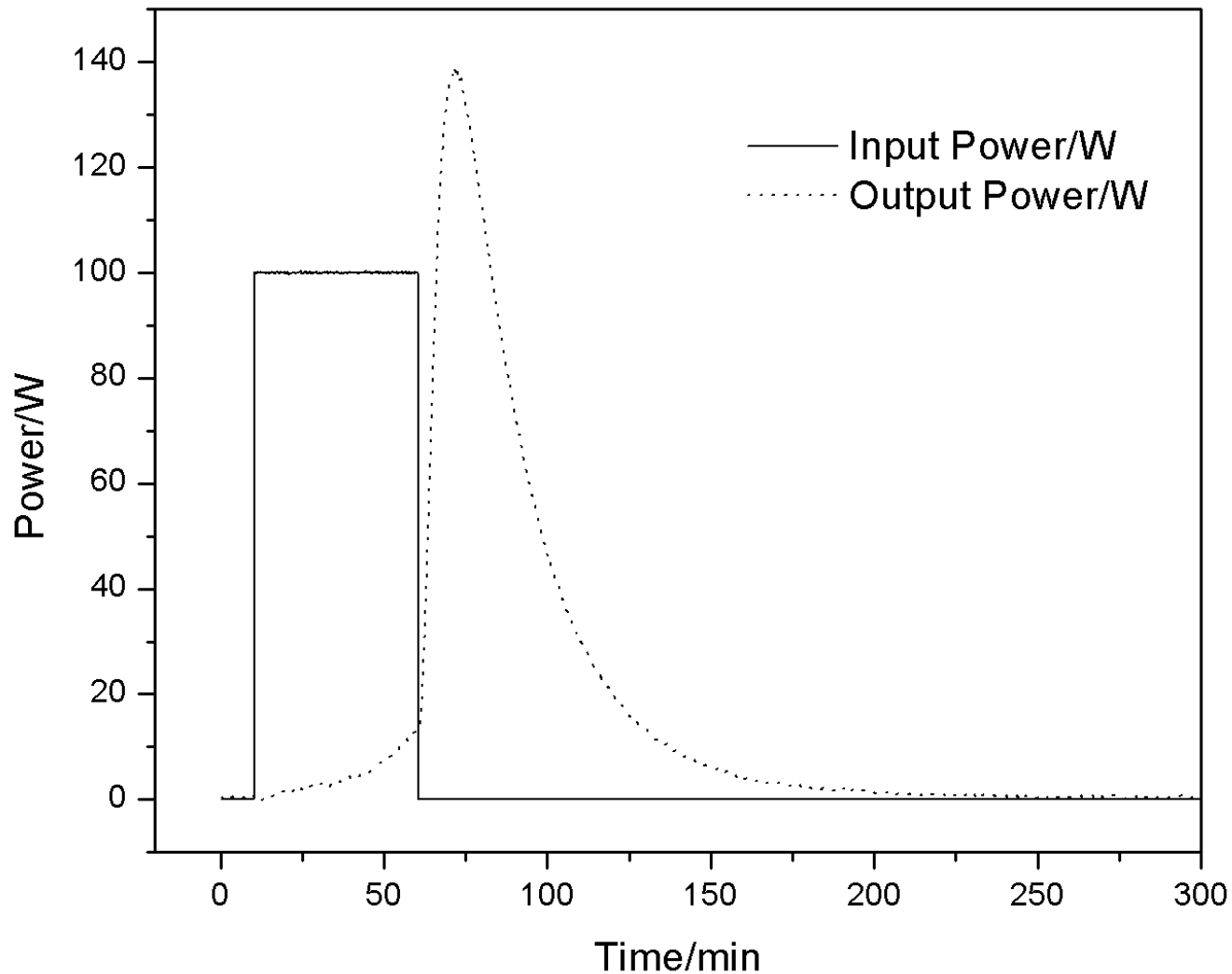
Flow Calorimeter System



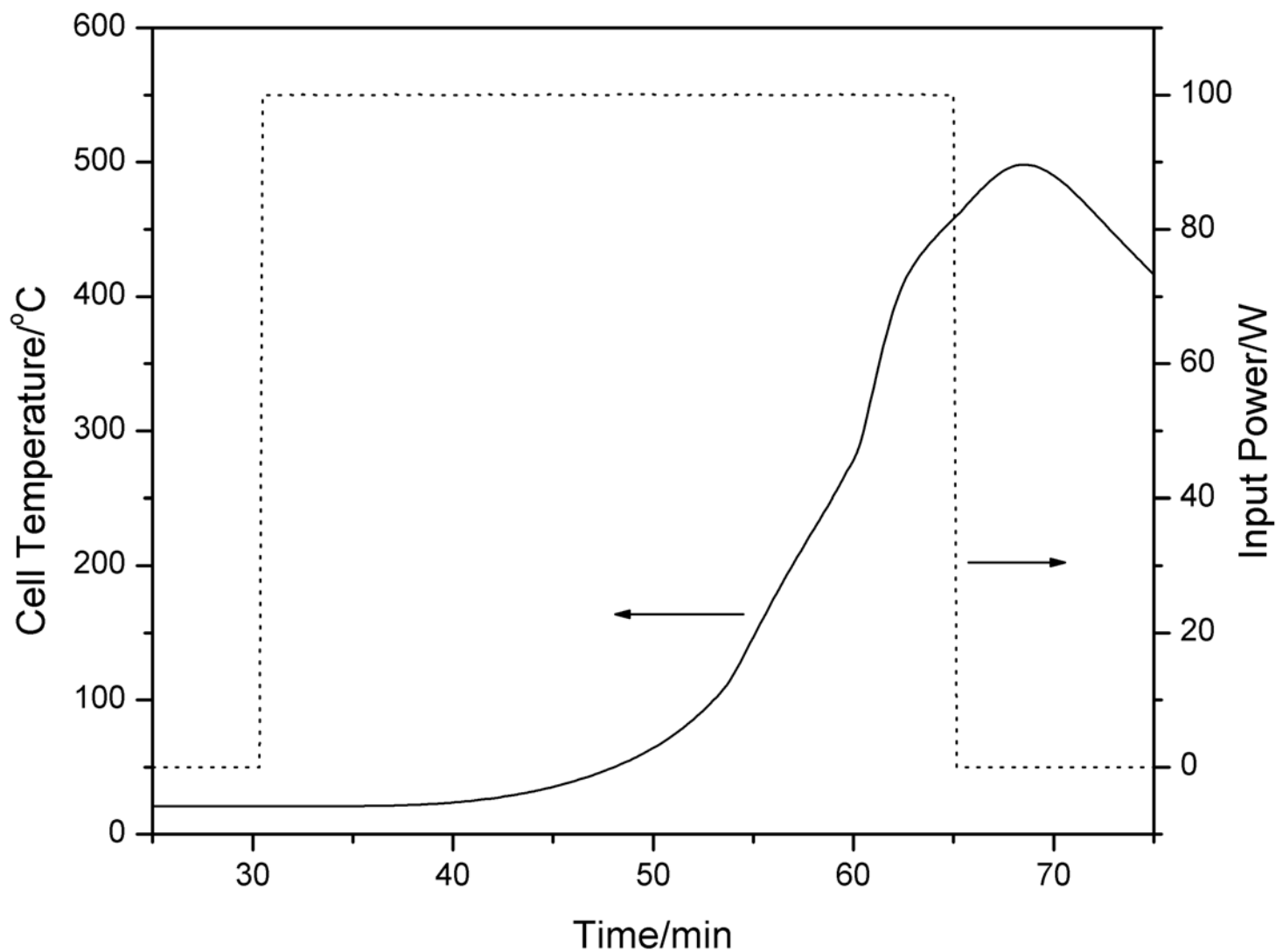
Schematic of the water flow calorimeter used to measure the energy balance of the NaH catalyst reaction to form hydrinos



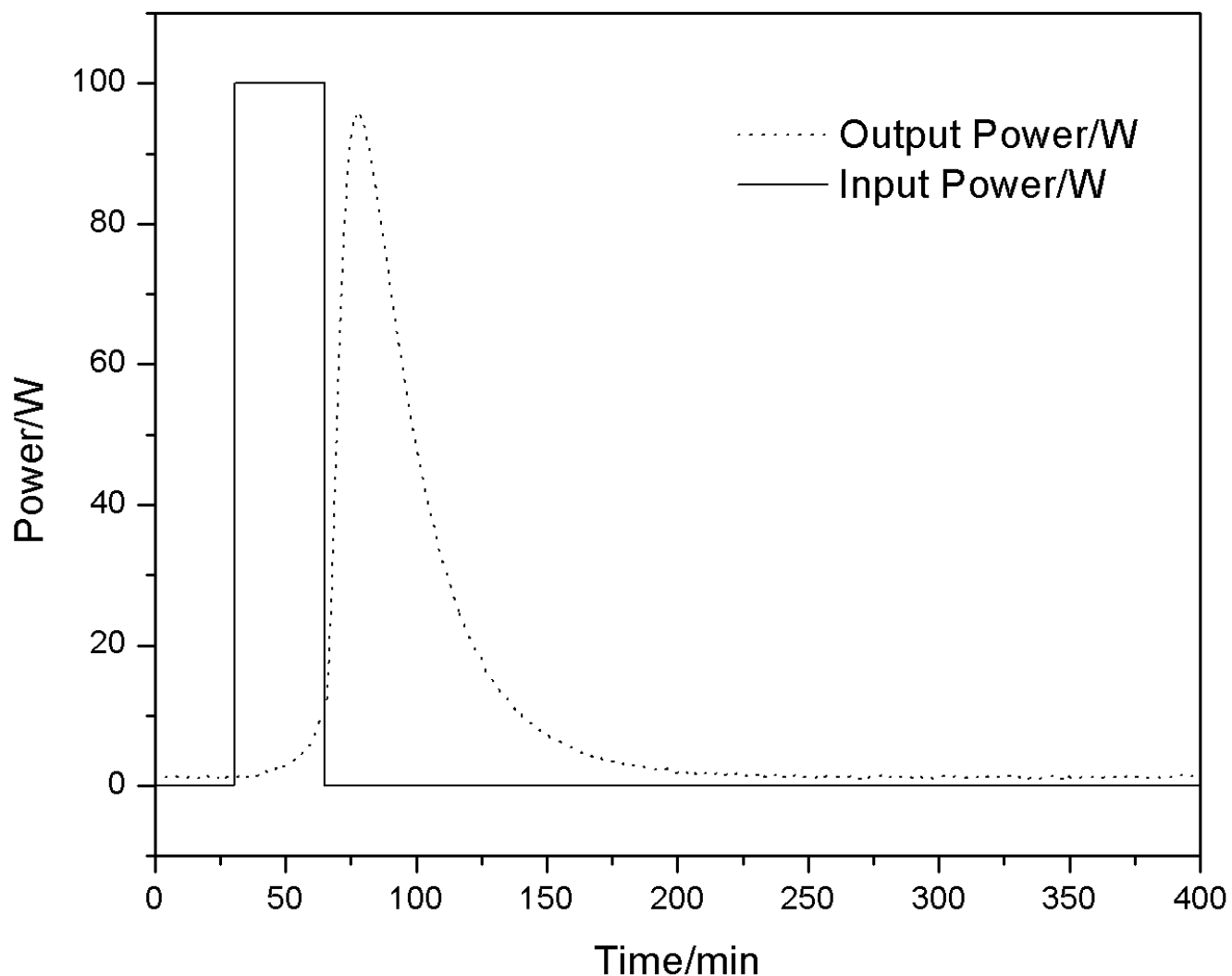
Temperature versus time for the calibration run with an evacuated test cell and resistive heating only.



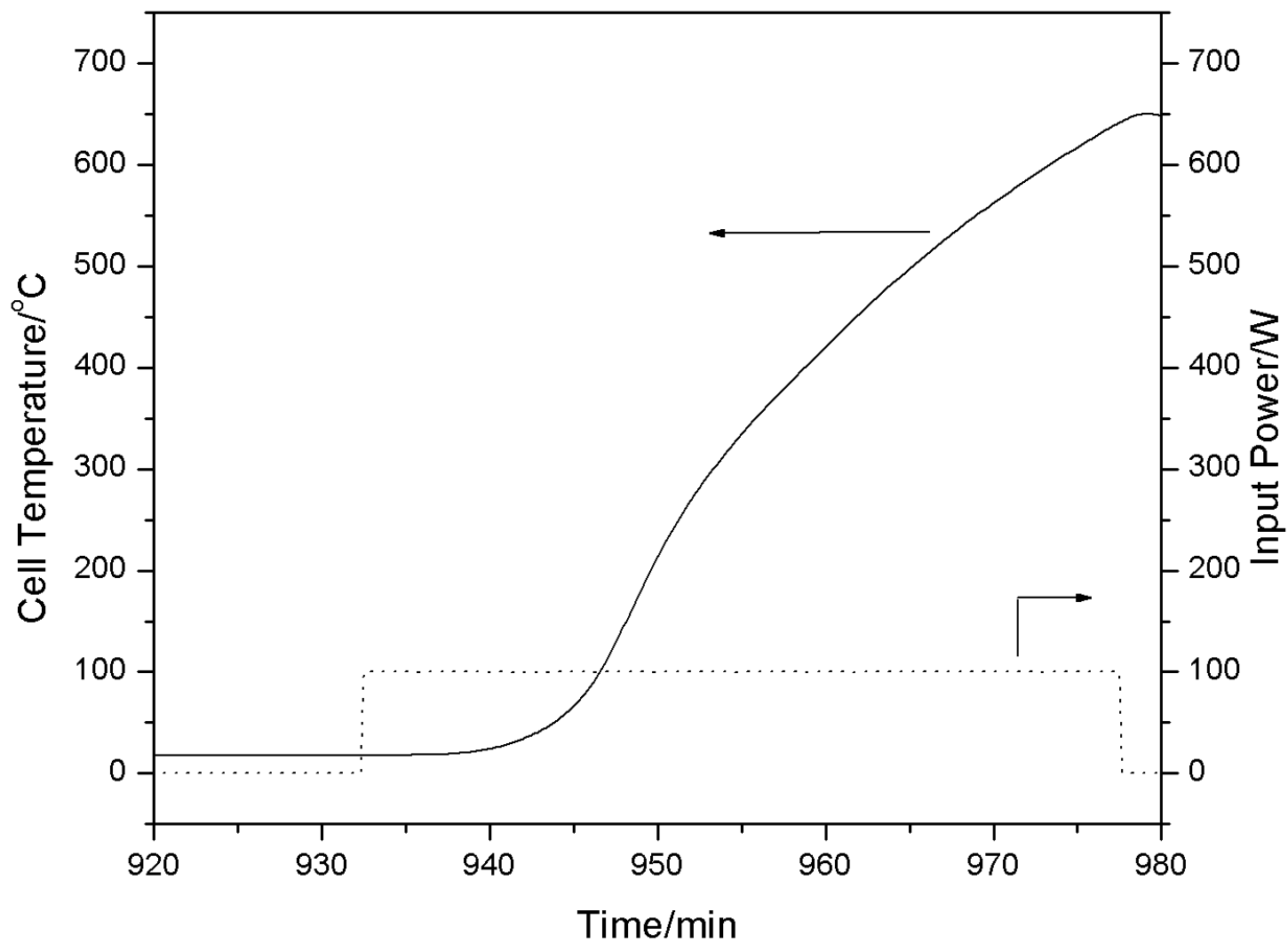
Power versus time for the calibration run with an evacuated test cell and resistive heating only. The numerical integration of the input and output power curves yielded an output energy of 292.2 kJ and an input energy of 303.1 kJ corresponding to a coupling of flow of 96.4% of the resistive input to the output coolant.



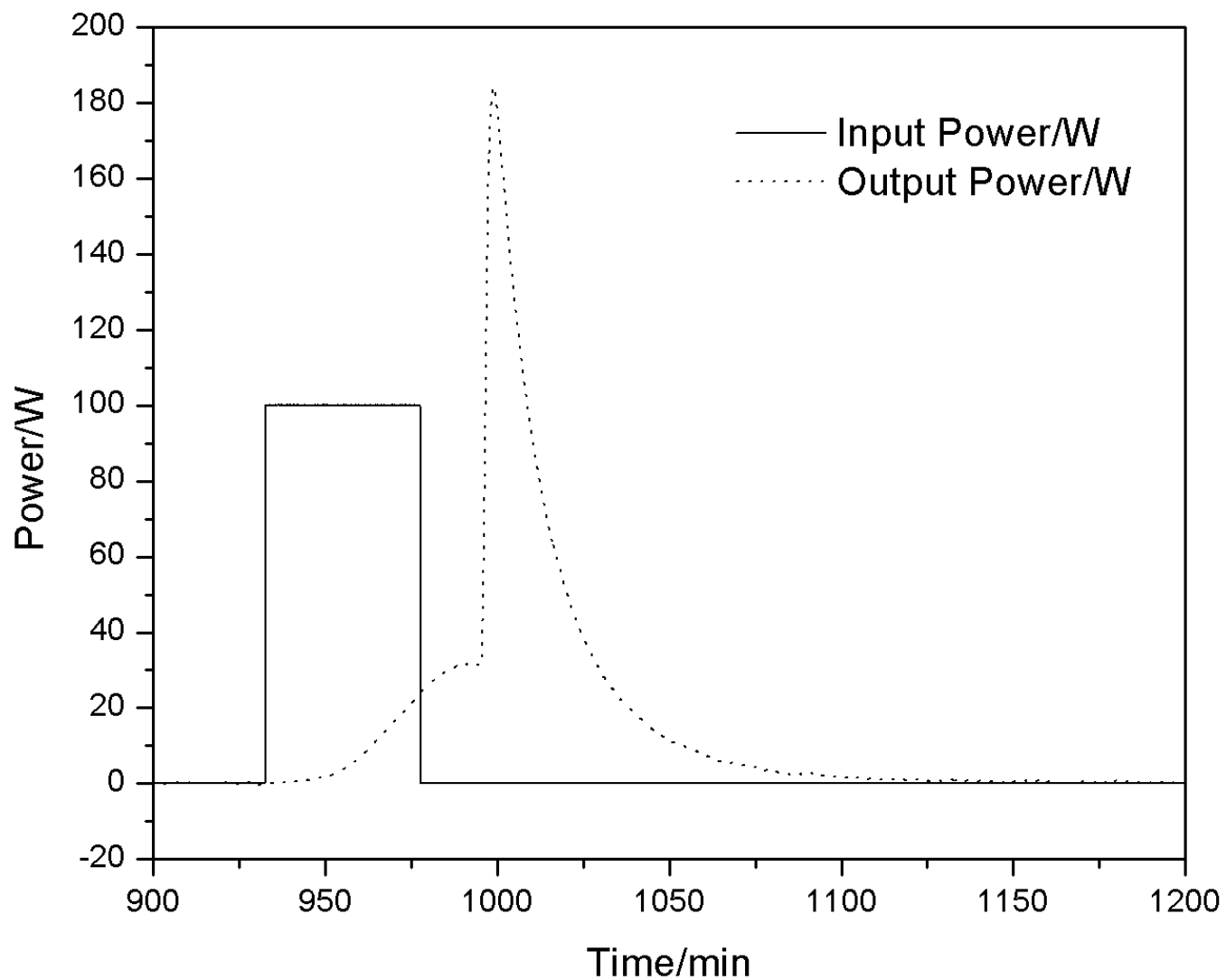
The cell temperature with time for the hydriano reaction with the cell containing the reagents comprising the catalyst material, 1g *Li*, 0.5g *LiNH₂*, 10g *LiBr*, and 15g *Pd / Al₂O₃*. The reaction liberated 19.1 kJ of energy in less than 120 s to develop a system-response-corrected peak power in excess of 160 W.



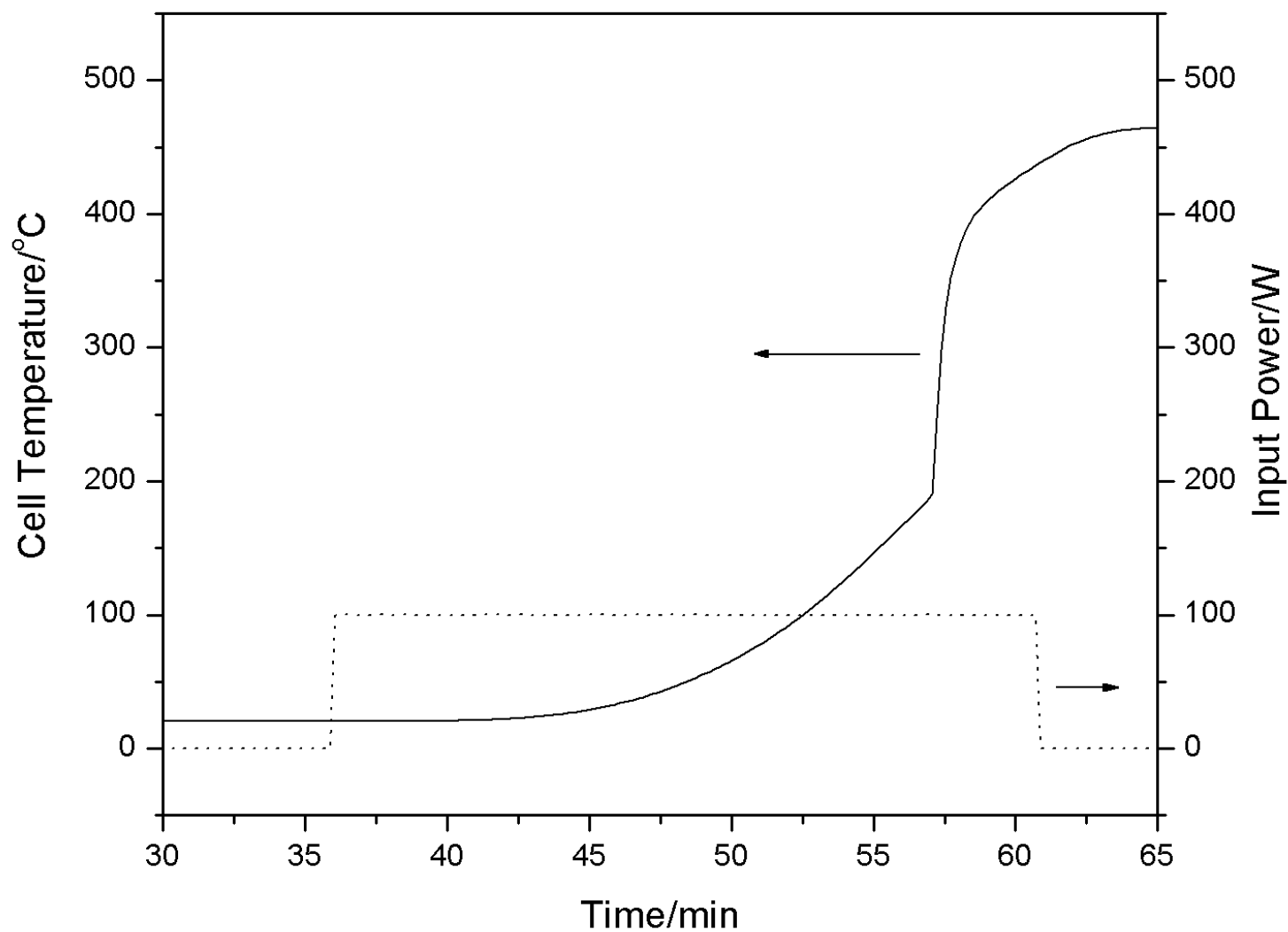
The coolant power with time for the hydrino reaction with the cell containing the reagents comprising the catalyst material, 1g *Li*, 0.5g *LiNH₂*, 10g *LiBr*, and 15g *Pd / Al₂O₃*. The numerical integration of the input and output power curves with the calibration correction applied yielded an output energy of 227.2 kJ and an input energy of 208.1 kJ corresponding to an excess energy of 19.1 kJ.



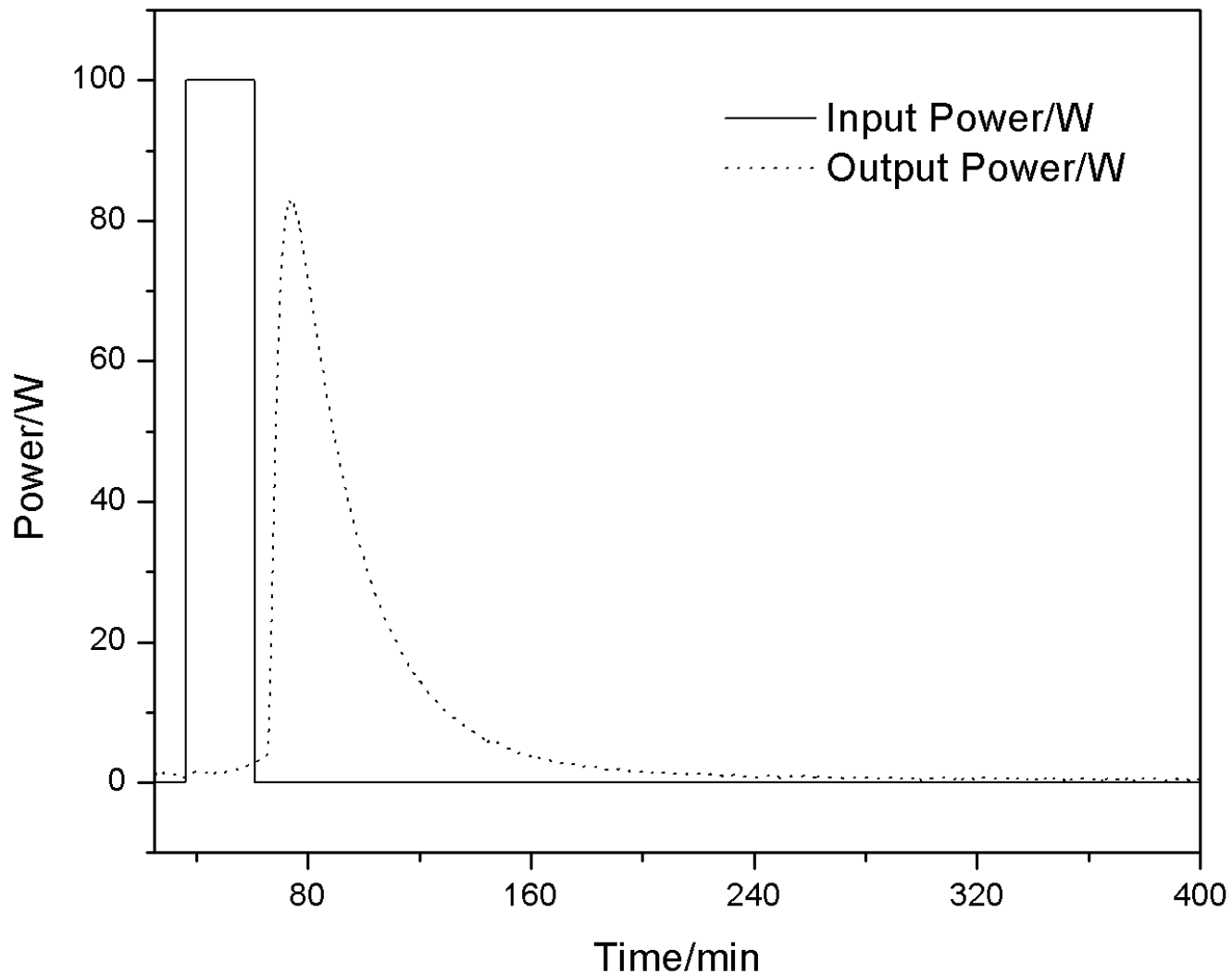
The cell temperature with time for the R-Ni control power test with the cell containing the reagents comprising the starting material for R-Ni, 15g Ni/Al alloy powder, and 3.28g of Na.



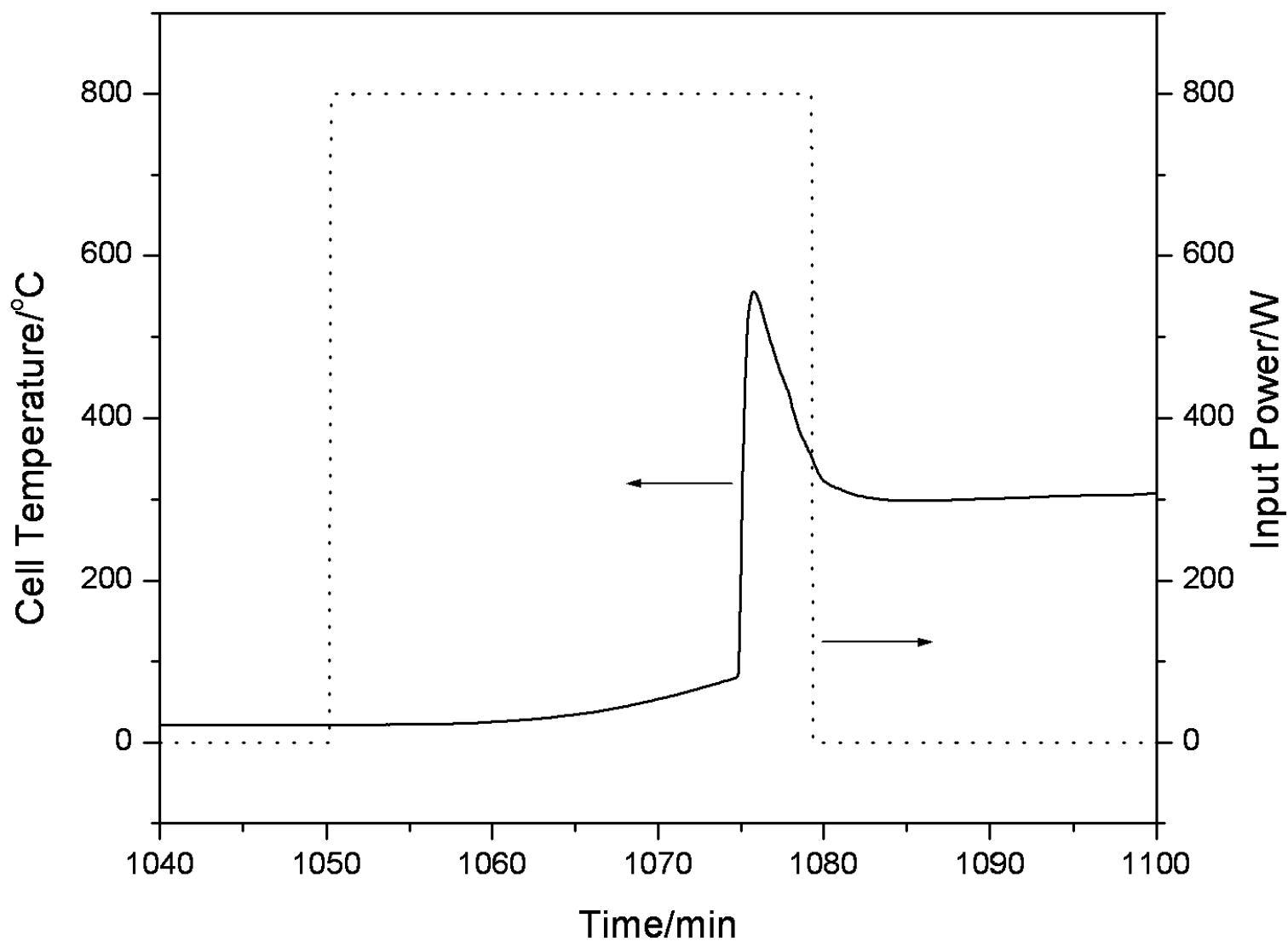
The coolant power with time for the R-Ni control power test with the cell containing the reagents comprising the starting material for R-Ni, 15g Ni/Al alloy powder, and 3.28g of Na. Energy balance was obtained with the calibration-corrected numerical integration of the input and output power curves yielding an output energy of 384 kJ and an input energy of 385 kJ.



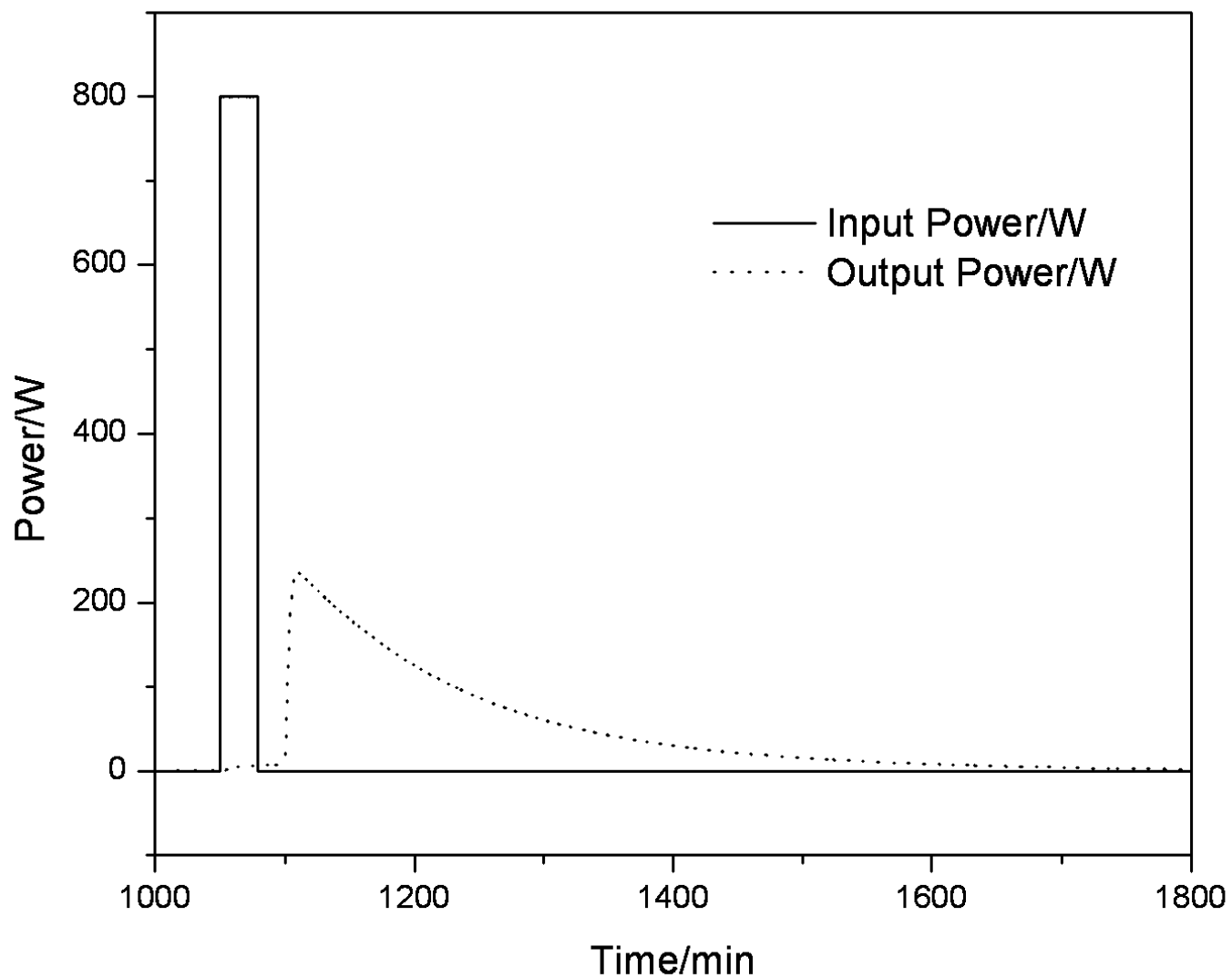
The cell temperature with time for the hydrido reaction with the cell containing the reagents comprising the catalyst material, 15g Na doped R-Ni, and 3.28g of Na. The reaction liberated 36 kJ of energy in less than 90 s to develop a system-response-corrected peak power in excess of 0.5 kW.



The coolant power with time for the hydride reaction with the cell containing the reagents comprising the catalyst material, 15g Na doped R-Ni, and 3.28g of Na. The numerical integration of the input and output power curves with the calibration correction applied yielded an output energy of 185.1 kJ and an input energy of 149.1 kJ. The excess energy was 36 kJ.

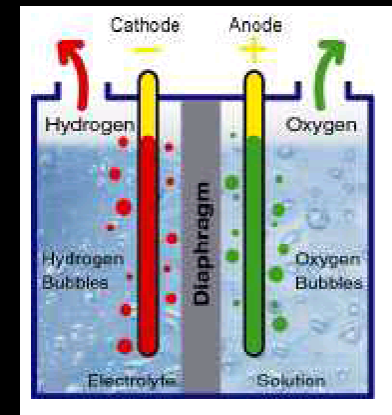
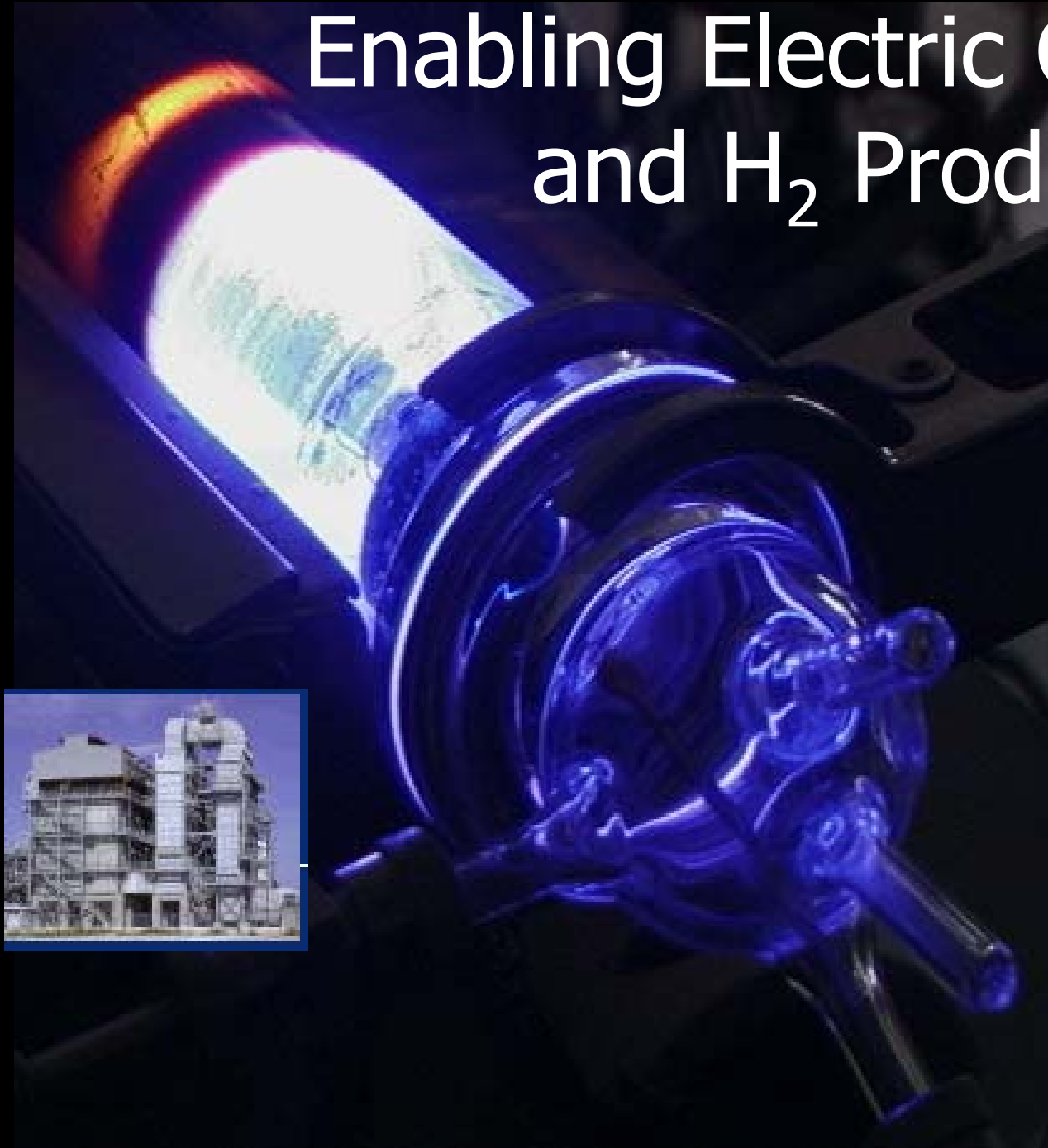


The cell temperature with time for the hydrino reaction with the scale-up cell containing the reagents comprising the catalyst material, 1kg NaOH-doped R-Ni 2400. The cell temperature jumped from 85.6°C to 518°C in 35 s wherein the reaction liberated 753.1 kJ of energy in less time to develop a system-response-corrected peak power in excess of 50 kW.



The coolant power with time for the hydrino reaction with the scale-up cell containing the reagents comprising the catalyst material, 1kg NaOH-doped R-Ni 2400. The numerical integration of the input and output power curves with the calibration correction applied yielded an output energy of 2149.1 kJ and an input energy of 1396 kJ corresponding to an excess energy of 753.1 kJ.

Enabling Electric Generation and H₂ Production



Hydrogen Production as a Replacement Fuel for Gasoline to Power the Internal Combustion Engine

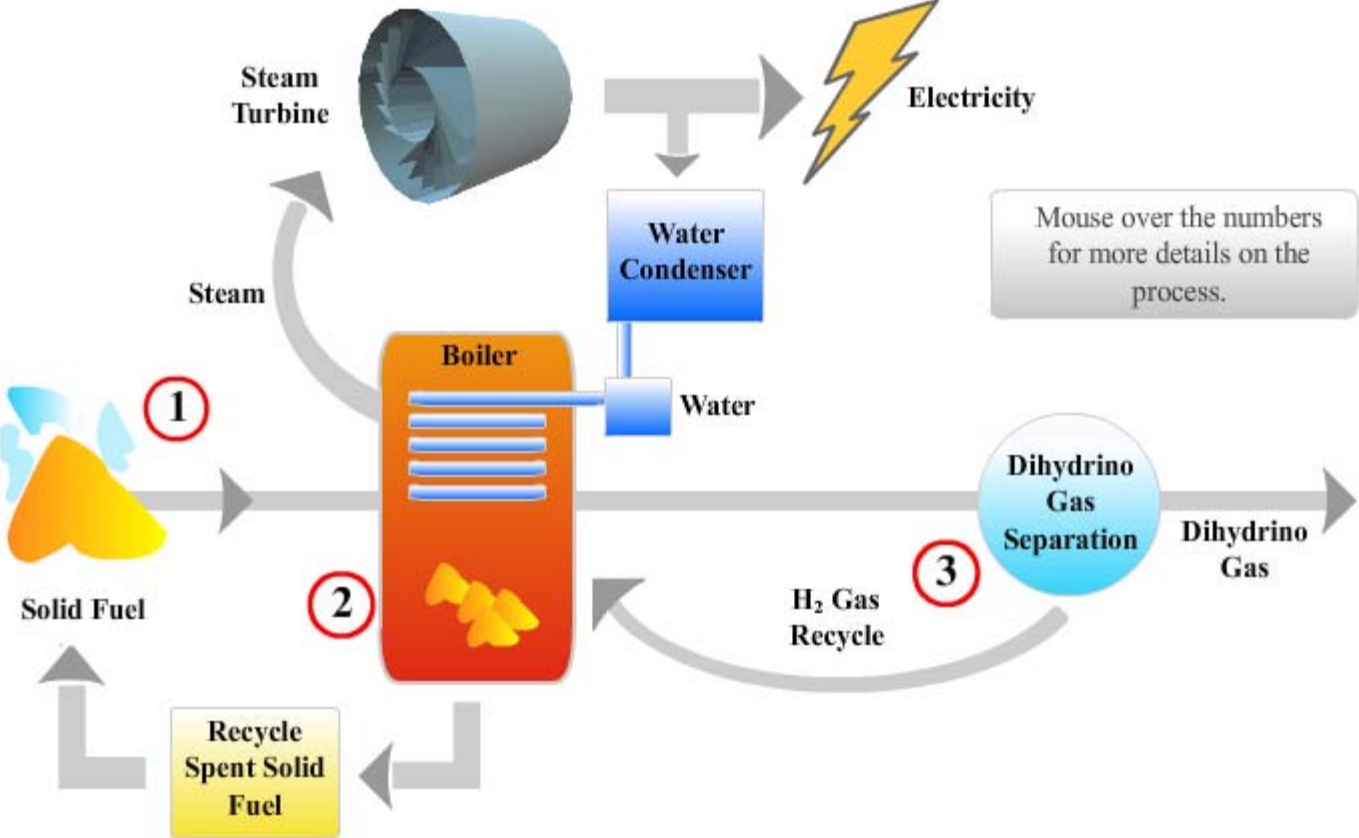


Hydrogenics Corporation's H₂ Gas Station

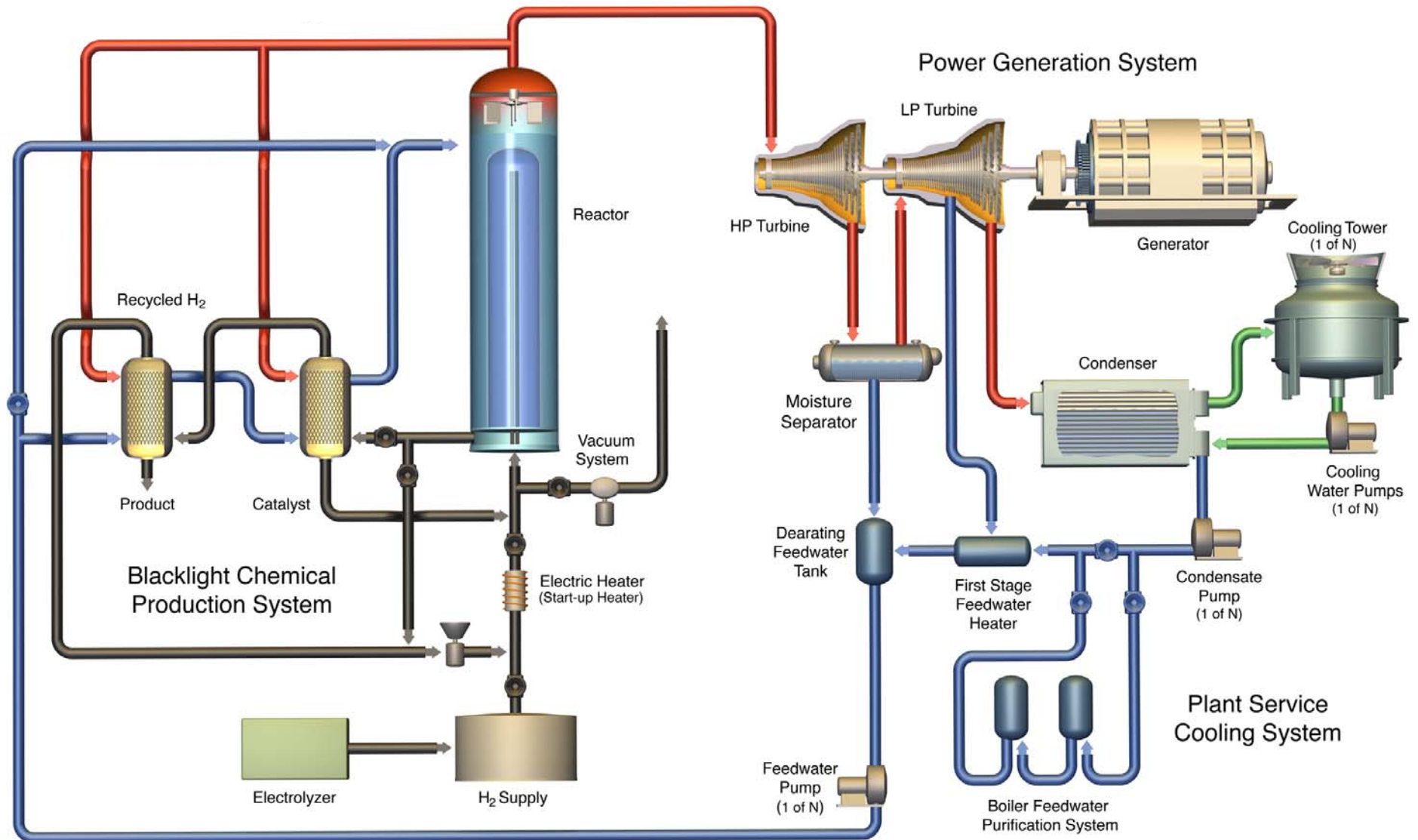
Distributed Generation (1 to 10 MWe)

- Power grid at the substation level
- Produce the fuel equivalent of a gasoline station
- Enable H₂ economy

BlackLight Plant Process



Plant Process Diagram



Unit Costs: BLP vs Competitors

| Technology Type | Average Generating Capacity (kW) | Power Density (W/cm ³) | Fuel Volumetric Energy Density (kWh/gal) | Fuel Mass Energy Density (kWh/kg) | Installed Cost (\$/kW) | Fuel Cost (\$/kWh) |
|------------------------------|----------------------------------|------------------------------------|--|-----------------------------------|------------------------|--------------------|
| BLP Energy Technology | 1000 | 20 | 23,000 | 6,000 | 500 | 0 |
| PEM Fuel Cell | 25 | 1 | 9 | 33 | 3,700** | 0.095 |
| Internal Combustion Engine | 100 | 40 | 33 | 12 | 1,000** | 0.108 |
| Industrial Gas Turbine | 1000 | 1 | 19 | 12 | 700 | 0.108 |
| Natural Gas Microturbine | 100 | 1 | 19 | 12 | 2,000 | 0.120 |
| Photovoltaic | 10 | 0.01* | N/A | N/A | 7,000 | 0 |
| Coal | 500,000 | 0.3 | N/A | 8.3 | 2,700 | 0.045 |
| Nuclear (HTGR) | 680,000 | 2 | N/A | N/A | 4,700 | 0.018 |

Source: Platts, EIA, Stone and Webster *Watts per square centimeter **Current Cost of stationary distributed generation equipment

BMW Hydrogen 7



Detailed Economic Model of Fuel Production from BlackLight Process

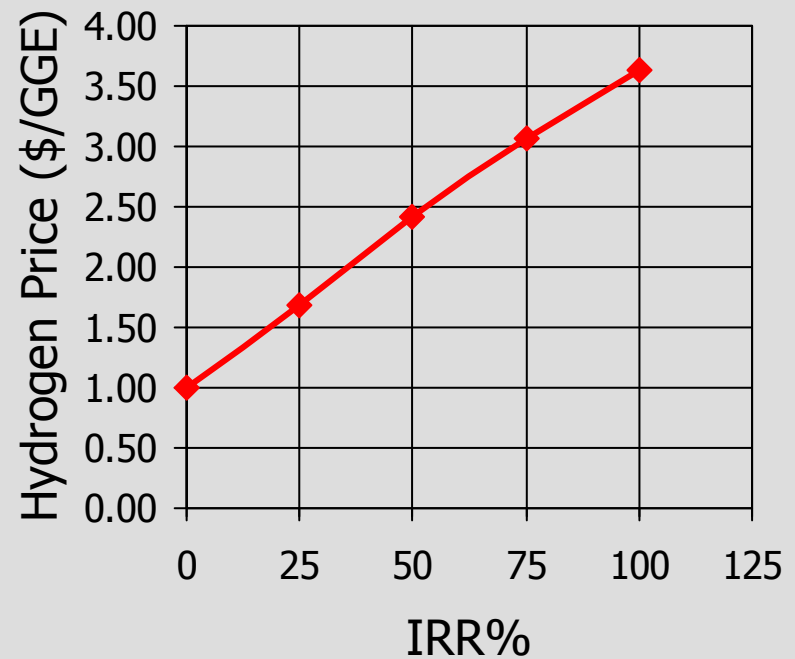
- Modeled Using Comprehensive DOE H2A Template
 - Capital Costs
 - Equipment, facility, installation and start-up expenses, working capital...
 - Annual Operating Costs
 - Feedstock, utilities, operation, maintenance, administration...
 - Technology performance assumptions
 - Process efficiency, documented industry specifications

Fuel Production Could be Highly Profitable

Station Economic Highlights (\$mm)

| | |
|--------------------------|-------|
| Total Capital Investment | \$2.3 |
| Annual O&M Cost | \$0.3 |

After Tax IRR



CONCLUSIONS

- Prediction of new energy source based on lower-energy states of hydrogen
- Confirmation by spectra, compounds, and other observations
- Significant **green** power and chemical applications



*BlackLight
Power*^{TM SM}

Greater than Fire^{TM SM}

493 Old Trenton Road
Cranbury, NJ 08512
Phone: 609-490-1090
Fax: 609-490-1066

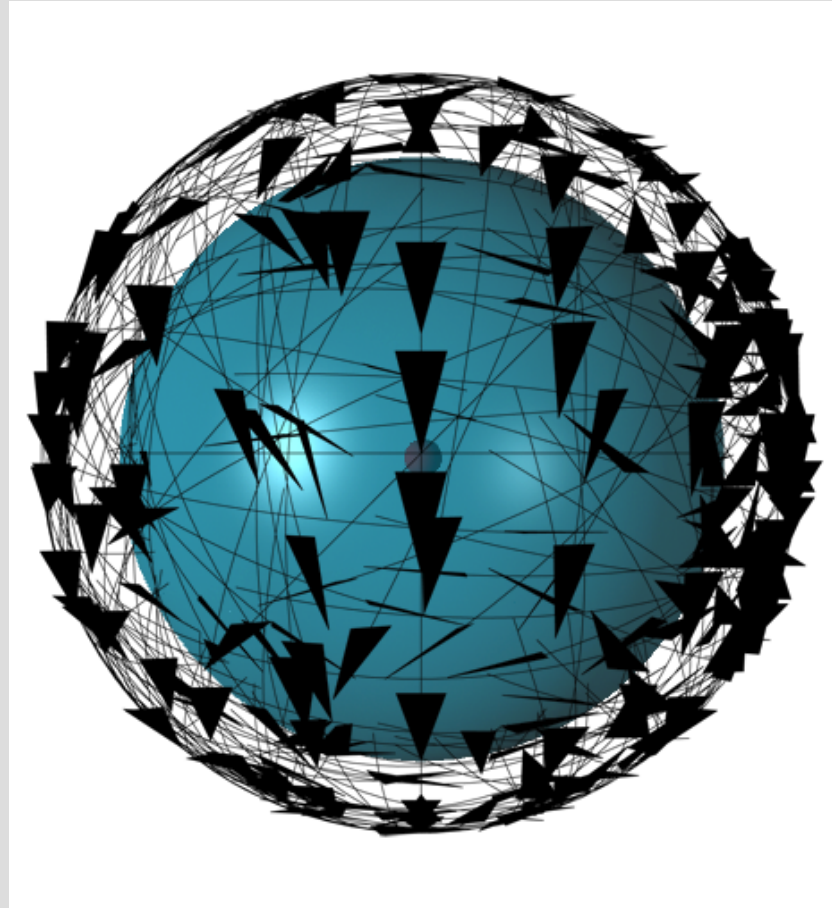
www.blacklightpower.com



BLACKLIGHT
POWER, Inc



Theoretical Modeling



Exact Solutions of Diatomic and Polyatomic Molecules

- Molecules are solved exactly by using the exact atomic-orbital solutions and the prolate spheroidal molecular orbitals as basis functions.
- The prolate spheroidal MO bridges the AOs and is matched to the energy of the AOs of each bond.
- Alternatively, AO electrons form an independent MO and the remaining electrons of the participating shell decrease in radius and energy.

Exact Solutions of Molecules

- For the first time in history, the functional groups, the key building blocks of organic chemistry, were solved from two basic equations.
- The solutions of the basic **300+ functional groups** of organic chemistry were obtained by using generalized forms of a geometrical and an energy equation for the nature of the H-H bond.
- The true physical structure and parameters of an infinite number of organic molecules up to infinite length and complexity can be obtained essentially instantly.
- There is no algorithm. In contrast, NIST presents 788 molecules for which there are over 100,000 attempted solutions, 150 per molecule on average, representing the combined worldwide effort of over half a century. (source: <http://srdata.nist.gov/cccbdb/default.htm>)
- Millsian modeling software instantaneously provides the physical structure and parameters of organic molecules at higher precision and accuracy than any other commercial product.
- Modeling recently extended to include organometallics, semiconductors, all allotropes of carbon, metals, proteins, RNA and DNA.

Partial List of Organic Functional Groups Solved by Classical Physics.

- Continuous-chain alkanes
 - Branched alkanes
 - Alkenes
 - Branched alkenes
 - Alkynes
 - Alkyl fluorides
 - Alkyl chlorides
 - Alkyl bromides
 - Alkyl iodides
 - Alkenyl halides
 - Aryl halides
 - Alcohols
 - Ethers
 - Primary amines
 - Secondary amines
 - Tertiary amines
 - Aldehydes
 - Ketones
 - Carboxylic acids
 - Carboxylic acid esters
 - Amides
 - N-alkyl amides
 - N,N-dialkyl amides
 - Urea
 - Carboxylic acid halides
 - Carboxylic acid anhydrides
 - Nitriles
 - Thiols
 - Sulfides
 - Disulfides
 - Sulfoxides
 - Sulfones
 - Sulfites
 - Sulfates
 - Nitroalkanes
 - Alkyl nitrates
 - Alkyl nitrites
 - Conjugated alkenes
 - Conjugated polyenes
 - Aromatics
 - Naphthalene
 - Toluene
 - Chlorobenzene
 - Phenol
 - Aniline
 - Aryl nitro compounds
 - Benzoic acid compounds
 - Anisole
 - Pyrrole
 - Furan
 - Thiophene
 - Imidazole
 - Pyridine
 - Pyrimidine
 - Pyrazine
 - Quinoline
 - Isoquinoline
 - Indole
 - Adenine
 - Fullerene (C₆₀)
 - Graphite
 - Phosphines
 - Phosphine oxides
 - Phosphites
 - Phosphates
-

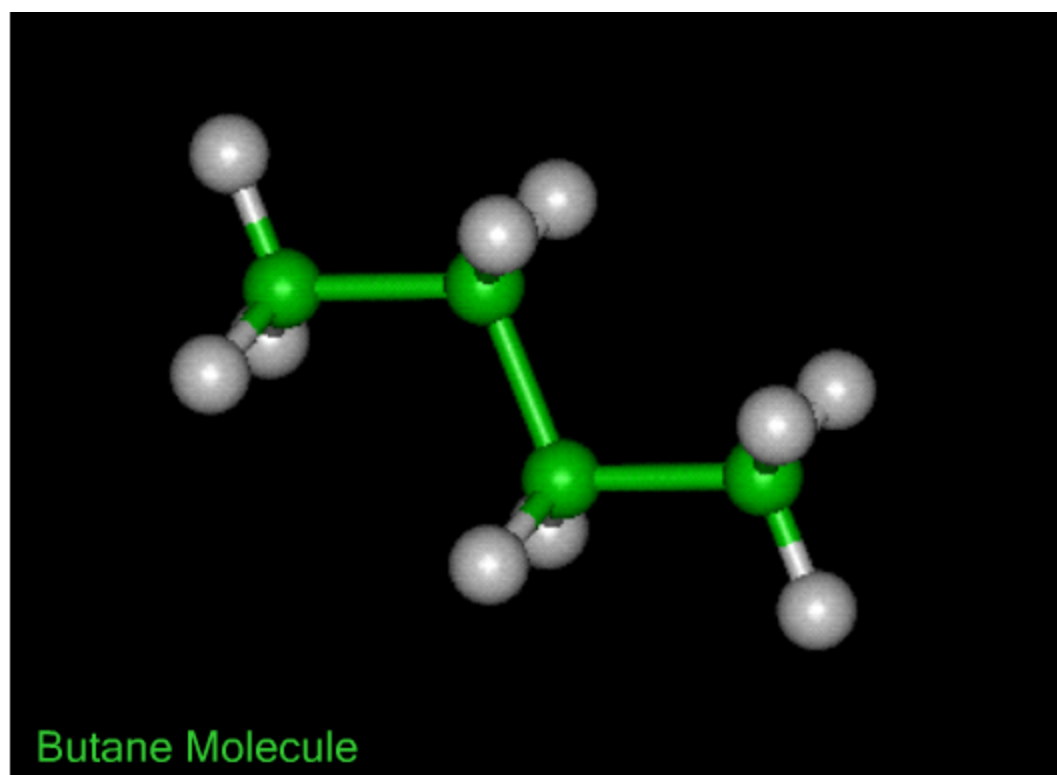
Partial List of Additional Molecules and Compositions of Matter Solved by Classical Physics.

- Solid Molecular Bond of the Three Allotropes of Carbon
 - Diamond
 - Graphite
 - Fullerene (C₆₀)
 - Solid Ionic Bond
 - Alkali-Hydride Crystal Structures
 - Lithium Hydride
 - Sodium Hydride
 - Potassium Hydride
 - Rubidium & Cesium Hydride
 - Potassium Hydroxide
 - Solid Metallic Bond of Alkali Metals
 - Alkali Metal Crystal Structures
 - Lithium Metal
 - Sodium Metal
 - Potassium Metal
 - Rubidium & Cesium Metals
 - Alkyl Aluminum Hydrides
 - Silicon Groups and Molecules
 - Silanes
 - Alkyl Silanes and Disilanes
 - Solid Semiconductor Bond of Silicon
 - Insulator-Type Semiconductor Bond
 - Conductor-Type Semiconductor Bond
 - Boron Molecules
 - Boranes
 - Bridging Bonds of Boranes
 - Alkoxy Boranes
 - Alkyl Boranes
 - Alkyl Borinic Acids
 - Tertiary Aminoboranes
 - Quaternary Aminoboranes
 - Borane Amines
 - Halido Boranes
 - Organometallic Molecular Functional Groups and Molecules
 - Alkyl Aluminum Hydrides
 - Bridging Bonds of Organoaluminum Hydrides
 - Organogermanium and Digermanium
 - Organolead
 - Organoarsenic
 - Organoantimony
 - Organobismuth
 - Organic Ions
 - 1° Amino
 - 2° Amino
 - Carboxylate
 - Phosphate
 - Nitrate
 - Sulfate
 - Silicate
 - Proteins
 - Amino Acids
 - Peptide Bonds
 - DNA
 - Bases
 - 2-deoxyribose
 - Phosphate Backbone
-

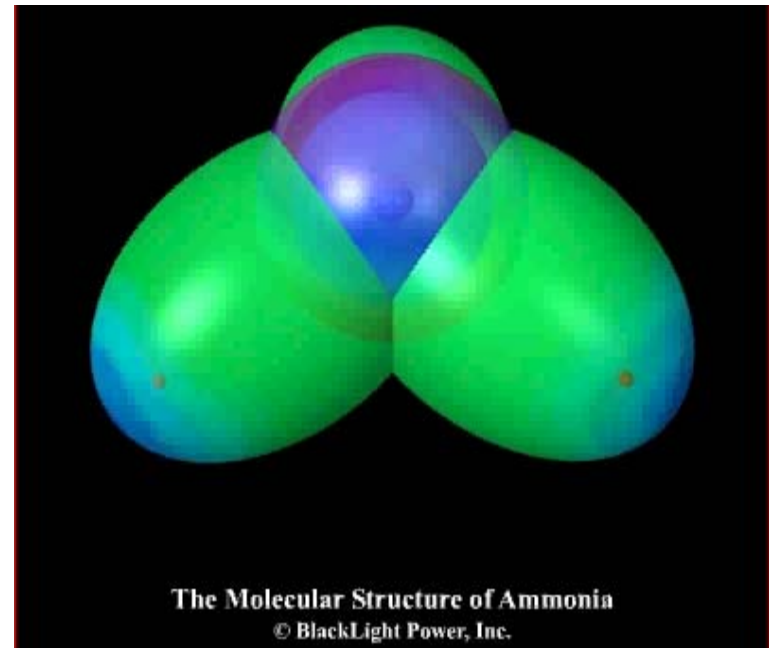
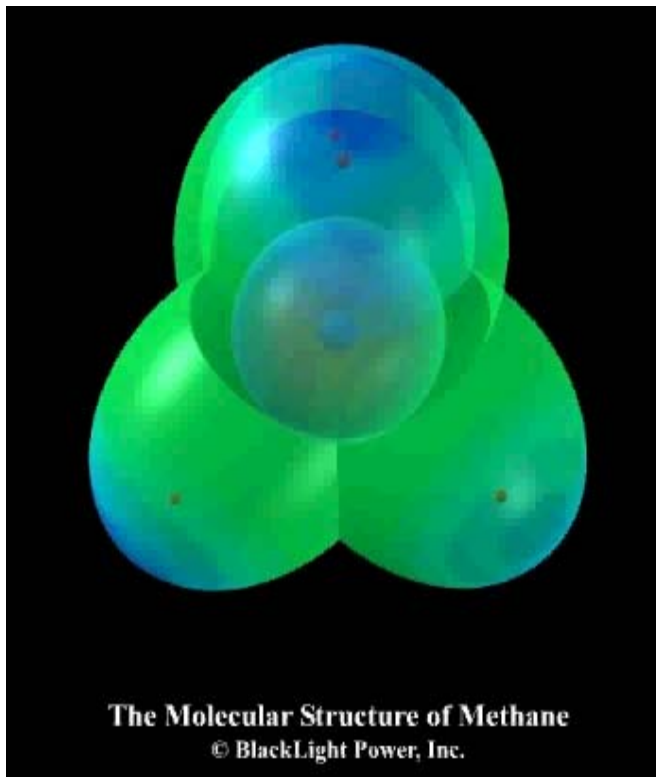
THEORY PRODUCT: Molecular Modeling Software

- General: opportunity to improve processes, discover new molecules, new synthetic pathways, new materials, and find new properties and applications for known molecules
- For Pharma: exact solutions can facilitate drug design, identify active structures, predict optimal synthetic pathways, products, and yields

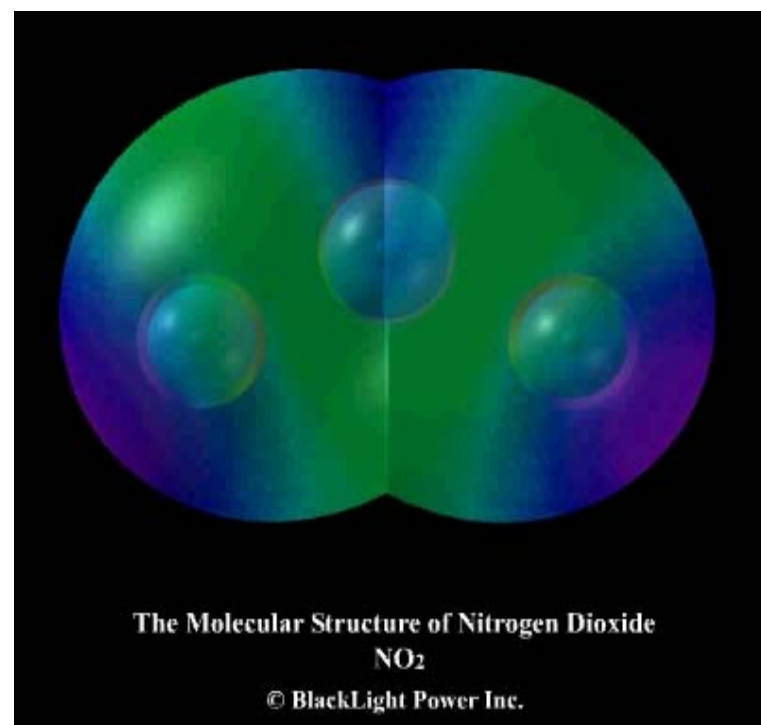
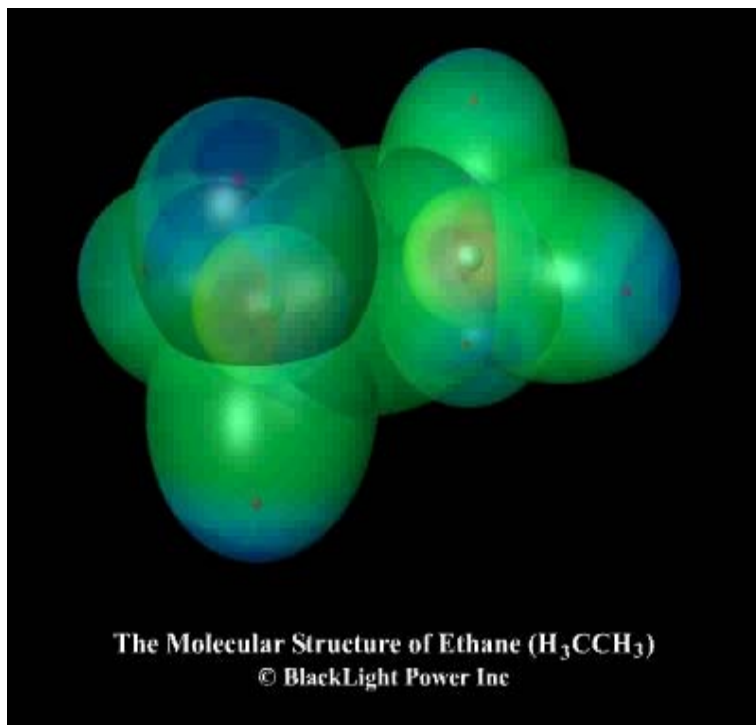
Molecular Structure



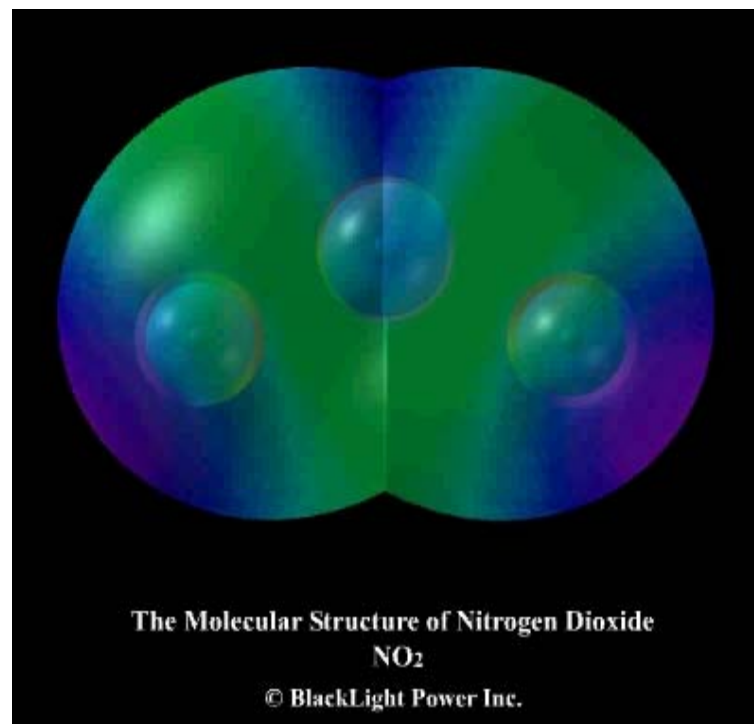
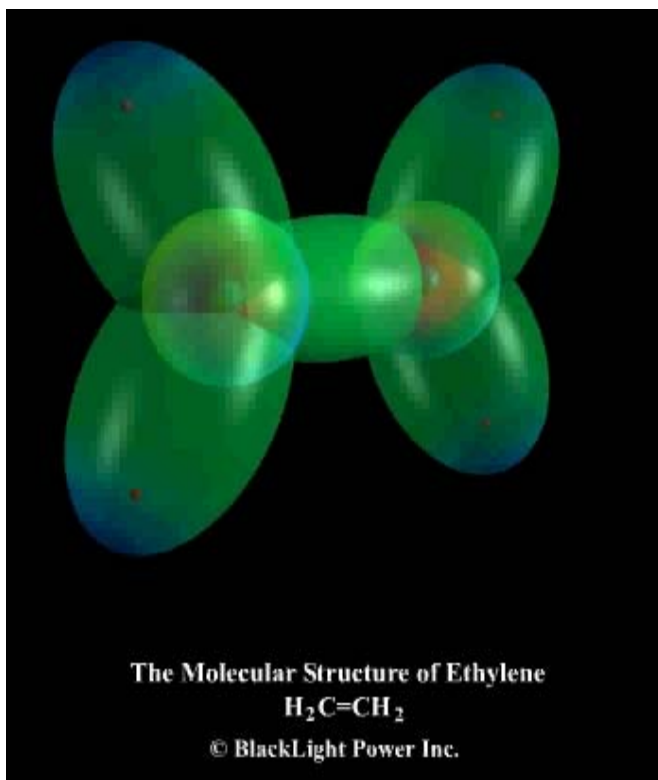
Methane and Ammonia Solutions



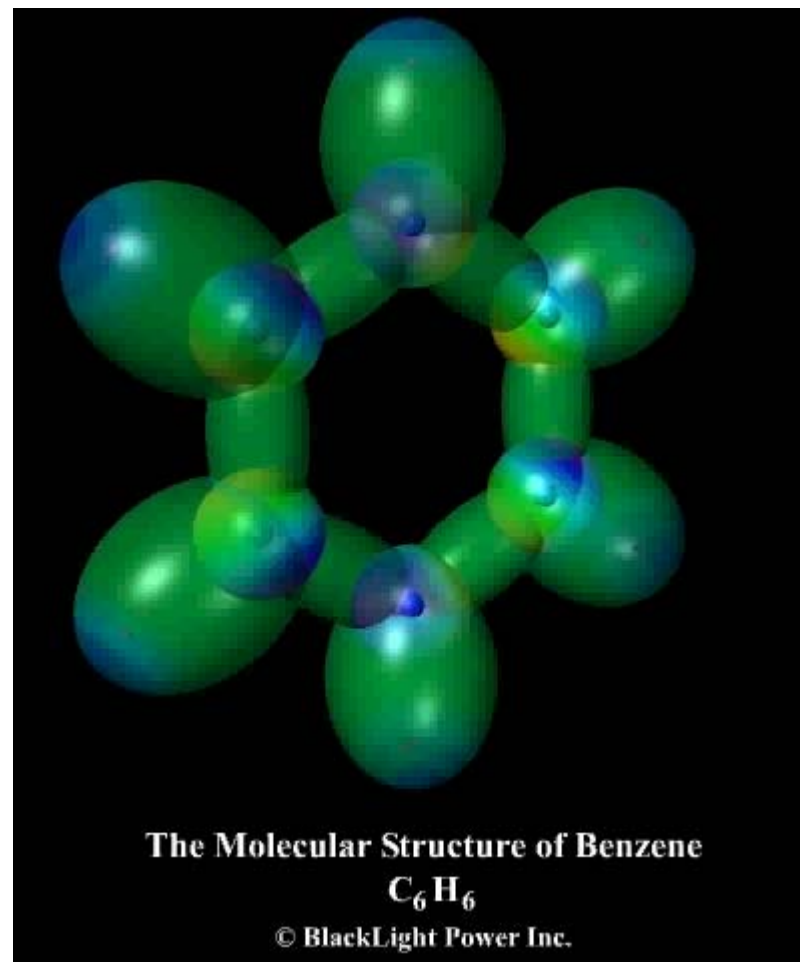
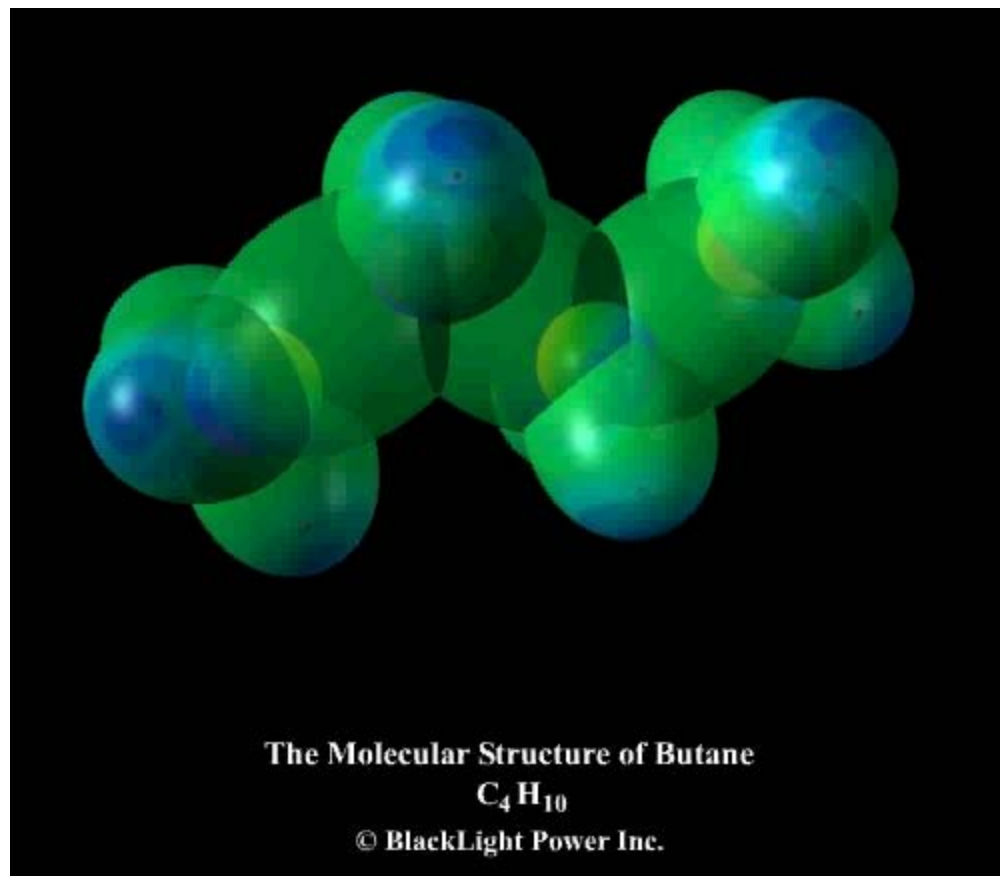
Ethane and Nitrogen Dioxide



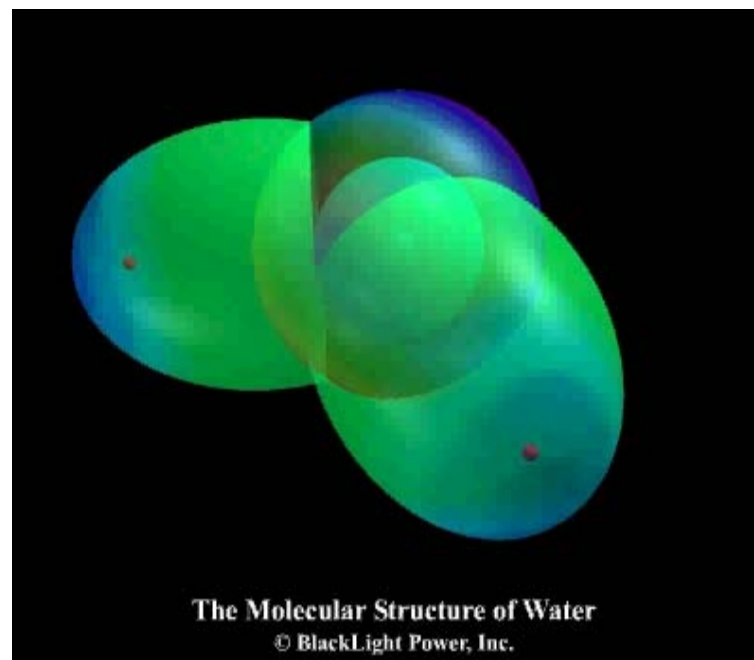
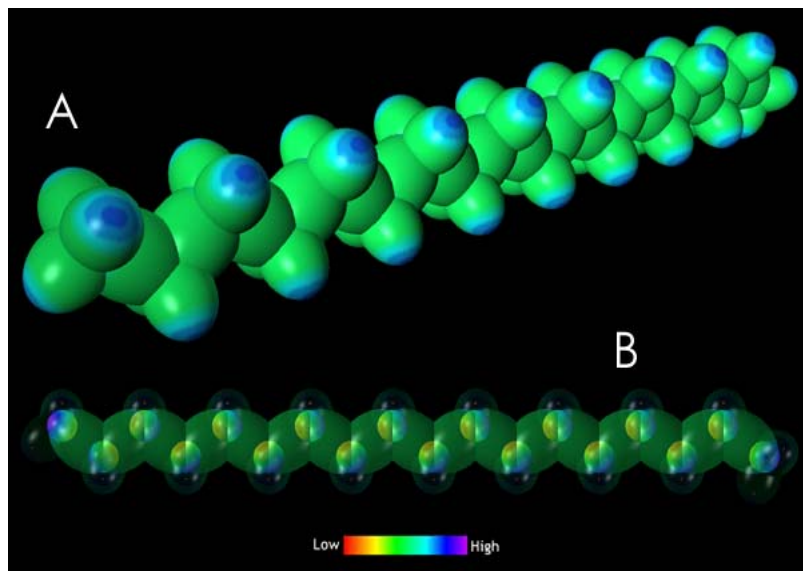
Ethylene and Nitrogen Dioxide Solutions



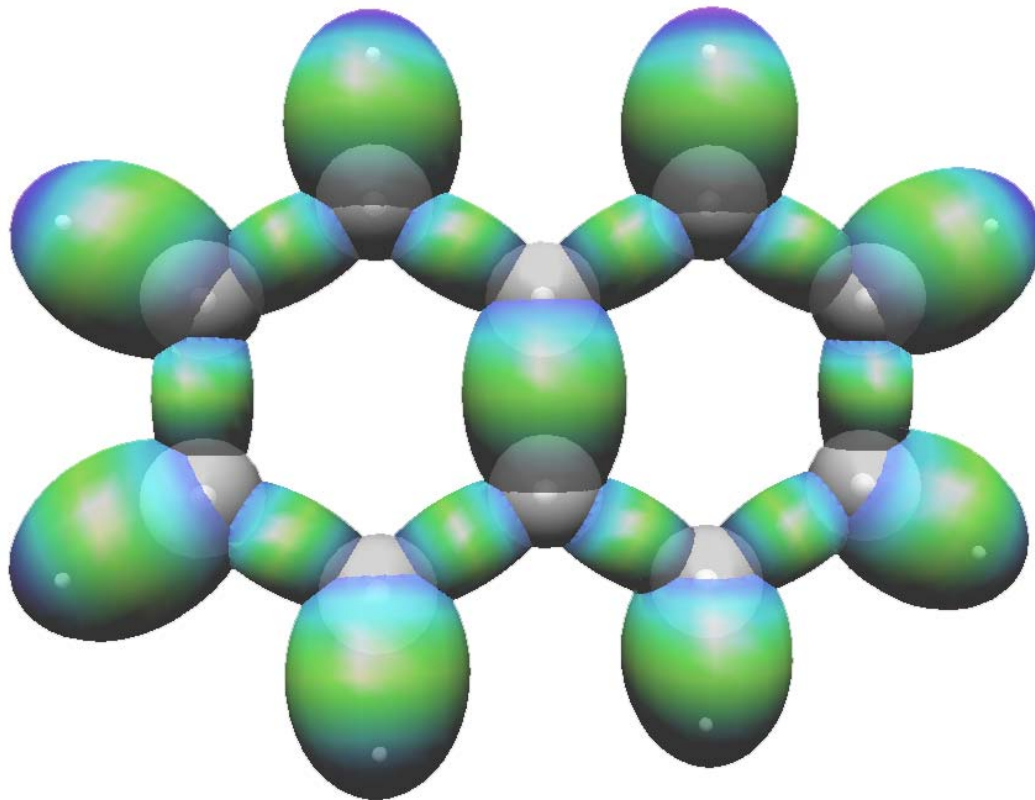
Butane and Benzene Solutions



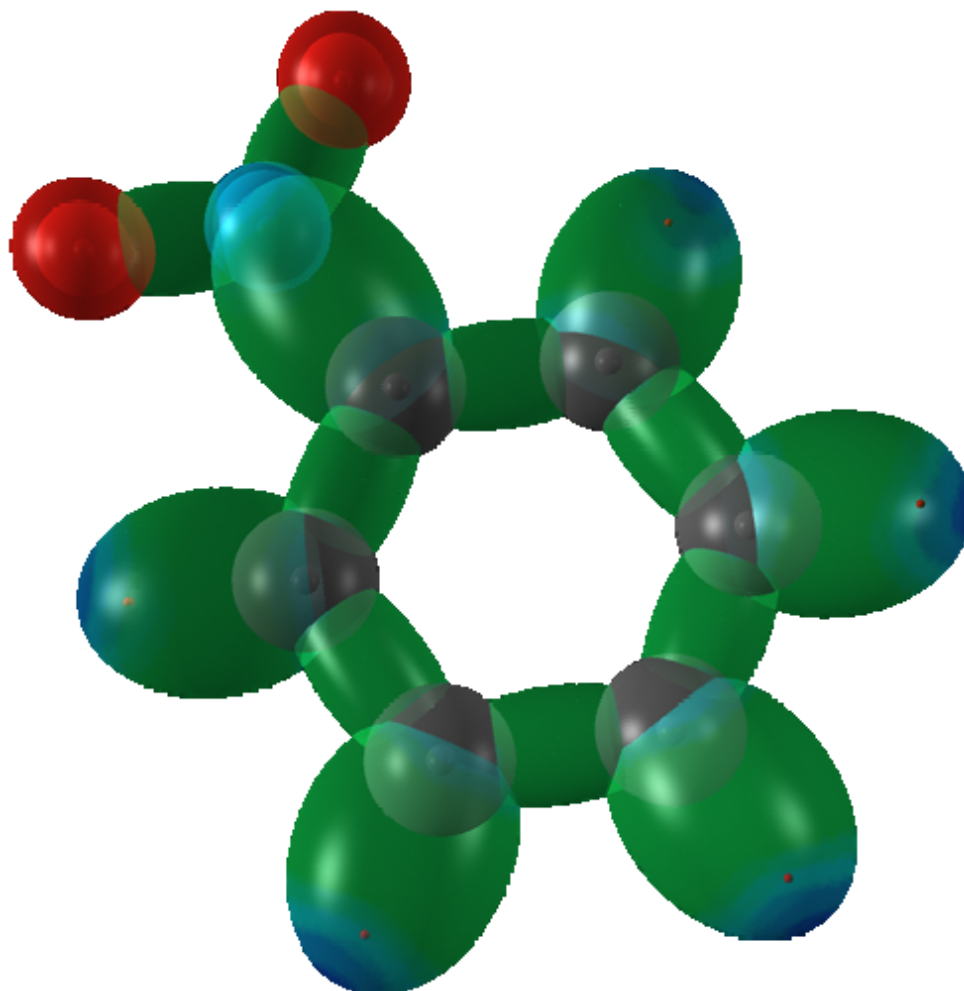
Infinite Length Hydrocarbons and Water Solutions



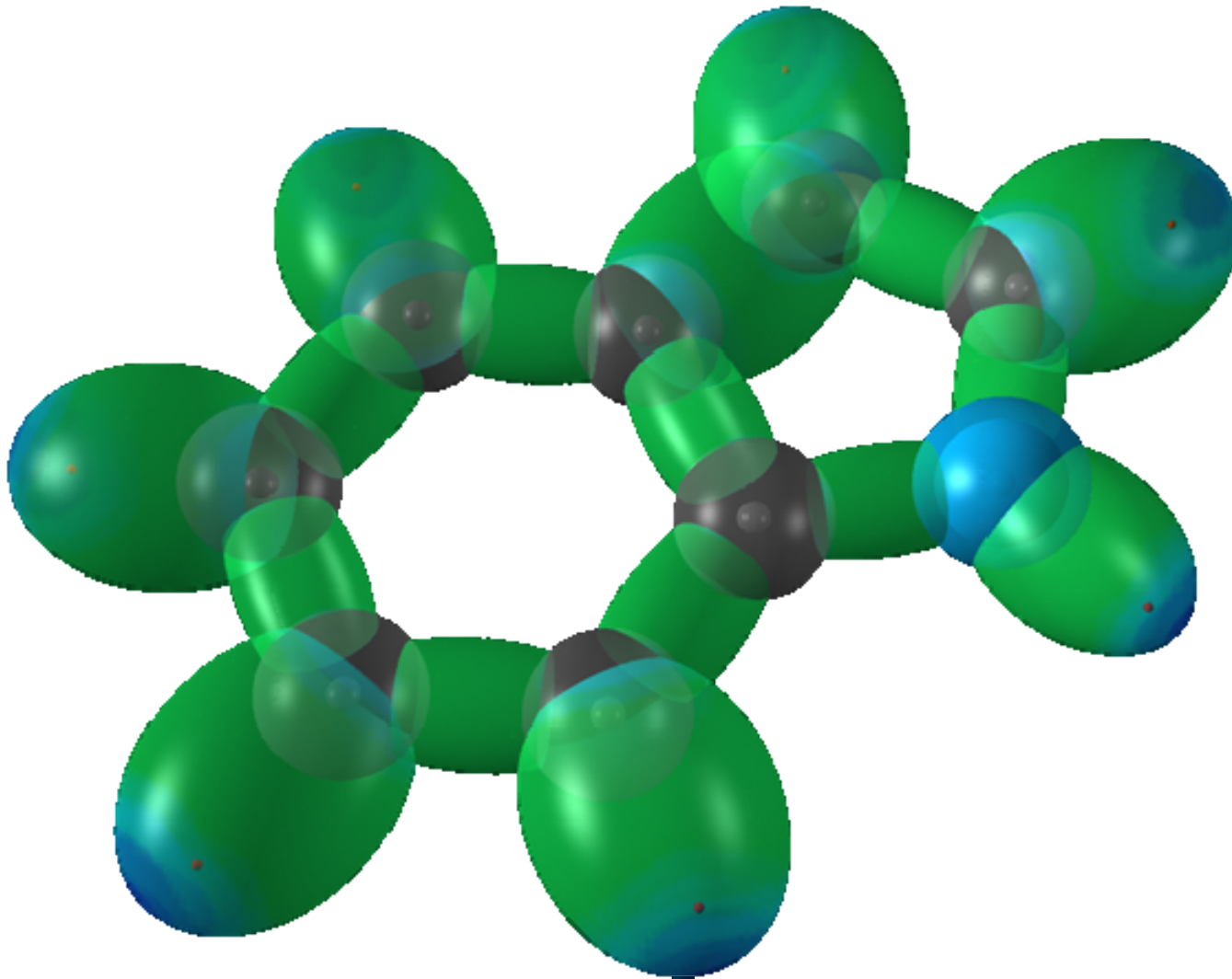
Naphthalene



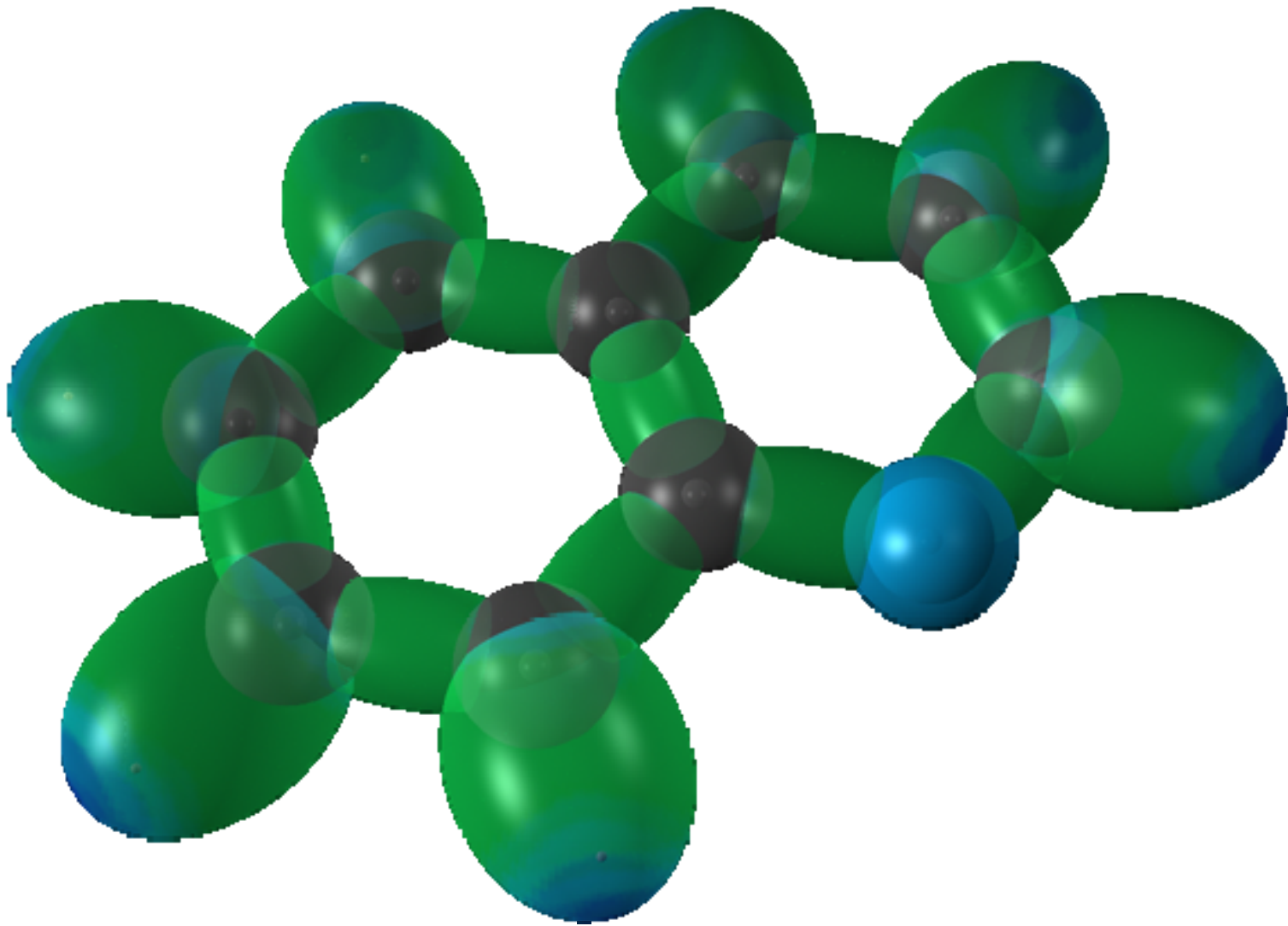
Nitrobenzene



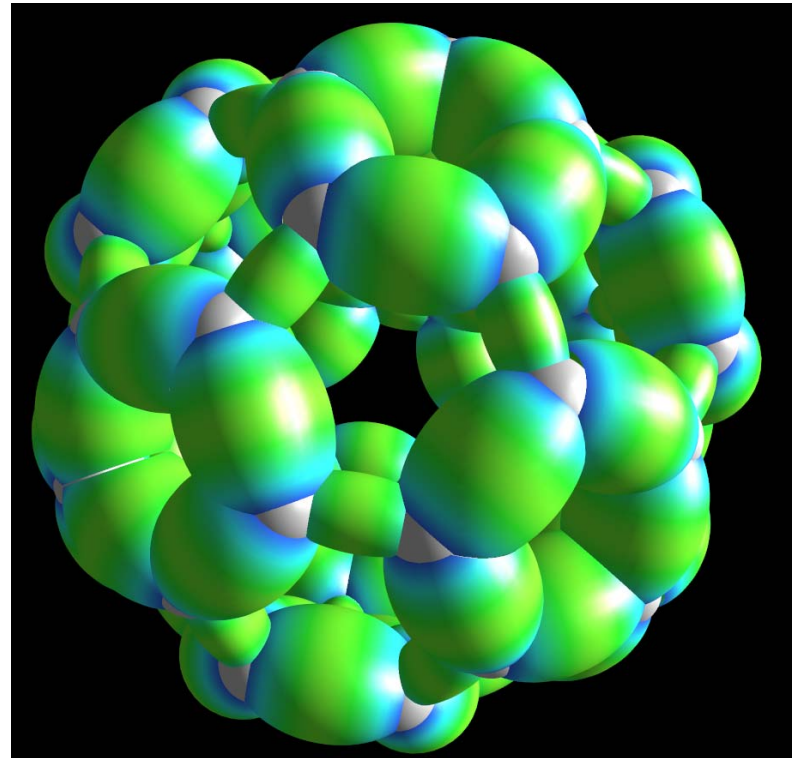
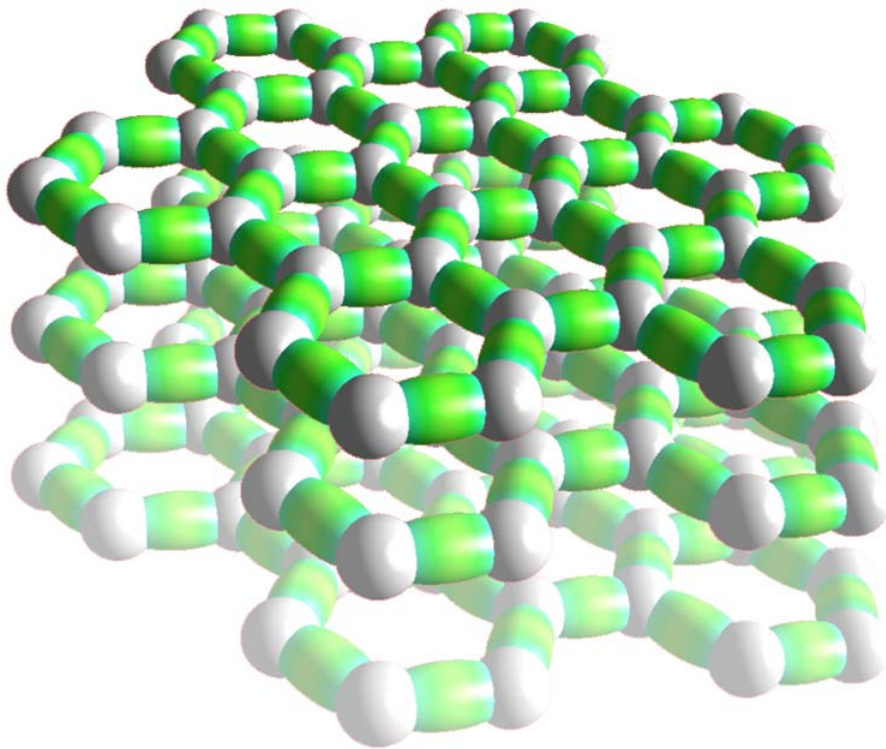
Indole



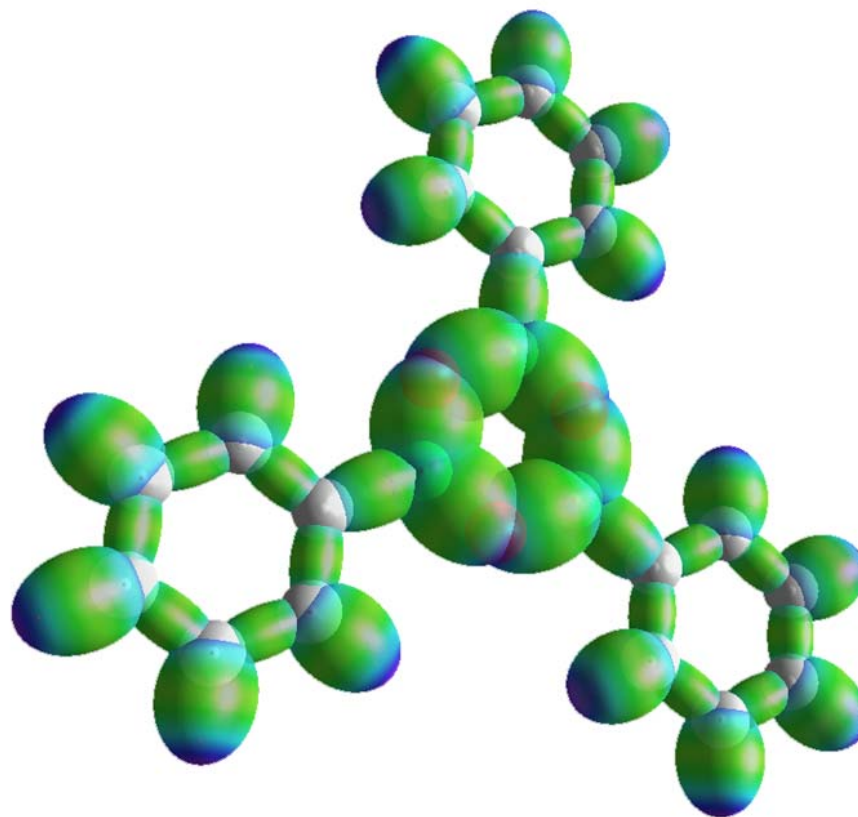
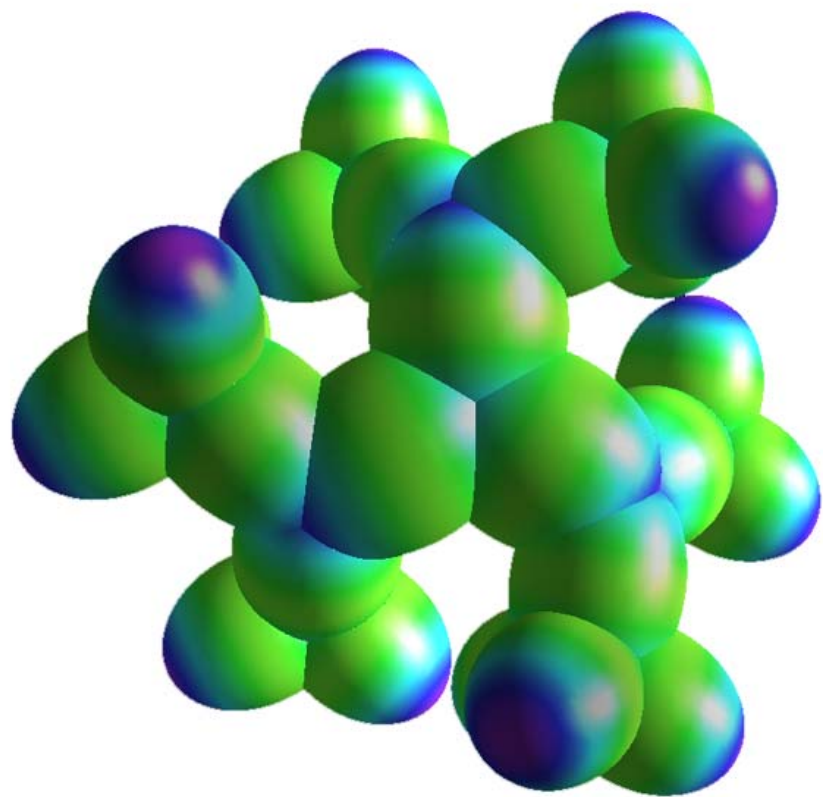
Quinolene



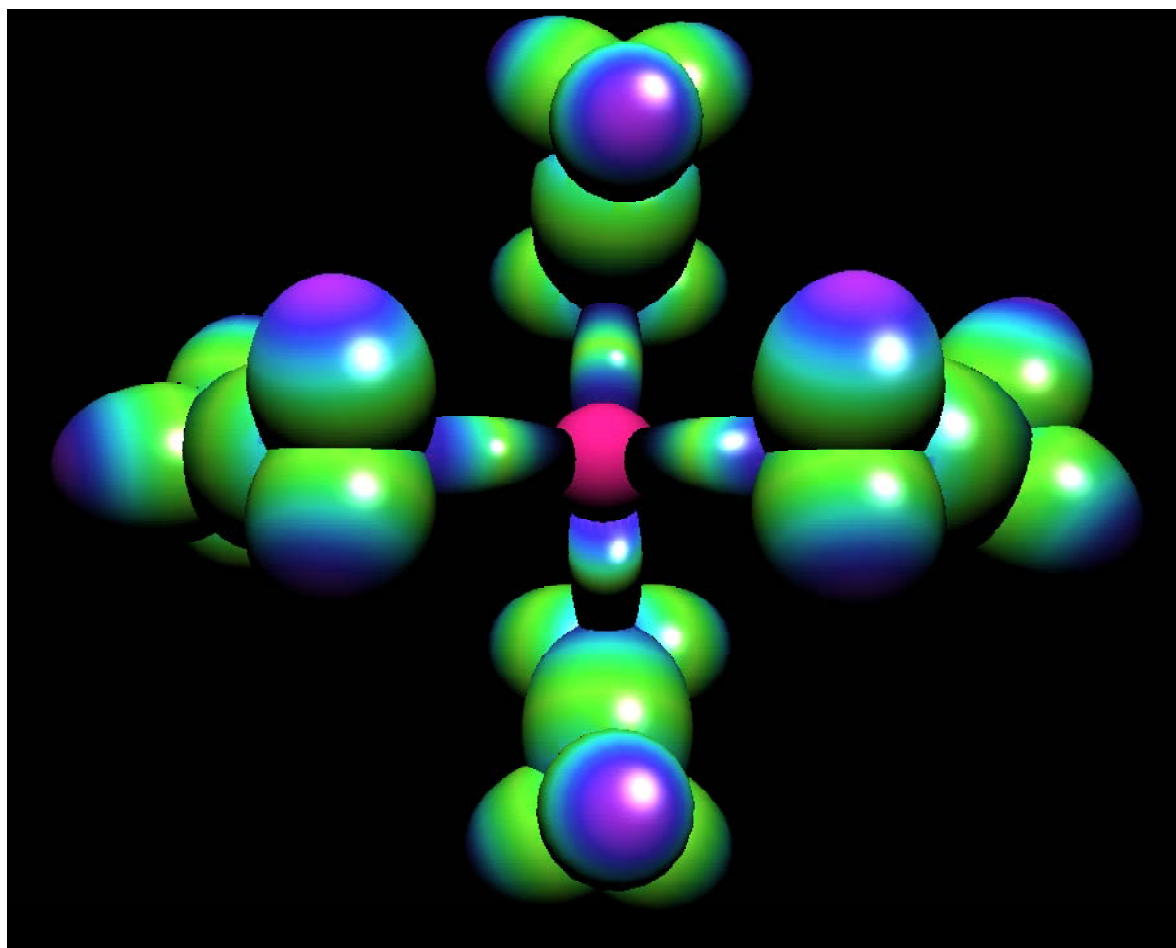
Allotropes of Carbon



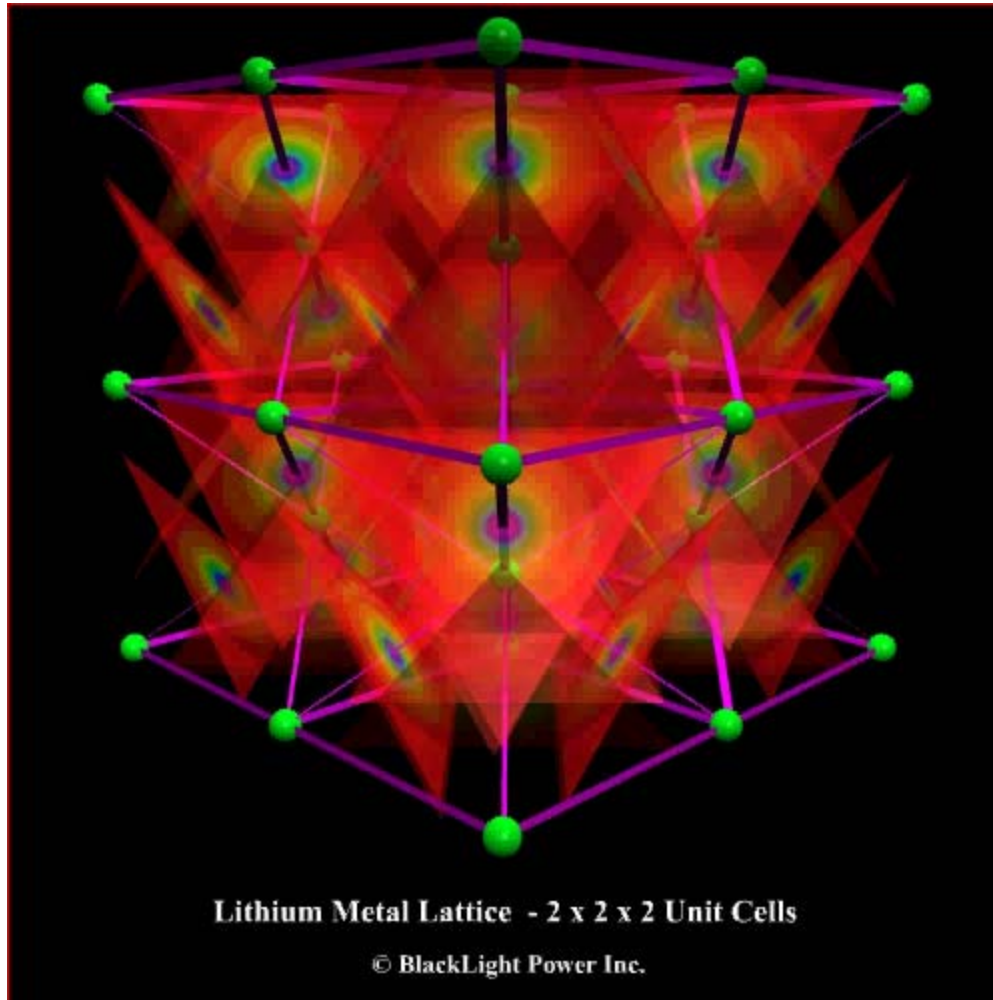
Boron: Boranes and Borinic Acids



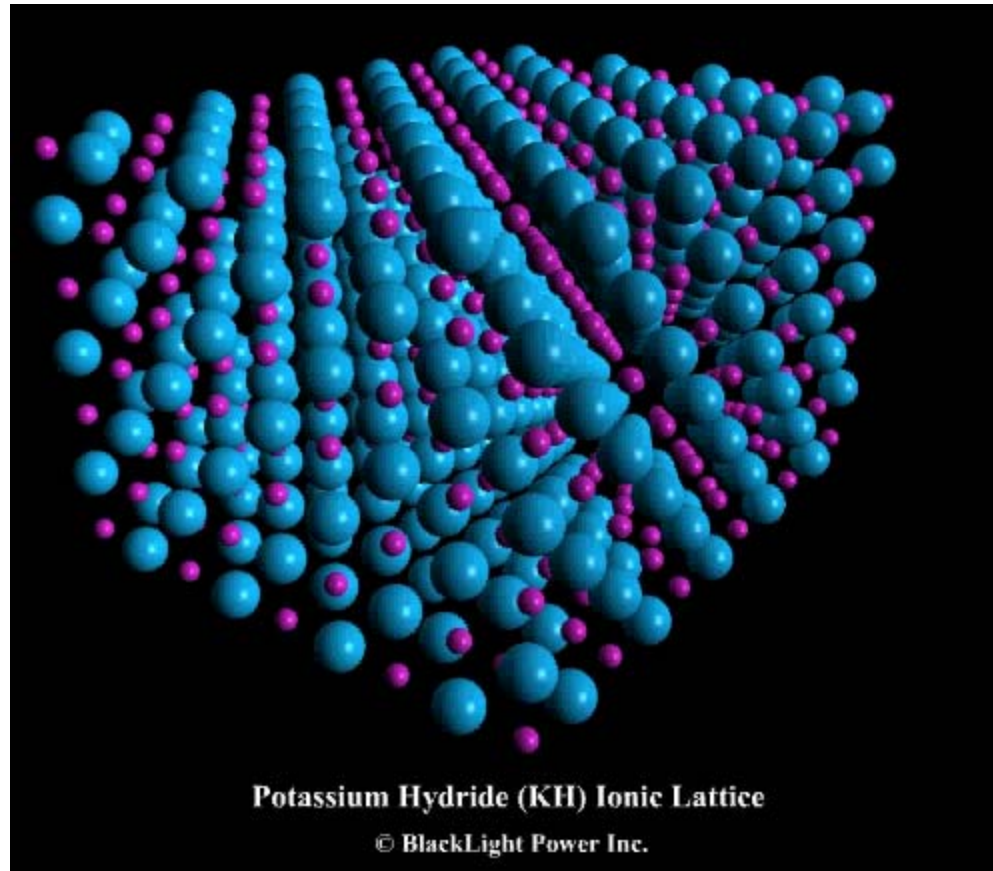
Organometallics: Tetraethyl-lead



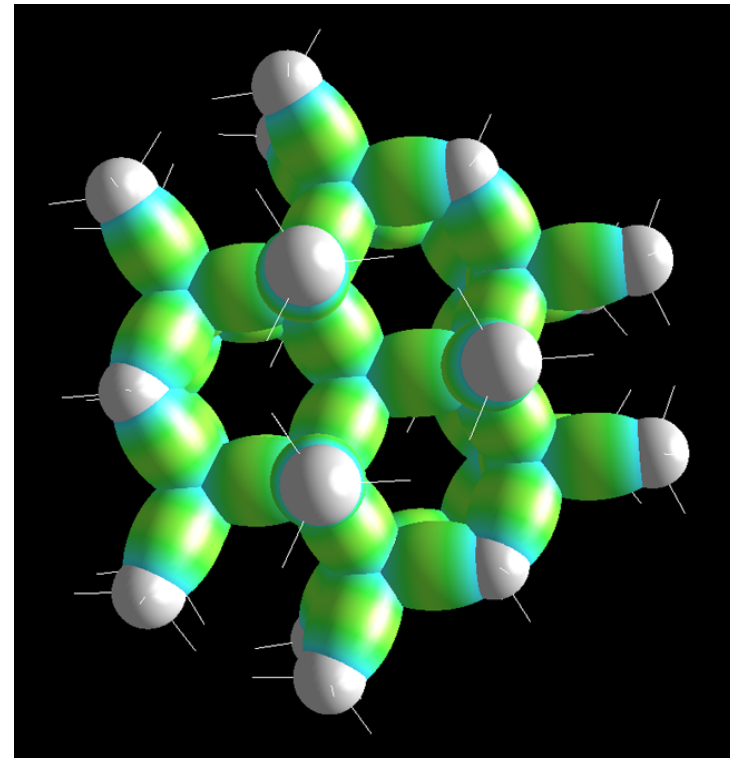
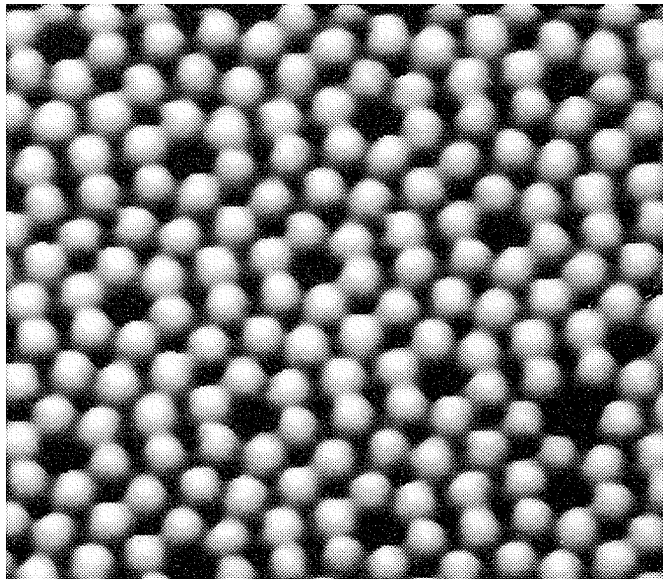
Metals



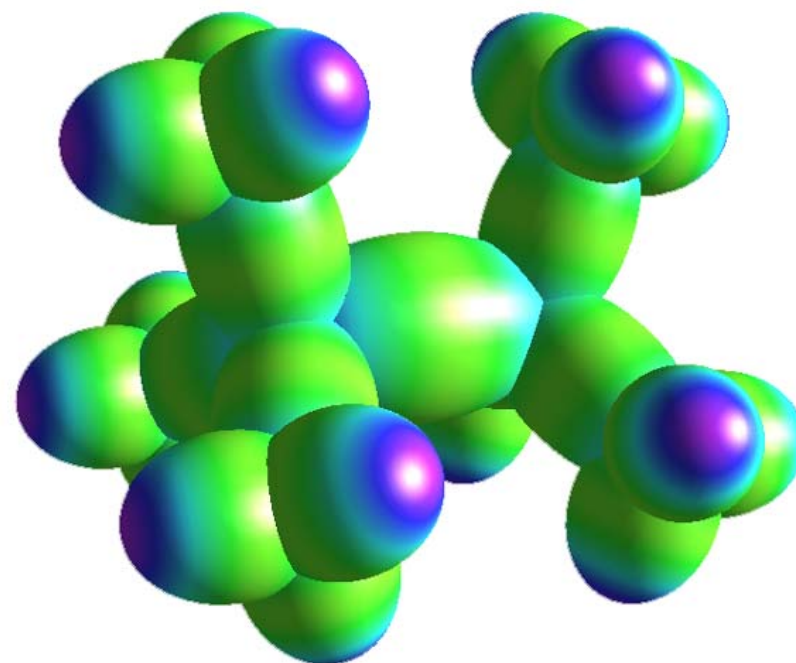
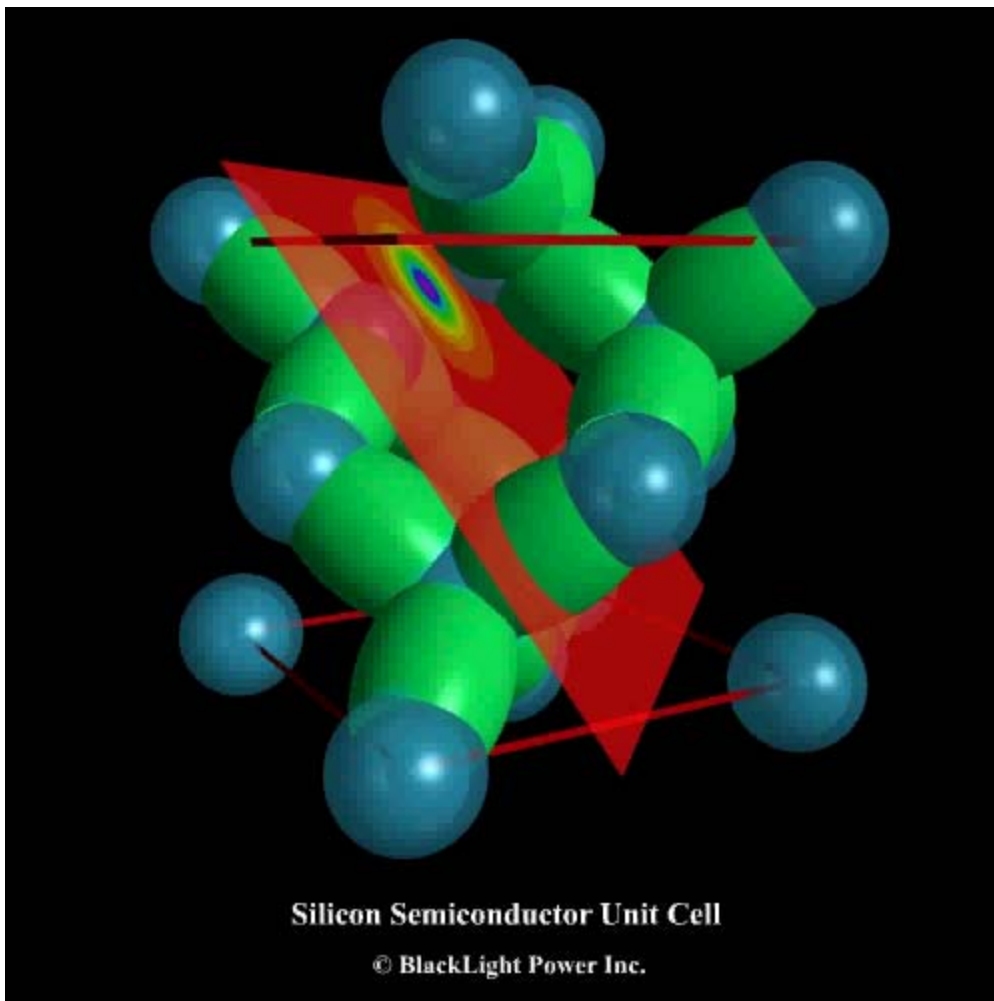
Metal Hydrides



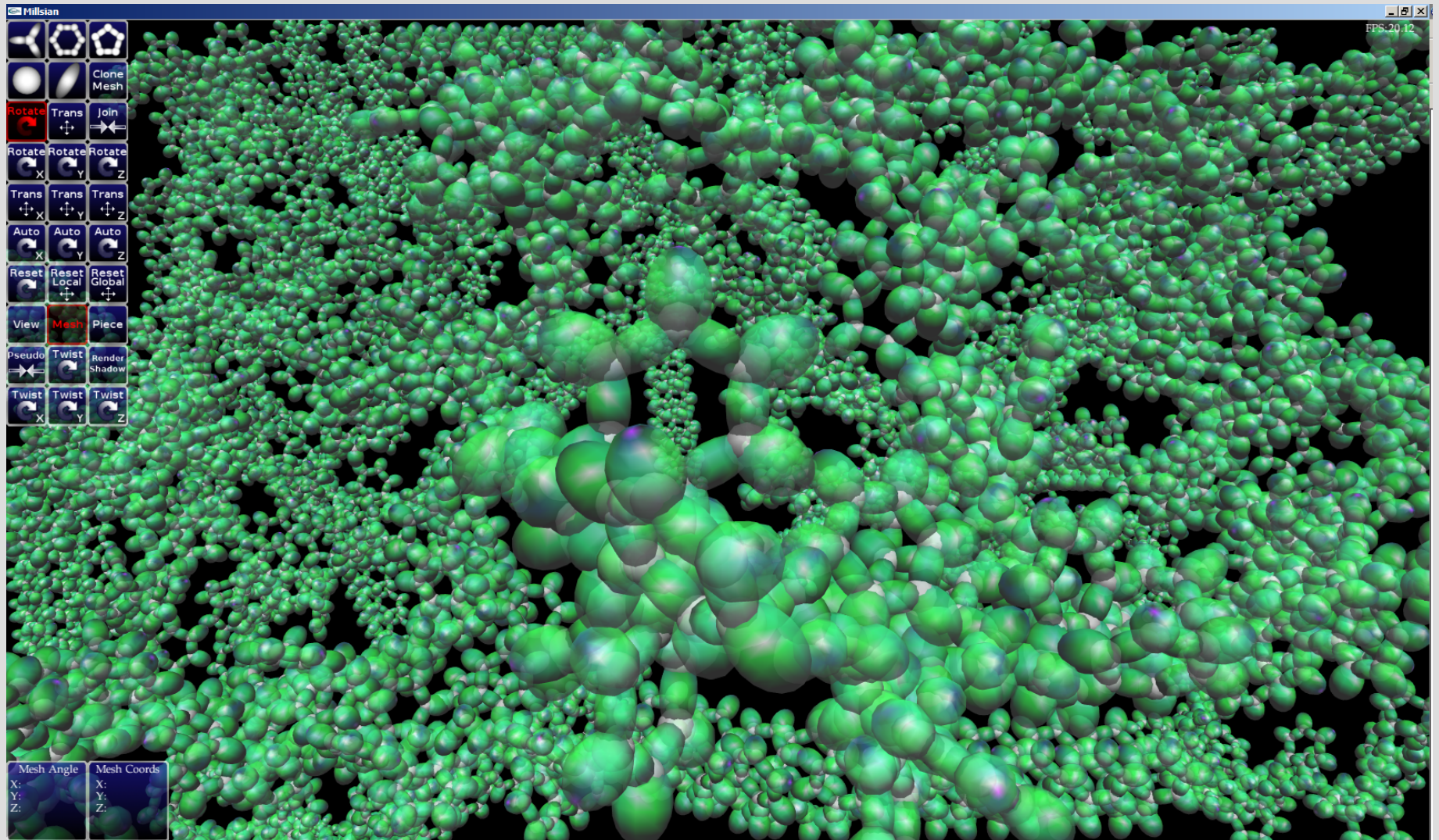
Silicon Structure and Model



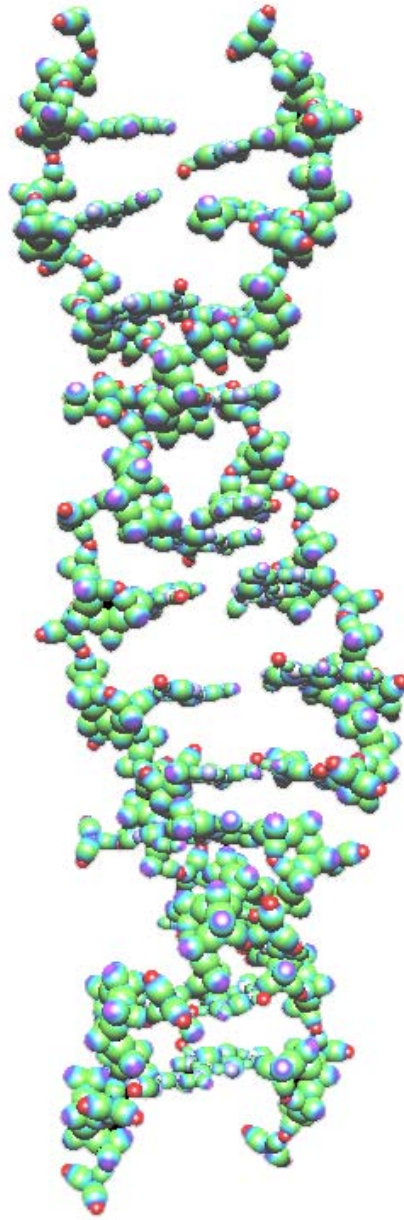
Semiconductor and Alkyl silanes



Polystyrene



DNA

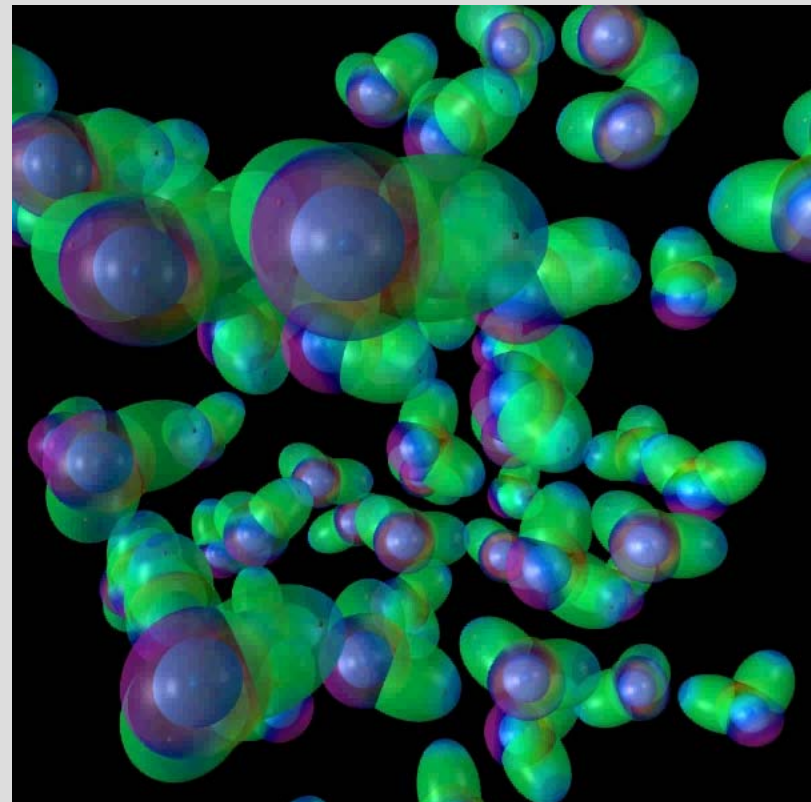


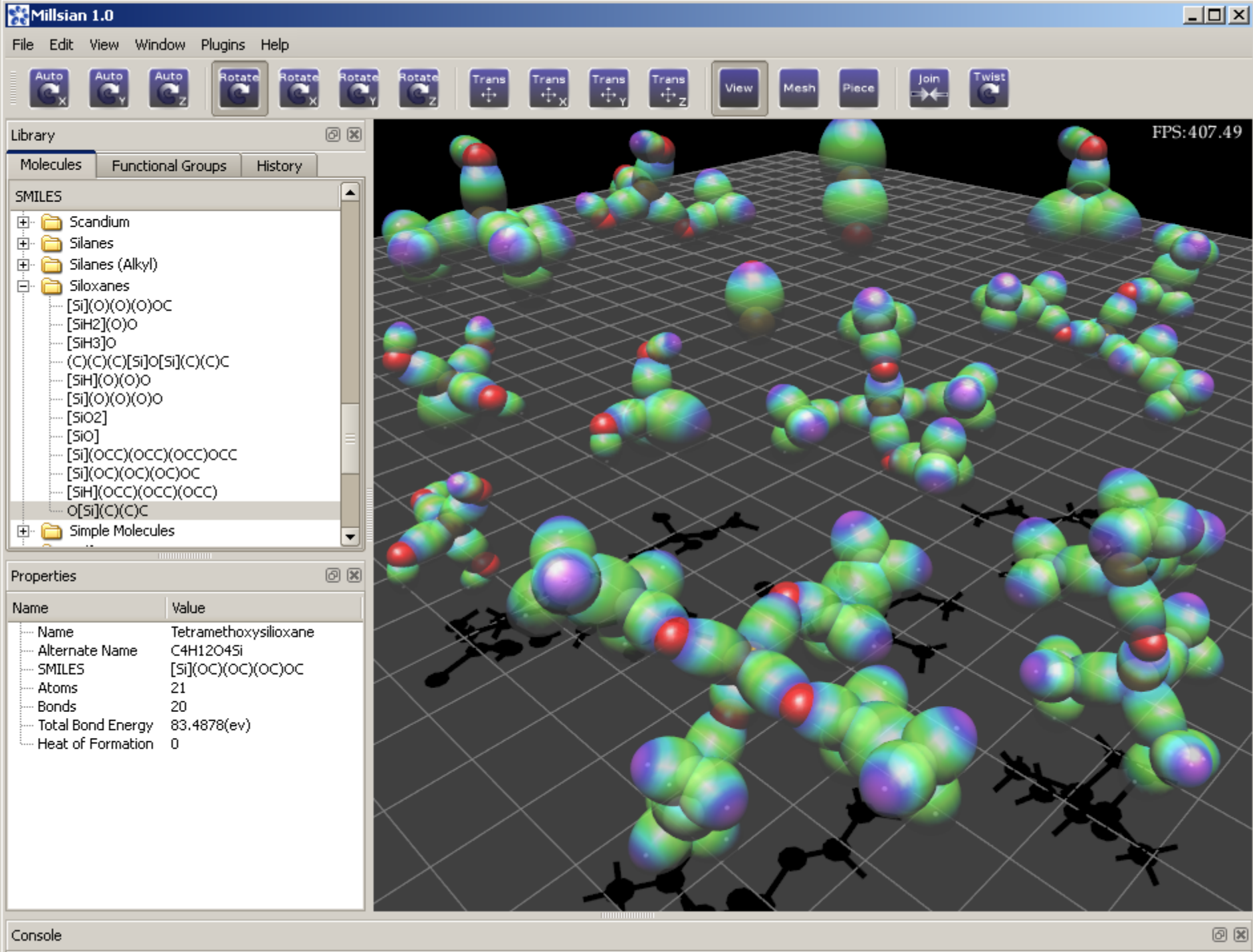
Outputs and Potential Applications

- **Geometric parameters and structure** (bond distances, bond angles, molecular orbital axes, radius of each atomic orbital)
 - Measuring sticks for arbitrary points on molecule
 - Cross sections for collisions with other particles and reactivity
 - Shadow feature that allows molecules to be superimposed and compared for differences and similarities to find regions of biological activity
- **Charge densities of all atomic and molecular orbitals**
 - Predict reactivity
 - Calculate dipoles and higher multipole moments
 - Parameters to calculate fields, interactions, and physical properties
 - Parameters to solve field interaction for lowest energy conformation, dynamics, refractive index, melting and boiling points
- **Component energies of all atomic and molecular orbitals** (potential energy, kinetic energy, nuclear repulsive energy, magnetic potential energy)
 - Predict reactivity
 - Parameters for Lagrangian to solve for vibrational and rotational levels and IR spectrum
 - Other spectroscopic quantities
 - Calculate thermodynamic parameters of entropy and heat capacity
 - Use enthalpies to calculate kinetics and equilibrium constants
- **Other General Applications to Outputs**
 - Calculate the topography of a drug site based on drug structure-activity profile
 - Point and click feature for charge density, bond energy, component energies, distance parameters
 - Fit a site application-identify the ideal molecule to fit a 3-dimensional topography (enzymatic site)
 - Chemistry simulations and reaction dynamics
 - Protein folding problem
 - DNA and RNA structure

Dynamic Simulations Using Exact Solutions

Modeling may become more accurate and productive than experimental screening with orders of magnitude reduction in cost, time, and risk





Millsian 1.0

File Edit View Window Plugins Help



Library

Molecules Functional Groups History

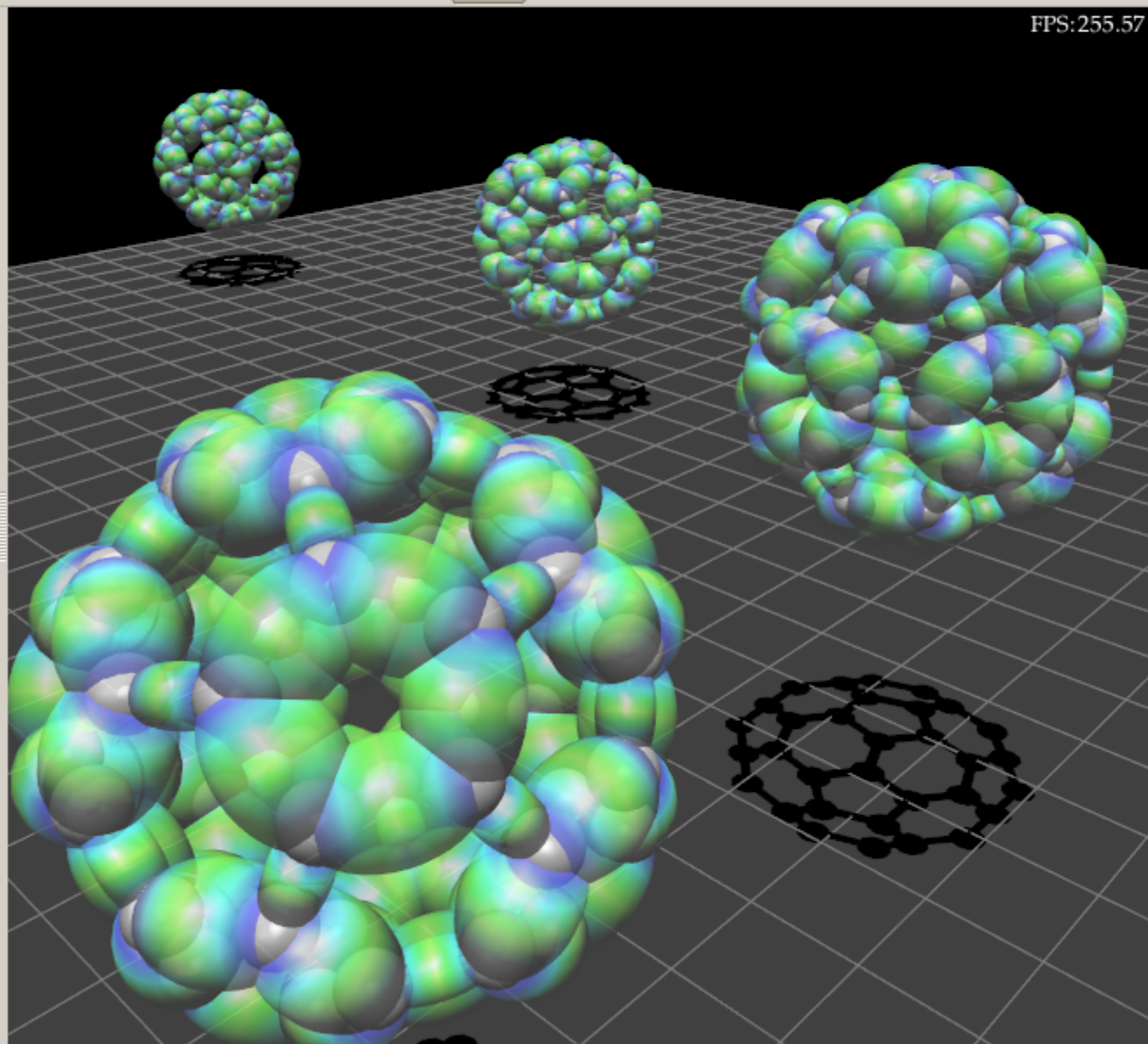
SMILES

- [-] Boranes (Alkoxy)
- [-] Boranes (Alkyl)
- [-] Boranes (Amino)
- [-] Boron Chlorides
- [-] Boron Fluorides
- [-] Bromides
- [-] Bromides (Alkyl)
- [-] Carbon Allotropes
 - C60
 - (C(C)(C)(C)(C))26
 - (C(C)(C)(C)(C))51
 - (c1(-)c(-)c(-)c(-)c(-)c1)x
- [-] Carboxylic Acids
- [-] Chlorides
- [-] Chlorides (Alkyl)
- [-] Chromium

Properties

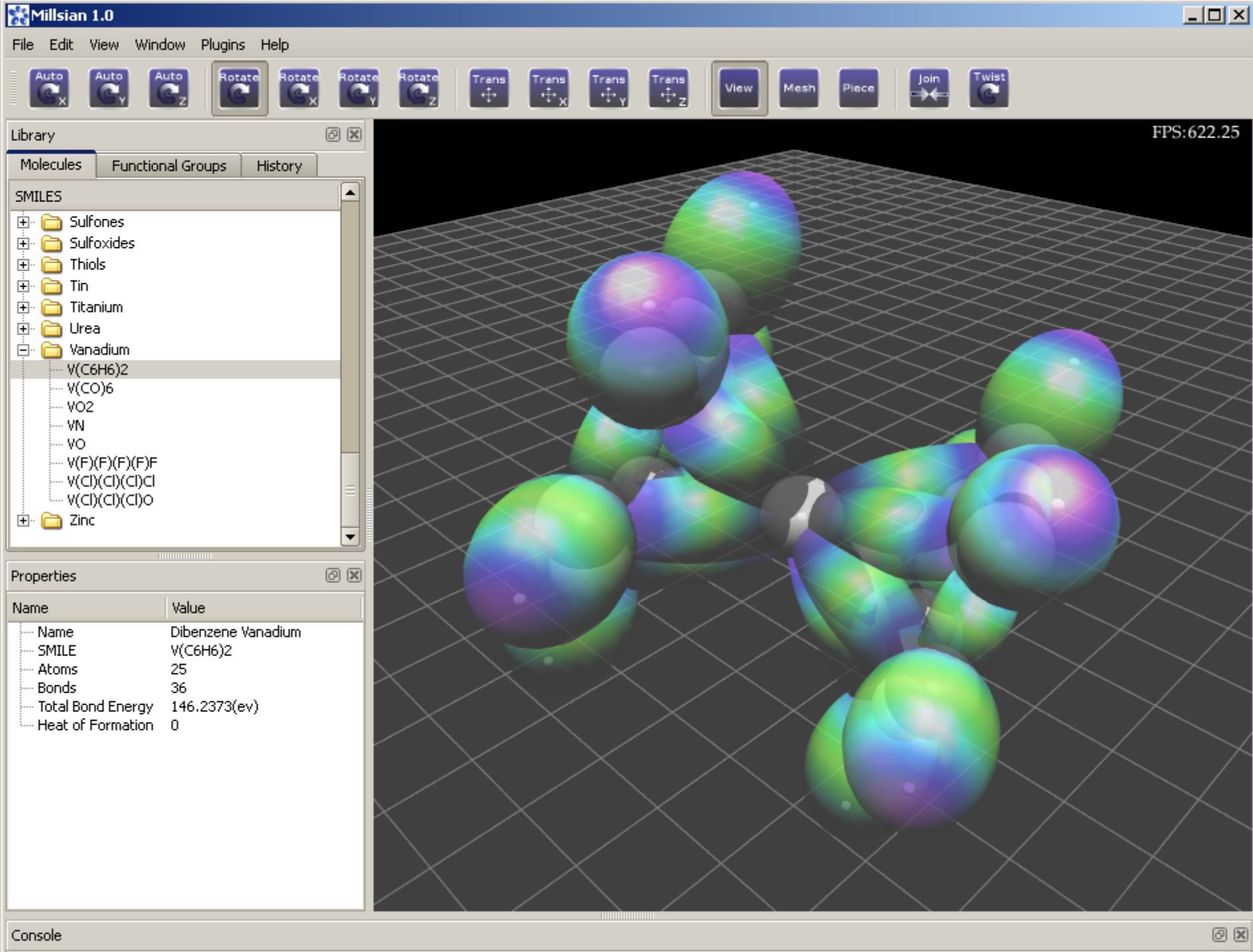
| Name | Value |
|-------------------|--------------|
| Name | C60 |
| SMILES | C60 |
| Atoms | 60 |
| Bonds | 90 |
| Total Bond Energy | 419.7556(ev) |
| Heat of Formation | 0 |

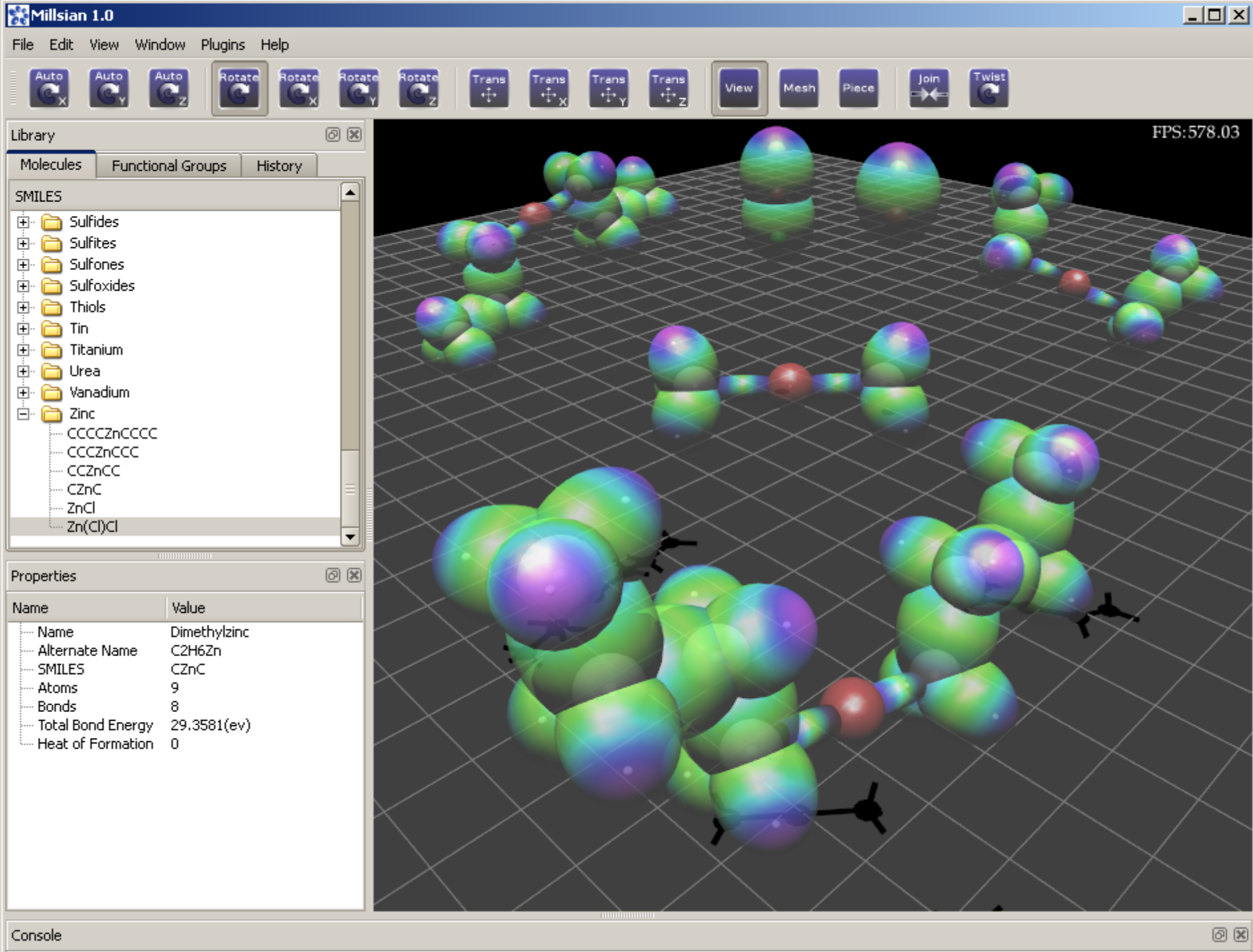
FPS: 255.57



Console







Millsian Demo

